RÉPUBLIQUE ALGÉRIENNE DÉMOCRATIQUE ET POPULAIRE
MINISTÈRE DE L'ENSEIGNEMENT SUPÉRIEUR ET DE LA RECHERCHE SCIENTIFIQUE

Ecole Nationale Polytechnique

Département d'Electrotechnique

المدرسة الوطنية المتعددة التقنيات
Ecole Nationale Polytechnique

Laboratoire de Recherche en Électrotechnique (LRE)

Laboratoire de Commande des Processus (LCP)

THESIS for the award of the Third Cycle D-LMD Doctorate degree in Electrotechnics

Presented by:

HOGGUI ABDELFATTAH

Comparative Study of Control Strategies Applied to the Five-Phase Induction Machine

Publicly defended on (02/07/2025) before the following jury:

President:	BOUKHETALA Djamel	Professor	ENP
Supervisor:	MAHMOUDI Mohand Oulhadj	Professor	ENP
Co-Supervisor:	BENACHOUR Ali	MCA	ENSTA
Examiners:	MOUALDIA Abdelhafidh	Professor	Medea University
	BERKOUK El Madjid	Professor	ENP

ENP 2025

RÉPUBLIQUE ALGÉRIENNE DÉMOCRATIQUE ET POPULAIRE
MINISTÈRE DE L'ENSEIGNEMENT SUPÉRIEUR ET DE LA RECHERCHE SCIENTIFIQUE

Ecole Nationale Polytechnique

Département d'Electrotechnique

المدرسة الوطنية المتعددة التقنيات
Ecole Nationale Polytechnique

Laboratoire de Recherche en Électrotechnique (LRE)

Laboratoire de Commande des Processus (LCP)

THESIS for the award of the Third Cycle D-LMD Doctorate degree in Electrotechnics

Presented by:

HOGGUI ABDELFATTAH

Comparative Study of Control Strategies Applied to the Five-Phase Induction Machine

Publicly defended on (02/07/2025) before the following jury:

President:	BOUKHETALA Djamel	Professor	ENP
Supervisor:	MAHMOUDI Mohand Oulhadj	Professor	ENP
Co-Supervisor:	BENACHOUR Ali	MCA	ENSTA
Examiners:	MOUALDIA Abdelhafidh	Professor	Medea University
	BERKOUK El Madjid	Professor	ENP

ENP 2025

RÉPUBLIQUE ALGÉRIENNE DÉMOCRATIQUE ET POPULAIRE
MINISTÈRE DE L'ENSEIGNEMENT SUPÉRIEUR ET DE LA RECHERCHE SCIENTIFIQUE

Ecole Nationale Polytechnique

Département d'Electrotechnique

المدرسة الوطنية المتعددة التقنيات
Ecole Nationale Polytechnique

Laboratoire de Recherche en Électrotechnique (LRE)

Laboratoire de Commande des Processus (LCP)

Thèse pour l'obtention du titre de Docteur du Troisième Cycle D-LMD en Électrotechnique

Présenté par:

HOGGUI ABDELFATTAH

Étude comparative des stratégies de commande appliquées à la machine asynchrone pentaphasée

Soutenue publiquement le 02/07/2025 devant le jury suivant :

Président:	BOUKHETALA Djamel	Professeur	ENP
Directeur de thèse:	MAHMOUDI Mohand Oulhadj	Professeur	ENP
Co-directeur de thèse:	BENACHOUR Ali	MCA	ENSTA
Examinateurs:	MOUALDIA Abdelhafidh	Professeur	Université de Médéa
	BERKOUK El Madjid	Professeur	ENP

ENP 2025

الملخص

تركز هذه الأطروحة على دراسة وتنفيذ تقنيات التحكم المتقدمة للمحركات الحثية خماسية الأطوار، التي تتميز بموثوقيتها العالية، وأدائها المتفوق، وقدرتها على تحمل الأعطال مقارنة بالأنظمة التقليدية ثلاثية الأطوار. تتناول الدراسة ثلاث استراتيجيات تحكم رئيسية: التحكم المباشر بالعزم (DTC)، التحكم المباشر بالعزم مع التضمين المتجهي (DTC-SVM)، والتحكم التنبؤي ذو المجموعة المنتهية (FCS-MPC). بالإضافة إلى ذلك، تقدم الأطروحة تطورين رئيسيين: دمج الشبكات العصبية الاصطناعية (ANNs) لتحسين أداء التحكم، وتطبيق نظام التكيف المرجعي (MRAS) للتحكم في السرعة بدون مستشعر ميكانيكي. تسلط النتائج الضوء على نقاط القوة والضعف لكل تقنية، مما يوفر رؤى حول ملاءمتها للتطبيقات الصناعية المختلفة. يفتح هذا العمل المجال لمزيد من الأبحاث لتطوير تقنيات هجينة تستفيد من نقاط القوة لكل منها وتكييفها للتعامل مع ظروف الأعطال والاستفادة الكاملة من المزايا التي تقدمها المحركات الحثية خماسية الأطوار.

الكلمات المفتاحية: الأنظمة متعددة الأطوار ـ محرك حثي خماسي الأطوار ـ مغير جهد خماسي الأطوار ذو مستويين ـ التحكم المباشر بالعزم ـ تعديل متجه الفضاء ـ التحكم التنبؤي ـ الشبكات العصبية الاصطناعية ـ التحكم بدون مستشعر سرعة ـ النظام التكيفي المرجعي.

Résumé

Cette thèse porte sur l'étude et la mise en œuvre de techniques de commande avancées pour les machines asynchrones pentaphasées, qui sont de plus en plus appréciées pour leur fiabilité accrue, leurs performances élevées et leurs capacités de tolérance aux défauts par rapport aux systèmes triphasés conventionnels. La recherche explore et compare trois stratégies de commande majeures : la commande directe du couple (DTC), la commande directe du couple avec modulation vectorielle (DTC-SVM) et le contrôle prédictif à ensemble fini (FCS-MPC). En outre, la thèse introduit deux avancées importantes : l'intégration de réseaux de neurones artificiels (RNA) pour améliorer les performances de commande et la mise en œuvre d'un système adaptatif à modèle de référence (MRAS) pour une commande sans capteur de vitesse. Les résultats mettent en évidence les forces et les limites de chaque technique, offrant des perspectives sur leur pertinence pour des applications industrielles spécifiques. Ce travail ouvre la voie à de futures recherches visant à développer des approches hybrides combinant les forces de ces méthodes et à les adapter pour gérer les conditions de défaut, exploitant pleinement les avantages des machines asynchrones pentaphasées.

Mots-clés : Systèmes multiphasés -Machine asynchrone pentaphasée - Onduleur à cinq bras à deux niveaux - Commande directe du couple - Modulation vectorielle d'espace - Contrôle prédictif - Réseaux de neurones artificiels - Commande sans capteur de vitesse - Système adaptatif à modèle de référence.

Abstract

This thesis focuses on the study and implementation of advanced control techniques for five-phase induction motors, which are increasingly valued for their enhanced reliability, superior performance, and fault-tolerant capabilities compared to conventional three-phase systems. The research explores and compares three prominent control strategies: Direct Torque Control (DTC), Direct Torque Control with Space Vector Modulation (DTC-SVM), and Finite Control Set Model Predictive Control (FCS-MPC). Additionally, the thesis introduces two significant advancements: the integration of artificial neural networks (ANNs) to enhance control performance and the implementation of a Model Reference Adaptive System (MRAS) for speed sensorless control. The results highlight the strengths and limitations of each technique, providing insights into their suitability for various industrial applications. This work paves the way for further research into hybrid approaches that combine the strengths of these methods and tailor them to handle fault conditions, fully harnessing the advantages offered by five-phase induction motors.

Keywords: Multiphase Systems - Five-Phase Induction Motor - Two-Level Five-Phase Voltage Source Inverter - Direct Torque Control - Space Vector Modulation - Predictive Control - Artificial Neural Networks - Speed Sensorless Control - Model Reference Adaptive System.

Remerciements

I thank Allah, the Almighty, for granting me the strength, patience, and health throughout these long years of study.

I would like to express my deepest gratitude to my thesis supervisors, **Prof. Mohand Oulhadj MAHMOUDI** (ENP) and **Prof. Ali BENACHOUR** (ENSTA), for their guidance, trust, and continuous support throughout the course of this work.

I am honored to extend my sincere thanks to **Prof. Djamel BOUKHETALA** (ENP), *President of the Jury*, for presiding over the defense of this thesis.

My heartfelt appreciation also goes to the esteemed jury members for their valuable time, constructive comments, and insightful feedback:

- **Prof. Abdelhafidh MOUALDIA** (Medea University)
- **Prof. El Madjid BERKOUK** (ENP)

I am also truly grateful to all the **professors of the Electrotechnics Department** for their teaching and support throughout my academic journey.

Finally, I warmly thank all those—colleagues, friends, and family—who have contributed in any way to my academic and personal development.

Contents

List of Tables

List of Figures

List of Acronyms

- **SVM** : Space Vector Modulation
- **DTC** : Direct Torque Control
- **DTC-SVM** : Direct Torque Control with Space Vector Modulation
- **FCS-MPC** : Finite Control Set Model Predictive Control
- **T-NPC** : T-Type Neutral-Point Clamped (Three-Level Inverter)
- **NN** : Neural Network
- **LM** : Levenberg-Marquardt Optimizer
- **PI Controllers** : Proportional-Integral Controllers
- **MRAS** : Model Reference Adaptive System
- **THD** : Total Harmonic Distortion

General Introduction

General Introduction

In recent years, the use of electric drives in embedded systems instead of conventional motors has intensified. This is the case for the propulsion of electric vehicles and railway traction, all-electric ships, more-electric aircraft, and renewable energy sources [1–4]. The specific constraints imposed on the volume of these systems and the constant need to achieve higher power levels lead to optimizing the use of all components of the electric traction chain. Consequently, nominal operating regions are pushed to their limits, resulting in system faults or nonlinear behaviors such as voltage and current limitations or magnetic saturation. For example, the use of electric drives for the propulsion of electric vehicles requires controlling the drive over the entire speed range, including the flux-weakening region where voltage limits are reached.

Compared to conventional three-phase drives, multiphase drives reduce electrical constraints on machine components and power electronics, as they can handle more power with lower torque ripple, reduced current harmonic content, and intrinsic fault tolerance capabilities [5–8]. These advantages make them an ideal candidate for applications where limits may be reached and where reliability is of particular interest for economic and safety reasons. Recent research on multiphase drives aims to exploit their unique characteristics and present them to the industry as an alternative to three-phase drives. Indeed, the higher number of phases offers additional degrees of freedom in terms of control and design, which can improve overall system reliability and performance.

These advantages have motivated researchers to adapt control techniques, initially developed for three-phase systems, to multiphase systems to exploit the unique benefits of this advanced configuration [9–14]. However, despite the growing interest in these systems, there is a lack of in-depth studies directly comparing the performance of different control strategies applied to multiphase motors. This lack of comparative studies limits the understanding of the advantages and disadvantages of different approaches and complicates the choice of the most suitable strategy based on the specific requirements of each application.

The research presented in this thesis aims to fill this gap by proposing a comparative analysis of control methods applied to the five-phase induction motor, taken here as a representative example of multiphase systems. Unlike their traditional three-phase counterparts, this motor has five stator windings, providing higher reliability and distributing power over a greater number of phases, thereby reducing stress on each winding [15–21].

The studied strategies include Direct Torque Control (DTC), Direct Torque Control with Space Vector Modulation (DTC-SVM), and Finite Control Set Model Predictive Control (FCS-MPC). Through simulations in Matlab/Simulink and experimental validation on a 3.5 kW five-phase induction motor, the performance of these strategies was evaluated by examining their dynamic response during speed reference variations, their static response under steady-state conditions, as well as energy quality, particularly stator voltage and current. The objective is to identify the strengths and weaknesses of each approach to provide key elements for determining the optimal control technique to maximize the performance of five-phase induction motors based

on the specific requirements of each application.

To improve the robustness of these control strategies, Artificial Neural Networks (ANN) have been introduced to replace proportional-integral (PI) regulators, and a speed estimator based on the Model Reference Adaptive System (MRAS) has been integrated to enable robust sensorless control.

This thesis is structured to provide a comprehensive analysis of the comparative study between all these control techniques applied to five-phase induction motors, as follows:

- The first chapter presents the state of the art of multiphase machines, covering their advantages, classifications, and industrial applications.

- The second chapter focuses on the mathematical modeling of five-phase induction machines, followed by a discussion on the configuration and operation of two-level and T-NPC three-level inverters, along with their space vector modulation.

- The third chapter explores various control techniques applied to these machines, analyzing their theoretical foundations and key principles. Their performance is evaluated through simulations carried out in Matlab/Simulink, highlighting their advantages and limitations.

- The fourth chapter presents the experimental validation of the control strategies on a 3.5 kW five-phase induction machine, assessing their effectiveness by analyzing dynamic and steady-state performance under various operating conditions.

Finally, the thesis concludes with a general conclusion summarizing the obtained results and proposing perspectives for future research.

Chapter 1:
State of The Art of Multiphase Machines

Chapter 1

Chapter 1: State of The Art of Multiphase Machines

1.1 Introduction

Multiphase machines have garnered significant interest in recent years due to their numerous advantages over conventional three-phase machines. The increasing demand for high-performance electrical drives in industrial applications, electric transportation, and renewable energy systems has led to extensive research on multiphase systems. These machines offer improved fault tolerance, enhanced torque performance, and reduced harmonic content, making them well-suited for applications requiring high reliability and efficiency.

The evolution of multiphase machines has been driven by advancements in power electronics and control strategies, enabling greater flexibility and improved operational efficiency. Compared to traditional three-phase systems, multiphase machines provide additional degrees of freedom in control, allowing for better electromagnetic performance, reduced losses, and optimized power distribution. Furthermore, they enable advanced strategies such as harmonic current injection and fault-tolerant operation, making them a viable solution for next-generation electrical drive systems.

This chapter presents a comprehensive review of the state of the art of multiphase machines, focusing on their fundamental principles, classifications, advantages, and industrial applications. Given its advantages in terms of fault tolerance, torque ripple reduction, and improved power distribution, the five-phase induction machine is selected as the reference system for this thesis.

1.2 Historical Background of Multiphase Machines

Since the early twentieth century, one of the pioneering applications of high-power onboard electric propulsion has been in cruise ship propulsion systems. This development was driven by the ability to efficiently distribute power system components while eliminating the need for a large mechanical transmission shaft. A notable example of this innovation was the Normandie, which, in 1932, was equipped with four 30 MW motors, marking a prestigious milestone in electric propulsion [22, 23].

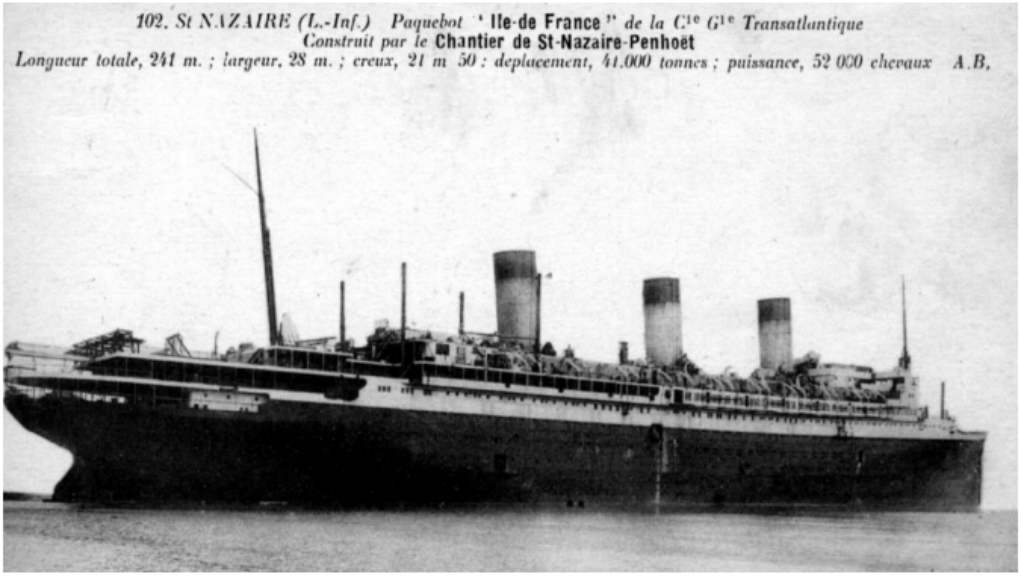

Figure 1.1: The NORMANDIE with four 30 MW motors

At that time, power electronics had not yet emerged, making it impractical to segment the power of three-phase machines. This necessity only became evident with the widespread adoption of static energy converters in later years.

An initial approach to power segmentation involved six-phase (hexaphase) machines, configured in two independent star connections. This multiphase topology leveraged well-established principles of three-phase winding design. In this arrangement, the magnetic poles generated by the windings were phase-shifted by 30°. The windings were typically supplied independently via full-wave current inverters, with currents carefully distributed among phase groups to mitigate mutual induction effects. A comprehensive synthesis of various multiphase (multi-star) machine configurations and related research was provided in [24].

Initially, multiphase machines did not garner immediate industrial interest and only gained traction following the foundational work of E.E. Ward and Harrer [25]. Their research introduced the first experimental investigations on inverter-fed five-phase induction motors, demonstrating that increasing the number of phases effectively reduced torque pulsations.

As the conventional three-phase paradigm evolved, odd-phase configurations such as five-phase and seven-phase systems became preferable, with windings connected through a single coupling mechanism. The shift toward an odd number of phases played a key role in reducing spatial harmonics, thereby minimizing electromagnetic torque ripples, as first suggested by E.E. Ward and Harrer. This characteristic proved advantageous for mechanical components in motion, as residual oscillatory torques were shifted to higher frequency ranges, where they were naturally attenuated by the mechanical load [26–28]. Such improvements in vibration reduction positioned multiphase machines as an optimal choice for electric ship propulsion, particularly in the cruise ship industry, where passenger comfort was paramount.

In military applications, stealth considerations further incentivized the adoption of segmented machine architectures. Notably, in 2003, Framatome/Jeumont introduced a system comprising two sets of thirteen-phase machines, while Alstom developed a three-set five-phase system for the British Navy's Type 45 destroyer.

Figure 1.2: Royal Navy Type 45 Destroyer HMS Dragon

By the 1980s, following significant advancements in power segmentation and torque smoothing, research focus shifted towards system redundancy. The study conducted by Thomas M. Jahns [29] underscored the advantages of increasing the number of independent phases to enhance redundancy in electric propulsion systems. This principle had already been applied in double-star machines, enabling operation in degraded mode at half of nominal power. The concept was further extended to highly multiphase machines, significantly improving reliability and availability in electric motorization.

From a conceptual standpoint, studies have demonstrated that power segmentation across multiple phases, combined with advanced winding techniques, enhances slot filling. Despite an increased number of power components, the overall volume of these components remains smaller compared to conventional three-phase systems. These advancements not only increase the power density of machines but also establish the number of phases as a crucial design parameter [30, 31], serving as an optimization factor in complex and advanced systems. Consequently, multiphase machines have transitioned from niche experimental concepts to practical solutions that significantly enhance the technical and economic balance of power systems.

The research of Toliyat et al. [32] explored the performance of induction machines with varying phase numbers in conjunction with static converters. Their work, Analysis of a Concentrated Winding Induction Machine for Adjustable Speed Drive Applications, provided critical insights into the potential of multiphase motor systems.

The theoretical framework for standard symmetrical multiphase induction machines has been comprehensively documented in multiple sources [33]. Additionally, Nelson and Krause [34] formulated voltage equations in phase variables and developed transformations to the d–q–o reference frame for multiphase machines with asymmetrical phase displacement.

F. Locment [30] conducted extensive research on the design and modeling of a seven-phase permanent magnet axial flux synchronous machine, investigating its vector control strategies under both normal and fault conditions. Similarly, B. Boussiala's [35] master's thesis focused on the vector control of multiphase asynchronous machines, with particular emphasis on seven-phase configurations.

The following sections present the fundamental principles underlying multiphase machines, explore various types and configurations, and outline the objectives of this study.

1.3 Operating Principle of Multiphase Machines

Similar to the operation of a three-phase induction motor, an n-phase induction motor functions based on Faraday's law of electromagnetic induction and Lenz's law citekhadar20211[23].

Multiphase machine has stator windings placed at specific angular positions. However, instead of three windings (separated by $\frac{2\pi}{3}$ electrical), it has n-windings (e.g. 5, 6, or more phases) that are distributed uniformly over the stator circumference (separated by $\frac{2\pi}{n}$ electrical). When a balanced n-phase voltage system is applied, with phase angles displaced by $\alpha = \frac{2\pi}{n}$, a rotating magnetic field is produced.

Initially, when the rotor is stationary, electromagnetic forces are induced in its windings as a result of the interaction with the rotating magnetic field. Since the rotor windings are short-circuited, circulating currents are established, leading to a reaction that opposes the cause of their induction, according to Lenz's law[36].

These currents generate a torque that causes the rotor to begin rotating in the same direction as the rotating magnetic field. As the rotor accelerates, the relative speed difference between the rotor and the magnetic field (slip) decreases, causing a reduction in the induced EMF and rotor currents. When this speed differential reaches zero, rotor currents cease, resulting in zero electromagnetic torque. The number of stator phases increases the smoothness of the torque, reducing the torque ripple. Depending on the shaft load, However, in practical operation, the rotor always stabilizes at a speed ω slightly lower than the synchronous speed ω_s, as determined by the applied shaft load. This principle is illustrated in Figure 1.3.

The machines slip is defined by the ratio: $g = \frac{\omega_s - \omega}{\omega_s}$.

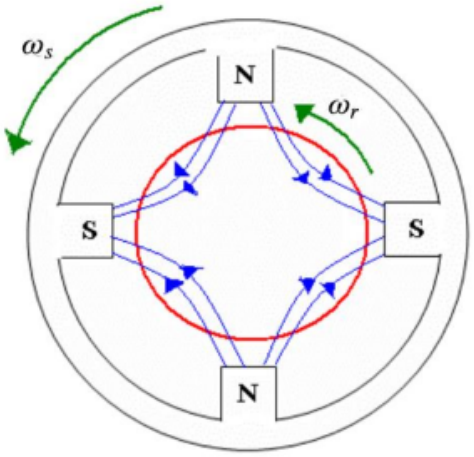

Figure 1.3: Operating Principle of Multiphase Machines

1.4 Characteristics of Multiphase Machines

The primary reason for transitioning from the conventional three-phase system to a multiphase (n-phase) system, where $n > 3$, particularly in high-power applications, lies in the distribution of electrical power among a greater number of phases. Consider a three-phase drive system designed to deliver mechanical power P to a load. The power inverter feeding this system must supply the same total power P, meaning each phase of the inverter is responsible

for $P/3$. However, when power demand exceeds certain thresholds, it becomes challenging to handle this load within the constraints of available power electronics technology.

Limitations such as the current or voltage capacities of power components, as well as the maximum feasible number of components that can be connected in series or parallel within a phase, can restrict the achievable power. To overcome these challenges, distributing the total power across more than three phases becomes necessary. This segmentation of power can be achieved using various approaches, thereby reducing the load on each phase and optimizing system performance For example, in a 5-phase system, each phase would handle only $P/5$, reducing the load per phase. This makes it easier to manage the power within the capabilities of the electronic components [37].

1.4.1 Classification of Multiphase Induction Machines

Multiphase induction machines can be categorized based on the parity of the number of phases. This classification allows for multiple configurations depending on the angular displacement between adjacent coils. The equivalent number of phases is given by:

$$nph_\gamma = \frac{\pi}{\gamma} \tag{1.1}$$

where γ represents the angular displacement between two adjacent coils.

Two primary types of multiphase induction machines can be distinguished.

1.4.1.1 Type 1 Multiphase Machines

These multiphase machines, commonly referred to as "multi-star machines," have a stator phase number (Nph_γ) that is a multiple of three. This configuration allows the phases to be organized into sets of three-phase stars, denoted as η. Various configurations are possible depending on the angular displacement γ between adjacent coils [37].

For instance, in a double-star machine ($Nph_\gamma = 6$ phases), the machine's characteristics vary based on the displacement between stars: $\gamma = 0$, $\gamma = \pi/6$, or $\gamma = \pi/3$. An equivalent number of phases is introduced, defined as [37]:

$$Nph_\gamma = \frac{\pi}{\gamma} \tag{1.2}$$

A machine with six phases, regularly shifted by $\pi/3$, exhibits the same operating characteristics (in terms of time harmonics) as a three-phase machine, for which $Nph = Nph_\gamma = 3$.

Table 1.1 presents different configurations of Type 1 Multiphase Machines**, highlighting the number of phases, the equivalent number of phases, the angular displacement, and the corresponding classification.

Table 1.1: Multiphase Machine Type 1

Nombre de phases (N_{ph})	**Nombre équivalent de phases** ($N_{ph\gamma}$)	**Décalage angulaire** (γ) degré	**Nom correspondant**
3	1.5	120	Triphasée
3	3	60	Semi six-phasée
6	3	60	Six-phasée
6	6	30	Semi-12 phase
12	6	30	12 phases
9	4.5	40	Neuf-phasée
9	9	20	Semi-18 phase
18	9	20	18 phases

In standard operation, it is generally recommended to isolate the neutrals of multi-star machines to optimize performance and reduce circulating currents.

1.4.1.2 Type 2 Multiphase Machines

In this type of machine, the number of stator phases Nph_γ is not a multiple of three. For machines with an odd number of phases, the phases are evenly spaced with a displacement given by [37]:

$$\frac{2\pi}{Nph} = 2\gamma \tag{1.3}$$

As a result, the number of phases is equal to the equivalent number of phases, i.e.,

$$Nph = Nph_\gamma = \frac{\pi}{\gamma} \tag{1.4}$$

Examples of Type 2 multiphase machines are listed in Table 1.2, highlighting the number of phases, the equivalent number of phases, the angular displacement, and the corresponding classification.

Table 1.2: Multiphase Machine Type 2

Nombre de phases (N_{ph})	**Nombre équivalent de phases** ($N_{ph\gamma}$)	**Décalage angulaire** (γ) degré	**Nom correspondant**
2	2	90	Biphasee
4	2	90	Titra-phasée
4	4	45	Semi-8phas
8	4	45	8-phases
5	5	36	5-phases
7	7	25.71	7-phases
10	10	18	Semi-10 phase
11	11	16.36	10 phases

1.4.2 Stator Winding Configurations

After classifying the different types of multiphase machines, odd-phase multiphase configurations can adopt various winding topologies. Among them, the symmetrical five-phase induction motor is one of the most widely utilized and serves as a representative example [36].

In the literature, two principal architectures for five-phase induction machines are identified. The first relies on a sinusoidal air-gap magnetomotive force (MMF) and requires purely sinusoidal voltages, making low-order harmonics unsuitable for motor input.

Conversely, the second approach leverages low-order harmonics to synthesize the air-gap MMF, with particular emphasis on third-harmonic injection, which significantly enhances torque production.

In five-phase induction machine drive systems, three main winding configurations are commonly used: star, pentagon, and pentacle connections.

Research findings indicate that the star connection performs better under normal operating conditions, whereas the pentagon connection provides higher maximum output and reduced torque ripple under fault conditions [36].

Additionally, for the same DC-link voltage magnitude, the pentagon connection increases the winding voltage by 17.69% compared to the star connection, while the pentacle configuration achieves a 90% voltage gain. Due to this advantage, the pentacle connection is preferred in high-speed five-phase induction machine applications with limited DC-link voltage [36]. The star and pentagon configurations are illustrated in Figure 1.4 [36].

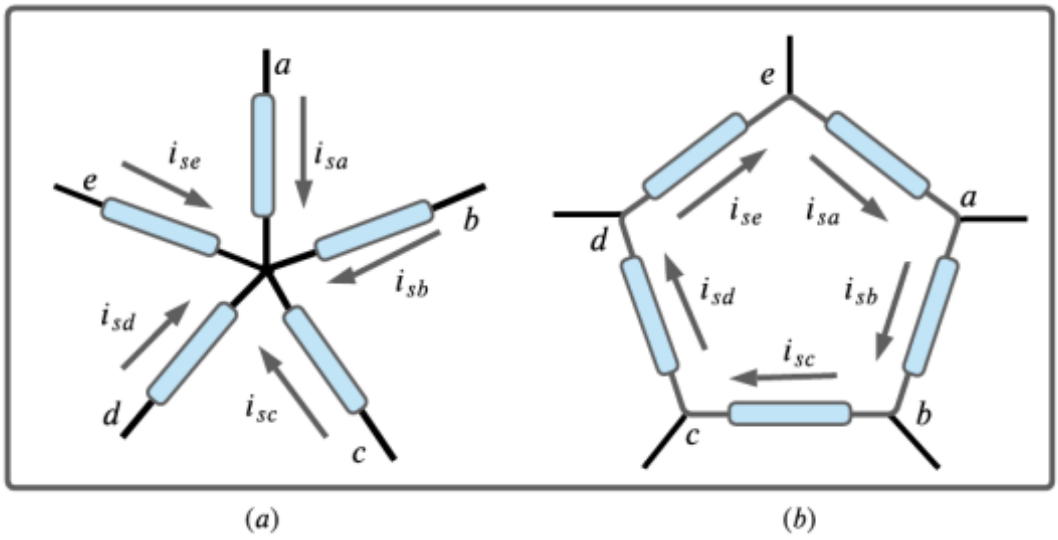

Figure 1.4: Different stator winding configurations: (a) star and (b) pentagon.

1.5 Emerging Applications and Future Prospects of Multiphase Machines

Recent advancements in multiphase machine research have led to their increasing adoption across various high-performance applications. Industries such as electric vehicles (EVs), railway traction, all-electric ships, more-electric aircraft, and renewable energy generation have recognized the potential benefits of multiphase machines, including enhanced reliability, fault tolerance, and efficiency [38].

The EV industry has increasingly adopted multiphase motors due to their superior performance characteristics, including improved fault tolerance, higher power density, and reduced torque ripple. Leading automotive manufacturers have already incorporated these technologies

into production vehicles:

- **BMW**: The i7 M70 employs a six-phase dual-inverter system with a power density of 2.41 kW/kg, while the iX M60 utilizes a second set of three-phase windings to enhance efficiency and redundancy [38].
- **Mercedes-Benz**: The EQS and EQE models integrate six-phase rear motors with dual three-phase windings, boosting power output and efficiency. The EQE motor, for instance, delivers 215 kW of power and 565 Nm of torque [39].
- **Kia EV6 GT**: Features a rear motor powered by two inverters, each supplying three-phase current to designated windings [40].
- **Ford F-150 Lightning**: Utilizes three STARD UHP six-phase electric motors for enhanced performance, as shown in Figure. 1.5 [41].
- **Koenigsegg Gemera**: Integrates a six-phase motor to optimize current distribution and thermal management [42].
- **NASCAR Electric Prototype**: Employs three six-phase motors—one at the front and two at the rear—for balanced power delivery [43].

Figure 1.5: Ford F-150 with a six-phase motor.

Beyond conventional road vehicles, multiphase motor technology has made significant inroads into motorsports and heavy-duty applications:

- **Motorsports**: The Audi e-tron FE07 Formula E car features a six-phase drivetrain [44], while the Porsche 919 LMP1 hybrid race car employs a 2×3-phase 800V traction motor [45].
- **Commercial Trucks**: Advanced Electric Machines (AEM) and TEVVA MOTORS LIMITED have designed six-phase motors to minimize torque ripple and noise in electric trucks [46].
- **Heavy-Duty Vehicles**: The Dana TM4 SUMO HP drive system incorporates a six-phase inverter to enhance power output. Additionally, Bus Stop Sales & Service has deployed a nine-phase DANA Sumo drive motor in electric buses, as illustrated in Figure. 1.6 [47, 48].

Figure 1.6: Electric bus with a nine-phase motor.

Despite these advancements, several challenges persist in fully leveraging multiphase machines. One of the primary difficulties lies in extending conventional three-phase control methodologies to multiphase systems, requiring the development of novel control strategies and algorithms. Additionally, there remains a gap in research regarding design optimization and parameter estimation techniques, which are crucial for maximizing system performance. Efficient fault detection and management algorithms are also essential to fully exploit the fault-tolerant capabilities of multiphase machines. Furthermore, multiphase generation systems, particularly in renewable energy applications, require further investigation to unlock their full potential [38].

However, despite the growing interest in these systems, a significant research gap remains in directly comparing the performance of different control strategies for multiphase machines. This lack of comparative studies limits the understanding of the strengths and weaknesses of various control methodologies, making it challenging to determine the optimal strategy for specific applications.

The research presented in this thesis aims to address this gap by conducting a comparative analysis of control methods applied to five-phase induction motors, serving as a representative example of multiphase systems. This study will contribute to a deeper understanding of multiphase machine control, facilitating the selection of the most appropriate strategy based on specific application requirements.

1.6 Advantages and Limitations

Machines with a high number of phases, compared to three-phase machines, offer numerous advantages [5–8]:

Advantages

- **Power Segmentation:** Having a higher number of phases implies that the power delivered by each phase is reduced, resulting in lower current passing through each component, thereby reducing the stress on each component.
- **Reliability:** In multiphase machines, up to $q-3$ phases can fail without losing control of the remaining phases, unlike three-phase machines, which require connecting the neutral point to the DC source midpoint. Increasing the number of phases further enhances the degrees of freedom available for machine control.
- **Minimization of Torque Ripples and Rotor Losses:** In a three-phase machine, the torque ripple, whose frequency is six times the fundamental frequency, is primarily caused by the components of the fifth and seventh harmonics. However, in multiphase machines, one of these harmonics does not produce a magnetomotive force (MMF), meaning that the corresponding torque harmonics are naturally eliminated. Additionally, since certain stator current harmonics do not generate MMF, the associated rotor-induced currents are absent for these harmonics. Consequently, a multiphase machine inherently experiences lower rotor losses compared to a three-phase machine.

Limitations

- The number of semiconductors increases with the number of phases, which can potentially increase the overall cost of the converter-machine system.
- The increase in the number of semiconductors, combined with the highly non-linear dynamic structure and the strong coupling between torque and flux, significantly complicates the control process.

1.7 Conclusion

This chapter has reviewed the state of the art of multiphase machines, highlighting their historical development, fundamental principles, classifications, advantages, and industrial applications. Multiphase machines offer significant benefits, including enhanced fault tolerance, improved power distribution, and reduced torque ripple, making them a viable alternative to conventional three-phase systems. However, challenges remain, particularly in terms of control complexity and the lack of comparative analysis of control strategies for multiphase machines. Addressing this gap is crucial for optimizing their performance and selecting the most suitable control method for specific applications.

The next chapter focuses on the mathematical modeling of five-phase induction motors and their associated inverters, establishing the theoretical foundation necessary for developing and implementing different control strategies.

Chapter 2:
Modeling of Five-Phase Induction Machines, and its Power Supply Multiphase Machines

Chapter 2

Chapter 2: Modeling of Five-Phase Induction Machines, and its Power Supply

2.1 Introduction

High-power electric drives pose significant challenges in modern research, with multiphase systems particularly those with more than three phases emerging as a promising solution [8, 13, 33, 49, 50]. The general theory of rotating machines, traditionally used for analyzing three-phase machines, can be effectively extended to multiphase configurations [33]. Among these, the five-phase induction motor has gained considerable attention due to its advantages, including reduced torque ripple at higher frequencies, increased power density, enhanced fault tolerance, and lower per-phase power requirements for a given motor output [8, 13, 49, 50].

The development of five-phase induction motor drives can be traced back to 1969, when a five-phase voltage source inverter was first proposed to power such motors [25]. These inverters play a crucial role in generating the required voltage waveforms, ensuring precise and efficient motor control. The two-level inverter provides a simple yet effective topology with well-defined switching states, while the T-NPC three-level inverter introduces additional voltage levels, allowing for more refined modulation strategies.

This chapter presents a comprehensive mathematical modeling of the five-phase induction motor and its associated two-level and T-NPC three-level inverters. The modeling of the machine begins with the formulation of equations in phase quantities, followed by their transformation into decoupled systems in orthogonal ($\alpha - \beta$) and (d-q) reference frames. In this representation, currents in the (d-q) frame directly contribute to torque and flux production, while the (x-y) components and zero-sequence component do not. This transformation enables the adaptation of established three-phase control strategies, such as Direct Torque Control (DTC), Direct Torque Control with Space Vector Modulation (DTC-SVM) and Finite Control Set Model Predictive Control (FCS-MPC), to the five-phase induction machines.

The chapter then focuses on the mathematical modeling of the two-level and T-NPC three-level five-phase inverters, detailing their switching states, space vector representation, and voltage calculations. The space vector modulation (SVM) strategies for these inverter topologies are presented, highlighting their role in generating sinusoidal output voltages by selecting optimal space vectors and determining their appropriate application times. Special attention is given to the elimination of unwanted voltage components in the $x - y$ plane, ensuring high-quality

output waveforms.

By establishing the theoretical foundation for both the five-phase induction motor and its associated inverter topologies, this chapter provides the necessary groundwork for the development and implementation of different control techniques in the following chapters.

2.2 Modeling of the Five-Phase Induction Machine

To determine the steady-state characteristics of an induction motor with "n" phases, a per-phase equivalent circuit can always be used. However, to determine the dynamic response, which is essential in variable speed drives, a dynamic modeling of the motor is necessary [13, 49].

The modeling of electric machines generally involves very complex equations. In fact, the distribution of windings and the inherent geometry of these machines make their models difficult to implement. However, the adoption of certain simplifying assumptions can help overcome this difficulty.

The mathematical foundations for modeling multiphase machines were established in the first half of the 20th century [26, 51–53]. The goal of these studies is to provide tools that simplify the analysis of systems described by a set of coupled differential equations with variable parameters.

The simplifying assumptions made in this work are as follows:

- The motor has a symmetric, unsaturated armature;
- Hysteresis and eddy currents are negligible;
- The air gap has uniform thickness, and the slotting effect is neglected;
- The self and mutual inductances are independent of the currents flowing in the different windings;
- The flux distribution along the air gap is assumed to be a sinusoidal waveform;
- The spatial distribution of all magneto-motive forces in the machine is sinusoidal;
- The skin effect is negligible;
- Considering a regular phase shift between each pair of sequential phases, the windings of all phases are assumed to be identical.

The five-phase induction machine, classified as a type 2 multiphase machine (characterized by a number of phases "n" not being a multiple of three [54]), consists of a fixed stator and a rotor that rotates around the machine's axis of symmetry. In the evenly spaced slots on the inner face of the stator, there are 5 identical windings with "p" pole pairs; their axes are spaced apart by an electrical angle of $\frac{2\pi}{5} = 72$ degrees. The rotor's electric circuit, known as a squirrel cage and commonly made of cast and molded aluminum, may also use copper bars, with their ends brazed onto two short-circuit rings [55].

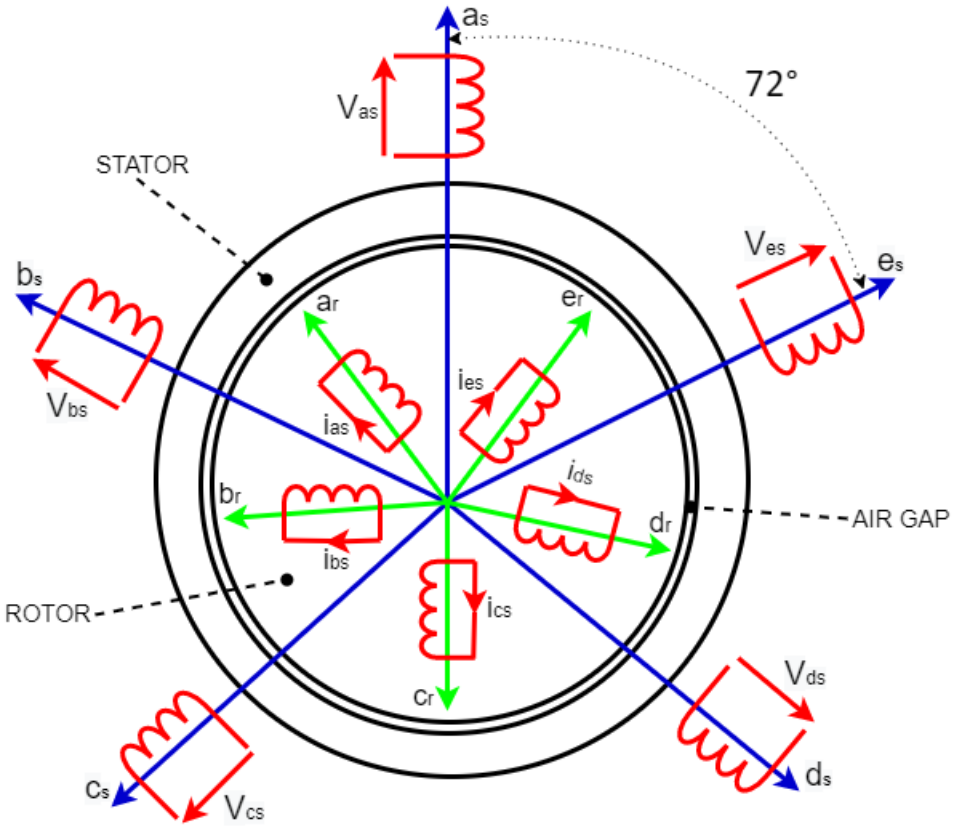

Figure 2.1: Schematic Representation of a Five-Phase Induction Machine

The stator windings, when excited by a balanced five-phase sinusoidal supply, produce a rotating magneto-motive force (MMF) with constant amplitude. The rotating field induces a response in the rotor and produces a useful torque. However, it is not easy to obtain pure sinusoidal voltages from static inverters. The inverter's output voltage contains temporal harmonic components that inject harmonic currents into the machine's stator windings. The five-phase connection eliminates the fifth and other harmonics of multiples of 5. However, other harmonics will still be present with varying amplitudes and phase sequences [56].

First, the voltage and torque equations for the symmetrical five-phase induction machine are established, expressed in phase quantities. Then, the modification made to the transformation associated with an arbitrary reference frame for a stationary circuit is presented, making it applicable to a rotating circuit.

2.2.1 Phase-Quantity Model

Several approaches to modeling multiphase machines are distinguished in the literature, among them the approach based on vector formalism from a concept called "multimachine." This approach mathematically assimilates the real multiphase machine to a set of fictitious two-phase and single-phase machines, where each fictitious machine corresponds to a vector subspace. The number of phases of each fictitious machine is directly related to the dimension of the associated subspace. In other words, the multiphase machine is viewed as an association of fictitious machines that are magnetically decoupled and mechanically coupled [24, 57–59]. Another modeling approach involves proposing control techniques using space vectors of multiphase machines, where the machine's actual quantities form a space vector that is decomposed into several orthogonal space vectors of dimension one or two. In this case, with simplifying as-

sumptions, the voltage equation of the actual machine splits into several completely decoupled equations [31, 32, 60–63].

The model of a five-phase induction machine in terms of voltage and flux can be written in matrix form as follows [33]:

$$\begin{cases} [v^s_{abcde}] = [R_s]\,[i^s_{abcde}] + \frac{d}{dt}\,[\phi^s_{abcde}] \\ [v^r_{abcde}] = [R_r]\,[i^r_{abcde}] + \frac{d}{dt}\,[\phi^r_{abcde}] = 0 \end{cases} \tag{2.1}$$

$$\begin{cases} [\phi^s_{abcde}] = [L_s]\,[i^s_{abcde}] + [L_{sr}]\,[i^r_{abcde}] \\ [\phi^r_{abcde}] = [L_r]\,[i^r_{abcde}] + [L_{rs}]\,[i^s_{abcde}] \end{cases} \tag{2.2}$$

The equations (2.1) and (2.2) can be written as follows:

$$[v^s_{abcde}] = [R_s]\,[i^s_{abcde}] + [L_s]\,\frac{d}{dt}\,[i^s_{abcde}] + \frac{d}{dt}\,[L_{sr} i^r_{abcde}] \tag{2.3}$$

$$[v^r_{abcde}] = [R_r]\,[i^r_{abcde}] + [L_r]\,\frac{d}{dt}\,[i^r_{abcde}] + \frac{d}{dt}\,[L_{rs} i^s_{abcde}] = 0 \tag{2.4}$$

The following definitions of phase voltages, currents, and fluxes apply to (2.1) and (2.2):

$$\begin{bmatrix} v^s_{abcde} \\ v^r_{abcde} \end{bmatrix} = \begin{bmatrix} v^s_a & v^s_b & v^s_c & v^s_d & v^s_e \\ v^r_a & v^r_b & v^r_c & v^r_d & v^r_e \end{bmatrix}^T \tag{2.5}$$

$$\begin{bmatrix} i^s_{abcde} \\ i^r_{abcde} \end{bmatrix} = \begin{bmatrix} i^s_a & i^s_b & i^s_c & i^s_d & i^s_e \\ i^r_a & i^r_b & i^r_c & i^r_d & i^r_e \end{bmatrix}^T \tag{2.6}$$

$$\begin{bmatrix} \phi^s_{abcde} \\ \phi^r_{abcde} \end{bmatrix} = \begin{bmatrix} \phi^s_a & \phi^s_b & \phi^s_c & \phi^s_d & \phi^s_e \\ \phi^r_a & \phi^r_b & \phi^r_c & \phi^r_d & \phi^r_e \end{bmatrix}^T \tag{2.7}$$

The stator and rotor inductances are represented in a matrix form similar to that of a three-phase machine. Due to energy conservation, the matrix $[L_s]$ is a symmetric 5×5 matrix of the form [64].

$$[L_s] = \begin{pmatrix} L_{aas} & L_{abs} & L_{acs} & L_{ads} & L_{aes} \\ L_{bas} & L_{bbs} & L_{bcs} & L_{bds} & L_{bes} \\ L_{cas} & L_{cbs} & L_{ccs} & L_{cds} & L_{ces} \\ L_{das} & L_{dbs} & L_{dcs} & L_{dds} & L_{des} \\ L_{eas} & L_{ebs} & L_{ecs} & L_{eds} & L_{ees} \end{pmatrix} \tag{2.8}$$

With:

- $L_{aas} = L_{bbs} = L_{ccs} = L_{dds} = L_{ees} = (L_{ls} + M)$ are the self-inductances of phases a, b, c, d, e.

- $L_{abs} = L_{bcs} = L_{cds} = L_{des} = L_{aes} = M\cos\alpha$ are the mutual inductances.
- $L_{acs} = L_{bds} = L_{ces} = L_{bes} = L_{ads} = M\cos 2\alpha$ are the mutual inductances.

For the five-phase machine with a phase shift $\alpha = \frac{2\pi}{5}$, the inductance matrix in equation (2.8) can be written as follows:

$$[L_s] = \begin{pmatrix} L_{ls}+M & M\cos\alpha & M\cos 2\alpha & M\cos 2\alpha & M\cos\alpha \\ M\cos\alpha & L_{ls}+M & M\cos\alpha & M\cos 2\alpha & M\cos 2\alpha \\ M\cos 2\alpha & M\cos\alpha & L_{ls}+M & M\cos\alpha & M\cos 2\alpha \\ M\cos 2\alpha & M\cos 2\alpha & M\cos\alpha & L_{ls}+M & M\cos\alpha \\ M\cos\alpha & M\cos 2\alpha & M\cos 2\alpha & M\cos\alpha & L_{ls}+M \end{pmatrix} \tag{2.9}$$

Similarly, the rotor inductance matrices are written as follows:

$$[L_r] = \begin{pmatrix} L_{aar} & L_{abr} & L_{acr} & L_{adr} & L_{aer} \\ L_{bar} & L_{bbr} & L_{bcr} & L_{bdr} & L_{ber} \\ L_{car} & L_{cbr} & L_{ccr} & L_{cdr} & L_{cer} \\ L_{dar} & L_{dbr} & L_{dcr} & L_{ddr} & L_{der} \\ L_{ear} & L_{ebr} & L_{ecr} & L_{edr} & L_{eer} \end{pmatrix} \tag{2.10}$$

$$[L_r] = \begin{pmatrix} L_{lr}+M & M\cos\alpha & M\cos 2\alpha & M\cos 2\alpha & M\cos\alpha \\ M\cos\alpha & L_{lr}+M & M\cos\alpha & M\cos 2\alpha & M\cos 2\alpha \\ M\cos 2\alpha & M\cos\alpha & L_{lr}+M & M\cos\alpha & M\cos 2\alpha \\ M\cos 2\alpha & M\cos 2\alpha & M\cos\alpha & L_{lr}+M & M\cos\alpha \\ M\cos\alpha & M\cos 2\alpha & M\cos 2\alpha & M\cos\alpha & L_{lr}+M \end{pmatrix} \tag{2.11}$$

According to the simplifying assumptions, all self-inductance coefficients are constant, and the mutual inductance coefficients depend only on the position of the windings. Thus, it is assumed at all times that the magnetic axis of the rotor phase (a) makes an angle θ with the magnetic axis of the stator phase (a) (instantaneous position of the rotor relative to the stator), as shown in Fig. 2.1. The mutual inductances between the stator and rotor windings can be obtained from [33]:

$$[L_{sr}] = M \begin{pmatrix} \cos\theta & \cos(\theta+\alpha) & \cos(\theta+2\alpha) & \cos(\theta-2\alpha) & \cos(\theta-\alpha) \\ \cos(\theta-\alpha) & \cos\theta & \cos(\theta+\alpha) & \cos(\theta+2\alpha) & \cos(\theta-2\alpha) \\ \cos(\theta-2\alpha) & \cos(\theta-\alpha) & \cos\theta & \cos(\theta+\alpha) & \cos(\theta+2\alpha) \\ \cos(\theta+2\alpha) & \cos(\theta-2\alpha) & \cos(\theta-\alpha) & \cos\theta & \cos(\theta+\alpha) \\ \cos(\theta+\alpha) & \cos(\theta+2\alpha) & \cos(\theta-2\alpha) & \cos(\theta-\alpha) & \cos\theta \end{pmatrix} \tag{2.12}$$

$$[L_{rs}] = [L_{sr}]^T$$

The stator and rotor resistance matrices are 5×5 diagonal matrices:

$$[R_s] = \text{diag}(R_s, R_s, R_s, R_s, R_s) \tag{2.13}$$

$$[R_r] = \text{diag}(R_r, R_r, R_r, R_r, R_r) \tag{2.14}$$

The derived expression from equation (2.2) is given by:

$$\frac{d}{dt}[\phi^s_{abcde}] = [L_s]\frac{d}{dt}[i^s_{abcde}] + \frac{d[L_{sr}]}{dt}[i^r_{abcde}] + [L_{sr}]\frac{d[i^r_{abcde}]}{dt} \tag{2.15}$$

The second term of the previous equation can be written as follows:

$$\frac{d[L_{sr}]}{dt}[i^r_{abcde}] = \frac{d[L_{sr}]}{d\theta_m}\frac{d\theta_m}{dt}[i^r_{abcde}] \tag{2.16}$$

The mechanical speed of the rotor is defined by: $\Omega_m = \frac{d\theta_m}{dt}$.

Equation (2.15) can be written in the following form:

$$\frac{d}{dt}[\phi^s_{abcde}] = [L_s]\frac{d}{dt}[i^s_{abcde}] + \Omega_m\frac{d[L_{sr}]}{d\theta_m}[i^r_{abcde}] + [L_{sr}]\frac{d[i^r_{abcde}]}{dt} \tag{2.17}$$

2.2.2 Calculation of Electromagnetic Torque

The mechanical equation of motion is given by:

$$J\frac{d^2\theta_m}{dt^2} + f\frac{d\theta_m}{dt} = T_{em} - T_r \tag{2.18}$$

where J and f are the moment of inertia and the friction coefficient, respectively, θ_m is the electrical rotation angle, and C_r is the load torque.

The electromagnetic torque T_{em}, obtained as a function of the stator and rotor phase currents, is expressed as the partial derivative of the magnetic co-energy with respect to the rotor position [65]:

$$T_{em} = \left(\frac{\partial W_{co}}{\partial \theta_m}\right)_{(i_s, i_r \text{ constant})} \tag{2.19}$$

In a linear magnetic system, the co-energy is equal to the stored magnetic energy:

$$W_{co} = \frac{1}{2}\begin{pmatrix}[i^s_{abcde}]^T & [i^r_{abcde}]^T\end{pmatrix}\begin{bmatrix}[L_s] & [L_{sr}] \\ [L_{sr}]^T & [L_r]\end{bmatrix}\begin{bmatrix}i^s_{abcde} \\ i^r_{abcde}\end{bmatrix} \tag{2.20}$$

which simplifies to:

$$W_{co} = \frac{1}{2}\left[i^s_{abcde}\right]^T [L_s] \left[i^s_{abcde}\right] + \frac{1}{2}\left[i^s_{abcde}\right]^T [L_{sr}] \left[i^r_{abcde}\right] + \frac{1}{2}\left[i^r_{abcde}\right]^T [L_{sr}]^T \left[i^s_{abcde}\right] + \frac{1}{2}\left[i^r_{abcde}\right]^T [L_r] \left[i^r_{abcde}\right] \tag{2.21}$$

It is clear that the matrices $[L_s]$ and $[L_r]$ contain only constant coefficients, so equation (2.19) reduces to:

$$T_{em} = \frac{1}{2}\left[i^s_{abcde}\right]^T \frac{\partial [L_{sr}]}{\partial \theta_m} \left[i^r_{abcde}\right] + \frac{1}{2}\left[i^r_{abcde}\right]^T \frac{\partial [L_{sr}]^T}{\partial \theta_m} \left[i^s_{abcde}\right] \tag{2.22}$$

Since the torque T_{em} is a scalar, each of the two terms of the torque must be scalar. And since the transpose of a scalar is obviously the scalar itself, it must be true that the second term is equal to its transpose [62], so:

$$\left[i^r_{abcde}\right]^T \frac{\partial [L_{sr}]^T}{\partial \theta_m} \left[i^s_{abcde}\right] = \left(\left[i^r_{abcde}\right]^T \frac{\partial [L_{sr}]^T}{\partial \theta_m} \left[i^s_{abcde}\right]\right)^T \tag{2.23}$$

From matrix algebra: $(A^T B^T C)^T = C^T B A$, we have:

$$\left[i^r_{abcde}\right]^T \frac{\partial [L_{sr}]^T}{\partial \theta_m} \left[i^s_{abcde}\right] = \left[i^s_{abcde}\right]^T \frac{\partial [L_{sr}]}{\partial \theta_m} \left[i^r_{abcde}\right] \tag{2.24}$$

Consequently, the first term in equation (2.22) is equal to the second. The torque equation then reduces to the final form:

$$T_{em} = \left[i^s_{abcde}\right]^T \frac{\partial [L_{sr}]}{\partial \theta_m} \left[i^r_{abcde}\right] \tag{2.25}$$

Up to this point, we have assumed, for simplicity, that the machine has only two poles. In general, p represents the number of pole pairs of the motor. It is clear that any inductance, which is a function of angular position, undergoes $p/2$ complete cycles when θ_m varies from 0 to 2π.

That is, $\theta = \frac{p}{2}\theta_m$, where θ is the rotor position in electrical radians (rad) [65].

As a function of θ, the motor torque is clearly given by:

$$T_{em} = \frac{p}{2}\left[i_{abcde}\right]^T \left[\frac{d[L]}{d\theta}\right] \left[i_{abcde}\right] = \frac{p}{2}\left[\left[i^s_{abcde}\right]^T \left[i^r_{abcde}\right]^T\right] \left[\frac{d[L]}{d\theta}\right] \begin{bmatrix} i^s_{abcde} \\ i^r_{abcde} \end{bmatrix} \tag{2.26}$$

With:

$$[L] = \begin{bmatrix} [L_s] & [L_{sr}] \\ [L_{sr}]^T & [L_r] \end{bmatrix}$$

The torque equation can then be elaborated as follows:

$$T_{em} = \frac{p}{2} \begin{bmatrix} 0 & [i^s_{abcde}]^T \frac{\partial [L_{sr}]}{\partial \theta} \\ [i^r_{abcde}]^T \frac{\partial [L_{rs}]}{\partial \theta} & 0 \end{bmatrix} \begin{bmatrix} i^s_{abcde} \\ i^r_{abcde} \end{bmatrix} \tag{2.27}$$

which simplifies to:

$$T_{em} = \frac{p}{2} \left([i^s_{abcde}]^T \frac{\partial [L_{sr}]}{\partial \theta} [i^r_{abcde}] + [i^r_{abcde}]^T \frac{\partial [L_{rs}]}{\partial \theta} [i^s_{abcde}] \right) \tag{2.28}$$

and since:

$$[i^r_{abcde}]^T \frac{\partial [L_{rs}]}{\partial \theta} [i^s_{abcde}] = [i^r_{abcde}]^T \frac{\partial [L_{sr}]^T}{\partial \theta} [i^s_{abcde}] = \left([i^s_{abcde}]^T \frac{\partial [L_{sr}]}{\partial \theta} [i^r_{abcde}] \right)^T \tag{2.29}$$

The electromagnetic torque becomes:

$$T_{em} = p [i^s_{abcde}]^T \frac{\partial [L_{sr}]}{\partial \theta} [i^r_{abcde}] \tag{2.30}$$

By substituting the stator and rotor currents from equations (2.6) and (2.12) into (2.30), we get the expanded form of the torque equation:

$$T_{em} = -pM \begin{pmatrix} (i_{as}i_{ar} + i_{bs}i_{br} + i_{cs}i_{cr} + i_{ds}i_{dr} + i_{es}i_{er}) \sin(\theta) \\ +(i_{es}i_{ar} + i_{as}i_{br} + i_{bs}i_{cr} + i_{cs}i_{dr} + i_{ds}i_{er}) \sin(\theta + \alpha) \\ +(i_{ds}i_{ar} + i_{es}i_{br} + i_{as}i_{cr} + i_{bs}i_{dr} + i_{cs}i_{er}) \sin(\theta + 2\alpha) \\ +(i_{cs}i_{ar} + i_{ds}i_{br} + i_{es}i_{cr} + i_{as}i_{dr} + i_{bs}i_{er}) \sin(\theta - 2\alpha) \\ +(i_{bs}i_{ar} + i_{cs}i_{br} + i_{ds}i_{cr} + i_{es}i_{dr} + i_{as}i_{er}) \sin(\theta - \alpha) \end{pmatrix} \tag{2.31}$$

The electromagnetic torque created in this way is then mechanically coupled to the load applied on the machine shaft, satisfying the following differential equation:

$$J \frac{d\omega_m}{dt} = T_{em} - C_r - \frac{f}{p} \omega_m \tag{2.32}$$

where p is the number of pole pairs and ω_m is the electrical rotational speed.

The equations describing the 5-phase machine are strongly coupled and contain time-dependent coefficients. To simplify the mathematical model of the machine, a decoupling transformation is applied, and the five-phase machine is transformed into an equivalent two-phase machine. This transformation is presented in the following section.

2.2.3 Two-Axis Transformation of Multiphase Machines

The current approach to modeling multiphase electric machines is based on the two-axis theory, which transforms a five-phase system into an equivalent two-phase system with axes $(d-q)$ (Fig. I.2), reducing the complexity of the model.

The Park transformation consists of transforming the stator and rotor windings into orthogonal equivalent windings. The transformation of physical quantities is carried out using the generalized Park matrix $P(\theta)$, which is given by the combination of the Concordia matrix $[C]$ (stationary reference frame) and the rotational reference matrix $[D]$. This transformation preserves instantaneous power, which allows the stator and rotor windings to be transformed into equivalent windings from an electrical and magnetic perspective, arranged along two perpendicular axes $(d-q)$ in two steps:

2.2.3.1 The Model in a Stationary Reference Frame

In general, the windings of the multiphase machine are shifted by $\alpha = 2\pi/n$ rad. The machine model described by equations ((2.1)-(2.32)) can be transformed using the Clarke transformation matrix in the power-invariant form [33, 52].

The transformation matrix can be written as [57, 58]:

- For even n:

$$[C] = \sqrt{\frac{2}{n}} \begin{bmatrix} 1 & \cos\left(\frac{2\pi}{n}\right) & \cos\left(\frac{4\pi}{n}\right) & \cdots & \cos\left(\frac{2(n-1)\pi}{n}\right) \\ 0 & \sin\left(\frac{2\pi}{n}\right) & \sin\left(\frac{4\pi}{n}\right) & \cdots & \sin\left(\frac{2(n-1)\pi}{n}\right) \\ \vdots & \vdots & \vdots & \ddots & \vdots \\ 1 & 0 & 1 & \cdots & 0 \\ 0 & 1 & 0 & \cdots & 1 \end{bmatrix} \tag{2.33}$$

- For odd n:

$$[C] = \sqrt{\frac{2}{n}} \begin{bmatrix} 1 & \cos\left(\frac{2\pi}{n}\right) & \cos\left(\frac{4\pi}{n}\right) & \cdots & \cos\left(\frac{2(n-1)\pi}{n}\right) \\ 0 & \sin\left(\frac{2\pi}{n}\right) & \sin\left(\frac{4\pi}{n}\right) & \cdots & \sin\left(\frac{2(n-1)\pi}{n}\right) \\ \vdots & \vdots & \vdots & \ddots & \vdots \\ 1 & \cos\left(\frac{(n-1)\pi}{n}\right) & \cdots & \cdots & \cos\left(\frac{2(n-1)2\pi}{n}\right) \\ 0 & \sin\left(\frac{(n-1)\pi}{n}\right) & \cdots & \cdots & \sin\left(\frac{2(n-1)2\pi}{n}\right) \\ \frac{\sqrt{2}}{2} & \frac{\sqrt{2}}{2} & \frac{\sqrt{2}}{2} & \cdots & \frac{\sqrt{2}}{2} \end{bmatrix} \tag{2.34}$$

For an odd number of phases n, the first two rows of matrix (2.34) define the components (α, β) where the stator-rotor coupling appears only in these equations, while the last row gives the zero component. Between the components (α, β) and the zero component, there are $(n-3)/2$ pairs of component lines (x, y), so one pair (x, y) for the five-phase machine [**?**].

From (2.34), the transformation matrix for a five-phase system ($\alpha = 2\pi/5$) is given by [31]:

$$[C] = \sqrt{\frac{2}{5}} \begin{bmatrix} 1 & \cos\alpha & \cos 2\alpha & \cos 3\alpha & \cos 4\alpha \\ 0 & \sin\alpha & \sin 2\alpha & \sin 3\alpha & \sin 4\alpha \\ 1 & \cos 2\alpha & \cos 4\alpha & \cos 6\alpha & \cos 8\alpha \\ 0 & \sin 2\alpha & \sin 4\alpha & \sin 6\alpha & \sin 8\alpha \\ \frac{1}{\sqrt{2}} & \frac{1}{\sqrt{2}} & \frac{1}{\sqrt{2}} & \frac{1}{\sqrt{2}} & \frac{1}{\sqrt{2}} \end{bmatrix} \begin{matrix} \alpha \\ \beta \\ x \\ y \\ o \end{matrix} \tag{2.35}$$

$$[C]^{-1} = \sqrt{\frac{2}{5}} \begin{bmatrix} 1 & 0 & 1 & 0 & 1/\sqrt{2} \\ \cos\alpha & \sin\alpha & \cos 2\alpha & \sin 2\alpha & 1/\sqrt{2} \\ \cos 2\alpha & \sin 2\alpha & \cos 4\alpha & \sin 4\alpha & 1/\sqrt{2} \\ \cos 3\alpha & \sin 3\alpha & \cos 6\alpha & \sin 6\alpha & 1/\sqrt{2} \\ \cos 4\alpha & \sin 4\alpha & \cos 8\alpha & \sin 8\alpha & 1/\sqrt{2} \end{bmatrix} \tag{2.36}$$

With the new quantities defined as:

$$\begin{aligned} \left[v^s_{\alpha\beta xy0}\right] &= [C]\,[v^s_{abcde}]\,, \quad \left[i^s_{\alpha\beta xy0}\right] = [C]\,[i^s_{abcde}]\,, \quad \left[\phi^s_{\alpha\beta xy0}\right] = [C]\,[\phi^s_{abcde}]\,, \\ \left[v^r_{\alpha\beta xy0}\right] &= [C]\,[v^r_{abcde}]\,, \quad \left[i^r_{\alpha\beta xy0}\right] = [C]\,[i^r_{abcde}]\,, \quad \left[\phi^r_{\alpha\beta xy0}\right] = [C]\,[\phi^r_{abcde}] \end{aligned} \tag{2.37}$$

The substitution of (2.35) in combination with (2.37) into the voltage equations of (2.1) leads to a transformed form of the voltage equations:

$$\begin{pmatrix} \left[v^s_{\alpha\beta xy0}\right] \\ \left[v^r_{\alpha\beta xy0}\right] \end{pmatrix} = \begin{pmatrix} [R_s] & 0 \\ 0 & [R_r] \end{pmatrix} \begin{pmatrix} \left[i^s_{\alpha\beta xy0}\right] \\ \left[i^r_{\alpha\beta xy0}\right] \end{pmatrix} + \frac{d}{dt} \begin{pmatrix} \left[\phi^s_{\alpha\beta xy0}\right] \\ \left[\phi^r_{\alpha\beta xy0}\right] \end{pmatrix} \tag{2.38}$$

which retains the same form as in the phase quantities model. The transformation of the flux equations gives:

$$\begin{pmatrix} \left[\phi^s_{\alpha\beta xy0}\right] \\ \left[\phi^r_{\alpha\beta xy0}\right] \end{pmatrix} = \begin{pmatrix} [C] & 0 \\ 0 & [C] \end{pmatrix} \begin{pmatrix} [L_s] & [L_{sr}] \\ [L_{rs}] & [L_r] \end{pmatrix} \begin{pmatrix} [C]^{-1} & 0 \\ 0 & [C]^{-1} \end{pmatrix} \begin{pmatrix} \left[i^s_{\alpha\beta xy0}\right] \\ \left[i^r_{\alpha\beta xy0}\right] \end{pmatrix} \tag{2.39}$$

$$\begin{pmatrix} \left[\phi^s_{\alpha\beta xy0}\right] \\ \left[\phi^r_{\alpha\beta xy0}\right] \end{pmatrix} = \begin{pmatrix} \left[L^s_{\alpha\beta xy0}\right] & \left[L^{sr}_{\alpha\beta xy0}\right] \\ \left[L^{rs}_{\alpha\beta xy0}\right] & \left[L^r_{\alpha\beta xy0}\right] \end{pmatrix} \begin{pmatrix} \left[i^s_{\alpha\beta xy0}\right] \\ \left[i^r_{\alpha\beta xy0}\right] \end{pmatrix} \tag{2.40}$$

With:

$$[L_{\alpha\beta xy0}] = \begin{pmatrix} \left[L^s_{\alpha\beta xy0}\right] & \left[L^{sr}_{\alpha\beta xy0}\right] \\ \left[L^{rs}_{\alpha\beta xy0}\right] & \left[L^r_{\alpha\beta xy0}\right] \end{pmatrix} = \begin{pmatrix} [C]\,[L_s]\,[C]^{-1} & [C]\,[L_{sr}]\,[C]^{-1} \\ [C]\,[L_{rs}]\,[C]^{-1} & [C]\,[L_r]\,[C]^{-1} \end{pmatrix} \tag{2.41}$$

The individual submatrices are furthermore equal to [33, 65]:

$$\left[L^s_{\alpha\beta xy0}\right] = \begin{bmatrix} L_{Ls} + \frac{5}{2}M & 0 & 0 & 0 & 0 \\ 0 & L_{Ls} + \frac{5}{2}M & 0 & 0 & 0 \\ 0 & 0 & L_{Ls} & 0 & 0 \\ 0 & 0 & 0 & L_{Ls} & 0 \\ 0 & 0 & 0 & 0 & L_{Ls} \end{bmatrix} \tag{2.42}$$

$$\left[L^r_{\alpha\beta xy0}\right] = \begin{bmatrix} L_{Lr}+\frac{5}{2}M & 0 & 0 & 0 & 0 \\ 0 & L_{Lr}+\frac{5}{2}M & 0 & 0 & 0 \\ 0 & 0 & L_{Lr} & 0 & 0 \\ 0 & 0 & 0 & L_{Lr} & 0 \\ 0 & 0 & 0 & 0 & L_{Lr} \end{bmatrix} \tag{2.43}$$

$$\left[L^{rs}_{\alpha\beta xy0}\right] = \frac{5}{2}M \begin{bmatrix} \cos(\theta) & \sin(\theta) & 0 & 0 & 0 \\ -\sin(\theta) & \cos(\theta) & 0 & 0 & 0 \\ 0 & 0 & 0 & 0 & 0 \\ 0 & 0 & 0 & 0 & 0 \\ 0 & 0 & 0 & 0 & 0 \end{bmatrix} \tag{2.44}$$

$$\left[L^{sr}_{\alpha\beta xy0}\right] = \frac{5}{2}M \begin{bmatrix} \cos(\theta) & -\sin(\theta) & 0 & 0 & 0 \\ \sin(\theta) & \cos(\theta) & 0 & 0 & 0 \\ 0 & 0 & 0 & 0 & 0 \\ 0 & 0 & 0 & 0 & 0 \\ 0 & 0 & 0 & 0 & 0 \end{bmatrix} \tag{2.45}$$

Where θ represents the instantaneous position of the rotor. Consequently, the components (x, y) of the stator and rotor are not coupled. Since the windings are orthogonal, there is no mutual coupling between the x components of the stator and the y components of the stator (and similarly for the rotor).

The torque developed by the machine is given by:

$$T_{em} = \frac{p}{2}\left(\begin{bmatrix}\left[i^s_{\alpha\beta xy0}\right]^T & \left[i^r_{\alpha\beta xy0}\right]^T\end{bmatrix}\right)\left(\begin{bmatrix}[C] & 0\\ 0 & [C]\end{bmatrix}\frac{d}{d\theta}\begin{bmatrix}0 & [L_{sr}]\\ [L_{rs}] & 0\end{bmatrix}\begin{bmatrix}[C]^{-1} & 0\\ 0 & [C]^{-1}\end{bmatrix}\right)\begin{bmatrix}\left[i^s_{\alpha\beta xy0}\right]\\ \left[i^r_{\alpha\beta xy0}\right]\end{bmatrix} \tag{2.46}$$

With:

$$\begin{pmatrix}[C] & 0\\ 0 & [C]\end{pmatrix}\frac{d}{d\theta}\begin{pmatrix}0 & [L_{sr}]\\ [L_{rs}] & 0\end{pmatrix}\begin{pmatrix}[C]^{-1} & 0\\ 0 & [C]^{-1}\end{pmatrix} = \begin{pmatrix}0 & [C]\,\frac{d[L_{sr}]}{d\theta}\,[C]^{-1}\\ [C]\,\frac{d[L_{rs}]}{d\theta}\,[C]^{-1} & 0\end{pmatrix} \tag{2.47}$$

The two submatrices are calculated as follows:

$$[C]\frac{d[L_{sr}]}{d\theta}[C]^{-1} = -\frac{5}{2}M \begin{bmatrix} \sin(\theta) & \cos(\theta) & 0 & 0 & 0 \\ -\cos(\theta) & \sin(\theta) & 0 & 0 & 0 \\ 0 & 0 & 0 & 0 & 0 \\ 0 & 0 & 0 & 0 & 0 \\ 0 & 0 & 0 & 0 & 0 \end{bmatrix} \tag{2.48}$$

And

$$[C]\frac{d[L_{rs}]}{d\theta}[C]^{-1} = -\frac{5}{2}M\begin{bmatrix}\sin(\theta) & -\cos(\theta) & 0 & 0 & 0\\ \cos(\theta) & \sin(\theta) & 0 & 0 & 0\\ 0 & 0 & 0 & 0 & 0\\ 0 & 0 & 0 & 0 & 0\\ 0 & 0 & 0 & 0 & 0\end{bmatrix} \tag{2.49}$$

Thus, the final form of the torque equation is given by:

$$T_{em} = pL_m\left[\cos(\theta)\left(i_{\alpha r}i_{\beta s} - i_{\beta r}i_{\alpha s}\right) - \sin(\theta)\left(i_{\alpha r}i_{\alpha s} + i_{\beta r}i_{\beta s}\right)\right] \tag{2.50}$$

With $L_m = (5/2)M$.

By substituting (2.42)-(2.45) into (2.39), then into (2.38), and taking into account that the rotor winding is short-circuited, the voltage equations can be written as follows:

$$\begin{cases} v_{\alpha s} = R_s i_{\alpha s} + (L_{ls}+L_m)\dfrac{di_{\alpha s}}{dt} + L_m\dfrac{d}{dt}\left(i_{\alpha r}\cos(\theta) - i_{\beta r}\sin(\theta)\right) = R_s i_{\alpha s} + \dfrac{d\phi_{\alpha s}}{dt}\\ v_{\beta s} = R_s i_{\beta s} + (L_{ls}+L_m)\dfrac{di_{\beta s}}{dt} + L_m\dfrac{d}{dt}\left(i_{\alpha r}\sin(\theta) + i_{\beta r}\cos(\theta)\right) = R_s i_{\beta s} + \dfrac{d\phi_{\beta s}}{dt}\\ v_{xs} = R_s i_{xs} + \dfrac{d\phi_{xs}}{dt} = R_s i_{xs} + L_{ls}\dfrac{di_{xs}}{dt}\\ v_{ys} = R_s i_{ys} + \dfrac{d\phi_{ys}}{dt} = R_s i_{ys} + L_{ls}\dfrac{di_{ys}}{dt}\\ v_{0s} = R_s i_{0s} + \dfrac{d\phi_{0s}}{dt} = R_s i_{0s} + L_{ls}\dfrac{di_{0s}}{dt}\end{cases} \tag{2.51}$$

$$\begin{cases} v_{\alpha r} = 0 = R_r i_{\alpha r} + L_r\dfrac{di_{\alpha r}}{dt} + L_m\dfrac{di_{\alpha s}}{dt} + \omega\phi_{\beta r} = R_r i_{\alpha r} + \dfrac{d\phi_{\alpha r}}{dt} + \omega\phi_{\beta r}\\ v_{\beta r} = 0 = R_r i_{\beta r} + L_r\dfrac{di_{\beta r}}{dt} + L_m\dfrac{di_{\beta s}}{dt} - \omega\phi_{\alpha r} = R_r i_{\beta r} + \dfrac{d\phi_{\beta r}}{dt} - \omega\phi_{\alpha r}\\ v_{xr} = 0 = R_r i_{xr} + \dfrac{d\phi_{xr}}{dt} = R_r i_{xr} + L_{lr}\dfrac{di_{xr}}{dt}\\ v_{yr} = 0 = R_r i_{yr} + \dfrac{d\phi_{yr}}{dt} = R_r i_{yr} + L_{lr}\dfrac{di_{yr}}{dt}\\ v_{0r} = 0 = R_r i_{0r} + \dfrac{d\phi_{0r}}{dt} = R_r i_{0r} + L_{lr}\dfrac{di_{0r}}{dt}\end{cases} \tag{2.52}$$

The flux equations in the stationary reference frame are given below:

$$\begin{cases} \phi_{\alpha s} = (L_{ls}+L_m)i_{\alpha s} + L_m i_{\alpha r} & \phi_{\alpha r} = (L_{lr}+L_m)i_{\alpha r} + L_m i_{\alpha s}\\ \phi_{\beta s} = (L_{ls}+L_m)i_{\beta s} + L_m i_{\beta r} & \phi_{\beta r} = (L_{lr}+L_m)i_{\beta r} + L_m i_{\beta s}\\ \phi_{xs} = L_{ls}i_{xs} & \phi_{xr} = L_{lr}i_{xr}\\ \phi_{ys} = L_{ls}i_{ys} & \phi_{yr} = L_{lr}i_{yr}\\ \phi_{0s} = L_{ls}i_{0s} & \phi_{0r} = L_{lr}i_{0r}\end{cases} \tag{2.53}$$

Equation (2.50) of the torque shows the interaction between the stator and rotor (α, β) components. From the rotor equations in system (2.52), and since the rotor is short-circuited,

the (x, y) components of the stator are decoupled from those of the rotor; thus, the (x, y) components of the rotor and the zero-sequence component equation can be removed. This leaves, for the model of the asynchronous machine, the first four equations of system (2.51), the first two equations of system (2.52), and the torque of equation (2.50).

2.2.3.2 The Model in a Rotating Reference Frame

To express all quantities in the same reference frame, the stator and rotor quantities are projected into a rotating reference frame $(d-q)$ shifted by θ_s with respect to the fixed reference frame. This transformation is done using the rotation matrix $[D]$ below. Since all (x, y) components and the zero-sequence components of the stator and rotor are decoupled, the rotating transformation should only be applied to the (α, β) components.

For the development of the new model, a reference frame $(d-q)$ rotating at a speed ω_s is considered, with its instantaneous position relative to the stationary reference frame equal to θ_s (Figure. 2.2). Similarly, the rotor reference frame $(\alpha' - \beta')$ rotates at a speed ω_r, with its instantaneous position relative to the stationary reference equal to θ. On the other hand, the position of the rotor with respect to the $(d-q)$ reference frame is defined by the coordinate δ, which depends at each instant on the slip speed ω_{gl} according to the following equation:

$$\delta = \theta_s - \theta = \int_0^t (\omega_s - \omega_r) \cdot dt = \int_0^t \omega_{gl} \cdot dt \tag{2.54}$$

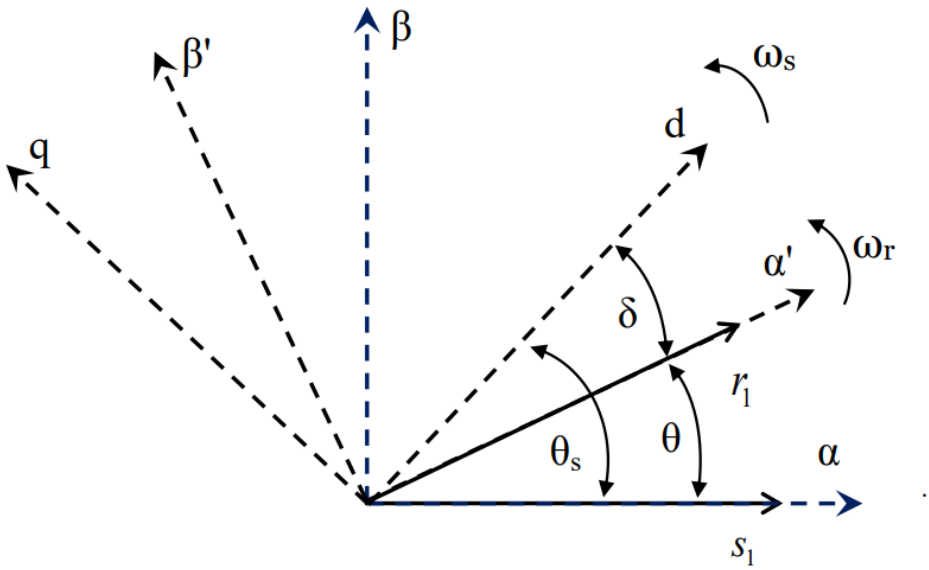

Figure 2.2: The rotating reference frame $d-q$

The transformation matrices for the stator and rotor are thus $[D_s]$ and $[D_r]$, defined as follows [50]:

$$[D_s] = \begin{bmatrix} \cos\theta_s & \sin\theta_s & [0]^{2\times3} \\ -\sin\theta_s & \cos\theta_s & \\ [0]^{3\times2} & & [I]^{3\times3} \end{bmatrix}, \quad [D_s]^{-1} = \begin{bmatrix} \cos\theta_s & -\sin\theta_s & [0]^{2\times3} \\ \sin\theta_s & \cos\theta_s & \\ [0]^{3\times2} & & [I]^{3\times3} \end{bmatrix} \tag{2.55}$$

$$[D_r] = \begin{bmatrix} \cos(\delta) & \sin(\delta) & [0]^{2\times3} \\ -\sin(\delta) & \cos(\delta) & \\ [0]^{3\times2} & & [I]^{3\times3} \end{bmatrix}, \quad [D_r]^{-1} = \begin{bmatrix} \cos(\delta) & -\sin(\delta) & [0]^{2\times3} \\ \sin(\delta) & \cos(\delta) & \\ [0]^{3\times2} & & [I]^{3\times3} \end{bmatrix} \tag{2.56}$$

The transformation of the stator and rotor variables is carried out using the same transformation expressions, with the difference that θ_s is replaced by δ (θ_s and δ are the transformation angles for the stator and rotor variables, respectively).

To simplify the model, the time-varying inductances are modified into constant inductances. The matrix $[P]$ given below is a transformation that conserves instantaneous power [66].

This base change can be applied to physical quantities (voltage, flux, and current) and leads to a matrix relation independent of the angle θ. This base change is called the Park transformation, Figure. 2.3.

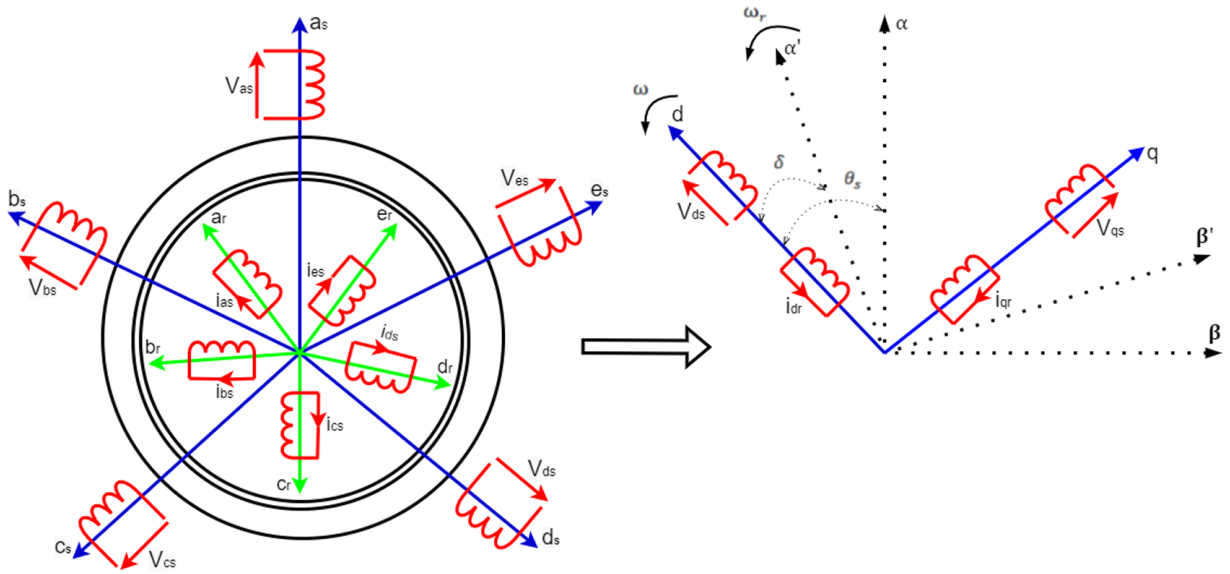

Figure 2.3: Park transformation applied to the five-phase induction machine

With $[P] = [D] \cdot [C]$, we have:

$$[P_s] = \sqrt{\frac{2}{5}} \begin{bmatrix} \cos(\theta_s) & \cos(\theta_s - \alpha) & \cos(\theta_s - 2\alpha) & \cos(\theta_s + 2\alpha) & \cos(\theta_s + \alpha) \\ -\sin(\theta_s) & -\sin(\theta_s - \alpha) & -\sin(\theta_s - 2\alpha) & -\sin(\theta_s + 2\alpha) & -\sin(\theta_s + \alpha) \\ 1 & \cos(2\alpha) & \cos(4\alpha) & \cos(4\alpha) & \cos(2\alpha) \\ 0 & \sin(2\alpha) & \sin(4\alpha) & -\sin(4\alpha) & -\sin(2\alpha) \\ \frac{1}{\sqrt{2}} & \frac{1}{\sqrt{2}} & \frac{1}{\sqrt{2}} & \frac{1}{\sqrt{2}} & \frac{1}{\sqrt{2}} \end{bmatrix} \tag{2.57}$$

The transformation of the rotor variables is similar using the expression of matrix (2.57), replacing θ_s with δ.

$$[P_r] = \sqrt{\frac{2}{5}} \begin{bmatrix} \cos(\delta) & \cos(\delta-\alpha) & \cos(\delta-2\alpha) & \cos(\delta+2\alpha) & \cos(\delta+\alpha) \\ -\sin(\delta) & -\sin(\delta-\alpha) & -\sin(\delta-2\alpha) & -\sin(\delta+2\alpha) & -\sin(\delta+\alpha) \\ 1 & \cos(2\alpha) & \cos(4\alpha) & \cos(4\alpha) & \cos(2\alpha) \\ 0 & \sin(2\alpha) & \sin(4\alpha) & -\sin(4\alpha) & -\sin(2\alpha) \\ \frac{1}{\sqrt{2}} & \frac{1}{\sqrt{2}} & \frac{1}{\sqrt{2}} & \frac{1}{\sqrt{2}} & \frac{1}{\sqrt{2}} \end{bmatrix} \tag{2.58}$$

It is noted that the components $(x, y, 0)$ in ((2.57) and (2.58)) are independent of θ (either θ_s or δ), which simplifies the Park matrix to the form shown below:

$$[P] = \sqrt{\frac{2}{5}} \begin{bmatrix} \cos(\theta) & \cos(\theta-\frac{2\pi}{5}) & \cos(\theta-\frac{4\pi}{5}) & \cos(\theta+\frac{4\pi}{5}) & \cos(\theta+\frac{2\pi}{5}) \\ -\sin(\theta) & -\sin(\theta-\frac{2\pi}{5}) & -\sin(\theta-\frac{4\pi}{5}) & -\sin(\theta+\frac{4\pi}{5}) & -\sin(\theta+\frac{2\pi}{5}) \end{bmatrix}. \tag{2.59}$$

Using these transformations, the equations in the $(d-q-x-y-0)$ domain can be written as follows [67]:

$$\begin{aligned} [v_{dqxyo}] &= [P_s]\,[v^s_{abcde}]\,, \quad \left[i^s_{dqxyo}\right] = [P_s]\,[i^s_{abcde}]\,, \quad \left[\phi^s_{dqxyo}\right] = [P_s]\,[\phi^s_{abcde}]\,, \\ \left[v^r_{dqxyo}\right] &= [P_r]\,[v^r_{abcde}]\,, \quad \left[i^r_{dqxyo}\right] = [P_r]\,[i^r_{abcde}]\,, \quad \left[\phi^r_{dqxyo}\right] = [P_r]\,[\phi^r_{abcde}]\,. \end{aligned} \tag{2.60}$$

The stator and rotor voltage equations for the five-phase induction machine in a $(d-q)$ reference frame rotating at synchronous speed ω_s are expressed as:

$$\begin{cases} v_{ds} = R_s i_{ds} - \omega_s \phi_{qs} + \dfrac{d\phi_{ds}}{dt} & v_{dr} = R_r i_{dr} - (\omega_s - \omega)\phi_{qr} + \dfrac{d\phi_{dr}}{dt} \\ v_{qs} = R_s i_{qs} + \omega_s \phi_{ds} + \dfrac{d\phi_{qs}}{dt} & v_{qr} = R_r i_{qr} + (\omega_s - \omega)\phi_{dr} + \dfrac{d\phi_{qr}}{dt} \\ v_{xs} = R_s i_{xs} + \dfrac{d\phi_{xs}}{dt} & v_{xr} = R_r i_{xr} + \dfrac{d\phi_{xr}}{dt} \\ v_{ys} = R_s i_{ys} + \dfrac{d\phi_{ys}}{dt} & v_{yr} = R_r i_{yr} + \dfrac{d\phi_{yr}}{dt} \\ v_{0s} = R_s i_{0s} + \dfrac{d\phi_{0s}}{dt} & v_{0r} = R_r i_{0r} + \dfrac{d\phi_{0r}}{dt} \end{cases} \tag{2.61}$$

After transformation, the fluxes ϕ_{dqxyo} for the stator and rotor can be written as follows:

$$\begin{cases} \phi_{ds} = (L_{ls} + L_m) i_{ds} + L_m i_{dr}, & \phi_{dr} = (L_{lr} + L_m) i_{dr} + L_m i_{ds} \\ \phi_{qs} = (L_{ls} + L_m) i_{qs} + L_m i_{qr}, & \phi_{qr} = (L_{lr} + L_m) i_{qr} + L_m i_{qs} \\ \phi_{xs} = L_{ls} i_{xs}, & \phi_{xr} = L_{lr} i_{xr} \\ \phi_{ys} = L_{ls} i_{ys}, & \phi_{yr} = L_{lr} i_{yr} \\ \phi_{0s} = L_{ls} i_{0s}, & \phi_{0r} = L_{lr} i_{0r} \end{cases} \tag{2.62}$$

To design the complete model, we present below the general mechanical equation and the different expressions of the electromagnetic torque developed by the machine:

$$\frac{d\omega_m}{dt} = \frac{p}{J} T_{em} - \frac{f}{J}\omega_m - \frac{p}{J} C_r \tag{2.63}$$

$$\begin{cases} T_{em} = p(\phi_{ds} i_{qs} - \phi_{qs} i_{ds}) \\ T_{em} = p(\phi_{qr} i_{dr} - \phi_{dr} i_{qr}) \\ T_{em} = p L_m (i_{dr} i_{qs} - i_{ds} i_{qr}) \\ T_{em} = p \dfrac{L_m}{L_r} (\phi_{dr} i_{qs} - \phi_{qr} i_{ds}) \end{cases} \tag{2.64}$$

Based on equations (2.61) and (2.62), it is evident that the primary difference between the five-phase motor model and the three-phase motor model lies in the presence of the x-y components in the d-q-x-y-o coordinate system, which do not exist in the three-phase model. The stator and rotor voltages in the x-y reference frame depend solely on their respective currents and fluxes, without any interaction with each other or with the d-q components. These x-y components do not contribute to flux generation or electromagnetic torque production, although they may result in additional losses [68–73]. However, these losses are considered negligible for this thesis [62, 68, 74–76].

Moreover, given the short-circuited rotor and the star-connected stator winding configuration, and assuming balanced five-phase components in both the stator and rotor, the zero-sequence components can be neglected. Consequently, the analysis primarily focuses on the d-q components, which are responsible for flux and torque production.

As a result, under these assumptions, the five-phase induction motor model effectively reduces to that of a three-phase motor. This simplification, as noted in several studies [68, 70, 77, 78], facilitates the application of conventional three-phase control methods, such as DTC, DTC-SVM, and FCS-MPC, to five-phase motors without compromising the accuracy of the results.

Figures 2.4 illustrate the rotor speed and electromagnetic torque responses of the five-phase induction machine supplied by five balanced sinusoidal voltages. After a short transient period, the machine reaches its steady-state operating point. A resistive load is applied during the simulation, causing a slight disturbance in the speed and a variation in the electromagnetic torque. The system quickly re-stabilizes, confirming the correct dynamic behavior of the developed model. The simulation was carried out using MATLAB/Simulink, and the parameters of the machine used are provided in a table in the appendix.

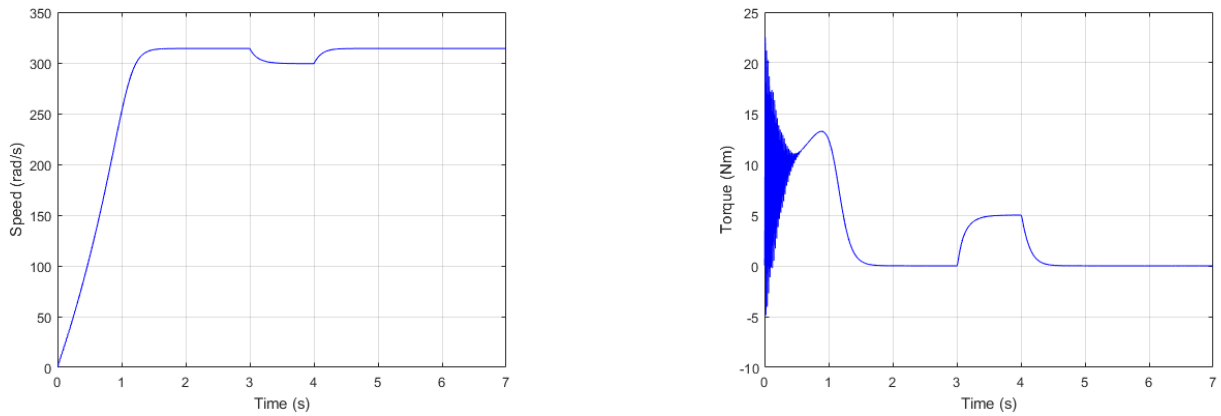

(a) Rotor speed (b) Electromagnetic torque

Figure 2.4: Responses of the five-phase induction machine supplied by five balanced sinusoidal voltages.

2.3 Two-Level Five-Phase Inverter

The two-level five-phase inverter, also known as a voltage source inverter (VSI), is a fundamental component in multiphase drive systems, providing enhanced reliability and performance compared to traditional three-phase inverters. The topology of this inverter is shown in Figure 2.5. It consists of five legs, each with two switches, represented as S_a, S_b, S_c, S_d, and S_e for the high-side switches and S'_a, S'_b, S'_c, S'_d, and S'_e for the low-side switches. Each leg interfaces with a corresponding phase of the load. The input to the inverter is a constant DC voltage V_{dc} (DC link), and the switches operate in a complementary manner to prevent short-circuiting the DC link and to maintain continuous current flow to the load.

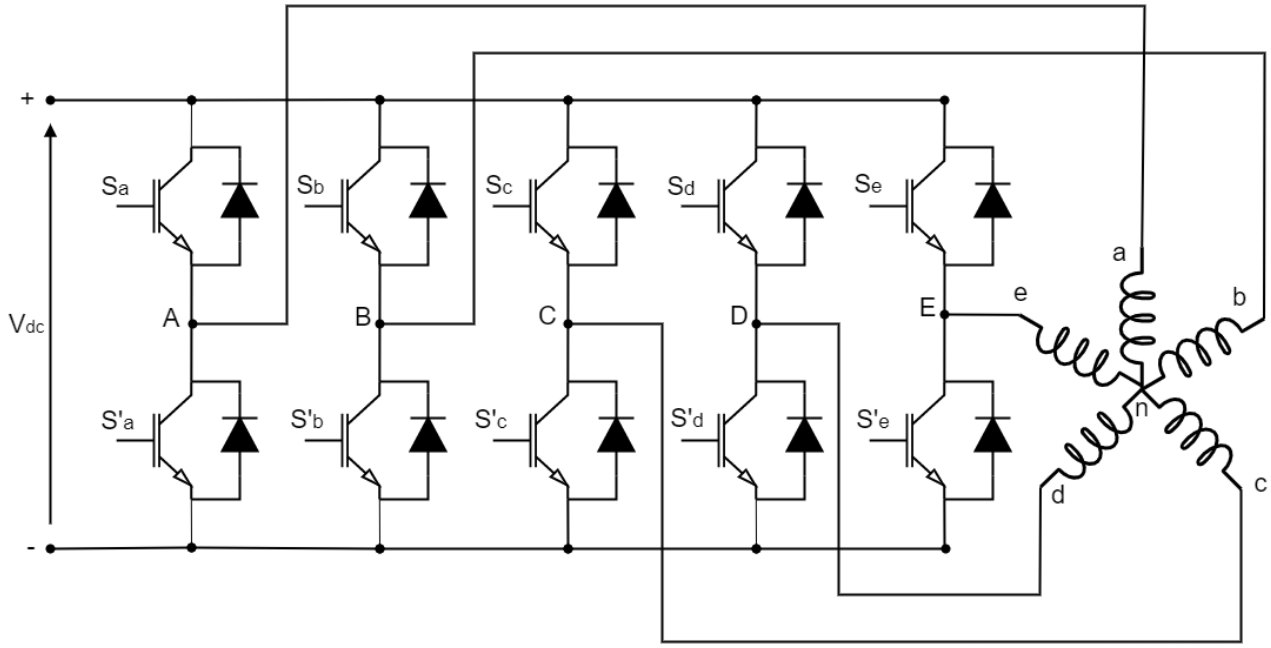

Figure 2.5: Circuit of a five-phase voltage source inverter.

In this configuration, each leg is governed by switching functions S_{1i} and S_{2i}, where i ranges from 1 to 5 for the five phases. These switching functions satisfy the following relation:

$$S_{1i} + S_{2i} = 1 \tag{2.65}$$

where S_{1i} and S_{2i} are the connection functions of a single leg, defined as:

$$S_{ij} = \begin{cases} 1 & \text{if switch } ij \text{ is on (conducting)} \\ 0 & \text{otherwise} \end{cases}$$

In this context:

- **State 1**: The upper switch is closed, and the lower switch is open, resulting in the leg voltage with respect to the neutral of the source (n) being V_{dc}.
- **State 0**: The upper switch is open, and the lower switch is closed, resulting in the leg voltage with respect to the neutral of the source (n) being zero.

The inverter's output voltage is governed by the switching states of the IGBTs. Given that each leg contains two IGBTs, there are 2^5 (32) possible switching states, resulting in 32 space voltage vectors. These vectors include two zero vectors and thirty active vectors, which have three distinct amplitudes and are distributed across ten 36-degree sectors, as illustrated in Figure 2.6.

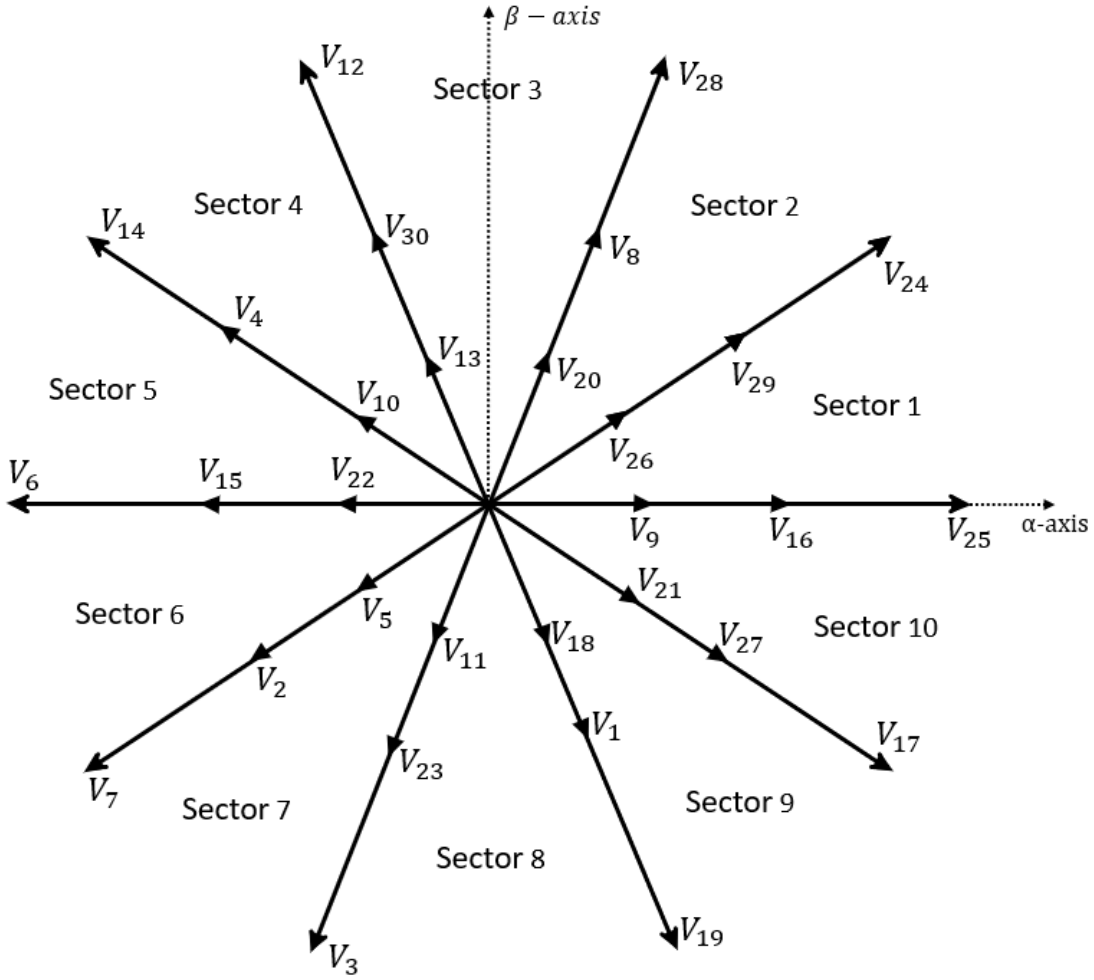

Figure 2.6: Space voltage vectors of the two-level five-phase inverter α-β plane.

The voltages $V_{aN}, V_{bN}, V_{cN}, V_{dN}$, and V_{eN} are defined as the voltages between nodes a, b, c, d, and e and the neutral point of the load. Specifically, V_{aN} represents the voltage between node a and the neutral of the load, V_{bN} represents the voltage between node b and the neutral of the load, and so on for the other phases.

To derive the mathematical model of the two-level five-phase inverter, consider the switching state (10000), where $S_a = 1$ and $S_b = S_c = S_d = S_e = 0$. In this state, the equivalent impedance seen by the load is determined by calculating the parallel combination of impedances. The equivalent impedance Z_{eq} is $\frac{Z}{4}$, resulting in a total impedance expressed as:

$$Z_{\text{total}} = Z + Z_{\text{eq}} = \frac{5Z}{4} \tag{2.66}$$

Using this total impedance, the current I flowing through the circuit is obtained as:

$$I = \frac{V_{DC}}{Z_{\text{total}}} = \frac{V_{DC}}{\frac{5Z}{4}} = \frac{4V_{DC}}{5Z} \tag{2.67}$$

With this current, the voltage V_{aN} can be determined as:

$$V_{aN} = I \cdot Z = \frac{4V_{DC}}{5} \tag{2.68}$$

The voltages for the other phases V_{bN}, V_{cN}, V_{dN}, and V_{eN}, can be expressed as:

$$V_{bN} = V_{cN} = V_{dN} = V_{eN} = -I \cdot Z_{\text{eq}} \tag{2.69}$$

Substituting the value of I from (2.67), these voltages become:

$$V_{bN} = V_{cN} = V_{dN} = V_{eN} = -\frac{V_{DC}}{5} \tag{2.70}$$

For a generalized case where all switching states S_a, S_b, S_c, S_d, and S_e are considered, the voltages relative to the neutral of the source are given by:

$$\begin{bmatrix} V_{an} \\ V_{bn} \\ V_{cn} \\ V_{dn} \\ V_{en} \end{bmatrix} = \begin{bmatrix} S_a \\ S_b \\ S_c \\ S_d \\ S_e \end{bmatrix} \cdot V_{DC} \tag{2.71}$$

The voltages relative to the neutral of the load are given by::

$$\begin{bmatrix} V_{aN} \\ V_{bN} \\ V_{cN} \\ V_{dN} \\ V_{eN} \end{bmatrix} = \frac{1}{5} \begin{bmatrix} 4 & -1 & -1 & -1 & -1 \\ -1 & 4 & -1 & -1 & -1 \\ -1 & -1 & 4 & -1 & -1 \\ -1 & -1 & -1 & 4 & -1 \\ -1 & -1 & -1 & -1 & 4 \end{bmatrix} \begin{bmatrix} V_{an} \\ V_{bn} \\ V_{cn} \\ V_{dn} \\ V_{en} \end{bmatrix} \tag{2.72}$$

Therefore, the mathematical model of the two-level five-phase inverter can be represented by a matrix equation that links each leg voltage relative to the load's neutral with the switching states and V_{DC}:

$$\begin{bmatrix} V_{aN} \\ V_{bN} \\ V_{cN} \\ V_{dN} \\ V_{eN} \end{bmatrix} = \frac{V_{DC}}{5} \begin{bmatrix} 4 & -1 & -1 & -1 & -1 \\ -1 & 4 & -1 & -1 & -1 \\ -1 & -1 & 4 & -1 & -1 \\ -1 & -1 & -1 & 4 & -1 \\ -1 & -1 & -1 & -1 & 4 \end{bmatrix} \begin{bmatrix} S_a \\ S_b \\ S_c \\ S_d \\ S_e \end{bmatrix} \tag{2.73}$$

This equation offers a systematic way to calculate the leg voltages as a function of V_{DC} and the switching states, forming the basis for controlling the inverter's output.

Table 2.1 lists the possible switching states and the corresponding output voltages in the α-β and x-y planes. It shows how the reference voltage magnitude $|V_{\text{ref}}|$ and phase angle θ_{out} vary with different switching configurations, providing insights into inverter control and modulation.

Table 2.1: The possible vectors and their output voltages.

Vectors	States	Plan $\alpha-\beta$		Plan $x-y$	
		$\lvert V_{\text{ref}}\rvert$	θ_{out}	$\lvert V_{\text{ref}}\rvert$	θ_{out}
Active Vectors					
V_1	[0 0 0 0 1]	$\frac{2}{5}V_{DC}$	$\frac{8\pi}{5}$	$\frac{2}{5}V_{DC}$	$\frac{6\pi}{5}$
V_2	[0 0 0 1 0]	$\frac{2}{5}V_{DC}$	$\frac{6\pi}{5}$	$\frac{2}{5}V_{DC}$	$\frac{2\pi}{5}$
V_3	[0 0 0 1 1]	$\frac{4}{5}\cos(\frac{\pi}{5})V_{DC}$	$\frac{7\pi}{5}$	$\frac{4}{5}\cos(\frac{2\pi}{5})V_{DC}$	$\frac{4\pi}{5}$
V_4	[0 0 1 0 0]	$\frac{2}{5}V_{DC}$	$\frac{4\pi}{5}$	$\frac{2}{5}V_{DC}$	$\frac{8\pi}{5}$
V_5	[0 0 1 0 1]	$\frac{4}{5}\cos(\frac{2\pi}{5})V_{DC}$	$\frac{6\pi}{5}$	$\frac{4}{5}\cos(\frac{\pi}{5})V_{DC}$	$\frac{7\pi}{5}$
V_6	[0 0 1 1 0]	$\frac{4}{5}\cos(\frac{\pi}{5})V_{DC}$	π	$\frac{4}{5}\cos(\frac{\pi}{5})V_{DC}$	0
V_7	[0 0 1 1 1]	$\frac{4}{5}\cos(\frac{\pi}{5})V_{DC}$	$\frac{6\pi}{5}$	$\frac{4}{5}\cos(\frac{2\pi}{5})V_{DC}$	$\frac{7\pi}{5}$
V_8	[0 1 0 0 0]	$\frac{2}{5}V_{DC}$	$\frac{2\pi}{5}$	$\frac{2}{5}V_{DC}$	$\frac{2\pi}{5}$
V_9	[0 1 0 0 1]	$\frac{4}{5}\cos(\frac{2\pi}{5})V_{DC}$	0	$\frac{4}{5}\cos(\frac{\pi}{5})V_{DC}$	π
V_{10}	[0 1 0 1 0]	$\frac{4}{5}\cos(\frac{2\pi}{5})V_{DC}$	$\frac{4\pi}{5}$	$\frac{4}{5}\cos(\frac{\pi}{5})V_{DC}$	$\frac{3\pi}{5}$
V_{11}	[0 1 0 1 1]	$\frac{4}{5}\cos(\frac{\pi}{5})V_{DC}$	$\frac{3\pi}{5}$	$\frac{4}{5}\cos(\frac{\pi}{5})V_{DC}$	$\frac{6\pi}{5}$
V_{12}	[0 1 1 0 0]	$\frac{4}{5}\cos(\frac{\pi}{5})V_{DC}$	$\frac{3\pi}{5}$	$\frac{4}{5}\cos(\frac{2\pi}{5})V_{DC}$	$\frac{6\pi}{5}$
V_{13}	[0 1 1 0 1]	$\frac{4}{5}\cos(\frac{2\pi}{5})V_{DC}$	$\frac{3\pi}{5}$	$\frac{4}{5}\cos(\frac{\pi}{5})V_{DC}$	$\frac{3\pi}{5}$
V_{14}	[0 1 1 1 0]	$\frac{4}{5}\cos(\frac{\pi}{5})V_{DC}$	$\frac{4\pi}{5}$	$\frac{4}{5}\cos(\frac{\pi}{5})V_{DC}$	$\frac{3\pi}{5}$
V_{15}	[0 1 1 1 1]	$\frac{2}{5}V_{DC}$	π	$\frac{2}{5}V_{DC}$	π
V_{16}	[1 0 0 0 0]	$\frac{2}{5}V_{DC}$	0	$\frac{2}{5}V_{DC}$	0
V_{17}	[1 0 0 0 1]	$\frac{4}{5}\cos(\frac{\pi}{5})V_{DC}$	$\frac{9\pi}{5}$	$\frac{4}{5}\cos(\frac{2\pi}{5})V_{DC}$	$\frac{8\pi}{5}$
V_{18}	[1 0 0 1 0]	$\frac{4}{5}\cos(\frac{2\pi}{5})V_{DC}$	$\frac{8\pi}{5}$	$\frac{4}{5}\cos(\frac{\pi}{5})V_{DC}$	$\frac{\pi}{5}$
V_{19}	[1 0 0 1 1]	$\frac{4}{5}\cos(\frac{\pi}{5})V_{DC}$	$\frac{8\pi}{5}$	$\frac{4}{5}\cos(\frac{\pi}{5})V_{DC}$	$\frac{\pi}{5}$
V_{20}	[1 0 1 0 0]	$\frac{4}{5}\cos(\frac{\pi}{5})V_{DC}$	$\frac{2\pi}{5}$	$\frac{4}{5}\cos(\frac{2\pi}{5})V_{DC}$	$\frac{8\pi}{5}$
V_{21}	[1 0 1 0 1]	$\frac{4}{5}\cos(\frac{2\pi}{5})V_{DC}$	$\frac{9\pi}{5}$	$\frac{4}{5}\cos(\frac{\pi}{5})V_{DC}$	$\frac{8\pi}{5}$
V_{22}	[1 0 1 1 0]	$\frac{4}{5}\cos(\frac{2\pi}{5})V_{DC}$	π	$\frac{4}{5}\cos(\frac{\pi}{5})V_{DC}$	0
V_{23}	[1 0 1 1 1]	$\frac{2}{5}V_{DC}$	$\frac{7\pi}{5}$	$\frac{2}{5}V_{DC}$	$\frac{9\pi}{5}$
V_{24}	[1 1 0 0 0]	$\frac{4}{5}\cos(\frac{\pi}{5})V_{DC}$	$\frac{\pi}{5}$	$\frac{4}{5}\cos(\frac{2\pi}{5})V_{DC}$	$\frac{2\pi}{5}$
V_{25}	[1 1 0 0 1]	$\frac{4}{5}\cos(\frac{\pi}{5})V_{DC}$	0	$\frac{4}{5}\cos(\frac{\pi}{5})V_{DC}$	π
V_{26}	[1 1 0 1 0]	$\frac{4}{5}\cos(\frac{2\pi}{5})V_{DC}$	$\frac{\pi}{5}$	$\frac{4}{5}\cos(\frac{\pi}{5})V_{DC}$	$\frac{2\pi}{5}$
V_{27}	[1 1 0 1 1]	$\frac{2}{5}V_{DC}$	$\frac{9\pi}{5}$	$\frac{2}{5}V_{DC}$	$\frac{3\pi}{5}$
V_{28}	[1 1 1 0 0]	$\frac{4}{5}\cos(\frac{\pi}{5})V_{DC}$	$\frac{2\pi}{5}$	$\frac{4}{5}\cos(\frac{2\pi}{5})V_{DC}$	$\frac{9\pi}{5}$
V_{29}	[1 1 1 0 1]	$\frac{2}{5}V_{DC}$	$\frac{\pi}{5}$	$\frac{2}{5}V_{DC}$	$\frac{7\pi}{5}$
V_{30}	[1 1 1 1 0]	$\frac{2}{5}V_{DC}$	$\frac{3\pi}{5}$	$\frac{2}{5}V_{DC}$	$\frac{\pi}{5}$
Zero Vectors					
V_{31}	[1 1 1 1 1]	0	-	0	-
V_0	[0 0 0 0 0]	0	-	0	-

2.3.1 Space Vector Modulation (SVM)

Space Vector Modulation (SVM) has been successfully adapted to a two-level five-phase voltage inverter, providing an efficient method for generating high-quality output voltages. Studies have shown that this inverter topology can generate nearly pure sinusoidal output voltages when appropriate SVM schemes are applied [67, 79]. Moreover, the large number of spatial vectors available offers significant flexibility in selecting the optimal combination for effective control of multiphase inverters.

As explained in section (2.3), a two-level five-phase inverter produces 32 space vectors that cover 360 degrees, forming a decagon with 10 sectors of 36 degrees each.

For three-phase drives, the reference voltage is obtained using two adjacent active space vectors [80], ensuring that the volt-second balance $\sum v_i t_i = v_s^* T_e$ is maintained [81]. Thus, as an extension in a two-level five-phase inverter, two adjacent active space vectors can also be used. However, the following section reveals that a simple extension of SVM leads to distortion in the output voltage. Consequently, it becomes evident that instead of two, four adjacent vectors, when used to implement the SVM of a two-level five-phase inverter, result in sinusoidal output voltages.

In general, an $n-1$ (where n is the number of phases) number of active space vectors is required to generate a sinusoidal output in multiphase voltage inverters [82].

The space vectors of phase voltages in the two orthogonal planes are defined using a power-invariant transformation as follows [83]:

$$V_{\alpha\beta} = \sqrt{\frac{2}{5}}\left[v_a + v_b e^{j\frac{2\pi}{5}} + v_c e^{j\frac{4\pi}{5}} + v_d e^{-j\frac{4\pi}{5}} + v_e e^{-j\frac{2\pi}{5}}\right] \tag{2.74}$$

$$V_{xy} = \sqrt{\frac{2}{5}}\left[v_a + v_b e^{j\frac{\pi}{5}} + v_c e^{j\frac{3\pi}{5}} + v_d e^{-j\frac{3\pi}{5}} + v_e e^{-j\frac{\pi}{5}}\right] \tag{2.75}$$

The space vectors thus obtained in the $(\alpha-\beta)$ plane are shown in Figure 2.7a. Since this is a five-phase system, the transformation is subsequently performed to obtain the space vectors in the $(x-y)$ plane using (2.75), and the resulting space vectors are shown in Figure 2.7b.

Figure 2.7a shows that the space vectors of the outer decagon in the $(\alpha-\beta)$ plane transform into the inner decagon in the $(x-y)$ plane (Figure 2.7b). The innermost decagon of the $(\alpha-\beta)$ plane forms the outer decagon of the $(x-y)$ plane, while the space vectors of the intermediate decagon remain in the same region. It is further observed that the phase sequence A, B, C, D, E in the $(\alpha-\beta)$ plane corresponds to the sequence A, D, B, E, C in the $(x-y)$ plane. Consequently, it can be inferred that the presence of the vector components in the $(x-y)$ plane introduces waveform distortions, generating unwanted third-order harmonics in the machine fed by an SVM voltage inverter [79]. Thus, during the development of modulation techniques, it is necessary to reduce or completely eliminate the $x-y$ components to obtain sinusoidal output voltages.

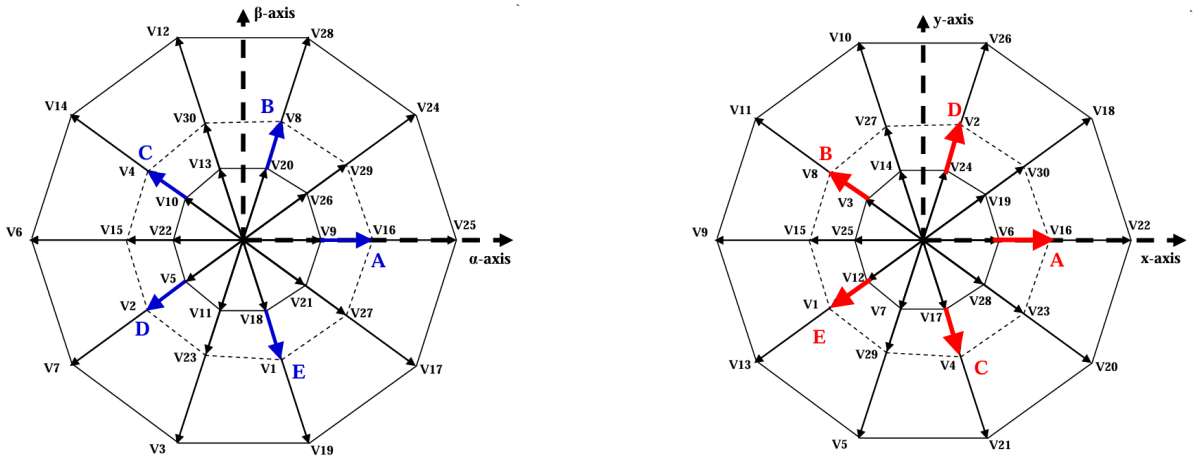

(a) α-β plane (b) $x-y$ plane

Figure 2.7: Space voltage vectors of the two-level five-phase inverter

2.3.1.1 SVM with Two Active Vectors

The SVM scheme discussed in this section utilizes the outermost decagon of space vectors in the $(\alpha-\beta)$ plane, as illustrated in Figure 2.7a. In this approach, two large adjacent active space vectors, along with two zero space vectors, are employed within a switching period to synthesize the reference input voltage.

The commutation is performed such that, during the first half of the switching period, the first zero vector is applied, followed by two large active state vectors, and then the second zero vector. The second half-cycle is the mirror image of the first. This is how symmetric space vector modulation is achieved.

To calculate the application times of the different vectors, refer to Figure 2.8, which shows the position of the two large adjacent space vectors and the reference vector within the first sector. The application times for the two large vectors, T_{al} and T_{bl}, are calculated using the following formulas:

$$t_a = \frac{|V_s^*| \sin\left(k\frac{\pi}{5} - \alpha\right)}{|V_l| \sin\left(\frac{\pi}{5}\right)} t_e \tag{2.76}$$

$$t_b = \frac{|V_s^*| \sin\left(\alpha - (k-1)\frac{\pi}{5}\right)}{|V_l| \sin\left(\frac{\pi}{5}\right)} t_e \tag{2.77}$$

With k being the sector number ($k = 1$ to 10), the application time for the zero space vector is given by:

$$t_0 = t_e - t_a - t_b$$

and:

$$|V_{al}| = |V_{bl}| = |V_l| = \sqrt{\frac{2}{5}} V_{DC} 2\cos(\pi/5), \quad |V_{am}| = |V_{bm}| = |V_m| = \sqrt{\frac{2}{5}} V_{DC}.$$

The symbol $\mathbf{V_s^*}$ represents the space vector of the reference voltage, while $|x|$ denotes the magnitude of a complex number $\bar{x}$. Indices "l" and "m" respectively designate the large and medium vectors.

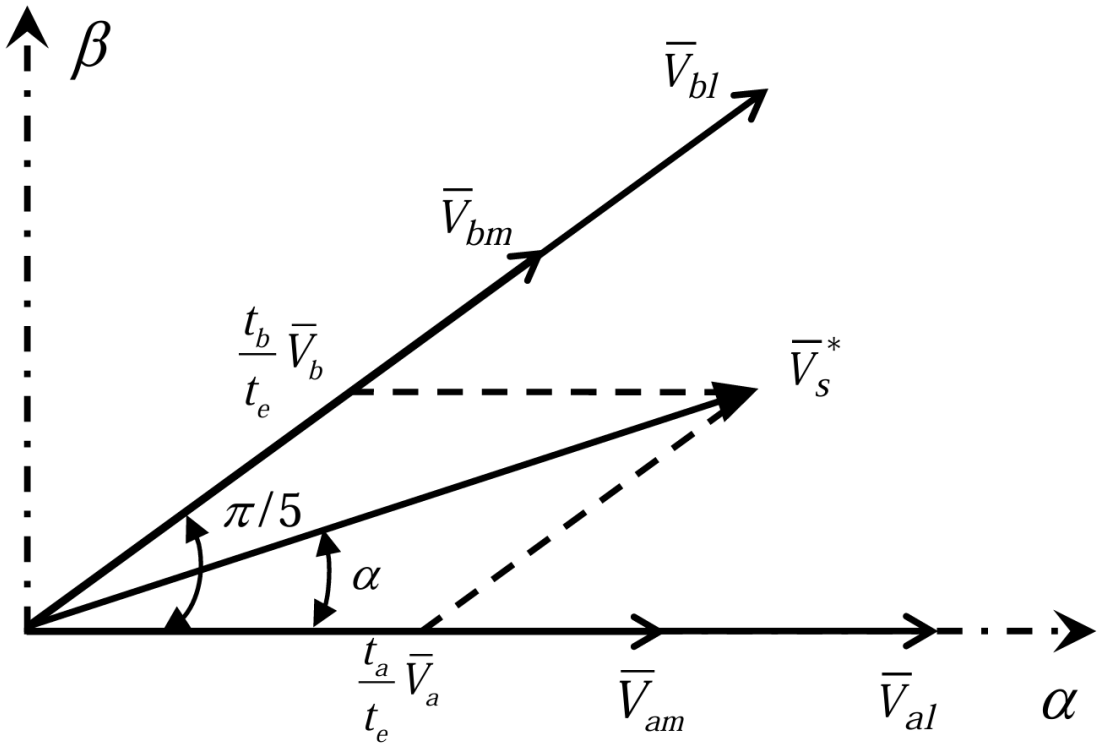

Figure 2.8: Reference and two large adjacent space vectors in sector 1.

The sequences of vectors applied in sectors 1 and 2 and the corresponding switching schemes are presented in Figure 2.9. In odd sectors, the vector on the left side relative to the reference is applied first, followed by the vector on the right side. In even sectors, the right-side vector is applied first, followed by the left-side vector.

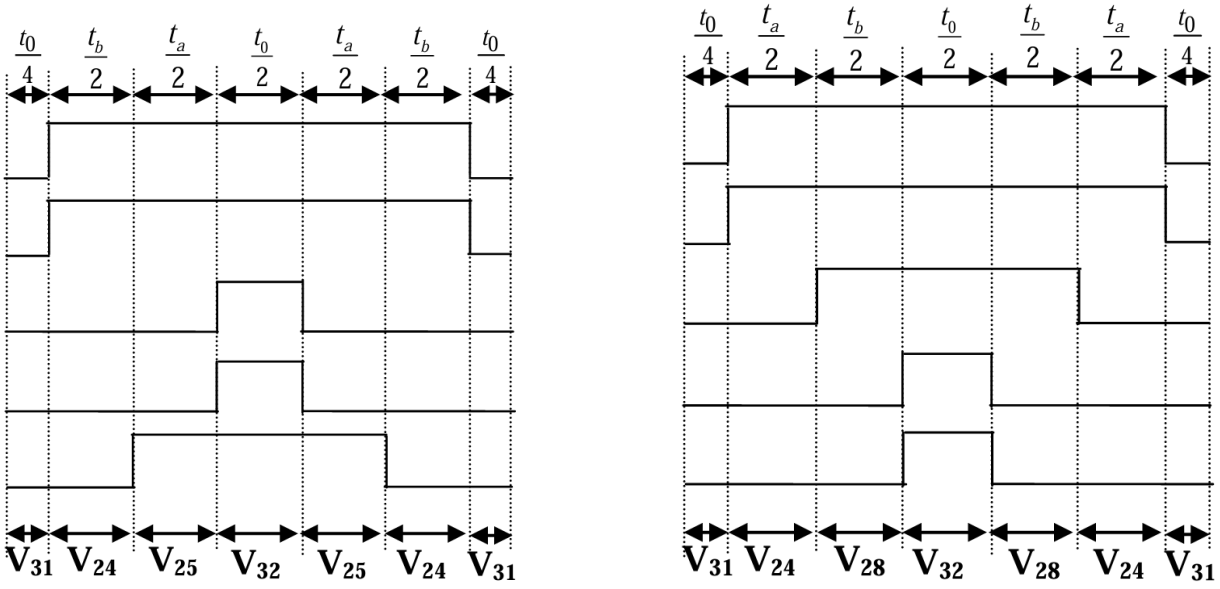

(a) Sector 1

(b) Sector 2

Figure 2.9: Inverter switching states for sectors 1 and 2

2.3.1.2 SVM with Four Active Vectors

In this section, an SVM scheme that utilizes four active space vectors (two medium and two large) within each sector is presented to generate the desired reference voltage at each sampling time step.

The purpose of the SVM technique is to generate output phase voltages where the most significant harmonics are neglected. The use of two medium adjacent space vectors along with two large active space vectors in each switching period ensures a zero mean value [84, 85], thus providing an almost perfectly sinusoidal output.

As shown in Figure 2.10, four active space vectors (two medium vectors and two large vectors) are applied in each sector to produce the desired reference voltage at each sampling period T_e. Consequently, the main task of SVM techniques is to determine the application times of each vector in each sector to synthesize the required output voltage vector [84, 86].

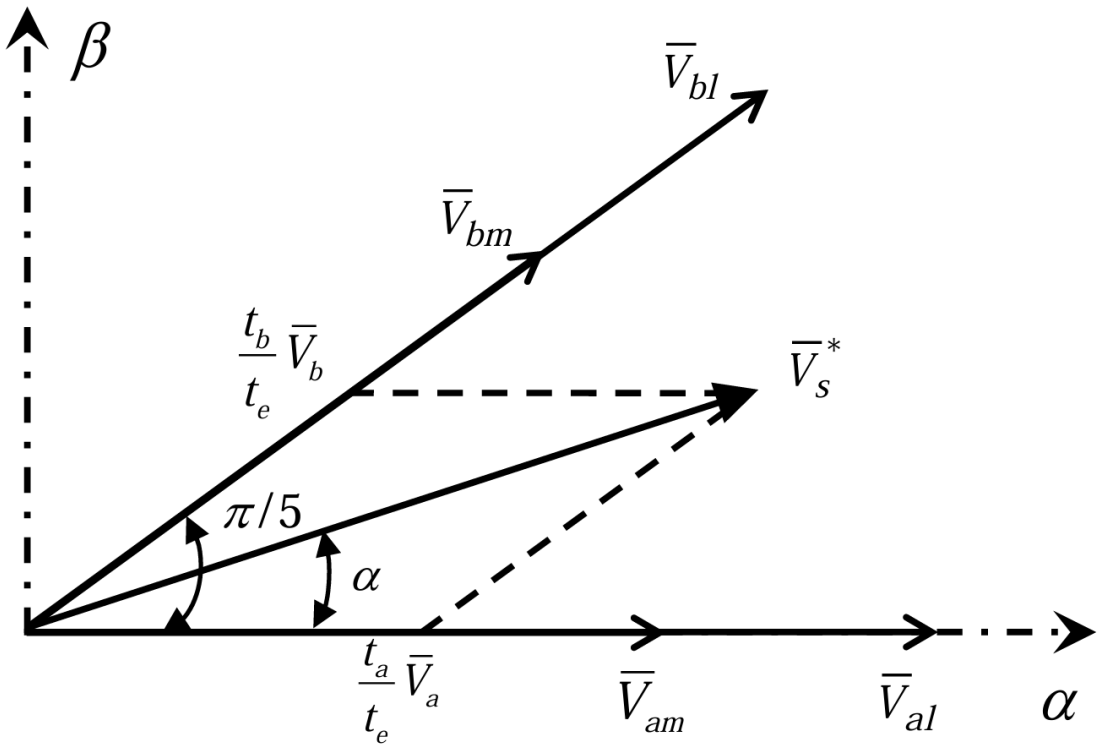

Figure 2.10: Reference and Four Space Vectors (Medium and Large) in Sector 1.

The four application times of the four vectors, denoted as $T_{al}, T_{bl}, T_{am}, T_{bm}$, are presented in Figure 2.11 and calculated based on equations (2.78) and (2.79) as follows [77]:

$$T_{al} = \frac{|V_l| \sin\left(\frac{\pi k}{5} - \alpha\right)}{|V_l| + |V_m| \sin\left(\frac{\pi}{5}\right)} \cdot T_s, \quad T_{bl} = \frac{|V_l| \sin\left(\alpha - \frac{(k-1)\pi}{5}\right)}{|V_l| + |V_m| \sin\left(\frac{\pi}{5}\right)} \cdot T_s \tag{2.78}$$

$$T_{am} = \frac{|V_m| \sin\left(\frac{\pi k}{5} - \alpha\right)}{|V_l| + |V_m| \sin\left(\frac{\pi}{5}\right)} \cdot T_s, \quad T_{bm} = \frac{|V_m| \sin\left(\alpha - \frac{(k-1)\pi}{5}\right)}{|V_l| + |V_m| \sin\left(\frac{\pi}{5}\right)} \cdot T_s \tag{2.79}$$

The application time of the zero voltage vector T_o is calculated as:

$$T_o = T_s - T_{al} - T_{am} - T_{bl} - T_{bm} \tag{2.80}$$

It is observed that the representation in the $(x-y)$ frame, using two Large vectors and two medium vectors, allows for the cancellation of these vectors among themselves, as shown in Figure 2.12 for sector 1 (and similarly for the other sectors). Vectors V_{16} and V_{29} are opposite to vectors V_{25} and V_{24}, respectively. Since the ratio of the lengths between the medium and the smallest vectors is 1.618, if the application time of the smallest vector is increased in the same proportion, they will have an equal volt-second value:

$$\bar{V}_s^* T_e = \bar{V}_{al} T_{al} + \bar{V}_{bl} T_{bl} + \bar{V}_{am} T_{am} + \bar{V}_{bm} T_{bm}$$

and will cancel each other out, thereby eliminating the $(x-y)$ components, reducing harmonics, and generating a sinusoidal output [86, 87].

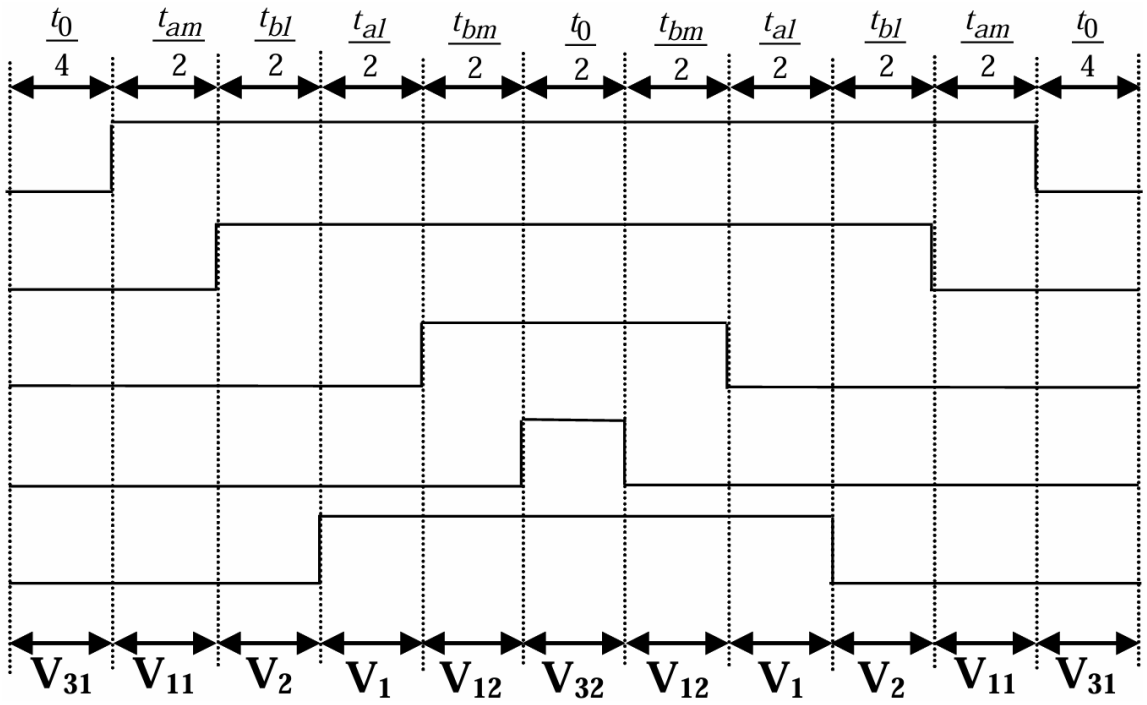

Figure 2.11: Inverter switching states for sector 1.

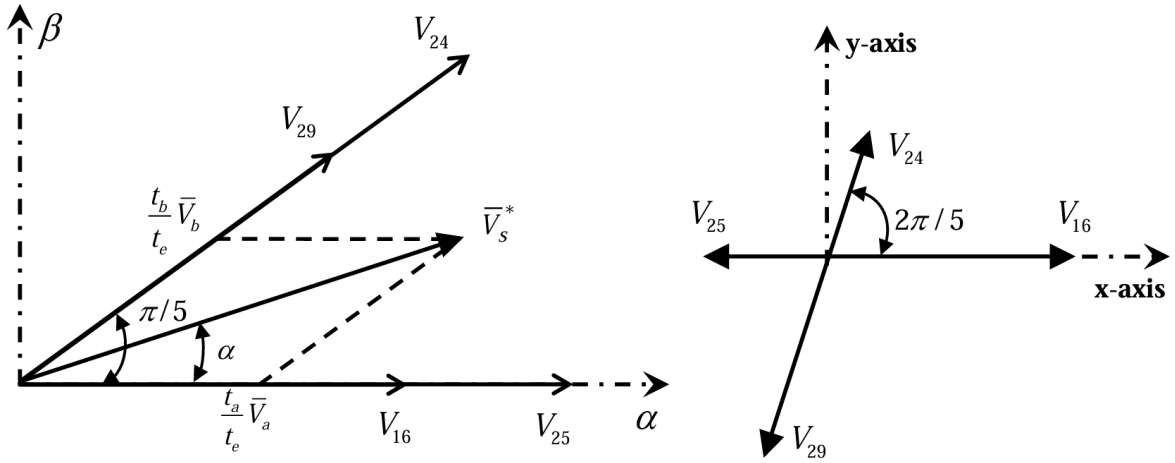

Figure 2.12: Principle of vector modulation using 4 vectors (planes $(\alpha-\beta)$ and $(x-y)$).

2.3.1.3 Simulation Results

Figures 2.13 and 2.14 present the simulation results for the SVM with two vectors and four vectors, respectively, applied to a two-level five-phase inverter. The results highlight the impact of the number of vectors used on the quality of the output voltage and current.

For the SVM with two vectors, the Total Harmonic Distortion (THD) of the output voltage is 87.46% and the THD of the current is 29.4%, revealing the presence of significant low-frequency harmonics, primarily caused by the inability of two adjacent vectors to cancel the resulting vectors in the x-y plane.

In contrast, for the SVM with four vectors, the THD of the output voltage is reduced to 56.78% and the THD of the current decreases to 12.7%. The phase voltages are significantly smoother, closely approximating ideal sinusoidal waveforms, and the overall harmonic content is notably reduced. This improvement is achieved through the use of four adjacent vectors, which not only reconstruct the reference voltage vector in the α-β plane but also simultaneously cancel the resulting vector in the x-y plane, thus minimizing low-frequency harmonics and ensuring high-quality output voltages.

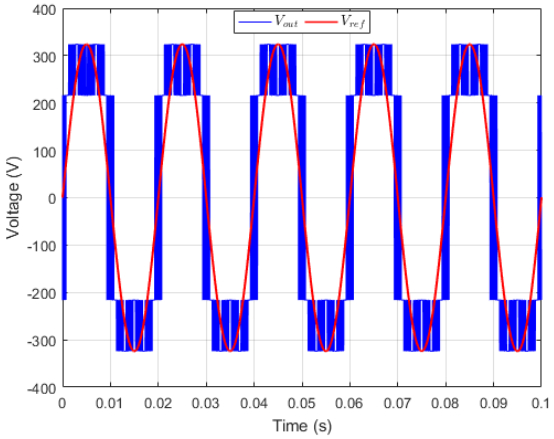

(a) voltages.

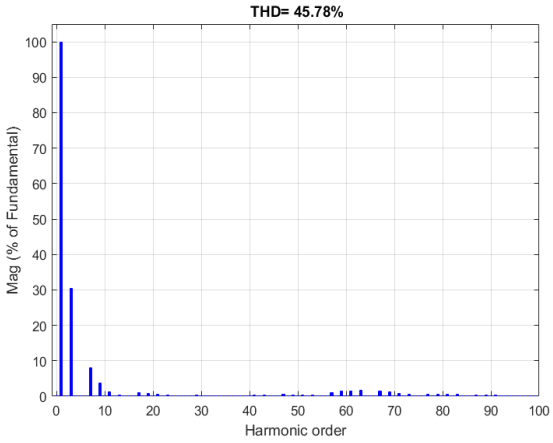

(b) Harmonic spectrum of voltages.

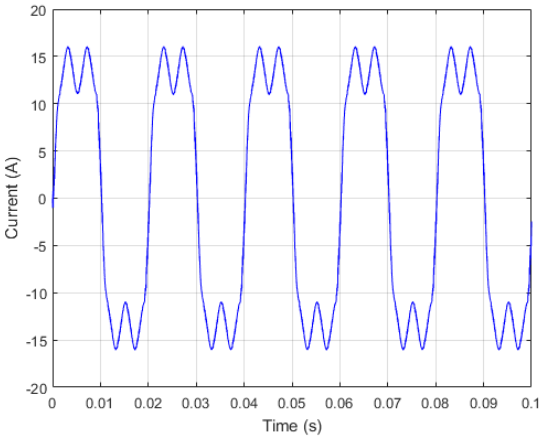

(c) Current.

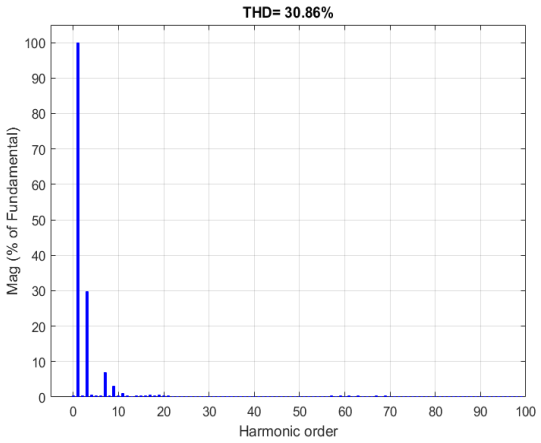

(d) Harmonic spectrum of current.

Figure 2.13: Simulation results for the SVM with two vectors.

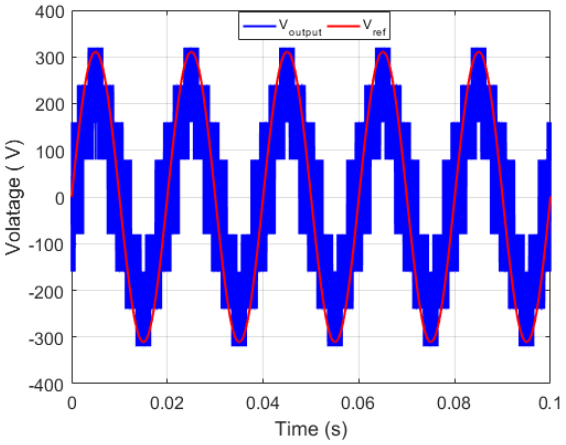

(a) voltages.

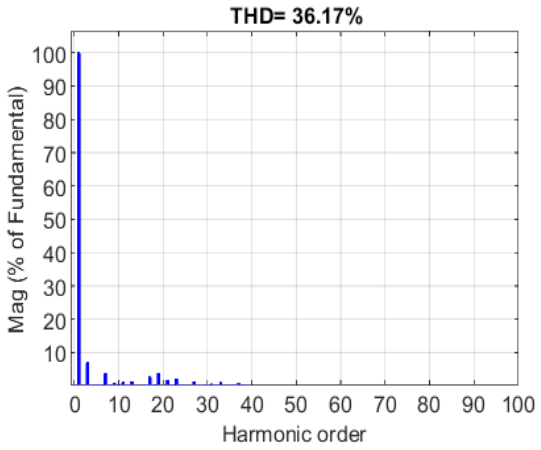

(b) Harmonic spectrum of voltages.

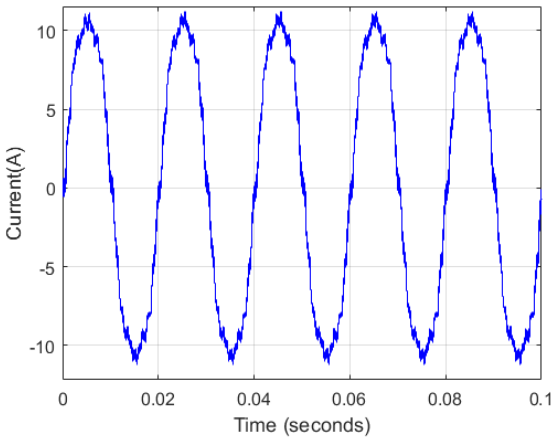

(c) Current.

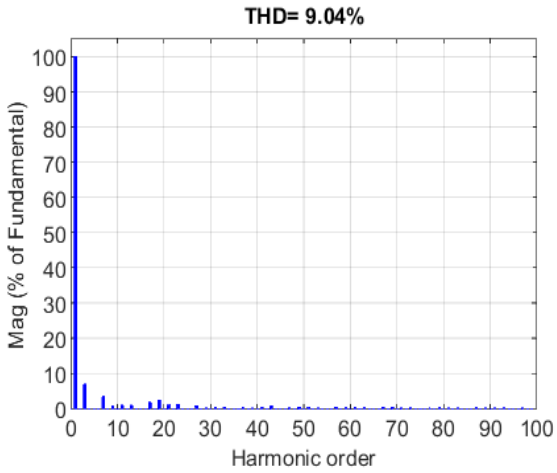

(d) Harmonic spectrum of current.

Figure 2.14: Simulation results for the SVM with four vectors.

2.4 Multilevel Five-Phase Inverter

Unlike traditional two-level inverters, which can only produce two voltage levels (positive and negative), multilevel inverters are capable of generating multiple intermediate voltage levels. The number of levels in an inverter is defined as the number of constant voltage values that can be generated between the output terminal and a reference node, usually the neutral point of the DC link. To be classified as a multilevel inverter, each phase of the inverter must generate at least three different voltage levels. This distinguishes the multilevel family from the conventional two-level voltage source inverter. Figure 2.15 illustrates several single-phase examples of multilevel inverter topologies, accompanied by their corresponding voltage waveforms for different numbers of levels. It should be noted that, generally, the different voltage levels are evenly spaced as multiples of V_{dc} [88].

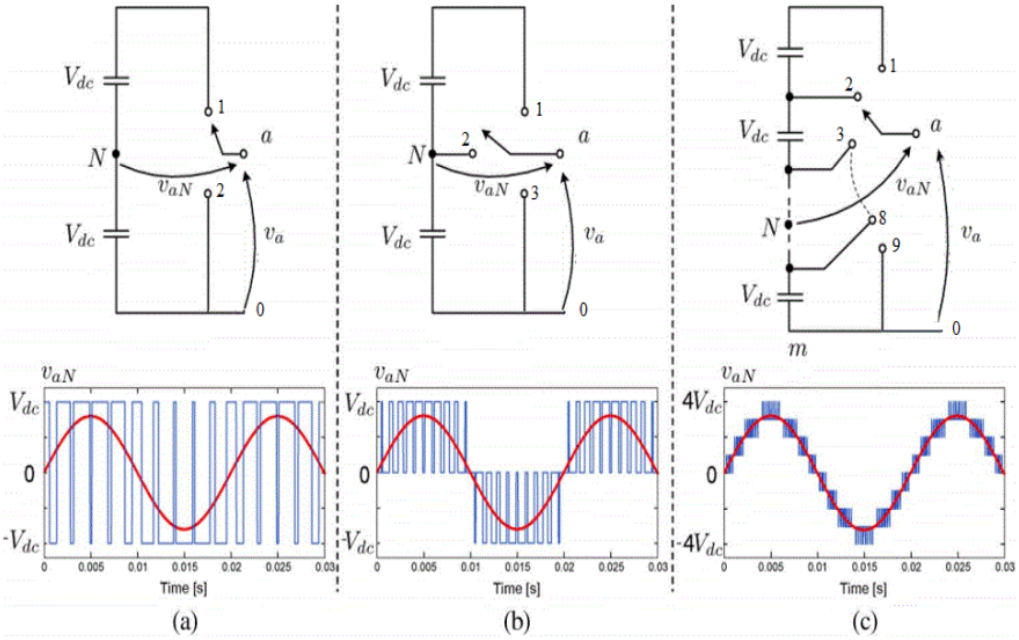

Figure 2.15: Diagram of a single-phase leg of an inverter with (a) 2 levels, (b) 3 levels, (c) 9 levels, and their corresponding voltage waveforms.

With the increase in the number of voltage levels used, several important advantages can be observed:

- A lower output voltage distortion (waveforms closer to a sinusoidal shape), leading to the consumption of less polluted current. This reduces torque ripple and additional losses caused by current harmonics [89].
- A reduction in the voltage gradient (dV/dt) [89].
- Fault tolerance: the inverter can operate in a two-level mode in the event of a fault in the midpoint switches [89].

In this thesis, these advantages have motivated the use of the T-NPC (Three-Level Neutral Point Clamped) topology, in addition to traditional two-level five-phase inverters, to supply the five-phase induction motor. Figure 2.16 presents the schematic diagram of the three-level five-phase T-NPC inverter.

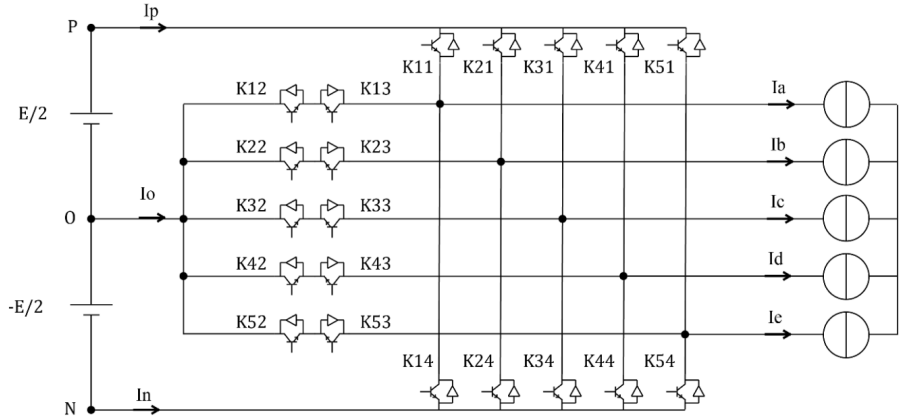

Figure 2.16: Diagram representing a three-level five-phase T-NPC inverter.

The three operating states of the three-level five-phase T-NPC inverter are as follows: The three operating states of the three-level five-phase T-NPC inverter are as follows:

- **Positive state (P):** The switch K_{i1} is conducting, while the switch K_{i3} is blocked, along with the switches of the midpoint. In the forward current direction, the conducting component is the switch K_{i1}. However, in the reverse direction, the diode D_{i1} takes over.
- **Negative state (N):** The switch K_{i4} and the diode D_{i4} conduct, while the switch K_{i2} remains blocked.
- **Neutral state (O):** The switches K_{i2} and K_{i3} are the only ones conducting. A direct current flows through the switch K_{i2} and the diode D_{i3}, while the reverse current flows through the switch K_{i3} and the diode D_{i2}.

Table 2.2: Possible cases of the switches.

State of the Switches				**Output Voltage**
K_{12}	K_{13}	K_{14}	K_{11}	
1	0	0	1	$E/2$
1	1	0	0	0
0	1	1	0	$-E/2$

The three-level five-phase T-NPC inverter includes one controllable switch in each half-bridge and two in each link between a phase and the midpoint. To simplify the control of the switches and to avoid any risk of short circuits, the respective switches K_{i1}, K_{i3}, and K_{i4}, K_{i2} must operate in a complementary manner. This operation also avoids the risk of an open circuit in a load phase when a controllable switch in the arm is not conducting, using a diode available in the midpoint branch.

The connection function of a switch located at phase i is defined as:

$$f_{ij} = \begin{cases} 1, & \text{if } K_{ij} \text{ is closed,} \\ 0, & \text{if } K_{ij} \text{ is open.} \end{cases} \tag{2.81}$$

Since the operation of K_{i1}, K_{i3}, K_{i4}, and K_{i2} must be complementary, it can be deduced that:

$$\begin{cases} f_{i1} = 1 - f_{i3}, \\ f_{i2} = 1 - f_{i4}. \end{cases} \tag{2.82}$$

The functions for the different states are defined as:

$$\begin{cases} f_{ic1} = f_{i1} \cdot f_{i2}, & \text{For state } P, \\ f_{ic2} = f_{i2} \cdot f_{i3}, & \text{For state } O, \\ f_{ic3} = f_{i4} \cdot f_{i3}, & \text{For state } N. \end{cases} \tag{2.83}$$

The conversion matrix of the inverter is as follows:

$$[C_v] = \begin{bmatrix} f_{1c1} & f_{1c2} & f_{1c3} \\ f_{2c1} & f_{2c2} & f_{2c3} \\ f_{3c1} & f_{3c2} & f_{3c3} \\ f_{4c1} & f_{4c2} & f_{4c3} \\ f_{5c1} & f_{5c2} & f_{5c3} \end{bmatrix} \tag{2.84}$$

The phase voltages with respect to the midpoint are defined by:

$$\begin{bmatrix} V_{a0} \\ V_{b0} \\ V_{c0} \\ V_{d0} \\ V_{e0} \end{bmatrix} = [C_v] \begin{bmatrix} \frac{V_{dc}}{2} \\ 0 \\ -\frac{V_{dc}}{2} \end{bmatrix} \tag{2.85}$$

The compound voltages are expressed by the following relations:

$$\begin{cases} U_{ab} = V_{a0} - V_{b0}, \\ U_{bc} = V_{b0} - V_{c0}, \\ U_{cd} = V_{c0} - V_{d0}, \\ U_{de} = V_{d0} - V_{e0}, \\ U_{ea} = V_{e0} - V_{a0}. \end{cases} \tag{2.86}$$

This can be expressed in matrix form as:

$$\begin{bmatrix} U_{ab} \\ U_{bc} \\ U_{cd} \\ U_{de} \\ U_{ea} \end{bmatrix} = \begin{bmatrix} f_{1c1} - f_{2c1} & f_{1c2} - f_{2c2} & f_{1c3} - f_{2c3} \\ f_{2c1} - f_{3c1} & f_{2c2} - f_{3c2} & f_{2c3} - f_{3c3} \\ f_{3c1} - f_{4c1} & f_{3c2} - f_{4c2} & f_{3c3} - f_{4c3} \\ f_{4c1} - f_{5c1} & f_{4c2} - f_{5c2} & f_{4c3} - f_{5c3} \\ f_{5c1} - f_{1c1} & f_{5c2} - f_{1c2} & f_{5c3} - f_{1c3} \end{bmatrix} \begin{bmatrix} \frac{V_{dc}}{2} \\ 0 \\ -\frac{V_{dc}}{2} \end{bmatrix} \tag{2.87}$$

The simple voltages with respect to the neutral can be determined by:

$$\begin{cases} V_{AN} = \frac{4V_{a0} - V_{b0} - V_{c0} - V_{d0} - V_{e0}}{5}, \\ V_{BN} = \frac{4V_{b0} - V_{a0} - V_{c0} - V_{d0} - V_{e0}}{5}, \\ V_{CN} = \frac{4V_{c0} - V_{a0} - V_{b0} - V_{d0} - V_{e0}}{5}, \\ V_{DN} = \frac{4V_{d0} - V_{a0} - V_{b0} - V_{c0} - V_{e0}}{5}, \\ V_{EN} = \frac{4V_{e0} - V_{a0} - V_{b0} - V_{c0} - V_{d0}}{5}. \end{cases} \tag{2.88}$$

By substituting (2.85) into (2.88), the mathematical model of the three-level five-phase T-NPC inverter is expressed as:

$$\begin{bmatrix} V_{AN} \\ V_{BN} \\ V_{CN} \\ V_{DN} \\ V_{EN} \end{bmatrix} = \frac{1}{5} \begin{bmatrix} 4f_{1c1} - f_{2c1} - f_{3c1} - f_{4c1} - f_{5c1} & 4f_{1c2} - f_{2c2} - f_{3c2} - f_{4c2} - f_{5c2} & 4f_{1c3} - f_{2c3} - f_{3c3} - f_{4c3} - f_{5c3} \\ 4f_{2c1} - f_{1c1} - f_{3c1} - f_{4c1} - f_{5c1} & 4f_{2c2} - f_{1c2} - f_{3c2} - f_{4c2} - f_{5c2} & 4f_{2c3} - f_{1c3} - f_{3c3} - f_{4c3} - f_{5c3} \\ 4f_{3c1} - f_{1c1} - f_{2c1} - f_{4c1} - f_{5c1} & 4f_{3c2} - f_{1c2} - f_{2c2} - f_{4c2} - f_{5c2} & 4f_{3c3} - f_{1c3} - f_{2c3} - f_{4c3} - f_{5c3} \\ 4f_{4c1} - f_{1c1} - f_{2c1} - f_{3c1} - f_{5c1} & 4f_{4c2} - f_{1c2} - f_{2c2} - f_{3c2} - f_{5c2} & 4f_{4c3} - f_{1c3} - f_{2c3} - f_{3c3} - f_{5c3} \\ 4f_{5c1} - f_{1c1} - f_{2c1} - f_{3c1} - f_{4c1} & 4f_{5c2} - f_{1c2} - f_{2c2} - f_{3c2} - f_{4c2} & 4f_{5c3} - f_{1c3} - f_{2c3} - f_{3c3} - f_{4c3} \end{bmatrix} \begin{bmatrix} \frac{V_{dc}}{2} \\ 0 \\ -\frac{V_{dc}}{2} \end{bmatrix}. \tag{2.89}$$

The input currents are given by:

$$\begin{bmatrix} I_p \\ I_o \\ I_n \end{bmatrix} = \begin{bmatrix} f_{1c1} & f_{2c1} & f_{3c1} & f_{4c1} & f_{5c1} \\ f_{1c2} & f_{2c2} & f_{3c2} & f_{4c2} & f_{5c2} \\ f_{1c3} & f_{2c3} & f_{3c3} & f_{4c3} & f_{5c3} \end{bmatrix} \begin{bmatrix} I_a \\ I_b \\ I_c \\ I_d \\ I_e \end{bmatrix} \tag{2.90}$$

2.4.1 Space Vector Modulation (SVM)

The space vectors of phase voltages in the two orthogonal planes are defined using a power-invariant transformation as follows:

$$V_{\alpha\beta} = \sqrt{\frac{2}{5}} \left[v_a + v_b e^{j\frac{2\pi}{5}} + v_c e^{j\frac{4\pi}{5}} + v_d e^{-j\frac{4\pi}{5}} + v_e e^{-j\frac{2\pi}{5}} \right] \tag{2.91}$$

The T-NPC inverter generates $3^5 = 243$ possible vectors. Figure 2.17 illustrates the representation of these vectors in the two reference frames ((P):2, (O):1, (N):0) [90].

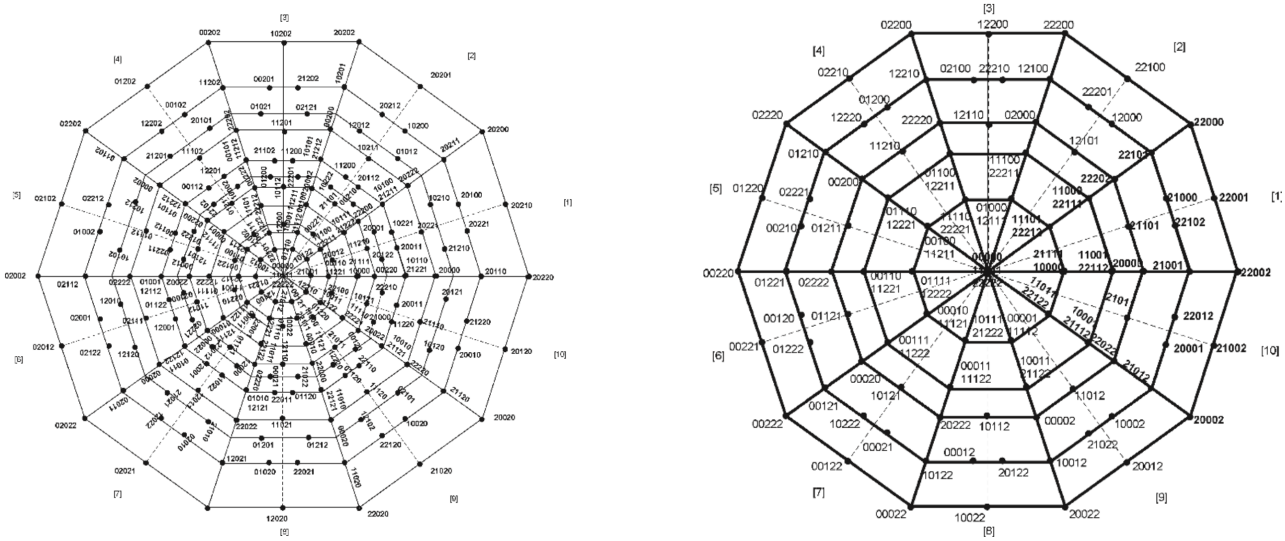

(a) $\alpha - \beta$ plane (b) $x - y$ plane

Figure 2.17: Space voltage vectors of the T-NPC inverter.

The $\alpha - \beta$ and $x - y$ planes are divided into 10 sectors. For each sector, the same set of vectors is found, with a shift of $\pi/5$ between adjacent sectors. The Table 2.3 provides the possible vectors in sector I, detailing the states, output voltages in both $\alpha - \beta$ and $x - y$ planes, along with the corresponding common mode voltage (CMV).

To move from one sector to another in the $\alpha - \beta$ plane, the entire set of states is shifted twice to the right and multiplied by a negative sign. For example, the state [1 0 -1 $-$ 1 0] corresponds to the vector $V_{\alpha\beta} = 1.0472\angle 0°$ in Sector I. For Sector II, the vector $V_{\alpha\beta} = 1.0472\angle 36°$ corresponds to the state [1 0 -1 0 1].

Table 2.3: The possible vectors in sector I.

Vectors	States	Plan $\alpha-\beta$		Plan $x-y$		MC Voltage
		$\frac{\lvert V_{\text{ref}}\rvert}{\sqrt{\frac{V_{dc}}{2}}}$	θ_{out}	$\frac{\lvert V_{\text{ref}}\rvert}{\sqrt{\frac{V_{dc}}{2}}}$	θ_{out}	
Zeros						
V_{01}	[0 0 0 0 0]	0	-	0	-	0
V_{02}	[1 1 1 1 1]	0	-	0	-	$V_{dc}/2$
V_{03}	[-1 -1 -1 -1 -1]	0	-	0	-	$-V_{dc}/2$
Active (sec I)						
V_1	[-1 1 0 0 -1]	0.1528	0°	1.0472	0°	$-V_{dc}/10$
V_2	[-1 0 1 -1 0]	0.2472	0°	0.6472	180°	$-3V_{dc}/10$
V_3	[1 0 0 0 1]	0.2472	0°	0.6472	0°	$V_{dc}/5$
V_4	[0 1 1 0 1]	0.2906	18°	1.2311	54°	0
V_5	[0 -1 -1 1 -1]	0.4000	0°	0.4000	0°	$-2V_{dc}/5$
V_6	[1 0 0 0 0]	0.4000	0°	0	0°	$V_{dc}/10$
V_7	[0 0 0 1 1]	0.4702	18°	0.7608	234°	0
V_8	[-1 -1 -1 1 1]	0.4944	0°	1.2944	180°	$-V_{dc}/10$
V_9	[1 1 1 -1 0]	0.5313	9.73°	0.9989	85.61°	$V_{dc}/5$
V_{10}	[-1 1 -1 1]	0.5313	26.26°	0.9989	228.38°	$-V_{dc}/5$
V_{11}	[-1 0 -1 0 0]	0.6173	13.61°	0.8596	314.26°	$-V_{dc}/10$
V_{12}	[1 0 1 0 1]	0.6173	22.38°	0.8596	153.73°	$V_{dc}/10$
V_{13}	[0 0 1 0 0]	0.6472	0°	0.2472	180°	$-V_{dc}/5$
V_{14}	[1 1 0 1 1]	0.6472	0°	0.2472	180°	$3V_{dc}/10$
V_{15}	[1 0 1 0 0]	0.7608	18°	0.4702	54°	0
V_{16}	[1 -1 1 -1 1]	0.8000	0°	0.8000	0°	$-3V_{dc}/10$
V_{17}	[1 0 0 1 1]	0.8596	9.73°	0.6173	265.61°	$V_{dc}/10$
V_{18}	[0 1 -1 1 1]	0.8596	26.26°	0.6173	202.38°	$-V_{dc}/10$
V_{19}	[1 0 1 1 1]	0.8944	0°	0.8944	180°	0
V_{20}	[1 1 0 1 0]	0.9989	13.61°	0.5313	134.26°	$V_{dc}/5$
V_{21}	[1 0 1 0 0]	0.9989	22.38°	0.5313	333.73°	$-V_{dc}/5$
V_{22}	[1 0 1 0 0]	1.0472	0°	0.1528	0°	$-V_{dc}/10$
V_{23}	[1 0 1 1 1]	1.2311	18°	0.2906	234°	0
V_{24}	[1 1 1 1 1]	1.2944	0°	0.4944	180°	$V_{dc}/10$

2.4.1.1 SVM with Two Active Vectors

The active vectors to be used, V_a and V_b, are vectors of the same amplitude, denoted as V_l, and shifted by $\pi/5$ between them. The reference vector can be expressed as follows:

$$V_{\text{ref}} = d_a V_a + d_b V_b + d_0 V_0 \tag{2.92}$$

where d_a, d_b, and d_0 are the duty cycles corresponding to these vectors, defined as:

$$\begin{aligned} d_a &= m_v \sin\left(\frac{\pi}{5} - \theta_{\text{out}}\right) \\ d_b &= m_v \sin\left(\theta_{\text{out}}\right) \\ d_0 &= 1 - d_a - d_b \end{aligned} \tag{2.93}$$

with:

$$0 \leq \theta_{\text{out}} \leq \frac{\pi}{5}, \quad m_v = \frac{|V_{\text{ref}}|}{V_l \sin(\pi/5)}$$

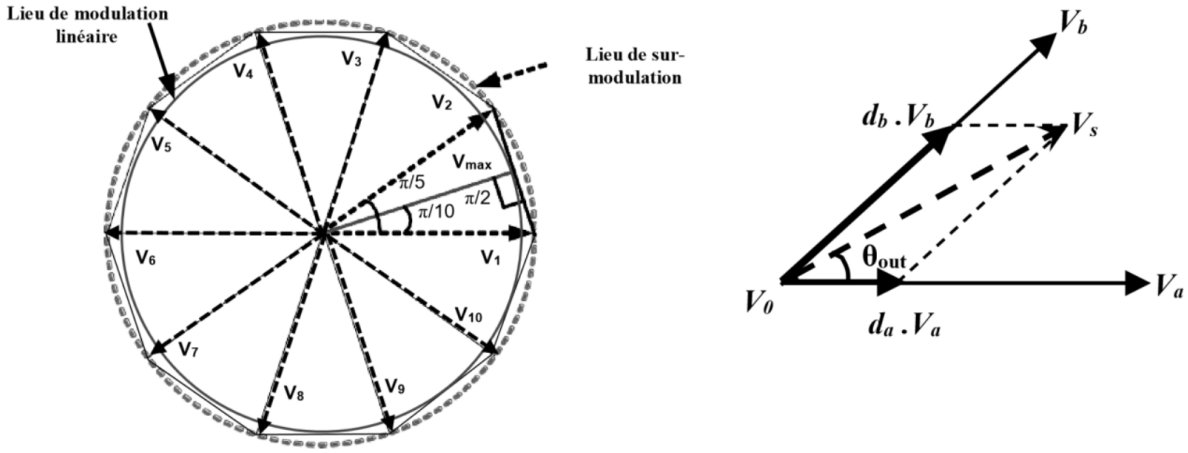

Figure 2.18: Linearity limit and projection of the reference vector.

To minimize the THD, the vectors with the smallest amplitudes in the $x - y$ plane are proposed. However, two essential points must be respected when choosing these vectors:

- The chosen vectors must have sufficient amplitudes to avoid losing the linearity of the strategy. This requires $V_l \cos(\pi/10) \geq V_{\text{ref}}$, as shown in Figure 2.18.
- The active vectors must not be too large relative to the reference vector to avoid very low duty cycles, which could significantly increase the margin of error during the calculation.

Table 2.4 summarizes the choice of active vectors for the case of a reference vector located in Sector I:

Table 2.4: Choice of vectors to use based on r for the case of sector I.

	$r = \frac{\lvert V_{\mathbf{ref}}\rvert}{(V_{\mathbf{dc}}/2)}$	**Vectors to Use**
reg 1	$0 < r \leq 0.5$	$V_{01} - V_{13}(II) - V_{14}(I) - V_{02}$
reg 2	$0.5 < r \leq 1.0472\cos(\pi/10)$	$V_{01} - V_{22}(I) - V_{22}(II)$
reg 3	$1.0472\cos(\pi/10) < r \leq 1.2311\cos(\pi/10)$	$V_{01} - V_{23}(I) - V_{23}(II)$
reg 4	$1.2311\cos(\pi/10) < r \leq 1.2944\cos(\pi/10)$	$V_{02} - V_{24}(I) - V_{24}(II) - V_{03}$

Figure 2.19 presents the sequencing and switching states for each region in Sector I.

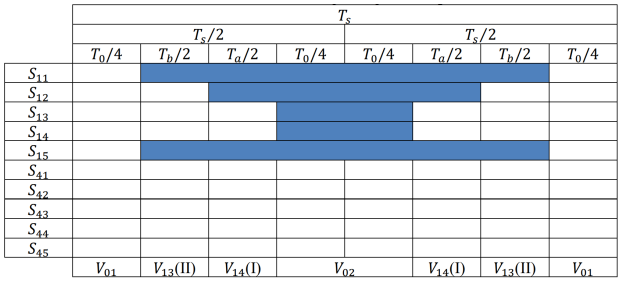

(a) Switch states for Region 1.

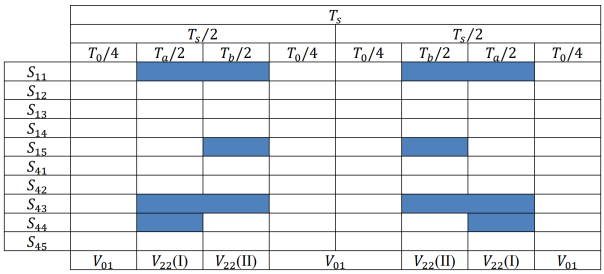

(b) Switch states for Region 2.

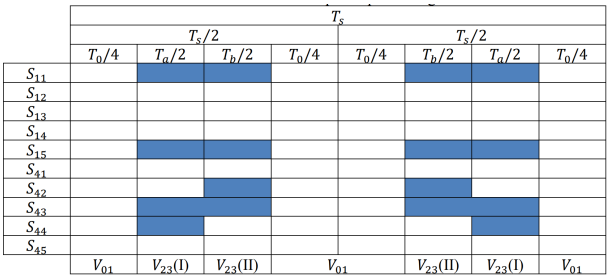

(c) Switch states for Region 3.

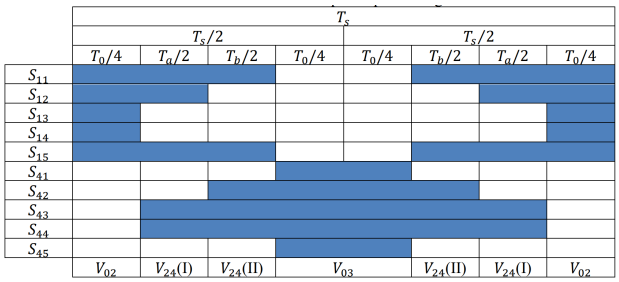

(d) Switch states for Region 4.

Figure 2.19: Sequencing and switching states for all regions in Sector I.

2.4.1.2 SVM with Four Active Vectors

This method allows reconstructing the reference vector in the $\alpha - \beta$ plane and simultaneously canceling the resultant vector in the $x - y$ plane, thereby offering reduced low-frequency harmonics. Its principle consists of selecting 4 active vectors, where each pair is in phase opposition in the $\alpha - \beta$ plane and out of phase in the $x - y$ plane, enabling the possibility of obtaining a null vector in the $x - y$ reference frame by adjusting the ratio of the duty cycles between each pair of vectors.

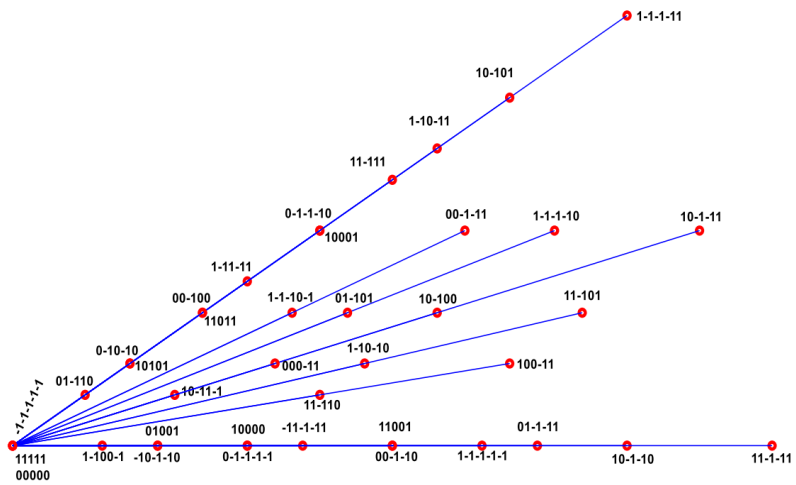

Figure 2.20: Presentation of all vectors in Sector I in the $\alpha - \beta$ plane.

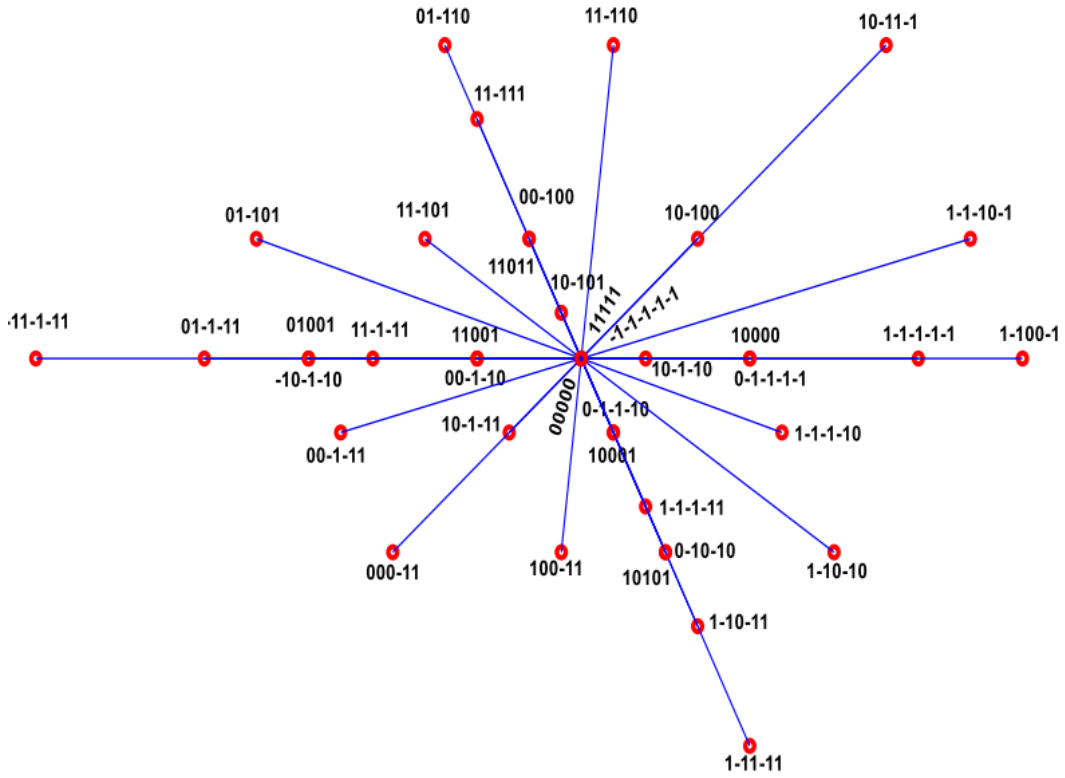

Figure 2.21: Presentation of all vectors in Sector I in the $x-y$ plane.

The reference vector is defined as follows:

$$V_{\text{ref}} = D_0V_0 + D_1V_1 + D_2V_2 + D_3V_3 + D_4V_4 \tag{2-35}$$

The goal is to calculate the duty cycles that allow achieving:

$$\begin{cases} V_{\alpha,\text{ref}} = |V_{\text{ref}}|\cos(\theta_{\text{out}}) \\ V_{\beta,\text{ref}} = |V_{\text{ref}}|\sin(\theta_{\text{out}}) \\ V_{x,\text{ref}} = 0 \\ V_{y,\text{ref}} = 0 \\ D_0 + D_1 + D_2 + D_3 + D_4 = 1 \end{cases} \tag{2-36}$$

By expanding these equations, the following is obtained:

$$\begin{pmatrix} D_0 \\ D_1 \\ D_2 \\ D_3 \\ D_4 \end{pmatrix} = \begin{pmatrix} V_{\alpha0} & V_{\alpha1} & V_{\alpha2} & V_{\alpha3} & V_{\alpha4} \\ V_{\beta0} & V_{\beta1} & V_{\beta2} & V_{\beta3} & V_{\beta4} \\ V_{x0} & V_{x1} & V_{x2} & V_{x3} & V_{x4} \\ V_{y0} & V_{y1} & V_{y2} & V_{y3} & V_{y4} \\ 1 & 1 & 1 & 1 & 1 \end{pmatrix}^{-1} \begin{pmatrix} |V_{\text{ref}}|\cos(\theta_{\text{out}}) \\ |V_{\text{ref}}|\sin(\theta_{\text{out}}) \\ 0 \\ 0 \\ 1 \end{pmatrix} \tag{2-37}$$

For the choice of vectors, the proposed method consists of using a variety of vectors to achieve only one switching per vector [91].

The selection of regions for this method is shown in Figure 2.22 [90]:

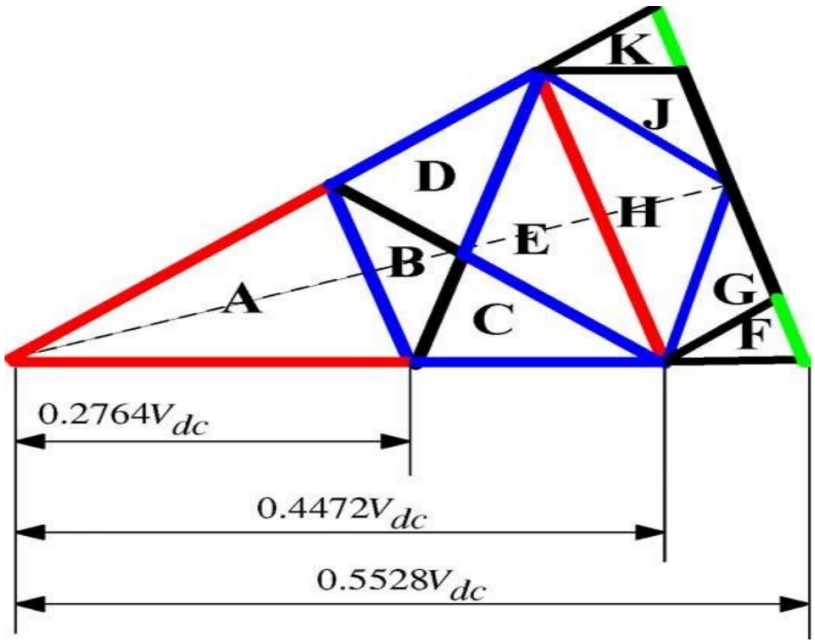

Figure 2.22: Presentation of the regions in a sector for Method 1.

To determine the conditions for transitioning from one region to another, it is necessary to project the reference vector onto the various axes defining the region. For example, for Region A, the following conditions are defined:

$$\begin{cases} |V_{\text{ref}}| \cos(\theta_{\text{out}}) \leq 0.2764 V_{\text{dc}} \\ |V_{\text{ref}}| \cos(\theta_{\text{out}} - \pi/5) \leq 0.2764 V_{\text{dc}} \\ |V_{\text{ref}}| \cos(\theta_{\text{out}} - \pi/10) \leq 0.2764 V_{\text{dc}} \cos(\pi/10) \end{cases} \tag{2-38}$$

Table 2.5 shows the order of vectors to be used for each region [90]:

Table 2.5: The set of vectors used for each region in Sector I.

Region	**Vectors**
Region A	$V_{13}(II)$, $V_6(I)$, $V_{15}(I)$, $V_6(I)$, $V_{13}(II)$
Region B	$V_{13}(I)$, $V_6(II)$, $V_{15}(II)$, $V_6(II)$, $V_{13}(I)$
Region C	$V_{13}(I)$, $V_6(II)$, $V_{15}(I)$, $V_{17}(I)$, $V_{13}(I)$
Region D	$V_{22}(I)$, $V_6(II)$, $V_{13}(I)$, $V_{14}(I)$
Region E	$V_{13}(I)$, $V_6(II)$, $V_{22}(II)$, $V_{22}(II)$
Region F	$V_{14}(I)$, $V_{20}(I)$, $V_{23}(I)$, $V_{17}(II)$
Region G	$V_{14}(I)$, $V_{20}(I)$, $V_{23}(I)$, $V_{23}(I)$
Region H	$V_{22}(I)$, $V_{22}(II)$, $V_{14}(I)$, $V_{22}(I)$
Region J	$V_{24}(I)$, $V_{21}(I)$, $V_{15}(I)$, $V_{23}(II)$
Region K	$V_{13}(II)$, $V_{22}(II)$, $V_{23}(II)$, $V_{14}(I)$

2.4.1.3 Simulation Results

Figures 2.23 and 2.24 present the simulation results for the SVM with two vectors and four vectors, respectively, applied to the three-level five-phase T-NPC inverter. The results demonstrate the influence of the number of vectors on the quality of the output voltage waveforms.

For the SVM with two vectors, the Total Harmonic Distortion (THD) of the output voltage is 52.37%, and the THD of the current is 17.97%. Compared to the two-level inverter, these results already show a significant improvement, which is attributed to the advantages of the multilevel topology, such as finer voltage steps and reduced output distortion. However, some low-frequency harmonic components persist due to the presence of x-y plane components when only two adjacent vectors are used.

In contrast, for the SVM with four vectors, the THD of the output voltage further decreases to 32.64%, and the THD of the current drops to 1.83%. This additional improvement is mainly due to the use of four adjacent vectors, which not only enhance the reconstruction of the reference voltage vector in the α-β plane but also ensure the cancellation of the resulting vector in the x-y plane, thus further minimizing the low-frequency harmonics and improving the quality of the output voltage waveforms.

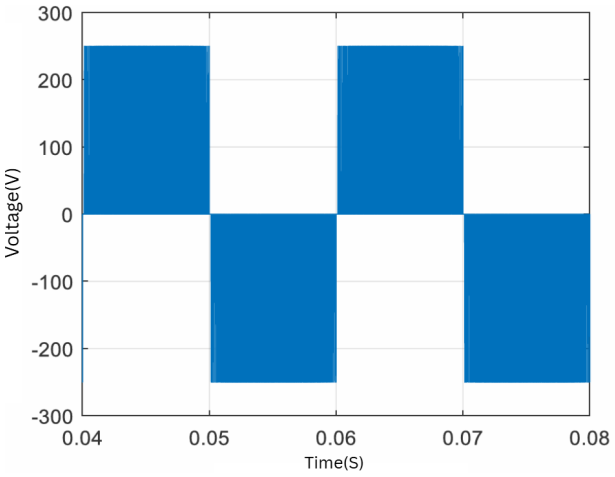

(a) voltages.

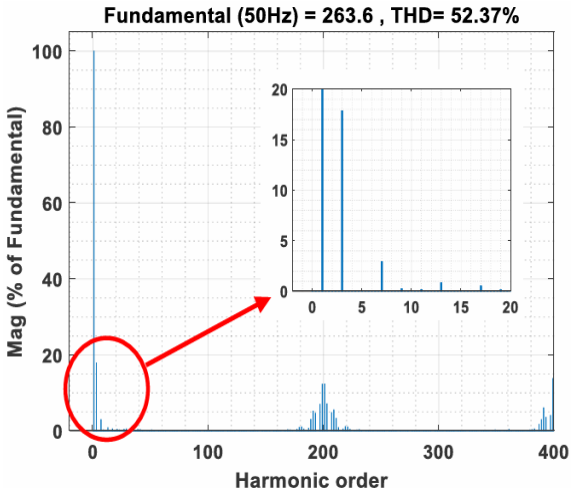

(b) Harmonic spectrum of voltages.

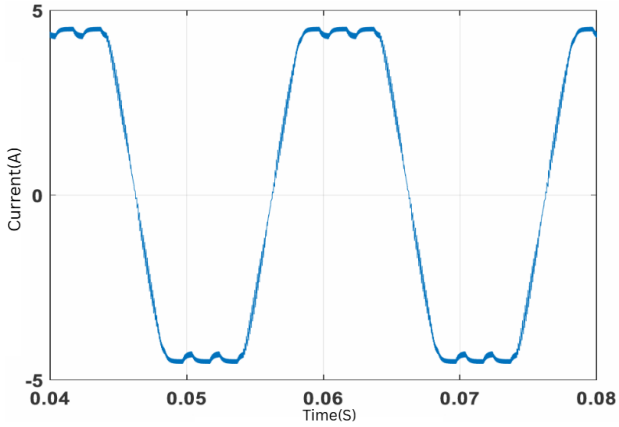

(c) Current.

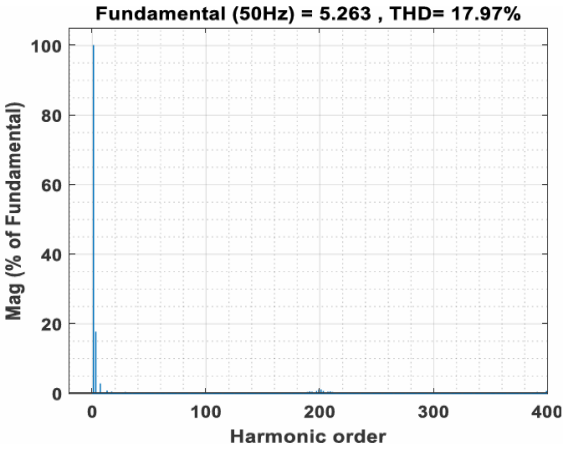

(d) Harmonic spectrum of current.

Figure 2.23: Simulation results for the SVM with two vectors.

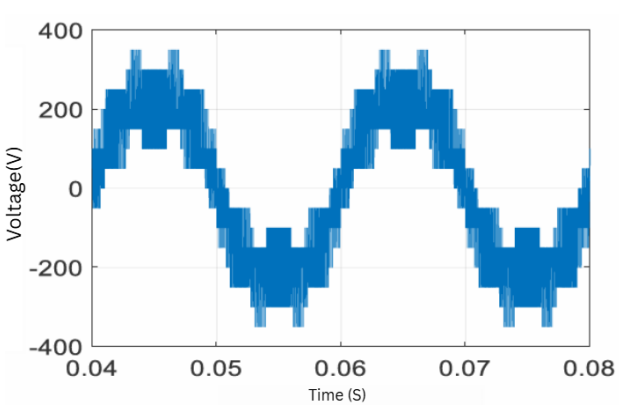

(a) voltages.

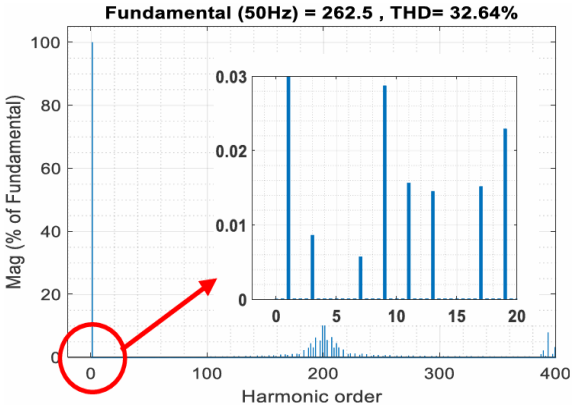

(b) Harmonic spectrum of voltages.

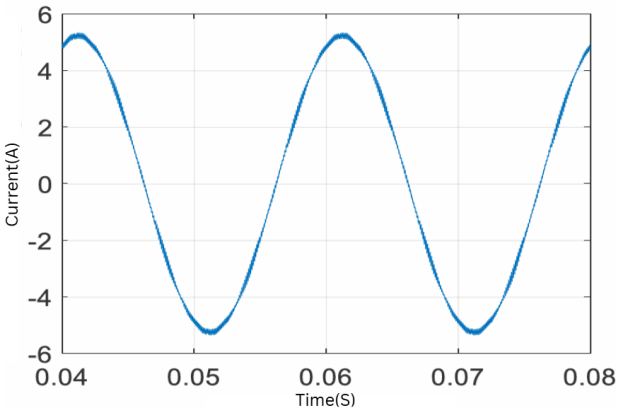

(c) Current.

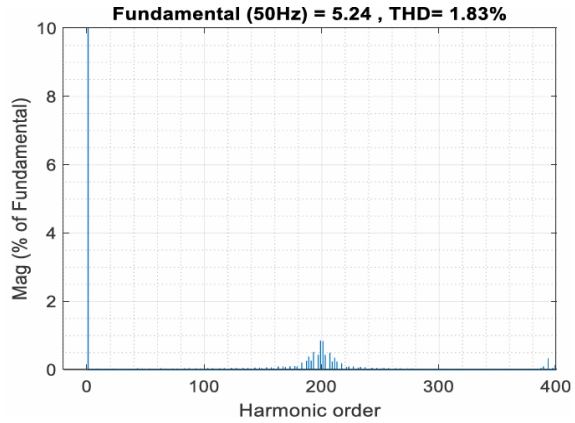

(d) Harmonic spectrum of current.

Figure 2.24: Simulation results for the SVM with four vectors.

2.5 Conclusion

In this chapter, the mathematical modeling of the symmetrical five-phase induction motor and the two-level and T-NPC three-level five-phase inverters has been comprehensively developed. The motor model was analyzed in detail across phase quantities, as well as stationary and rotating reference frames. A key distinction between the five-phase and three-phase models is the presence of $x-y$ components in the $d-q-x-y-o$ coordinate system. These $x-y$ components are fully decoupled from the $d-q$ components and from each other, meaning they do not contribute to flux or electromagnetic torque production, although they may introduce minor additional losses. However, for the purposes of this study, these losses are considered negligible.

Additionally, given the short-circuited rotor winding and the star configuration of the stator winding, and assuming balanced five-phase components in both the stator and rotor, the zero-sequence components can be neglected. Consequently, the analysis primarily focuses on the $d-q$ components, which are responsible for flux and torque production. This allows for a structured transformation of the five-phase induction motor model into a form similar to that of a three-phase machine, enabling the direct application of conventional control strategies.

The chapter also presented the mathematical modeling and space vector modulation (SVM) techniques for two-level and T-NPC three-level five-phase inverters. The modeling of the two-level inverter included the derivation of voltage states, space vector representation, and the

corresponding SVM techniques for generating sinusoidal output voltages. Similarly, the T-NPC three-level inverter was analyzed, emphasizing its ability to generate multiple voltage levels through distinct switching states and space vector configurations.

The SVM strategies formulated for these inverter topologies were designed to eliminate the resultant vector in the $x-y$ plane, thereby reducing low-frequency harmonics and ensuring high-quality sinusoidal output voltages. These models establish the theoretical foundation required for implementing advanced control techniques in five-phase induction motor drives.

The work presented in this chapter is a crucial step toward the practical implementation of five-phase motor control. In the next chapter, these inverter models will be integrated into the study and implementation of advanced control techniques, including Direct Torque Control (DTC), Direct Torque Control with Space Vector Modulation (DTC-SVM), and Finite Control Set Model Predictive Control (FCS-MPC).

Chapter 3:
Five-Phase Induction Machine Control Strategies

Chapter 3

Chapter 3: Five-Phase Induction Machine Control Strategies

3.1 Introduction

This chapter presents a comparative analysis of control methods applied to five-phase induction motors, serving as a representative example of multiphase systems. The study examines Direct Torque Control (DTC), Direct Torque Control with Space Vector Modulation (DTC-SVM), and Finite Control Set Model Predictive Control (FCS-MPC). Through simulations conducted in MATLAB/Simulink, the performance of these strategies is evaluated under various operating conditions.

The assessment focuses on:

- **Dynamic response** during speed reference changes and under sudden load disturbances.
- **Steady-state performance** under constant operating conditions.
- **Energy quality**, including stator current waveform shape, peak values, and harmonic content in both stator current and voltage.

The objective is to identify the strengths and limitations of each approach to determine the most suitable control strategy for optimizing the performance of five-phase induction motors based on specific application requirements.

To further enhance efficiency and robustness, artificial neural networks (ANNs) are introduced as replacements for traditional proportional-integral (PI) regulators, and a Model Reference Adaptive System (MRAS)-based speed estimator is integrated to enable robust sensorless control.

This chapter is structured to provide a comprehensive comparative study of these control techniques. Each method's fundamental principles are explored, followed by simulation results that highlight their effectiveness in various operational scenarios.

3.2 Direct Torque Control for a Five-Phase Induction Motor

The basic schematic of the DTC method applied to a five-phase induction motor is presented in Figure 3.1. This technique is based on determining the switching states to be applied to the inverter in order to directly control the stator flux and the electromagnetic torque. These quantities are maintained within limits defined by two hysteresis bands, using signals provided by the hysteresis regulators for torque and stator flux, as well as the signal indicating the position of the stator flux vector.

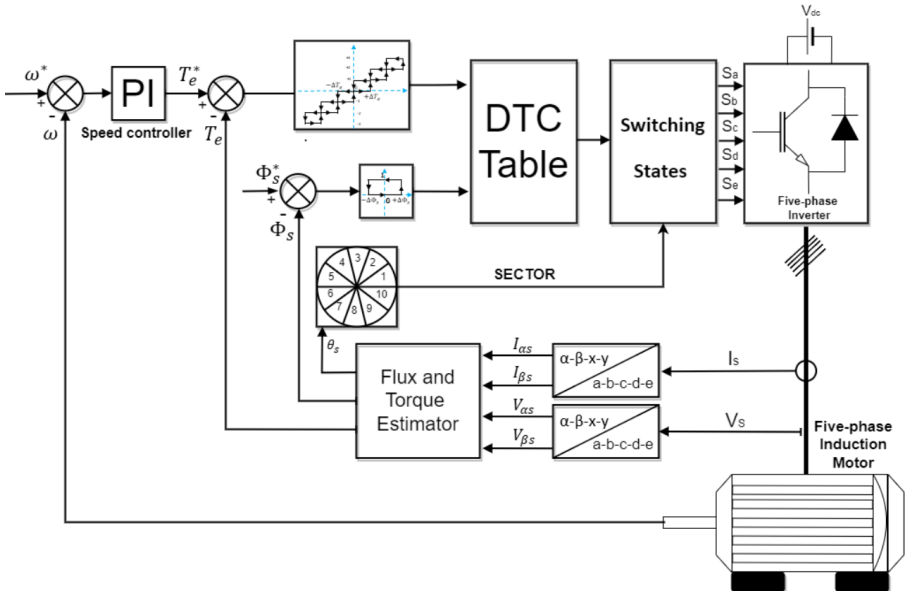

Figure 3.1: Block diagram of the DTC method.

To better understand the operation of Direct Torque Control, the following section details its fundamental principles and the mathematical formulations governing its behavior.

3.2.1 Basic Principle of Direct Torque Control

The operating principle of direct torque control applied to the five-phase induction machine is reduced to the $\alpha - \beta$ plane (torque and flux regulation), assuming that the components (x, y) are null.

From the stationary reference frame model of the induction machine, specifically equation (2.51), the expression for the stator flux is obtained as follows:

$$v^s_{\alpha\beta} = R_s i^s_{\alpha\beta} + \frac{d\phi^s_{\alpha\beta}}{dt} \tag{3.1}$$

By integrating equation (3.1), the stator flux vector as a function of time is obtained:

$$\phi^s_{\alpha\beta}(t) = \int_0^t (v^s_{\alpha\beta} - R_s i^s_{\alpha\beta})\, dt + \phi^s_{\alpha\beta}(0) \tag{3.2}$$

For simplification, ignoring the voltage drop in the stator resistance over a small sampling period T_e, equation (3.2) is rewritten as follows [92, 93]:

$$\phi^s_{\alpha\beta}(t) = \int_0^t v^s_{\alpha\beta} dt + \phi^s_{\alpha\beta}(0) \tag{3.3}$$

During a sampling period T_e, the applied voltage vector remains constant. Under this assumption, the following expressions hold [16]:

$$\begin{cases} \phi^s_{\alpha\beta}(T_e) \approx v^s_{\alpha\beta} T_e + \phi^s_{\alpha\beta}(0) \\ \Delta\phi^s_{\alpha\beta} \approx v^s_{\alpha\beta} T_e \end{cases} \tag{3.4}$$

where $\Delta\phi^s_{\alpha\beta} = \phi^s_{\alpha\beta}(T_e) - \phi^s_{\alpha\beta}(0)$ represents the variation of the stator flux vector.

Equation (3.4) shows that the variation of the stator voltage vector is proportional to the stator flux vector. Increasing the stator flux requires applying a voltage vector in the same direction as the flux, and conversely, reducing it necessitates applying a voltage vector in the opposite direction.

For the analysis of electromagnetic torque behavior, the equations of system (2.64) are combined, leading to the following expression in the $\alpha - \beta$ plane:

$$T_{em} = \frac{p \cdot L_m}{\sigma \cdot L_s L_r} \left(\vec{\phi^r_{\alpha\beta}} \times \vec{\phi^s_{\alpha\beta}} \right) = \frac{p \cdot L_m}{\sigma \cdot L_s L_r} \left| \phi^r_{\alpha\beta} \right| \cdot \left| \phi^s_{\alpha\beta} \right| \cdot \sin\delta \tag{3.5}$$

where δ is the angle between the stator and rotor flux vectors, referred to as the load angle.

Since the rotor time constant T_r is significantly larger than the stator time constant T_s, the rotor flux varies much more slowly than the stator flux, allowing it to be considered constant [92, 94].

A rapid variation in the angle between the two vectors results in an increase or decrease in torque, as it is proportional to the sine of the load angle δ (equation 3.5). This variation is induced by the application of a voltage vector, as indicated in equation (3.4).

Figure 3.2 illustrates the effect of a voltage space vector on both the magnitude of the stator flux and the load angle δ. Figure 3.2-a represents the vector diagram derived from the machine model equations, including the voltage drop in the stator resistance, while Figure 3.2-b presents the approach used for the control strategy.

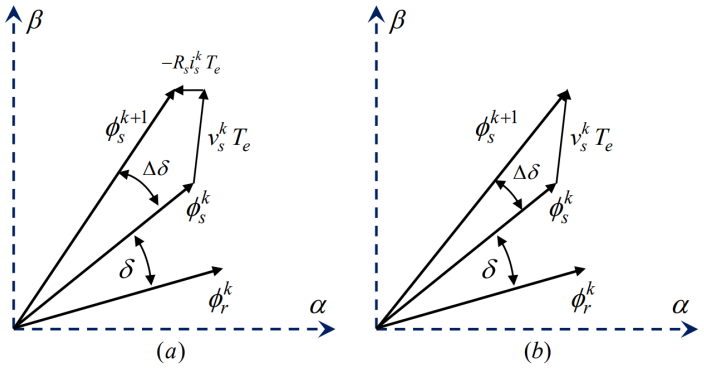

Figure 3.2: Impact of the voltage vector on the stator flux and load angle.

Accurate estimation of the stator flux and electromagnetic torque is essential for the effective implementation of DTC. The next section describes the methods used to reconstruct these quantities based on measurements and associated calculations.

3.2.2 Flux and Torque Estimator

The fundamental equations used to reconstruct the stator flux and consequently the electromagnetic torque are expressed from equations (2.51) as follows:

$$\begin{cases} \phi_\alpha^s = \int_0^t (v_\alpha^s - R_s i_\alpha^s) dt \\ \phi_\beta^s = \int_0^t (v_\beta^s - R_s i_\beta^s) dt \end{cases} \tag{3.6}$$

The stator current is measured, while the stator voltage depends on the switching states $(S_a, S_b, S_c, S_d, S_e)$ and the measured DC-link voltage V_{dc} at the inverter input. Using the Concordia transformation matrix (2.35), the voltages v_α^s and v_β^s are obtained as follows:

$$\begin{bmatrix} v_\alpha^s \\ v_\beta^s \end{bmatrix} = \sqrt{\frac{2}{5}} V_{dc} \begin{bmatrix} 1 & \cos\frac{2\pi}{5} & \cos\frac{4\pi}{5} & \cos\frac{6\pi}{5} & \cos\frac{8\pi}{5} \\ 0 & \sin\frac{2\pi}{5} & \sin\frac{4\pi}{5} & \sin\frac{6\pi}{5} & \sin\frac{8\pi}{5} \end{bmatrix} \begin{bmatrix} S_a \\ S_b \\ S_c \\ S_d \\ S_e \end{bmatrix} \tag{3.7}$$

The estimated flux is determined by its magnitude and position using the following relation:

$$\begin{cases} |\phi_s| = \sqrt{\phi_{\alpha s}^2 + \phi_{\beta s}^2} \\ \angle\phi_s = \hat{\theta}_s = \arctan\frac{\phi_{\beta s}}{\phi_{\alpha s}} \end{cases} \tag{3.8}$$

The electromagnetic torque can be estimated using equation (2.64) from the estimated flux and the measured stator currents in the $\alpha - \beta$ reference frame as follows:

$$\hat{T}_{em} = p\left(\phi_{\alpha s} i_{\beta s} - \phi_{\beta s} i_{\alpha s}\right) \tag{3.9}$$

Once the flux and torque have been estimated, an appropriate control strategy must be implemented to ensure these quantities remain within their desired ranges. The following section presents the hysteresis controllers used for flux and torque regulation.

3.2.3 Flux and Torque Controllers

For flux control, a two-level hysteresis controller is the simplest and most effective solution. This type of controller allows direct regulation of the flux amplitude while maintaining the extremity of the flux vector ϕ_s within a circular trajectory.

The output of the flux regulator defines the upper and lower thresholds for the flux amplitude. The two-level hysteresis comparator, used for flux regulation, ensures the condition:

$$\left|\phi_s^{ref} - \phi_s\right| < \Delta\phi_s \tag{3.10}$$

where ϕ_s^{ref} is the flux reference and $\Delta\phi_s$ is the hysteresis band of the regulator. The comparator outputs cflx = +1 to increase the flux and cflx = 0 to decrease it, as illustrated in Figure 3.3.

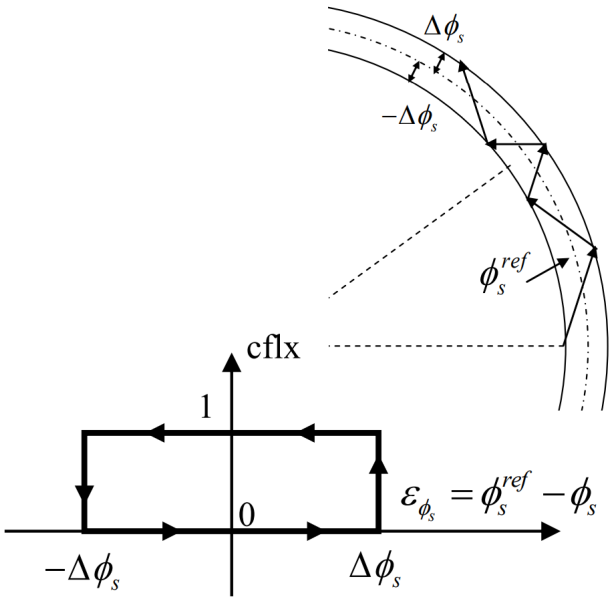

Figure 3.3: Two-level hysteresis comparator for flux control.

For the control of the electromagnetic torque, the output function of the hysteresis controller now operates with 7 levels instead of 3, ensuring that it satisfies the condition:

$$\left|T_{em}^{ref} - T_{em}\right| < \Delta T_{em} \tag{3.11}$$

where ΔT_{em} is the hysteresis band of the regulator.

The controller provides seven levels of torque control, meaning the output signal *tcpl* takes values in the range $-3, -2, -1, 0, 1, 2, 3$, depending on the deviation between the reference torque T_{em}^{ref} and the actual torque T_{em}.

- $tcpl = +3$ when the torque is significantly below the lower hysteresis limit, requiring a strong increase.
- $tcpl = +2$ when the torque is moderately below the lower limit, requiring a medium increase.
- $tcpl = +1$ when the torque is slightly below the lower limit, requiring a weak increase.
- $tcpl = 0$ when the torque is within the hysteresis band and should remain stable.
- $tcpl = -1$ when the torque is slightly above the upper limit, requiring a weak reduction.
- $tcpl = -2$ when the torque is moderately above the upper limit, requiring a medium reduction.
- $tcpl = -3$ when the torque is significantly above the upper limit, requiring a strong reduction.

This 7-level hysteresis control provides finer torque regulation compared to the traditional 3-level approach, improving control precision and reducing torque ripple.

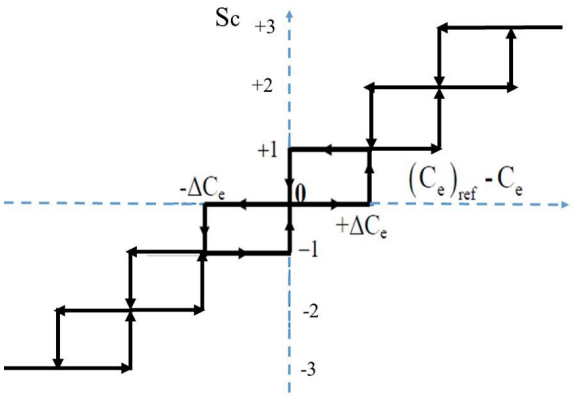

Figure 3.4: Hysteresis comparator for electromagnetic torque control with 7 levels.

For the control of the electromagnetic torque in the case of the T-NPC three-level five-phase inverter, an 11-level hysteresis comparator is used. This approach provides finer torque control, reducing torque ripple and improving dynamic performance. The controller satisfies the condition [95, 96]:

$$\left|T_{em}^{ref} - T_{em}\right| < \Delta T_{em} \tag{3.12}$$

where ΔT_{em} is the hysteresis band of the regulator.

The 11-level torque hysteresis control provides more precise regulation, meaning the output signal $tcpl$ takes values in the range:

$$tcpl \in \{-5, -4, -3, -2, -1, 0, 1, 2, 3, 4, 5\}$$

depending on the deviation between the reference torque T_{em}^{ref} and the actual torque T_{em}.

- $tcpl = +5$ when the torque is significantly below the lower hysteresis limit, requiring a very strong increase.
- $tcpl = +4$ when the torque is well below the lower limit, requiring a strong increase.
- $tcpl = +3$ when the torque is moderately below the lower limit, requiring a medium increase.
- $tcpl = +2$ when the torque is slightly below the lower limit, requiring a weak increase.
- $tcpl = +1$ when the torque is near the lower limit, requiring a minimal increase.
- $tcpl = 0$ when the torque is within the hysteresis band and should remain stable.
- $tcpl = -1$ when the torque is near the upper limit, requiring a minimal reduction.
- $tcpl = -2$ when the torque is slightly above the upper limit, requiring a weak reduction.
- $tcpl = -3$ when the torque is moderately above the upper limit, requiring a medium reduction.

- $tcpl = -4$ when the torque is well above the upper limit, requiring a strong reduction.
- $tcpl = -5$ when the torque is significantly above the upper limit, requiring a very strong reduction.

This 11-level hysteresis control further improves torque precision, offering smoother performance and enhanced dynamic response.

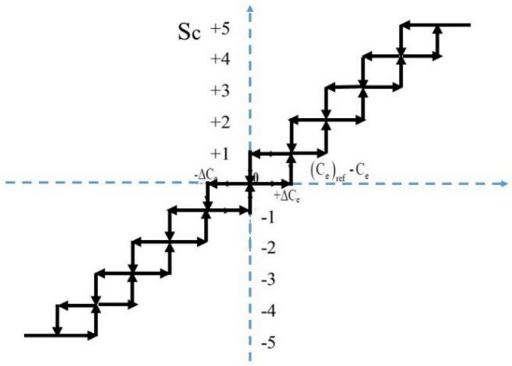

Figure 3.5: Hysteresis comparator for electromagnetic torque control with 11 levels.

The selection of the switching voltage vector is based on the outputs of both the flux and torque controllers. The flux control output determines whether the flux should increase or decrease, while the torque control output determines the magnitude and direction of the required torque correction. The next section details the selection process, considering the stator flux vector position and the specific control objectives to ensure optimal system performance.

3.2.4 Selection of the Voltage Vector

The selection of voltage vectors is carried out based on the position of the stator flux vector within one of the ten sectors of the voltage plane, as illustrated in Figure 3.6. The effect of these voltage vectors allows direct control of both the flux amplitude and the torque by selecting the appropriate vector from 32 possibilities.

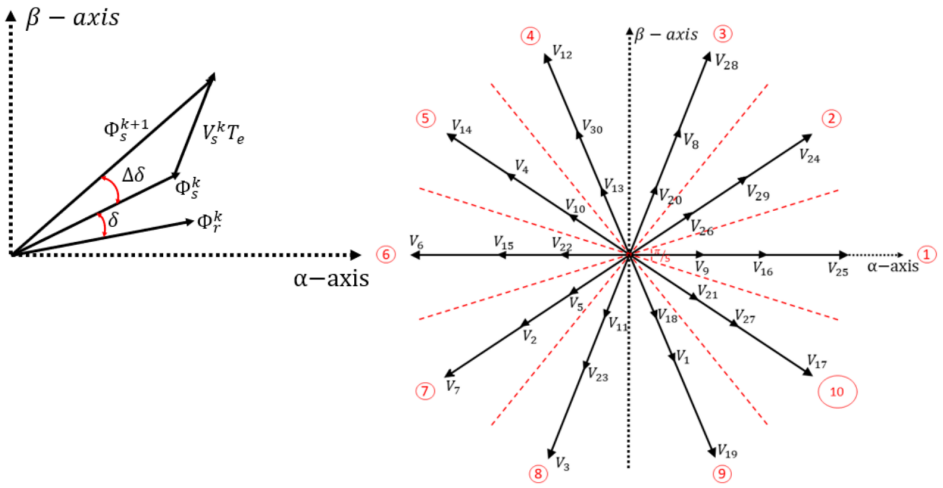

Figure 3.6: Effect of the voltage vector on the stator flux and the angle δ.

When the stator flux vector $\overline{\Phi}_s$ is located in a given sector i, flux and torque control is achieved by selecting one of the following voltage vectors: V_{i+1}^{123}, V_{i-1}^{123}, V_{i+4}^{123}, V_{i-4}^{123}, V_0, or V_{31}. The specific effects of each vector are detailed below:

- The vectors V_{i+1}^{123} or V_{i-1}^{123} increase the amplitude of the flux $\overline{\Phi}_s$.
  - When V_{i+1}^{123} is selected, the electromagnetic torque T_e increases with variable intensity (strong, medium, or weak).
  - When V_{i-1}^{123} is selected, the electromagnetic torque T_e decreases with variable intensity (strong, medium, or weak).
- The vectors V_{i+4}^{123} or V_{i-4}^{123} decrease the amplitude of the flux $\overline{\Phi}_s$.
  - When V_{i+4}^{123} is selected, the electromagnetic torque T_e increases with variable intensity (strong, medium, or weak).
  - When V_{i-4}^{123} is selected, the electromagnetic torque T_e decreases with variable intensity (strong, medium, or weak).
- The zero vectors V_0 and V_{31} stop the flux rotation, thereby reducing torque while maintaining the flux amplitude $\overline{\Phi}_s$ constant.

Table 3.1 presents the selected voltage vectors for each sector.

Table 3.1: Lookup table for the DTC method

$\Delta\Phi_s$	ΔT_e	S1	S2	S3	S4	S5	S6	S7	S8	S9	S10
1	+3	V24	V28	V12	V14	V6	V7	V3	V19	V17	V25
1	+2	V29	V8	V30	V4	V15	V2	V23	V1	V27	V16
1	+1	V26	V20	V13	V10	V22	V5	V11	V18	V21	V9
1	0	V0	V31	V0	V31	V0	V31	V0	V31	V0	V31
1	-1	V21	V9	V26	V20	V13	V10	V22	V5	V11	V18
1	-2	V27	V16	V29	V8	V30	V4	V15	V2	V23	V1
1	-3	V17	V25	V24	V28	V12	V14	V6	V7	V3	V19
0	+3	V14	V6	V7	V3	V19	V17	V25	V24	V28	V12
0	+2	V4	V15	V2	V23	V1	V27	V16	V29	V8	V30
0	+1	V10	V22	V5	V11	V18	V21	V9	V26	V20	V13
0	0	V31	V0	V31	V0	V31	V0	V31	V0	V31	V0
0	-1	V5	V11	V18	V21	V9	V26	V20	V13	V10	V22
0	-2	V2	V23	V1	V27	V16	V29	V8	V30	V4	V15
0	-3	V7	V3	V19	V17	V25	V24	V28	V12	V14	V6

To assess the performance of the different control strategies applied to the five-phase induction machine, a series of simulations were conducted using MATLAB/Simulink under various operating conditions. The goal is to evaluate both steady-state and dynamic behaviors by analyzing key performance indicators such as response time, torque ripple, flux regulation, current quality, and system stability.

For consistency across all methods, two test scenarios were applied. The first scenario investigates the system's response to step changes in speed reference under constant load, with the speed increasing from 50 rad/s to 200 rad/s in increments of 50 rad/s, followed by a reduction to 150 rad/s. The second scenario focuses on the system's dynamic response to sudden load variations at fixed speeds (100 rad/s and 150 rad/s), where the load shifts from no-load to full-load and vice versa. These tests enable a comparative evaluation of the different control strategies under identical operating conditions.

3.2.5 Simulation Results

Figures 3.7 and 3.9 present the results of the first test for DTC using two-level and three-level five-phase inverters, respectively. They show the main electromagnetic and electrical variables, including the rotor speed and its reference, the electromagnetic torque and its reference, and the stator flux magnitude and its reference. They also include the stator current and its harmonic spectrum, as well as the inverter output voltage and its harmonic content. These results provide insight into the system's behavior under varying speed conditions.

Figures 3.8 and 3.10 present the results of the second test for DTC using two-level and three-level five-phase inverters, respectively. The electromagnetic torque and rotor speed are shown to evaluate performance indicators such as speed deviation, settling time, and stability during load disturbances.

In Figure 3.7a for the two-level inverter, the rotor speed closely follows its reference without overshoot during both acceleration and deceleration. The motor transitions from 100 rad/s to 150 rad/s and from 200 rad/s to 150 rad/s in approximately 0.12 seconds. In Figure 3.9a for the three-level inverter, these transitions are achieved slightly faster, in approximately 0.09 s and 0.12 s respectively.

Figure 3.7b for the two-level inverter shows that the electromagnetic torque follows its reference in both forward and reverse operation. The average maximum torque ripple is approximately 0.03851 Nm. Figure 3.9b for the three-level inverter shows a significant reduction in torque ripple, with an average maximum value of approximately 0.005995 Nm.

In Figure 3.7c for the two-level inverter, the stator flux magnitude follows its reference value with minor deviations observed during speed changes. The flux ripple reaches up to 0.01181 Wb throughout the test. In Figure 3.9c for the three-level inverter, the tracking is improved, with a reduced flux ripple of approximately 0.007611 Wb.

For the electrical performance of the DTC, the results show that the stator currents increase in both magnitude and frequency as the speed increases. During speed variations, the peak current reaches approximately 7.36 A with the two-level inverter and is reduced to 3.93 A using the three-level inverter. The stator current waveforms exhibit variability due to the variable switching frequency. The total harmonic distortion (THD) of the stator current is 22.59% for the two-level inverter and improves to 17.25% with the three-level one. Regarding the inverter output voltage, the THD is 129.68% for the two-level configuration and decreases to 78.61% for the three-level inverter.

Figures 3.8 and 3.10 show that the DTC strategy effectively handles the sudden load increase and decrease for the two-level and three-level inverters, respectively, with the actual torque T_{em} closely following the reference T_r. For the two-level inverter, at a reference speed of 100 rad/s, the rotor speed drops by 1.03 rad/s during load application, with a settling time of approximately 0.14 s. At 150 rad/s, the speed drop reaches 1.05 rad/s, with a settling time of 0.16 s. When the load is removed, overshoot values of 1.29 rad/s and 1.46 rad/s are observed at 100 rad/s and 150 rad/s, with corresponding settling times of 0.136 s and 0.138 s. In contrast, the three-level inverter exhibits improved dynamic performance: the rotor speed drops are limited to 0.6 rad/s and 0.61 rad/s, with faster settling times of 0.07 s and 0.09 s, respectively. The overshoot values are also reduced to 0.43 rad/s and 0.52 rad/s, with corresponding settling times of 0.08 s and 0.102 s, highlighting the enhanced robustness of the three-level inverter.

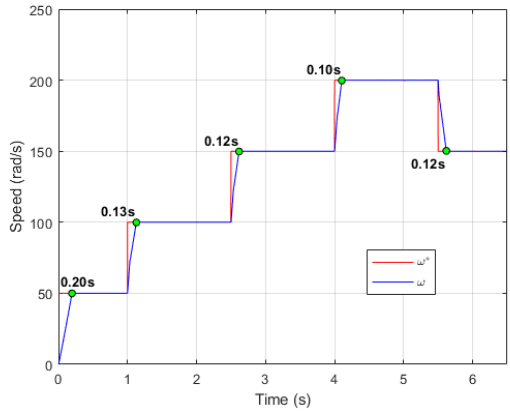

(a) Speed and its reference

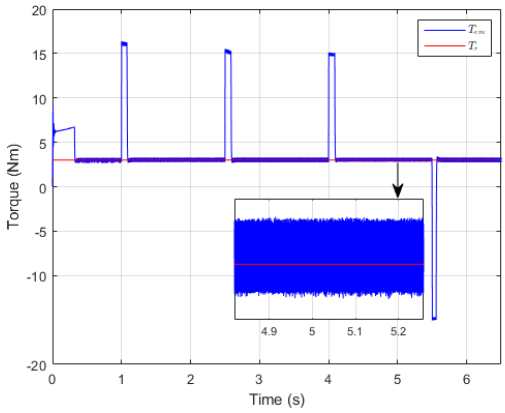

(b) Electromagnetic torque and its reference.

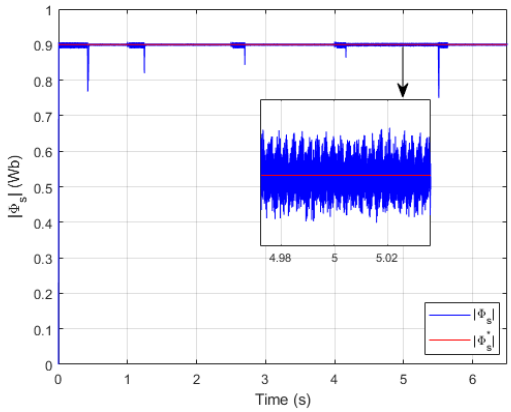

(c) Stator flux and its reference

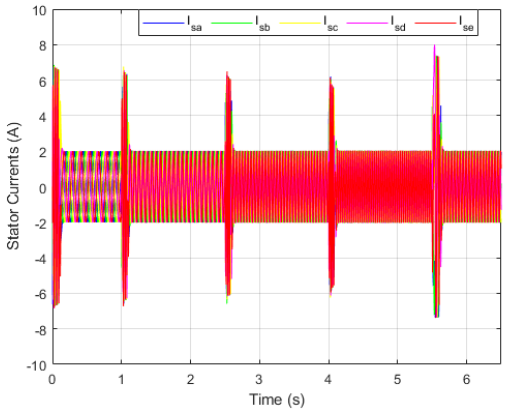

(d) Stator current

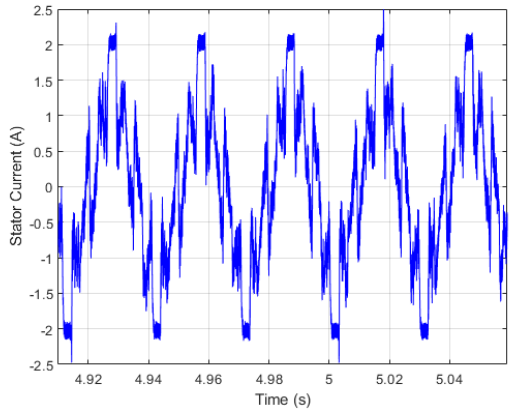

(e) Stator current

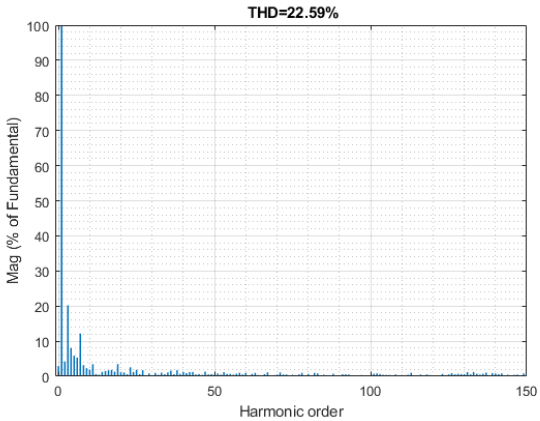

(f) FFT of stator current

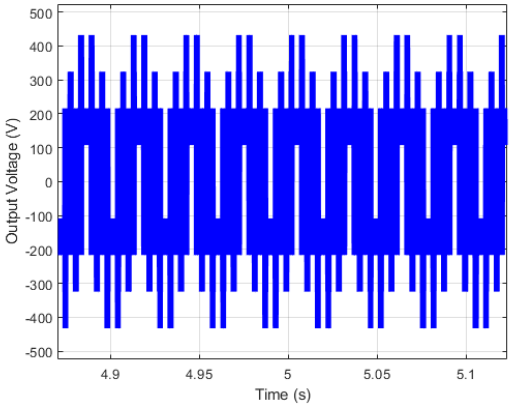

(g) Output voltage

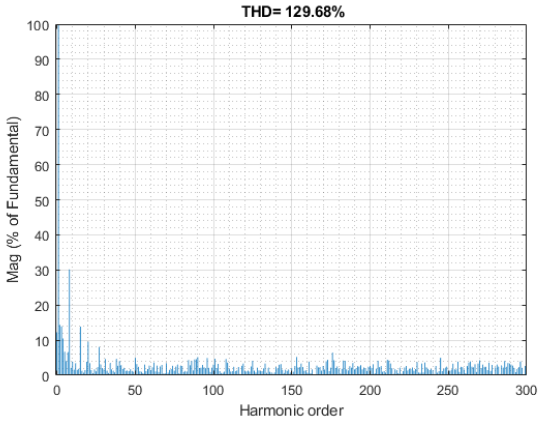

(h) FFT of output voltage

Figure 3.7: Simulation results for DTC using a two-level five-phase inverter

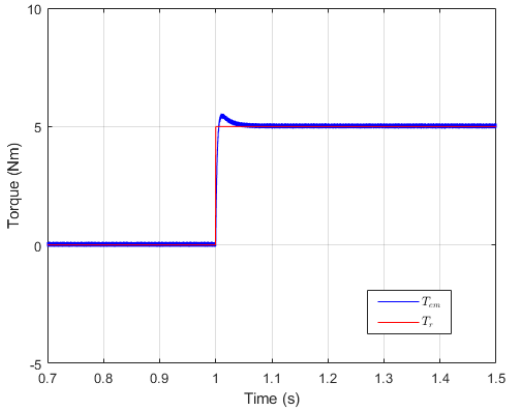

(a) Torque and its reference

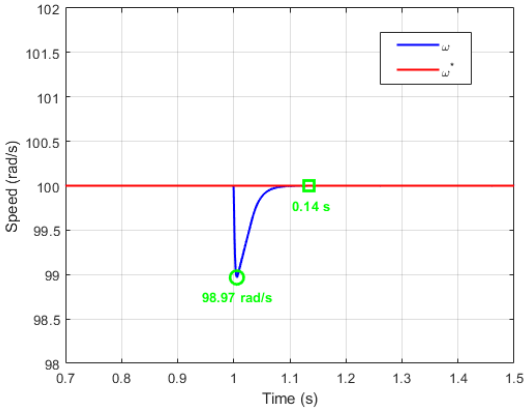

(b) Speed and its reference

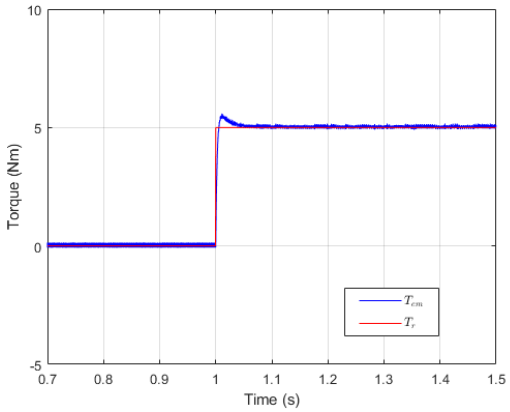

(c) Torque and its reference

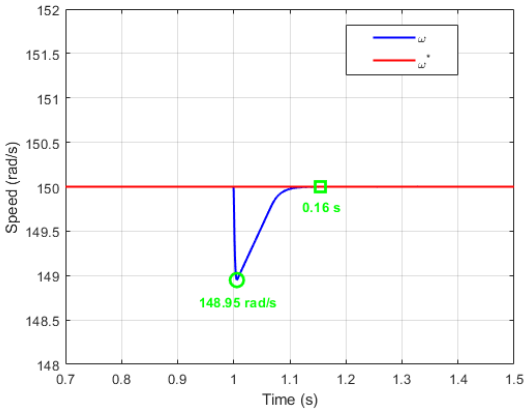

(d) Speed and its reference

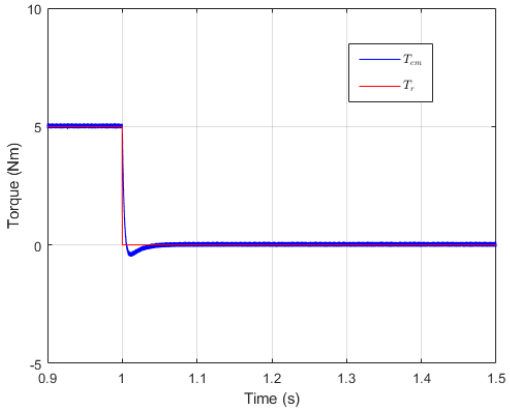

(e) Torque and its reference

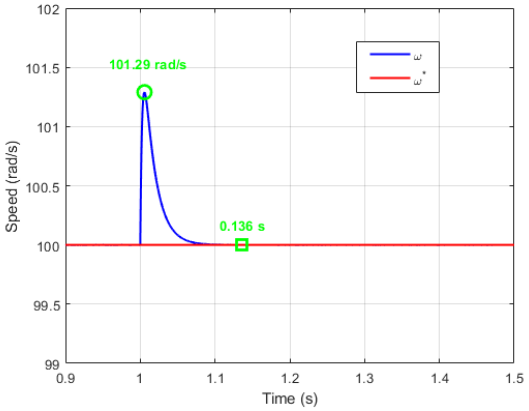

(f) Speed and its reference

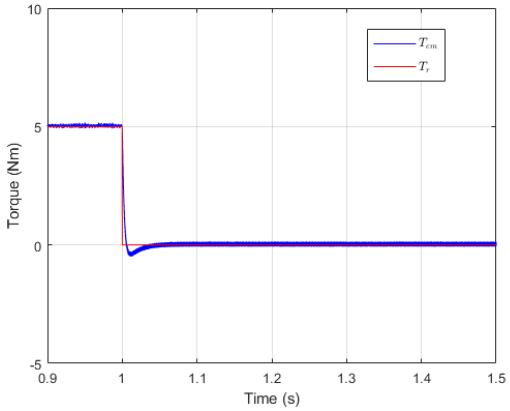

(g) Torque and its reference

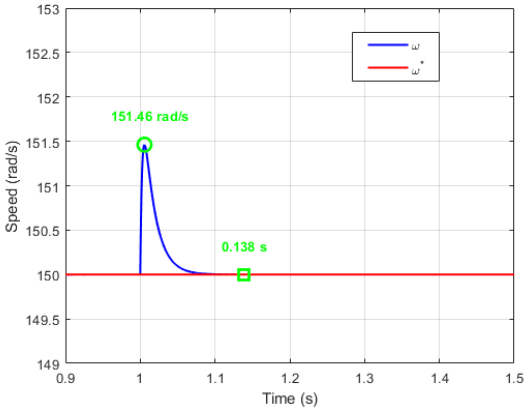

(h) Speed and its reference

Figure 3.8: Torque and speed response of DTC using a two-level five-phase inverter during load variation

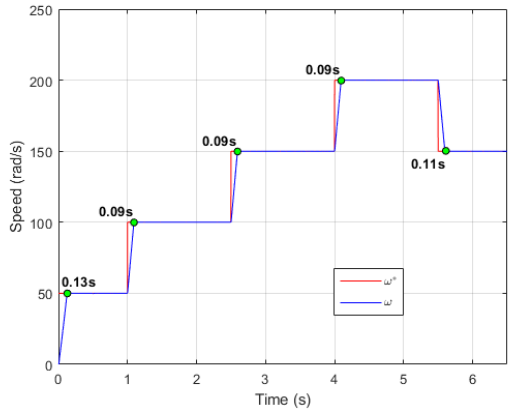

(a) Speed and its reference

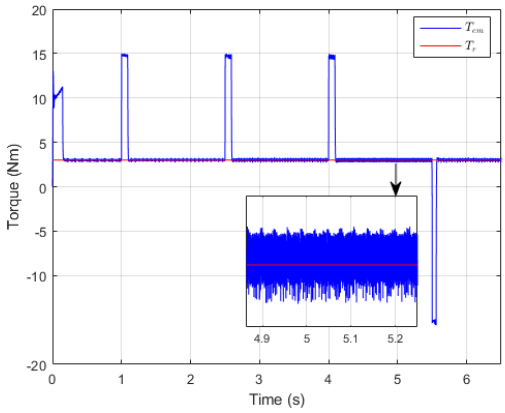

(b) Electromagnetic torque and its reference.

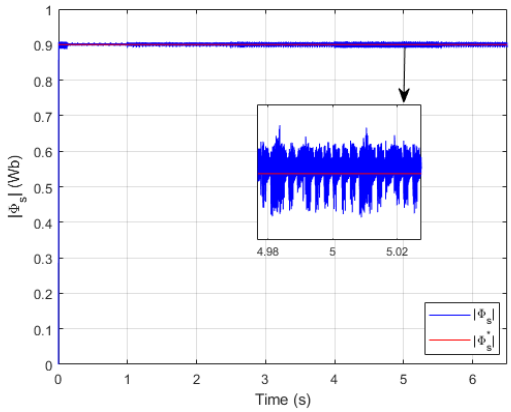

(c) Stator flux and its reference

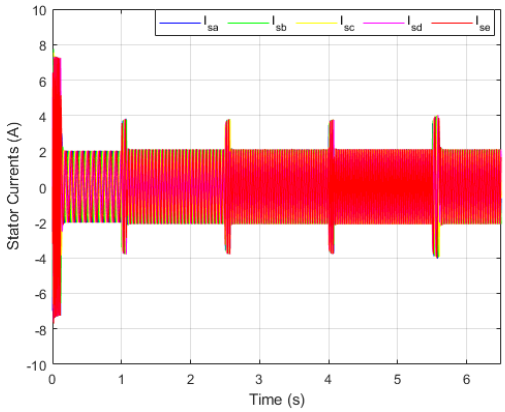

(d) Stator current

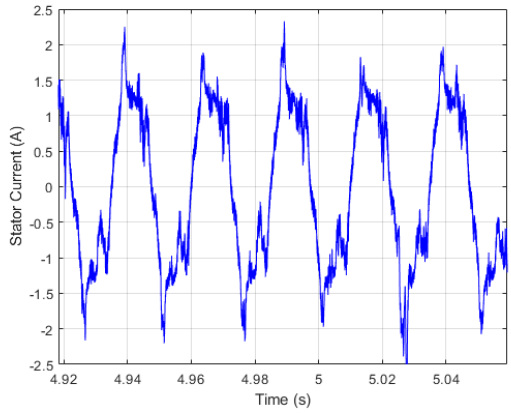

(e) Stator current

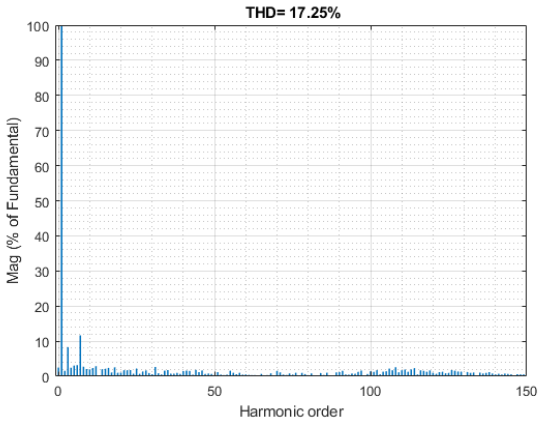

(f) FFT of stator current

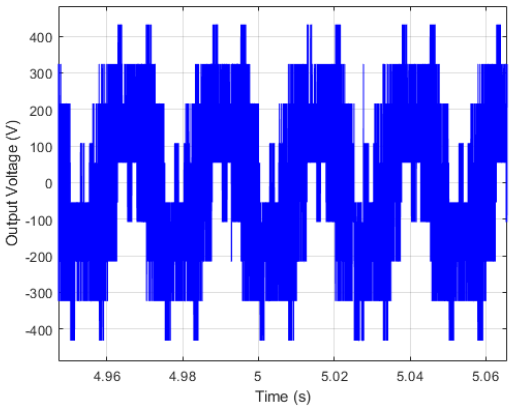

(g) Output voltage

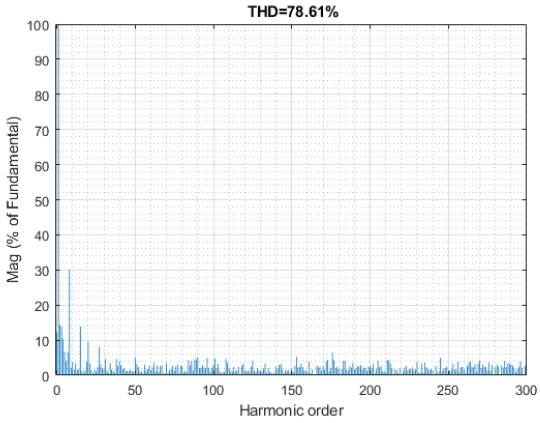

(h) FFT of output voltage

Figure 3.9: Simulation results for DTC using a T-NPC three-level five-phase inverter

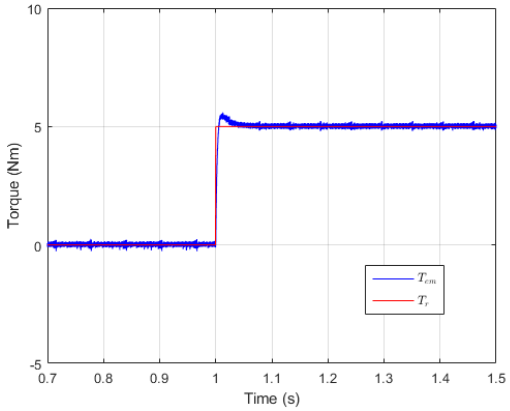

(a) Torque and its reference

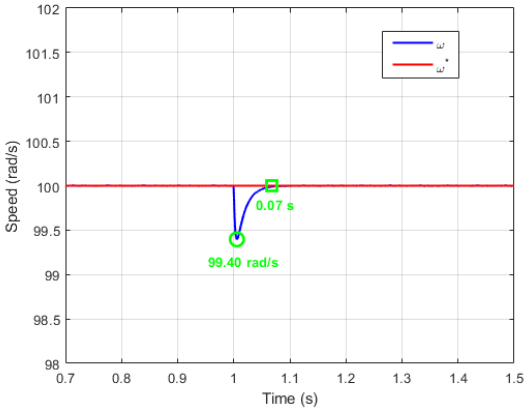

(b) Speed and its reference

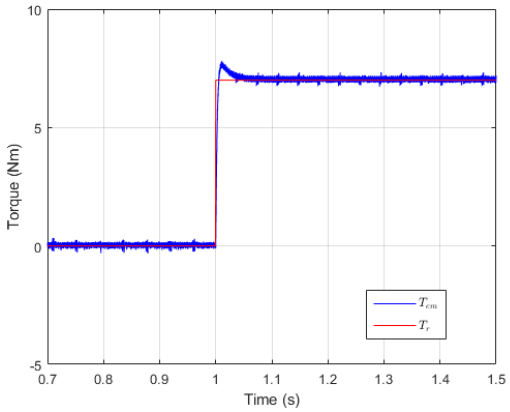

(c) Torque and its reference

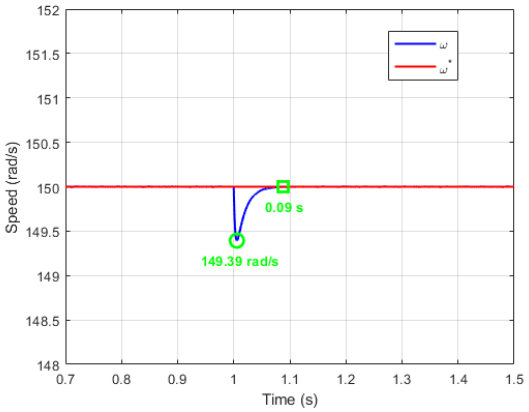

(d) Speed and its reference

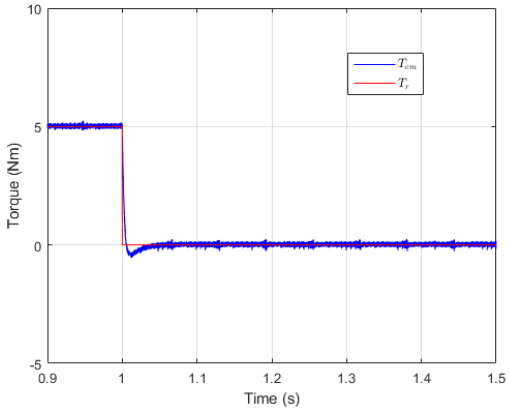

(e) Torque and its reference

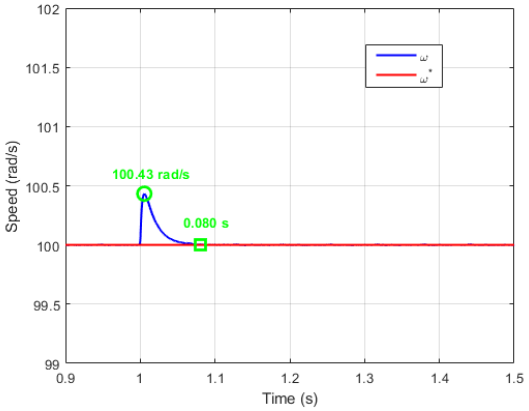

(f) Speed and its reference

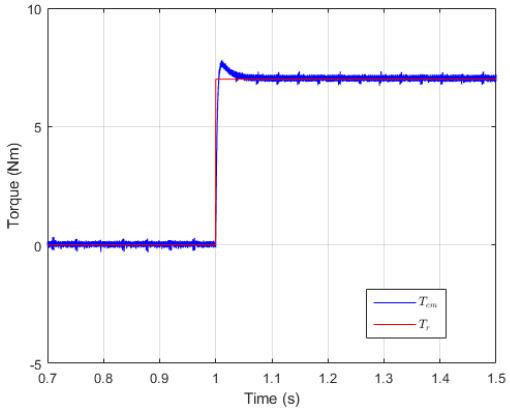

(g) Torque and its reference

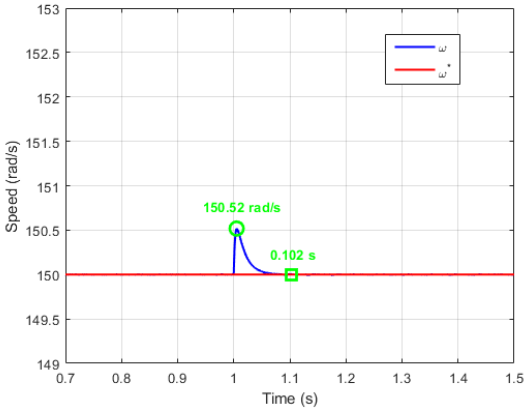

(h) Speed and its reference

Figure 3.10: Torque and speed response of DTC using a T-NPC three-level five-phase inverter during load variation

3.3 Direct Torque Control with Space Vector Modulation for a Five-Phase Induction Motor

The DTC-SVM method used is based on closed-loop regulation of torque and stator flux in the stator flux reference frame. Figure 3.11 illustrates the control structure, which relies on two PI-type regulators for controlling torque and stator flux.

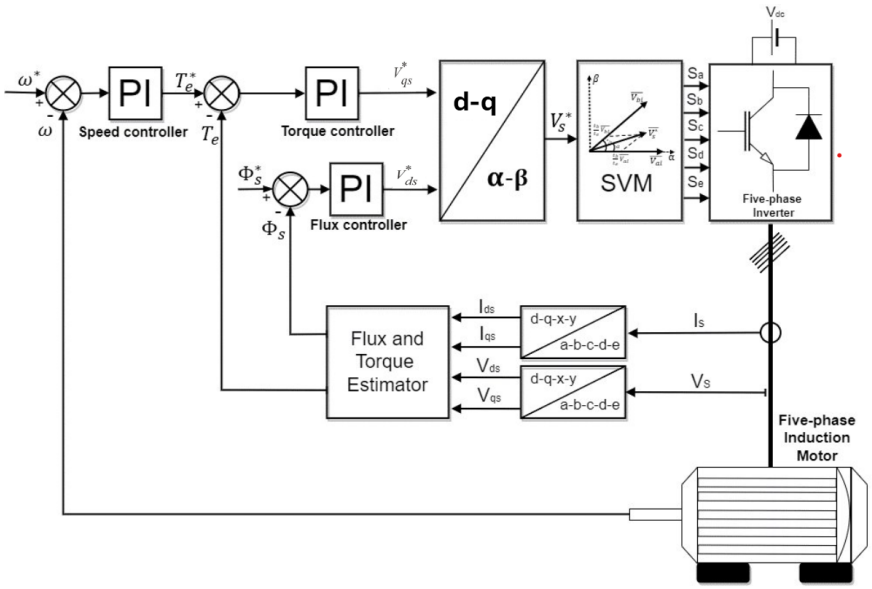

Figure 3.11: Block diagram of DTC-SVM.

The control strategy is based on a simplified description of the stator voltage components in the stator flux coordinate system ($\Phi_{ds} = \Phi_s$, $\Phi_{qs} = 0$). Consequently, the stator voltage equations derived from system (2.61),(2.62) and the torque expressions (2.64) are given as follows:

$$\begin{aligned} V_{ds} &= R_s I_{ds} + \frac{d\Phi_s}{dt} \\ V_{qs} &= R_s I_{qs} + \omega \Phi_s \\ T_e &= p\Phi_s I_{qs} \end{aligned} \tag{3.13}$$

Neglecting the voltage drop across the stator resistance (R_s), system (3.13) shows that the V_{ds} component primarily influences the variation of the stator flux amplitude, while the V_{qs} component controls the torque. The outputs of the PI regulators for flux and torque represent the reference stator voltage components (V_{ds} and V_{qs}) in the stator flux reference frame, as illustrated in Figure 3.12. These reference voltages are then transformed into the stationary $\alpha - \beta$ reference frame to enable voltage synthesis via SVM.

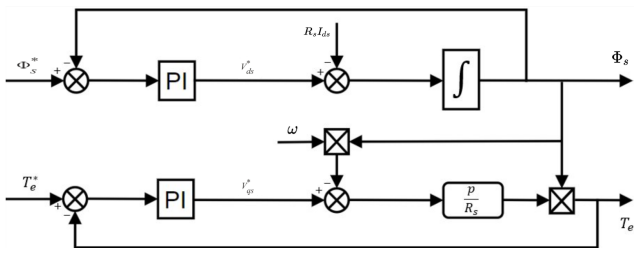

Figure 3.12: Closed-loop regulation.

Two SVM strategies are considered for generating the desired reference voltage at each sampling time [86, 97]. The first strategy, discussed in Section 2.3.1.1, utilizes two adjacent active space voltage vectors, while the second, covered in Section 2.3.1.2, uses four active space voltage vectors (two medium and two large) in each sector.

3.3.1 Simulation Results

Figure 3.13 and Figure 3.14 present the results of the first test for the DTC-SVM strategy using two and four vectors, respectively. The figures show the main electromagnetic and electrical variables, including the rotor speed and its reference, the electromagnetic torque and its reference, and the stator flux magnitude and its reference. They also include the stator current and its harmonic spectrum, as well as the inverter output voltage and its harmonic content. These results provide insight into the system's behavior under varying speed conditions.

Figure 3.15 and Figure 3.16 show the results of the second test, which focuses on the system response to sudden load variations at constant speeds. The rotor speed and electromagnetic torque are analyzed to evaluate indicators such as speed deviation, settling time, and stability under load disturbances.

For the case of two vectors, the rotor speed follows its reference without overshoot during both acceleration and deceleration. The motor transitions from 100 rad/s to 150 rad/s in approximately 0.15 s and from 200 rad/s to 150 rad/s in approximately 0.14 s. The electromagnetic torque follows its reference in both rotational directions, with an average maximum torque ripple of approximately 0.007551 Nm. The stator flux magnitude follows its reference with minor deviations during speed changes, resulting in a flux ripple reaching up to 0.00641 Wb.

For the four-vector case, the rotor speed also follows its reference without overshoot. The transition from 100 rad/s to 150 rad/s occurs in approximately 0.2 s, and from 200 rad/s to 150 rad/s in approximately 0.15 s. The electromagnetic torque tracks the reference with an average maximum ripple of about 0.00472 Nm. The stator flux magnitude shows minor deviations during transients, with a flux ripple up to 0.002530 Wb.

In terms of electrical performance, the stator currents increase in both magnitude and frequency as the speed increases for both techniques. The peak stator current reaches approximately 4.17 A for the two-vector case and 4.26 A for the four-vector case. The stator current waveforms are closer to a sinusoidal shape in both cases, due to the fixed switching frequency used in DTC-SVM. The stator current THD is 29.66% for two vectors and 13.78% for four vectors. As for the inverter output voltage, the THD is 110.03% and 97.27%, respectively. In the four-vector case, most harmonics are concentrated in the medium- and high-frequency ranges, which are generally easier to filter.

Figures 3.15 and 3.16 show that both the two-vector and four-vector DTC-SVM strategies effectively handle the sudden load increase and decrease, with the actual torque T_{em} closely following the reference T_r. For the two-vector configuration, the rotor speed drops by 0.78 rad/s at 100 rad/s and 0.87 rad/s at 150 rad/s, with settling times of 0.11 s and 0.13 s. After load removal, overshoot values of 0.86 rad/s and 0.94 rad/s are recorded, with settling times of 0.11 s and 0.124 s. For the four-vector case, the speed drop is 0.69 rad/s at 100 rad/s and 0.78 rad/s at 150 rad/s, with corresponding settling times of 0.1 s and 0.12 s. Overshoot values after load removal are also 0.69 rad/s and 0.82 rad/s, with settling times of 0.101 s and 0.122 s.

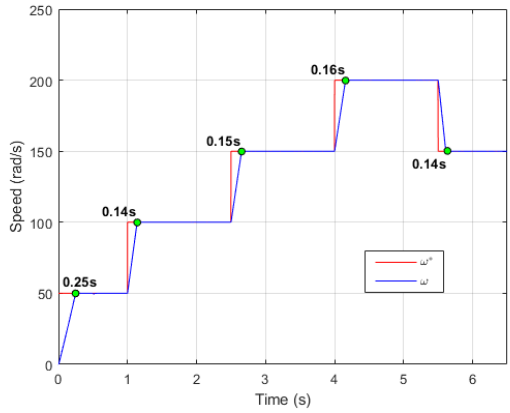

(a) Speed and its reference

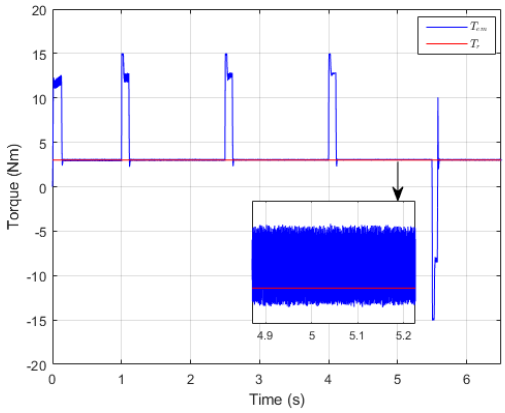

(b) Electromagnetic torque and its reference.

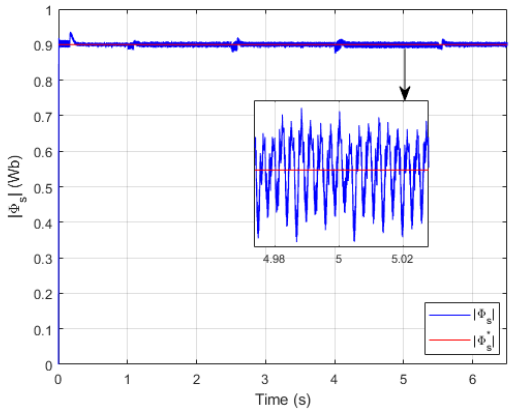

(c) Stator flux and its reference

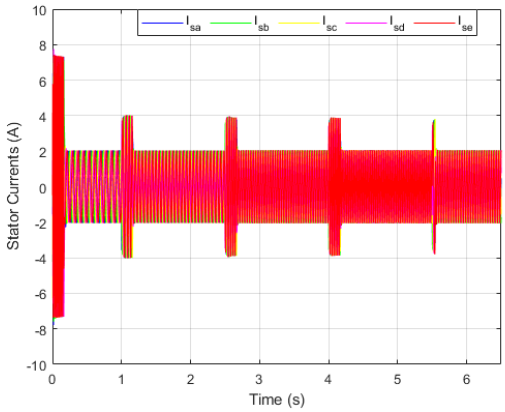

(d) Stator current

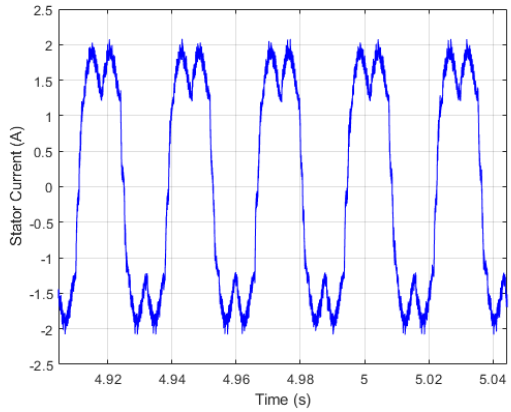

(e) Stator current

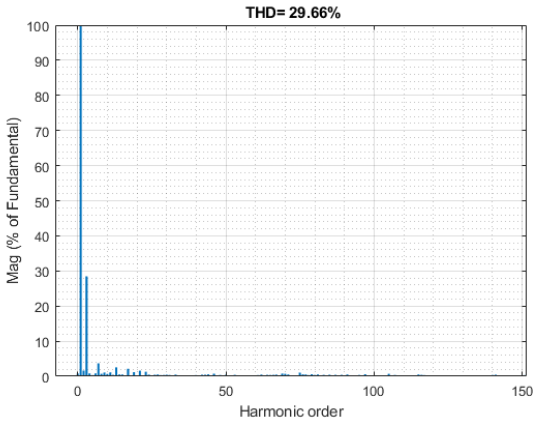

(f) FFT of stator current

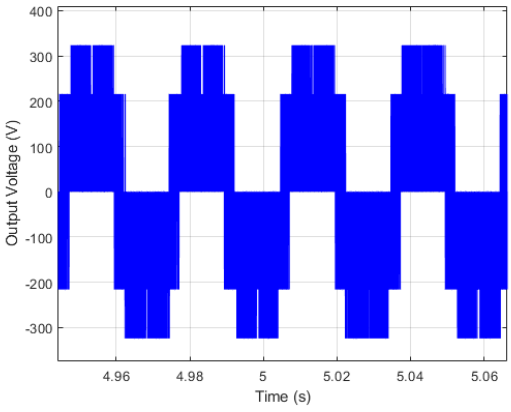

(g) Output voltage

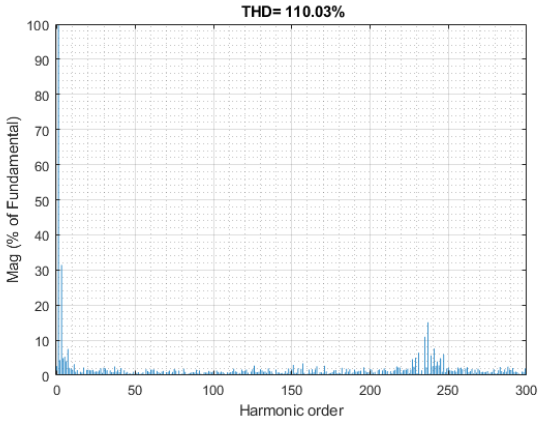

(h) FFT of output voltage

Figure 3.13: Simulation results for DTC-SVM using two active vectors

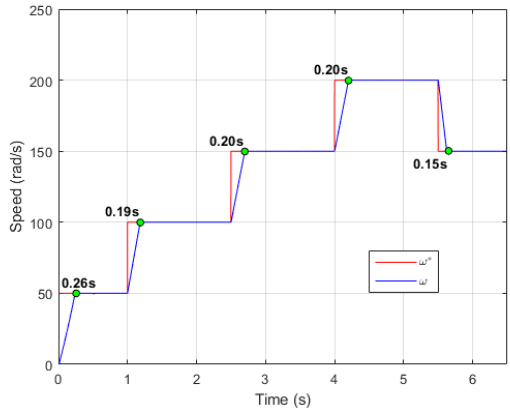

(a) Speed and its reference

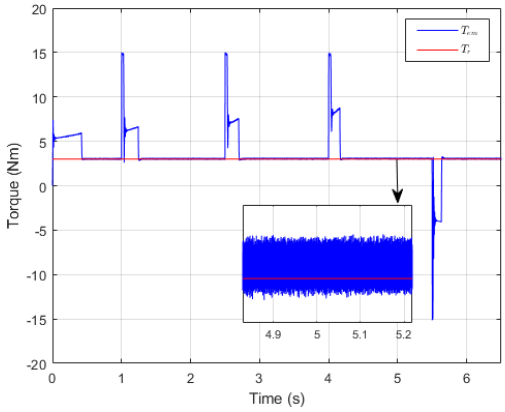

(b) Electromagnetic torque and its reference.

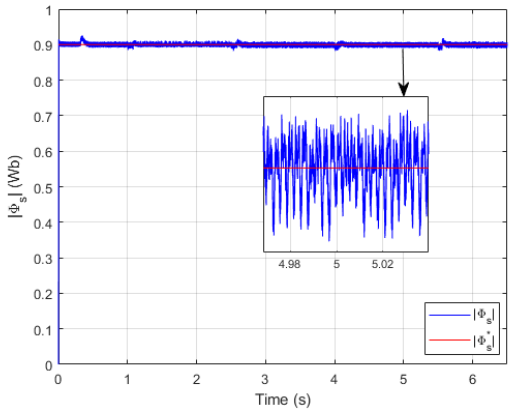

(c) Stator flux and its reference

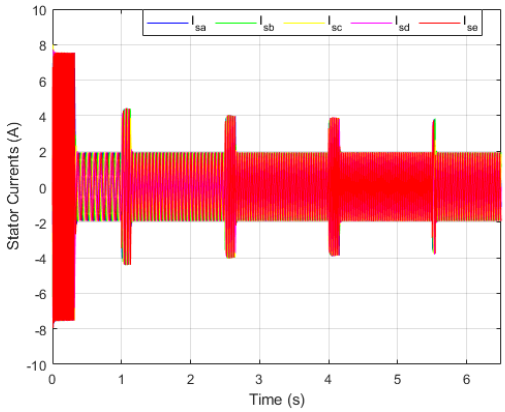

(d) Stator current

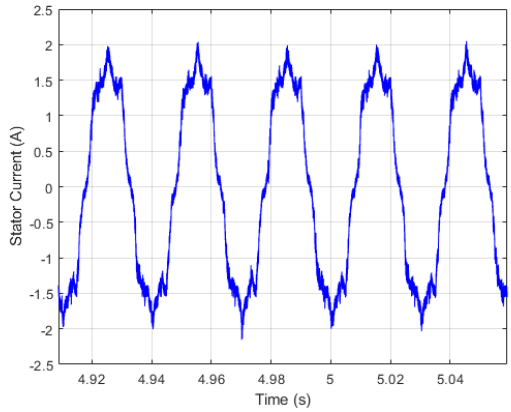

(e) Stator current

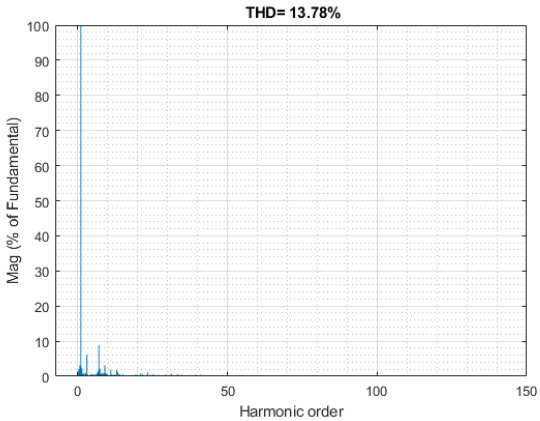

(f) FFT of stator current

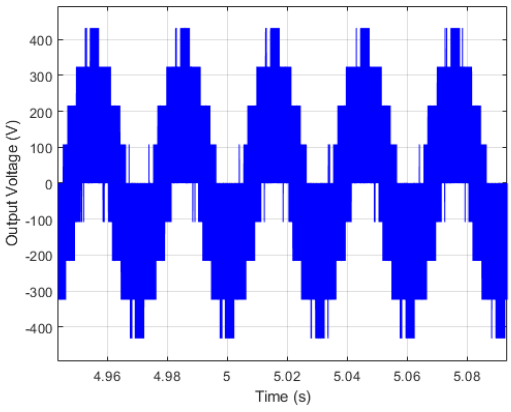

(g) Output voltage

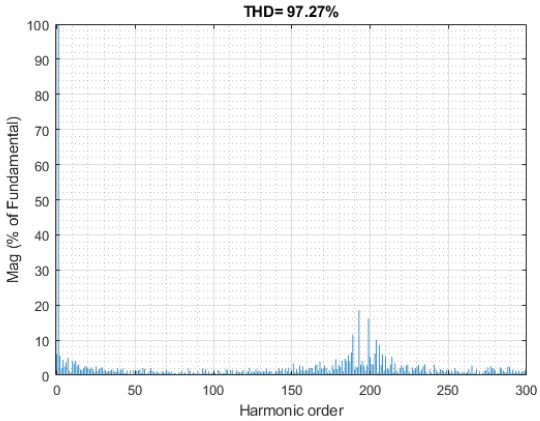

(h) FFT of output voltage

Figure 3.14: Simulation results for DTC-SVM using four active vectors

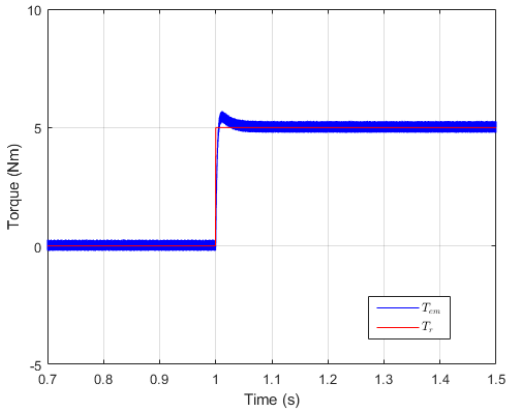

(a) Torque and its reference

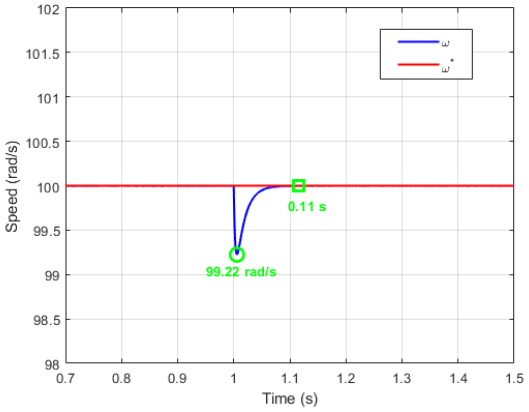

(b) Speed and its reference

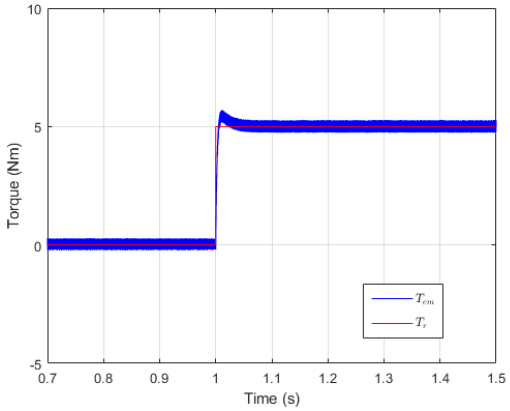

(c) Torque and its reference

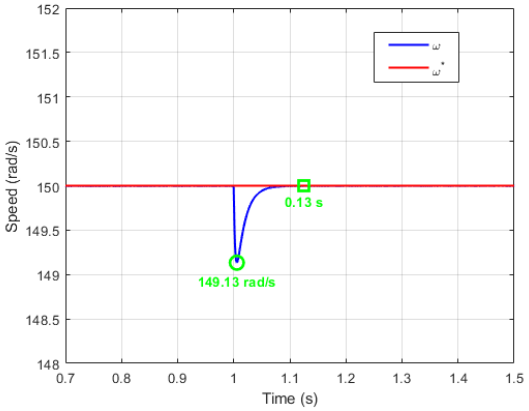

(d) Speed and its reference

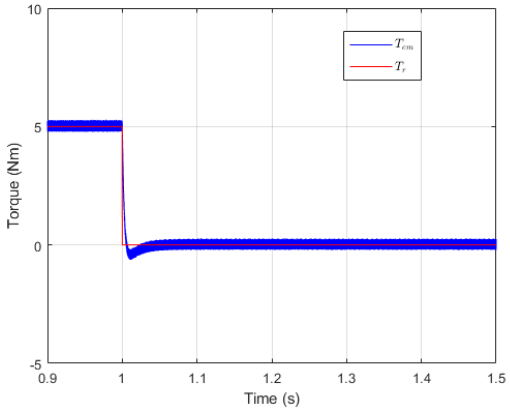

(e) Torque and its reference

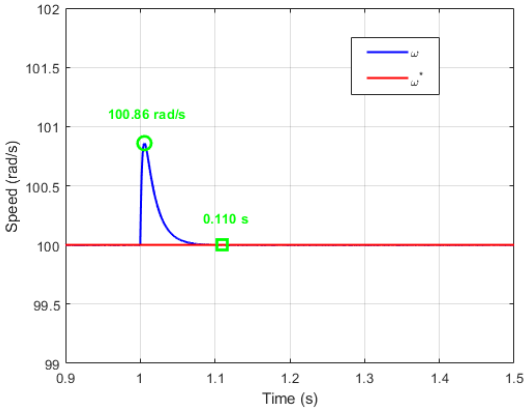

(f) Speed and its reference

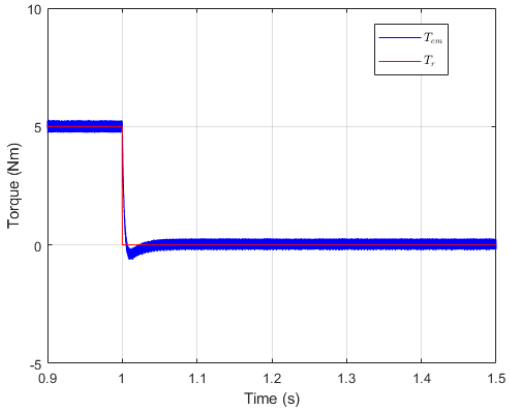

(g) Torque and its reference

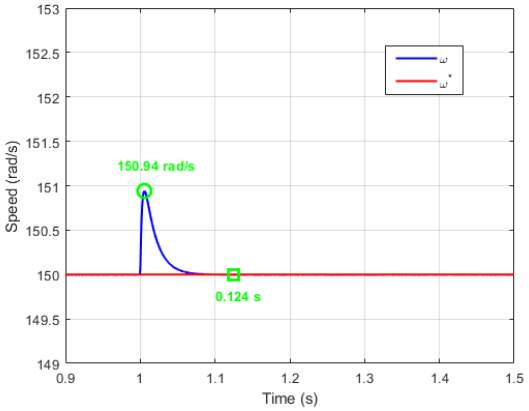

(h) Speed and its reference

Figure 3.15: Torque and speed response of DTC-SVM using two active vectors during load variation

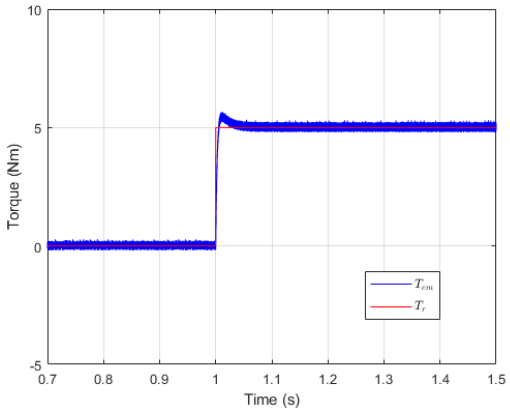

(a) Torque and its reference

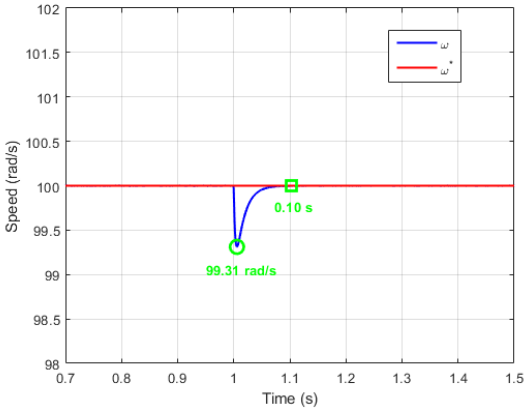

(b) Speed and its reference

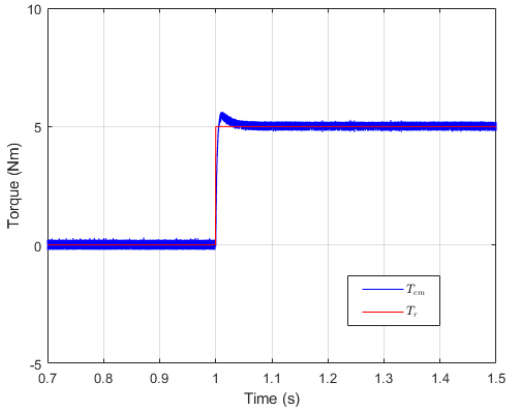

(c) Torque and its reference

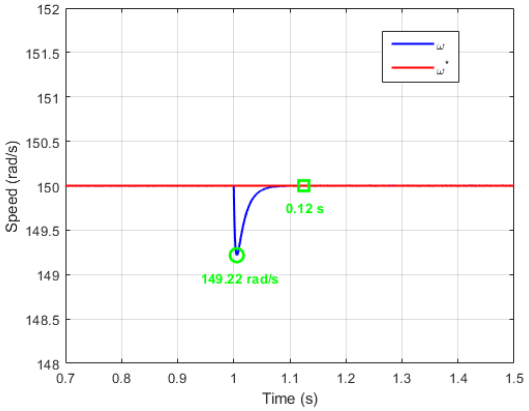

(d) Speed and its reference

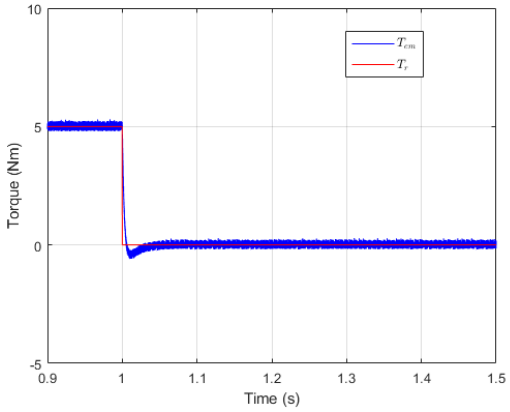

(e) Torque and its reference

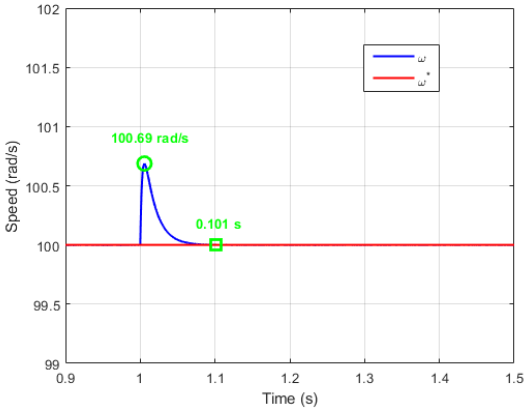

(f) Speed and its reference

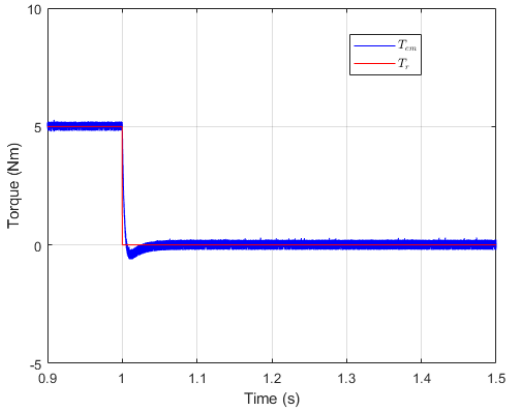

(g) Torque and its reference

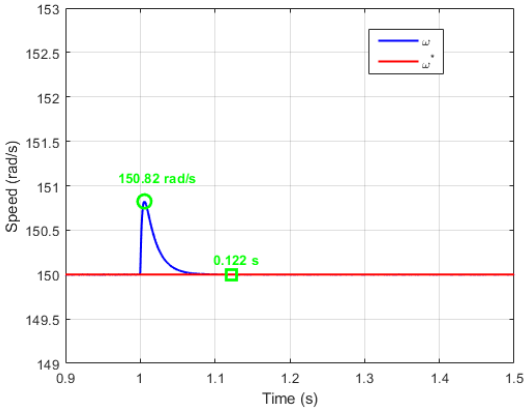

(h) Speed and its reference

Figure 3.16: Torque and speed response of DTC-SVM using four active vectors during load variation

3.4 Finite Control Set Model Predictive Control for a Five-Phase Induction Motor

The block diagram of the FCS-MPC method for a five-phase induction motor is presented in Figure 3.17. This diagram illustrates the control loop, including the predictive model, cost function evaluation, and the selection of optimal switching states.

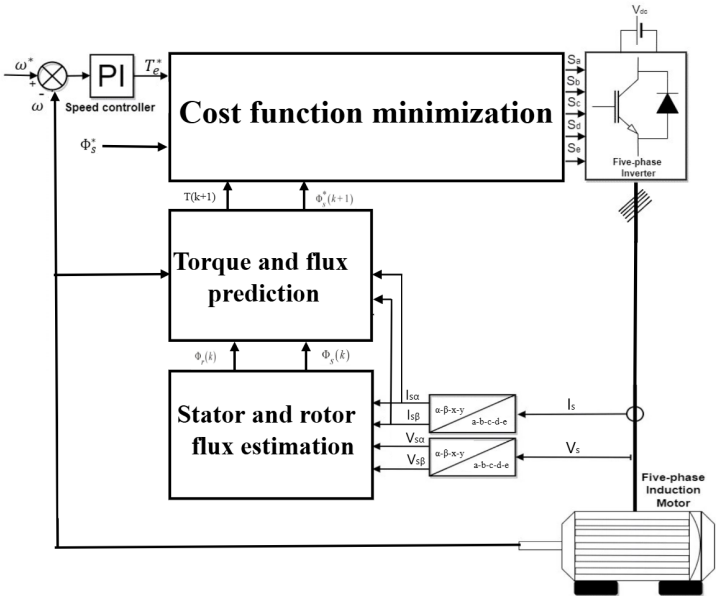

Figure 3.17: Block diagram of the FCS-MPC method.

In the context of a five-phase induction motor, the FCS-MPC method uses the mathematical model of the motor in the stationary reference frame to predict future states, including stator currents as well as stator and rotor fluxes, based on the possible switching states of the inverter. This process involves discretizing the motor's dynamic equations and using these discrete models to forecast the motor's behavior over a short prediction horizon. At each sampling interval, the controller evaluates the predicted states for all potential voltage vectors (combinations of five-phase inverter switching) and calculates a cost function that typically includes tracking errors [98–100].

The continuous-time model given by system (2.61) and (2.62) in a reference frame rotating at an arbitrary speed ω can be transformed into the stationary reference frame (α-β-x-y-o) and discretized using the sampling period T_s for numerical control implementation. In this study, only the α-β components are considered for simplification. The resulting discrete stator flux equations are:

$$\begin{aligned} \Phi_{s\alpha}[k+1] &= \Phi_{s\alpha}[k] + T_s\left(V_{s\alpha}[k] - R_s I_{s\alpha}[k]\right) \\ \Phi_{s\beta}[k+1] &= \Phi_{s\beta}[k] + T_s\left(V_{s\beta}[k] - R_s I_{s\beta}[k]\right) \end{aligned} \tag{3.14}$$

The discrete rotor flux equations are:

$$\begin{aligned} \Phi_{r\alpha}[k+1] &= \left(1 - \frac{R_r T_s}{L_r}\right)\Phi_{r\alpha}[k] + T_s\omega_m\Phi_{r\beta}[k] + \frac{R_r T_s L_m}{L_r} I_{s\alpha}[k] \\ \Phi_{r\beta}[k+1] &= \left(1 - \frac{R_r T_s}{L_r}\right)\Phi_{r\beta}[k] - T_s\omega_m\Phi_{r\alpha}[k] + \frac{R_r T_s L_m}{L_r} I_{s\beta}[k] \end{aligned} \tag{3.15}$$

The rotor currents in terms of rotor flux are:

$$\begin{aligned} I_{r\alpha}[k+1] &= \frac{\Phi_{r\alpha}[k+1] - L_m I_{s\alpha}[k+1]}{L_r} \\ I_{r\beta}[k+1] &= \frac{\Phi_{r\beta}[k+1] - L_m I_{s\beta}[k+1]}{L_r} \end{aligned} \tag{3.16}$$

The stator flux in terms of stator and rotor currents is given by:

$$\begin{aligned} \Phi_{s\alpha}[k+1] &= L_s I_{s\alpha}[k+1] + L_m I_{r\alpha}[k+1] \\ \Phi_{s\beta}[k+1] &= L_s I_{s\beta}[k+1] + L_m I_{r\beta}[k+1] \end{aligned} \tag{3.17}$$

Finally, the stator currents are updated as follows:

$$\begin{aligned} I_{s\alpha}[k+1] &= \left(1 + \frac{T_s}{\tau_\sigma}\right) I_{s\alpha}[k] + \frac{T_s}{\tau_\sigma}\left(\frac{1}{R_\sigma}\left(\frac{k_r}{\tau_r}\Phi_{r\alpha}[k] + k_r\omega_m\Phi_{r\beta}[k]\right) + V_{s\alpha}[k]\right) \\ I_{s\beta}[k+1] &= \left(1 + \frac{T_s}{\tau_\sigma}\right) I_{s\beta}[k] + \frac{T_s}{\tau_\sigma}\left(\frac{1}{R_\sigma}\left(\frac{k_r}{\tau_r}\Phi_{r\beta}[k] - k_r\omega_m\Phi_{r\alpha}[k]\right) + V_{s\beta}[k]\right) \end{aligned} \tag{3.18}$$

Where:

- $\sigma = 1 - \frac{L_m^2}{L_r L_s}$
- $\tau_\sigma = \frac{\sigma L_s}{R_\sigma}$
- $k_r = \frac{L_m}{L_r}$
- $\tau_r = \frac{L_r}{R_r}$
- $R_\sigma = R_s + k_r^2 R_r$
- ω_m is the mechanical angular speed

The future electromagnetic torque is predicted using the following equation:

$$T_e[k+1] = \frac{5}{2} p \left(\Phi_{s\alpha}[k+1] I_{s\beta}[k+1] - \Phi_{s\beta}[k+1] I_{s\alpha}[k+1]\right) \tag{3.19}$$

The cost function used in this study aims to minimize the error on the torque and stator flux, ensuring precise motor control. It is given by:

$$J = \lambda_T \left|T_e[k+1] - T_{\text{ref}}\right| + \lambda_\Phi \left|\Phi_s[k+1] - \Phi_{s,\text{ref}}\right| \tag{3.20}$$

Where:

- λ_T and λ_Φ are weighting coefficients for torque and flux errors.
- $T_e[k+1]$ is the predicted electromagnetic torque at the next step.

- T_{ref} is the reference torque.
- $\Phi_s[k+1]$ is the predicted stator flux magnitude at the next step.
- $\Phi_{s,\text{ref}}$ is the reference stator flux magnitude.

The control action that minimizes the cost function is applied to the inverter. This involves evaluating all 32 possible voltage vectors and selecting the one that minimizes the cost, ensuring minimal tracking error and efficient control.

3.4.1 Simulation Results

Figure 3.18 presents the results of the first test for the FCS-MPC strategy, showing the main electromagnetic and electrical variables, including the rotor speed and its reference, the electromagnetic torque and its reference, and the stator flux magnitude and its reference. It also includes the stator current and its harmonic spectrum, as well as the inverter output voltage and its harmonic content. These results provide insight into the system's behavior under varying speed conditions.

Figure 3.19 presents the results of the second test, which focuses on the system response to sudden load variations at constant speeds. The rotor speed and electromagnetic torque are analyzed to evaluate indicators such as speed deviation, settling time, and stability during load disturbances.

In Figure 3.18a, the rotor speed follows its reference without overshoot during both acceleration and deceleration. The motor transitions from 100 rad/s to 150 rad/s in approximately 0.08 s and from 200 rad/s to 150 rad/s in approximately 0.1 s.

Figure 3.18b shows that the electromagnetic torque follows its reference in both forward and reverse operation, with an average maximum torque ripple of approximately 0.01065 Nm.

In Figure 3.18c, the stator flux magnitude follows its reference value with very small deviations during speed changes, resulting in a flux ripple reaching up to 0.00086 Wb throughout the test.

For the electrical performance of the FCS-MPC strategy, the stator currents increase in both magnitude and frequency as the speed increases. During speed variations, the peak stator current reaches approximately 8.66 A. The stator current waveforms present variability due to the variable switching frequency. The total harmonic distortion (THD) of the stator current is 26.9%. Regarding the inverter output voltage, the THD is 58.82%, with most harmonics concentrated in the low-frequency range, which are generally more difficult to filter.

Figure 3.19 shows that the FCS-MPC strategy effectively handles the sudden load increase and decrease, with the actual torque T_{em} closely following the reference T_r. At a reference speed of 100 rad/s, the rotor speed drops by 0.34 rad/s during load application, with a settling time of 0.04 s. At 150 rad/s, the speed drop reaches 0.41 rad/s, with a settling time of 0.05 s. When the load is removed, overshoot values of 0.34 rad/s and 0.47 rad/s are observed at 100 rad/s and 150 rad/s, with corresponding settling times of 0.036 s and 0.042 s.

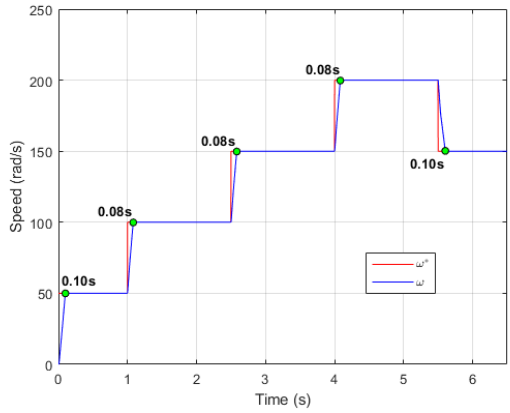

(a) Speed and its reference

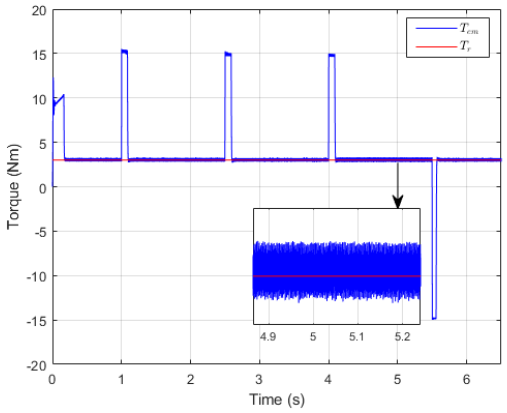

(b) Electromagnetic torque and its reference.

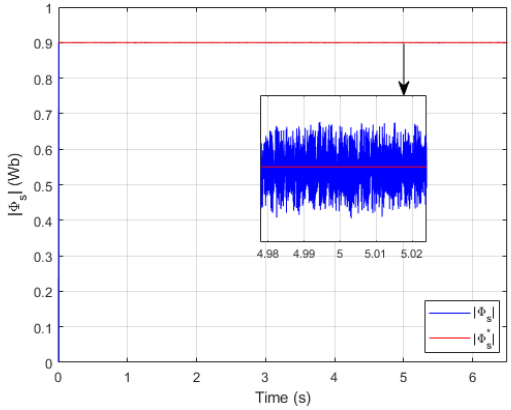

(c) Stator flux and its reference

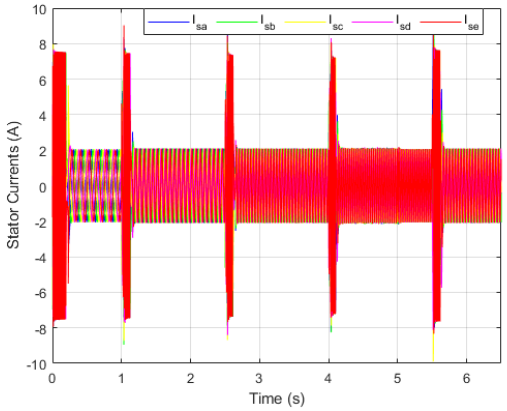

(d) Stator current

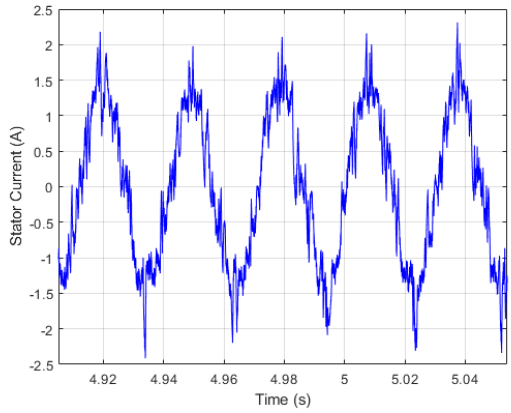

(e) Stator current

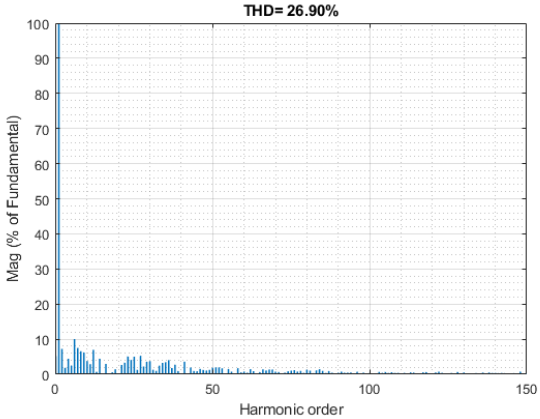

(f) FFT of stator current

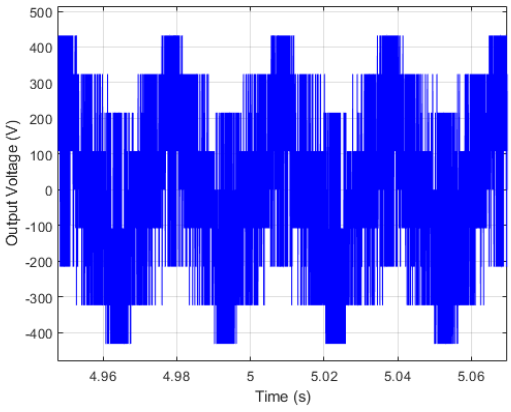

(g) Output voltage

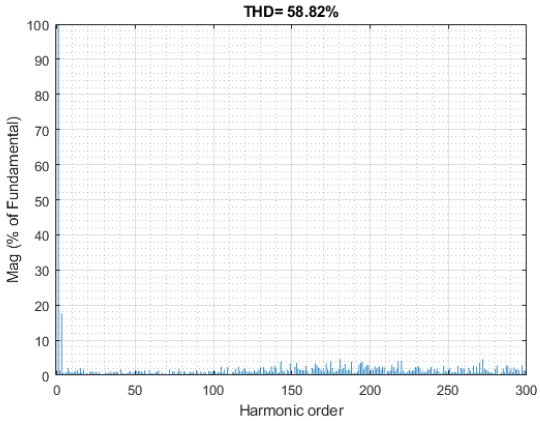

(h) FFT of output voltage

Figure 3.18: Simulation results for FCS-MPC

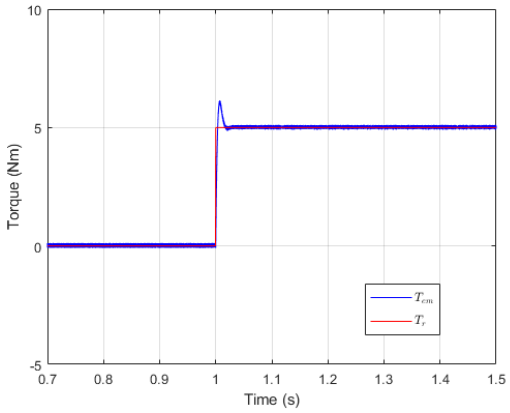

(a) Torque and its reference

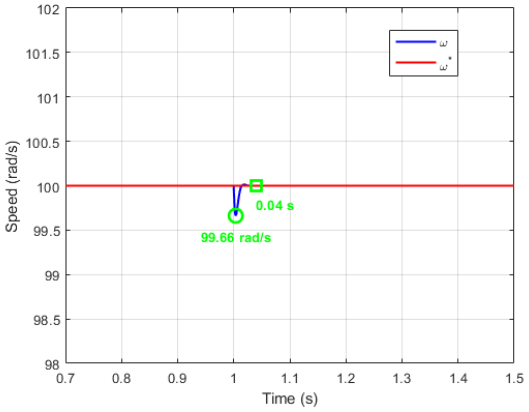

(b) Speed and its reference

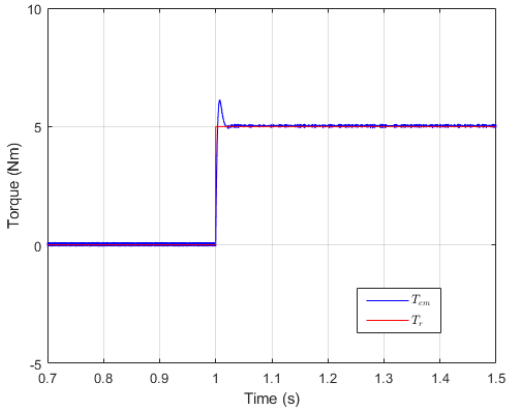

(c) Torque and its reference

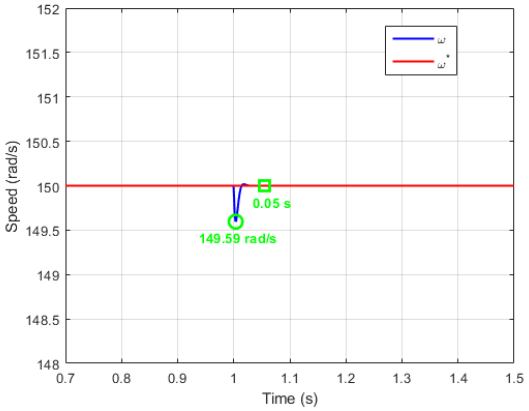

(d) Speed and its reference

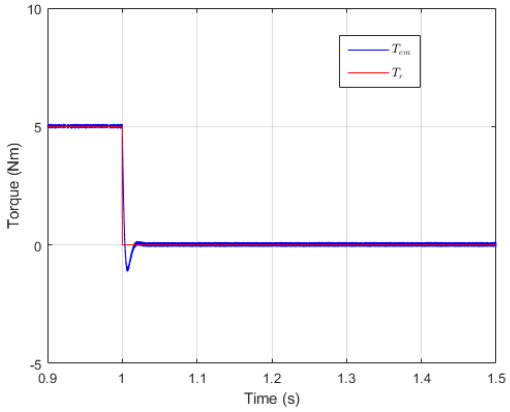

(e) Torque and its reference

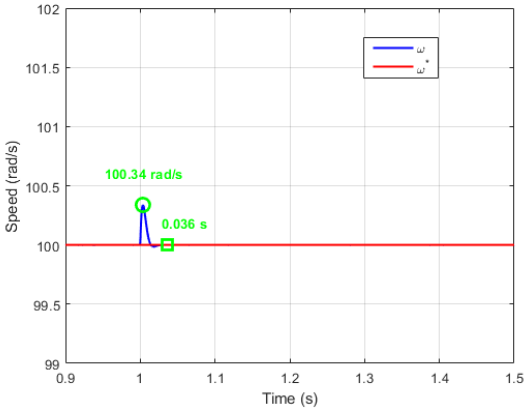

(f) Speed and its reference

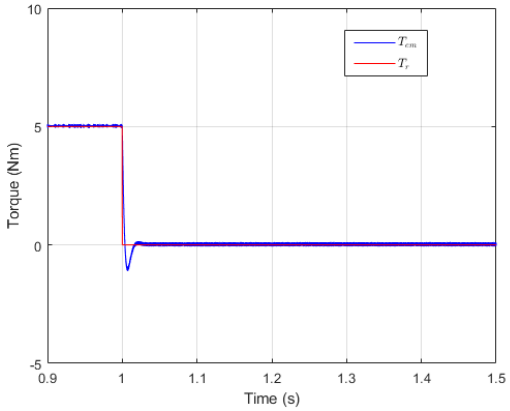

(g) Torque and its reference

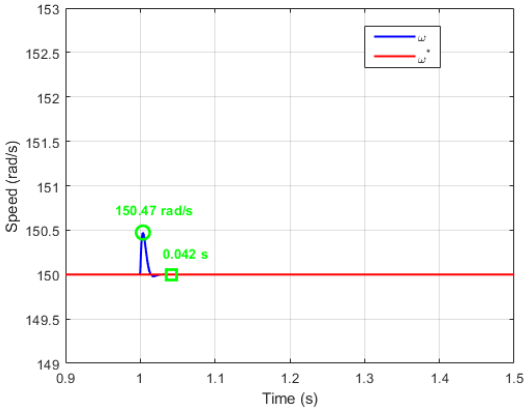

(h) Speed and its reference

Figure 3.19: Torque and speed response of FCS-MPC during load variation

Figure 3.20 shows the impact of a 30% increase in stator resistance on the stator flux for the different control strategies. Only the FCS-MPC control is significantly affected: the amplitude of the stator flux drops from its reference value of 0.9 Wb to 0.83 Wb, along with an observable increase in ripple. In contrast, both DTC and DTC-SVM strategies show only slight deviations, with negligible impact on flux amplitude or ripple highlighting their superior robustness to resistance variations. This sensitivity in FCS-MPC arises from its reliance on an accurate machine model, making it the least robust to parameter changes.

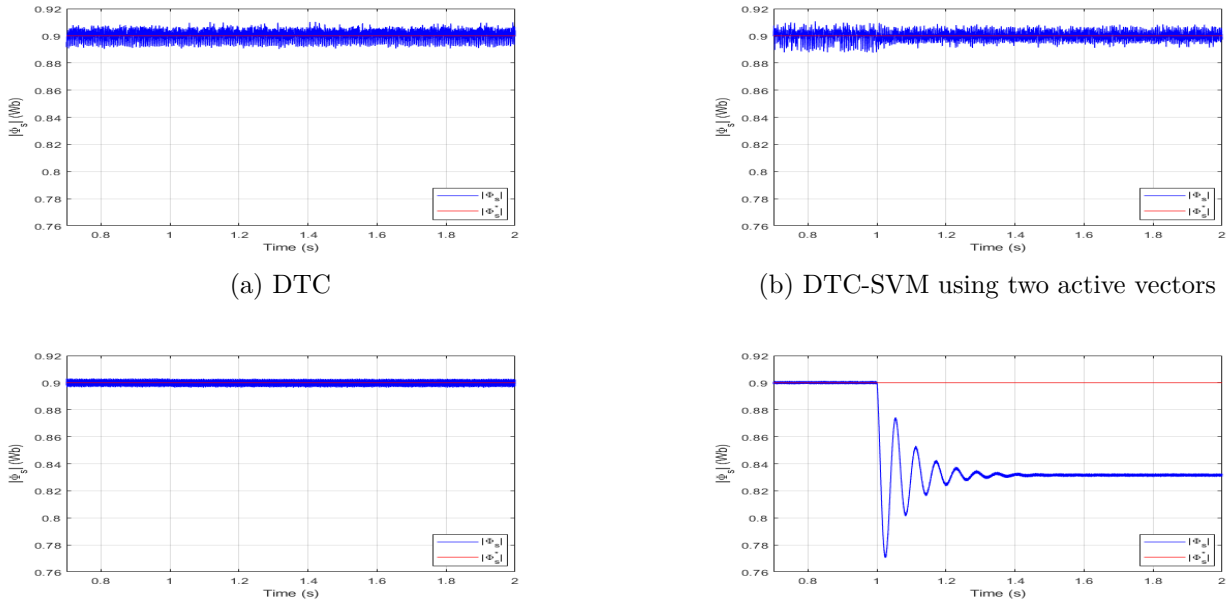

(a) DTC

(b) DTC-SVM using two active vectors

(c) DTC-SVM using four active vectors.

(d) FCS-MPC.

Figure 3.20: Stator flux response under a 30% increase in stator resistance for different control strategies.

All control strategies demonstrate effective rotor speed tracking, accurately following the reference signal during both acceleration and deceleration without overshoot. This confirms reliable speed regulation across all methods. In terms of dynamic response, FCS-MPC achieves the fastest speed transitions, followed by the classical DTC method. DTC-SVM with two vectors provides slightly slower responses, while the four-vector configuration exhibits the lowest speed dynamics among the tested strategies.

Regarding electromagnetic torque behavior, all control strategies maintain close tracking of the torque reference under varying operating conditions. However, the amplitude of torque ripple varies significantly among the methods. DTC-SVM with four vectors achieves the lowest torque ripple, followed by the two-vector DTC-SVM approach. The FCS-MPC strategy results in moderate torque ripple levels, while the classical DTC exhibits the highest ripple. These observations highlight differences in torque regulation quality across the evaluated controllers.

In terms of stator flux regulation, all control strategies are able to follow the flux reference with minimal deviation. FCS-MPC demonstrates the most precise flux control, exhibiting the lowest ripple amplitude. DTC-SVM with four vectors follows, offering improved flux stability compared to the two-vector configuration. The classical DTC method shows the highest flux ripple among the tested strategies, particularly during transient conditions. These results reflect the varying ability of each method to maintain consistent flux levels under dynamic operation.

For the stator current, the results show that the DTC-SVM control with four vectors achieves the lowest total harmonic distortion (THD), due to the effective elimination of x–y plane components and the use of a fixed switching frequency, which enables the generation of current

waveforms closest to a sinusoidal shape. In comparison, the DTC and FCS-MPC strategies result in higher THD values. Their variable switching frequencies introduce more variability in the current waveforms, which also exhibit higher peak amplitudes during speed transitions. Using only two vectors in the DTC-SVM control does not eliminate the x–y plane components, leading to the highest THD among the evaluated methods, despite operating with a fixed switching frequency.

For the output voltage, the FCS-MPC strategy yields the lowest total harmonic distortion (THD), though most of its harmonics are concentrated in the low-frequency range, which are typically more difficult to filter. The DTC-SVM method with four vectors produces a voltage spectrum dominated by medium- and high-frequency harmonics, which are easier to filter and contribute to the lower current THD observed in this configuration. In contrast, the DTC-SVM approach using two vectors results in higher voltage distortion due to its inability to eliminate the x–y plane components, unlike the four-vector version. The classical DTC control exhibits the highest voltage THD, primarily influenced by its variable switching frequency.

All control strategies effectively handle sudden load changes, with the electromagnetic torque closely tracking its reference during both load application and removal. However, notable differences in speed regulation performance are observed. FCS-MPC demonstrates the fastest recovery and the smallest speed deviation, indicating a strong capacity for disturbance rejection. DTC-SVM with two and four vectors offers comparable dynamic responses, with consistent settling times and speed variations, though the four-vector version shows slightly improved regulation. The classical DTC method maintains effective torque tracking but exhibits longer settling times and more pronounced speed deviation under transient conditions. These results reflect the varying dynamic capabilities of the control methods when subjected to abrupt load disturbances.

Table 3.2 summarizes the simulation results comparing the performances of the DTC, DTC-SVM with 2 vectors, DTC-SVM with 4 vectors, and FCS-MPC control strategies for the five-phase induction motor.

Table 3.2: Comparative results between DTC, DTC-SVM with 2 vectors, DTC-SVM with 4 vectors, and FCS-MPC.

Parameter	**DTC**	**DTC-SVM (2 vect.)**	**DTC-SVM (4 vect.)**	**FCS-MPC**
Response time	Fast	Moderate	Slow	Very fast
Torque ripple	Very high	Medium	Low	Moderately high
Flux ripple	Very high	Medium	Low	Very low
Stator current shape	More variable	Near-sinusoidal	Near-sinusoidal	More variable
Stator current peak	7.36 A	4.17 A	4.26 A	8.66 A
Stator current THD	22.59%	29.66%	13.78%	26.9%
Voltage THD	129.68%	110.03%	97.27%	58.82%
Load change response (no-load to full-load)	High drop, long recovery	Moderate drop, short recovery	Small drop, fast recovery	Very small drop, very fast recovery
Load change response (full-load to no-load)	High overshoot, long recovery	Moderate overshoot, short recovery	Small overshoot, fast recovery	Very small overshoot, very fast recovery

3.5 Intelligent Control

Conventional control techniques, such as DTC, DTC-SVM, and FCS-MPC, incorporate proportional-integral (PI) regulators in their control schemes. However, PI regulators exhibit limitations, particularly due to saturation, variations in motor parameters, and changes in operating conditions. Since they are often optimized for specific motor parameters and particular operating conditions, any change in these conditions requires a readjustment of the PI parameters, which limits the system's adaptability.

To overcome these limitations, artificial neural networks (ANNs) have been introduced as an alternative approach. ANNs, inspired by the biological structure of the human brain, were first conceptualized by McCulloch and Pitts in 1943 [101]. They function based on problem-solving mechanisms similar to those of the human brain [70]. The structure of an ANN, as illustrated in Figure 3.21, primarily consists of three layers: the input layer, the hidden layers, and the output layer.

The input layer consists of a set of input values X_j and associated weights W_{ij}. The hidden layers perform weighted summations of the inputs and apply activation functions to model complex nonlinear behaviors. The number of neurons and layers is typically determined through experimentation to optimize model performance [102]. The output layer generates the final control signals.

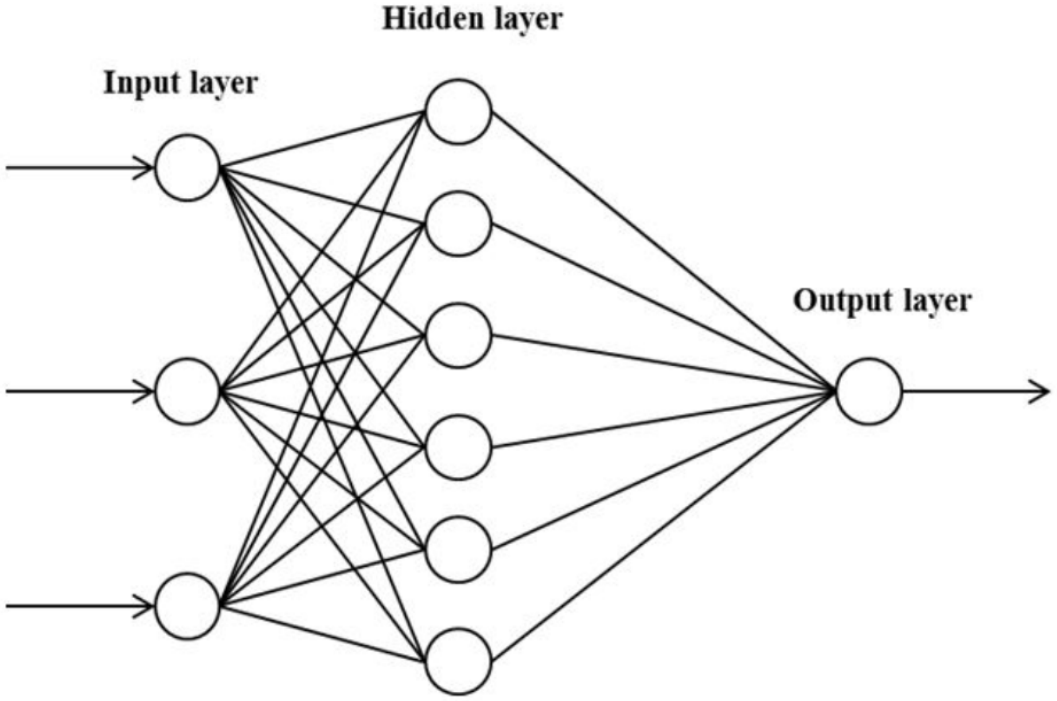

Figure 3.21: Structure of Artificial Neural Networks (ANNs).

The ANN control strategy is trained using multiple PI regulators, each optimized for specific operating conditions such as varying speed ranges and torque levels. The data generated by these PI regulators are collected to train the ANN to replicate their behavior. Subsequently, the PI parameters are adjusted for different operating conditions, and the corresponding data are also used for training. This process is repeated over multiple scenarios to generalize the ANN's adaptability.

In this study, two separate ANNs are designed for the DTC-SVM control strategy: one dedicated to replacing the PI speed controller and another combining the PI flux and torque controllers. For the speed controller, the ANN has an input layer with 2 neurons: one neuron receives the speed reference signal, and the second neuron receives an additional input expressed as $\frac{K \times T_s}{Z-1}$ multiplied by the original signal, which helps improve training efficiency and dynamic response. The hidden layer contains 10 neurons to capture nonlinear dynamics, and the output layer consists of 1 neuron delivering the control signal. For the combined flux and torque controller, the ANN has an input layer with 4 neurons: two neurons for the flux and torque reference signals, and two neurons for their corresponding additional inputs in the form $\frac{K \times T_s}{Z-1}$ times each original input. Similarly, this ANN uses 10 neurons in the hidden layer and 1 neuron in the output layer. The hidden layers in both ANNs use a hyperbolic tangent sigmoid activation function (*tansig*), while a linear activation function is applied at the output to ensure continuous control. The mean squared error (MSE) is selected as the cost function to minimize the difference between the ANN outputs and the PI controller responses during training. In the case of the MPC strategy, only the PI speed controller is replaced by an ANN with the same structure (2 input neurons including the additional input, 10 hidden neurons, and 1 output neuron), while the torque and flux controllers remain handled within the predictive control framework. This design allows each ANN to accurately replicate the behavior of the conventional PI regulators while improving robustness and dynamic adaptability without manual parameter tuning.

The summation function in the ANN is given by:

$$Z_j = \sum_{j=1}^{n} X_j W_{ij} \tag{3.21}$$

where W_{ij} represents the weight of the j^{th} input to the i^{th} neuron. The activation function $F_n(Z)$ is applied after the summation function to obtain the exact output.

The training process of the ANN involves the backpropagation algorithm, which iteratively adjusts the network's weights using gradient descent to minimize the associated loss function. The key idea behind backpropagation is to compute the gradients of the loss function with respect to each weight in the network, indicating the necessary adjustments to reduce error. Backpropagation consists of two phases: forward propagation, where input data is transmitted through the network layer by layer using the current weights, and backward propagation, where gradients are computed from the output layer back to the input layer. The weights are updated iteratively until the loss function is minimized [103].

During forward propagation, the input data flows through the network, computing activations at each neuron. The final output is compared with the target value, and the error is calculated. In backward propagation, the error is used to adjust the weights by propagating gradients backward using the chain rule of differentiation. The process is repeated over multiple iterations (epochs) until the loss function reaches an acceptable level.

To improve training efficiency, optimization algorithms such as Levenberg-Marquardt (LM) are often employed. The LM optimizer is particularly effective for solving nonlinear minimization problems, providing faster convergence and higher accuracy in determining optimal weights [103].

Once trained, the ANN acts as a universal controller capable of dynamically adapting to different operating scenarios without requiring manual recalibration, unlike conventional PI regulators. This adaptability makes ANN-based control strategies particularly suitable for

five-phase induction motor applications, where varying load conditions, speed variations, and dynamic torque demands require a robust and adaptive control approach.

3.5.1 Simulation Results

Figure 3.22 illustrates how neural networks (NNs) replace the conventional PI regulators in the DTC-SVM control with four vectors. Specifically, the NNs take over the roles of the PI speed controller, PI torque controller, and PI flux controller. These networks are trained across multiple operating ranges to ensure adaptability to a wide variety of scenarios.

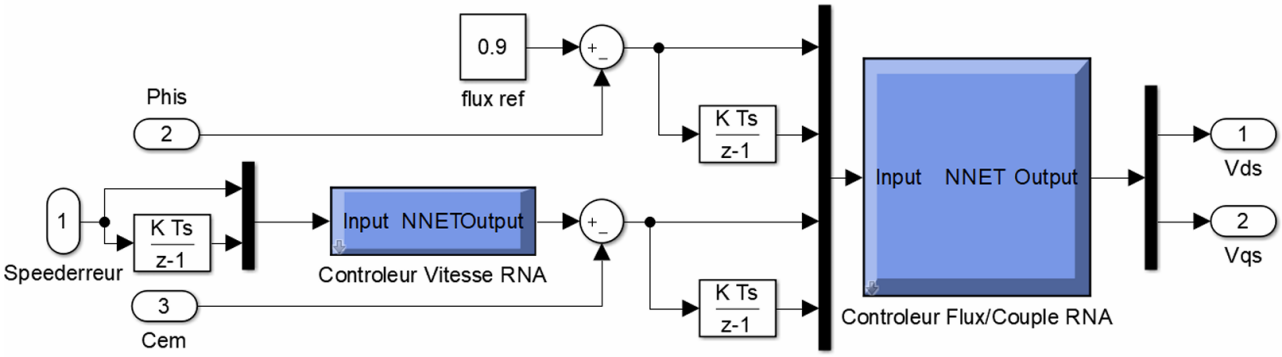

Figure 3.22: Diagram of NN controllers for the DTC-SVM control with four vectors.

For the FCS-MPC control, the PI speed controller has been directly replaced by a controller based on neural networks (NNs), as illustrated in Figure 3.23.

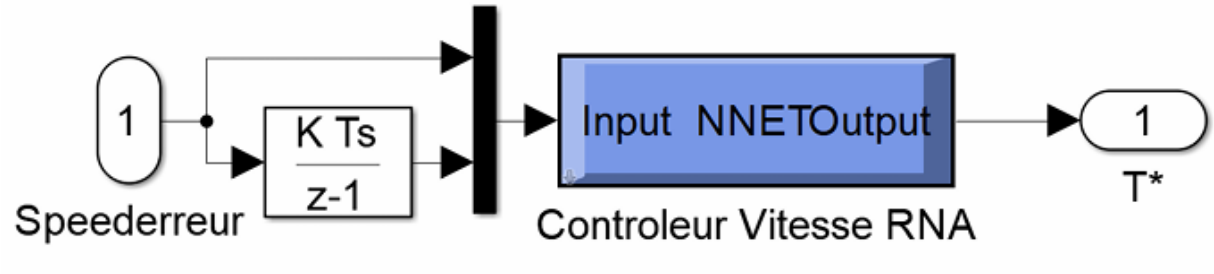

Figure 3.23: NN controllers for the FCS-MPC case.

The simulation results, presented in Figure 3.24 and Figure 3.25, show that the NN provides precise and robust control in both DTC-SVM with four vectors and FCS-MPC. These results confirm that the NN is an effective and suitable alternative to conventional PI control.

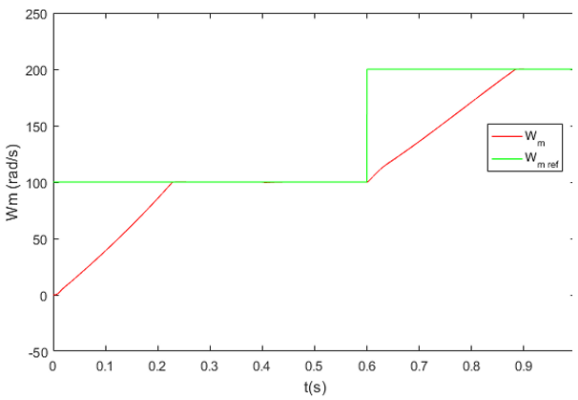

(a) Speed with an NN controller

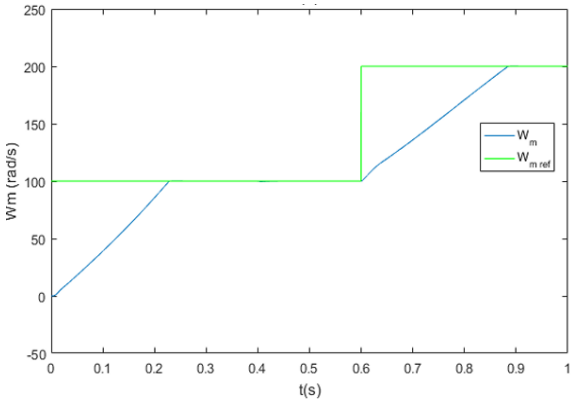

(b) Speed with a PI controller

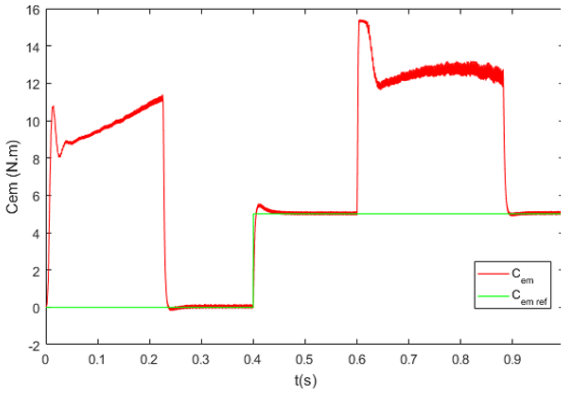

(c) Torque with an NN controller

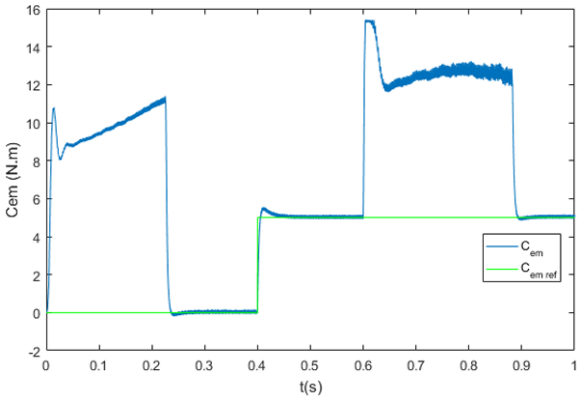

(d) Torque with a PI controller.

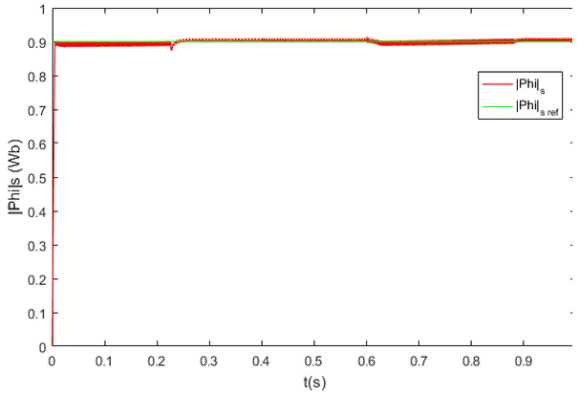

(e) Stator flux with an NN controller

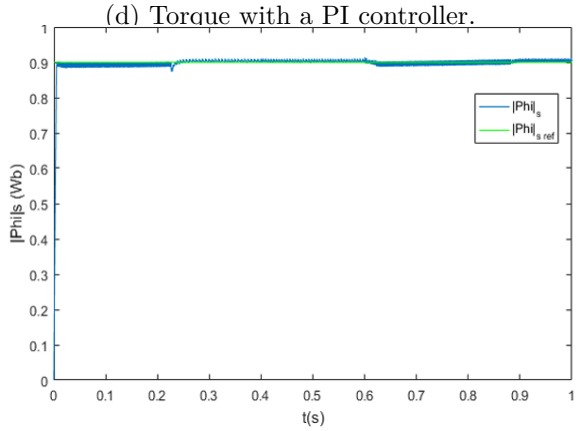

(f) Stator flux with a PI controller

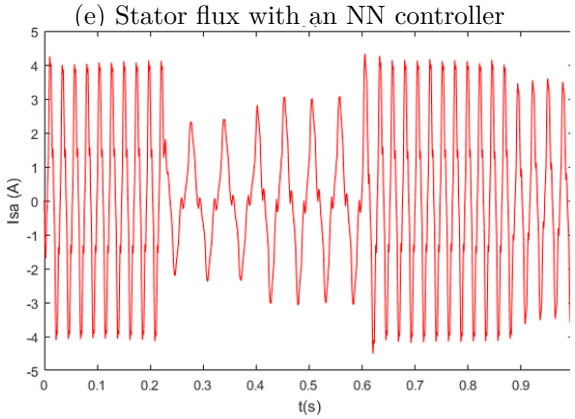

(g) Stator current with an NN controller

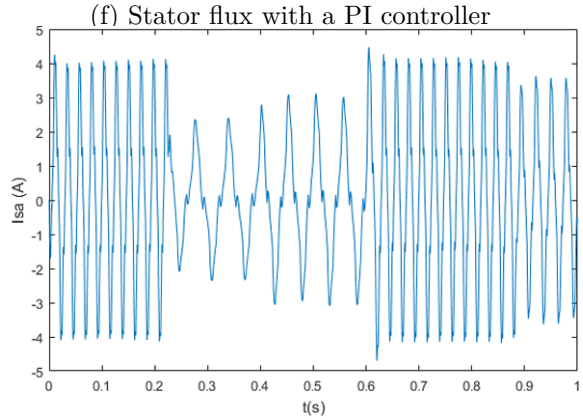

(h) Stator current with a PI controller

Figure 3.24: Comparison of the performance between NN and PI controllers in the DTC-SVM with four vector case.

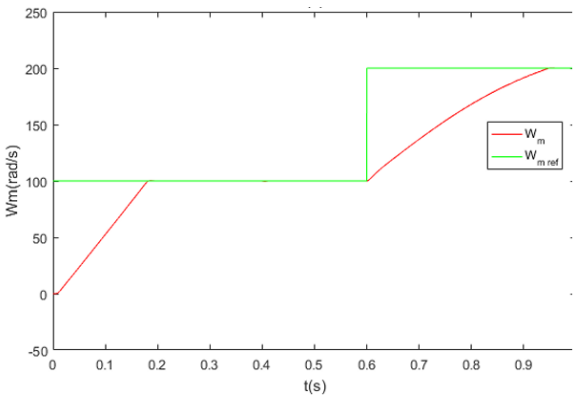

(a) Speed with an NN controller

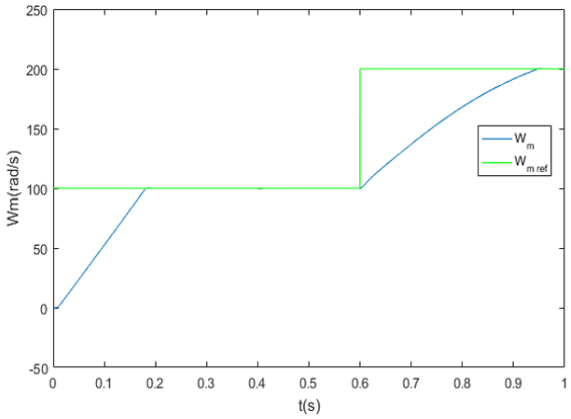

(b) Speed with a PI controller

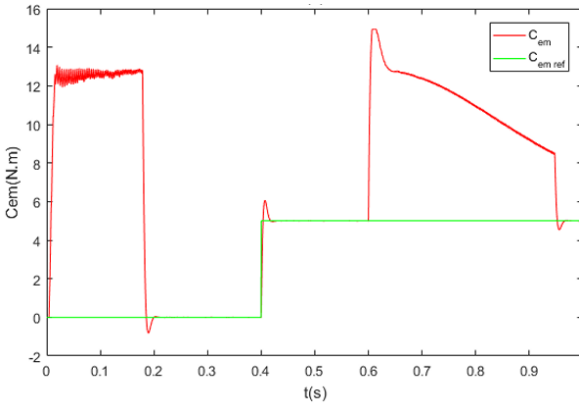

(c) Torque with an NN controller

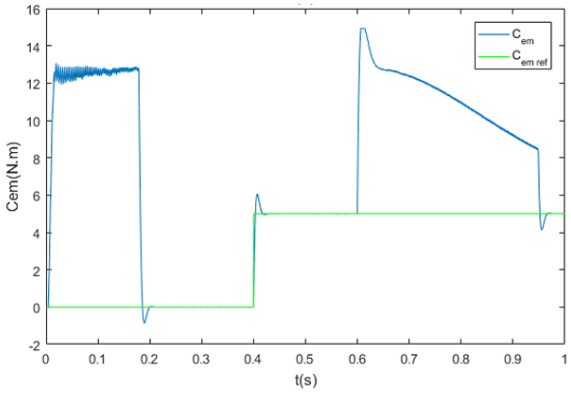

(d) Torque with a PI controller.

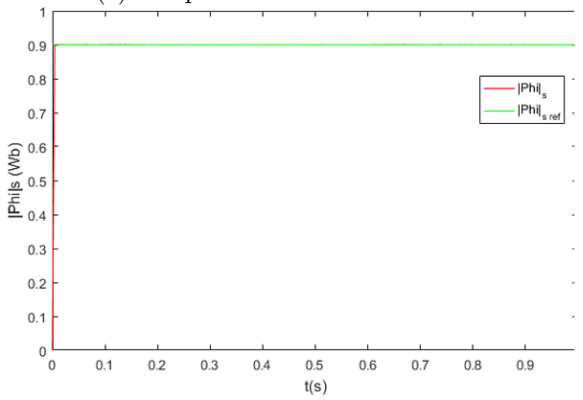

(e) Stator flux with an NN controller

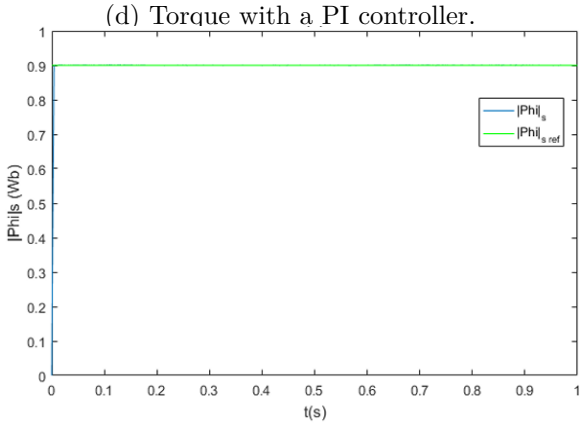

(f) Stator flux with a PI controller

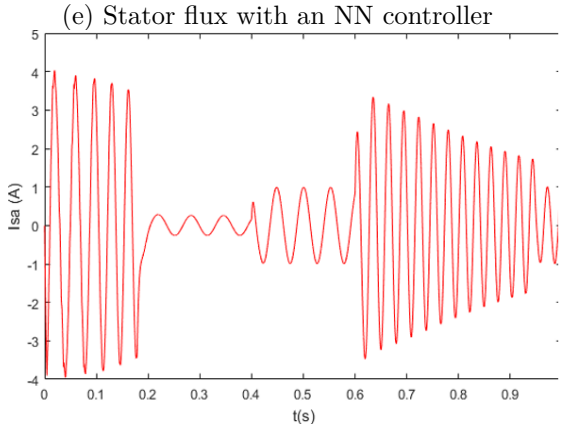

(g) Stator current with an NN controller

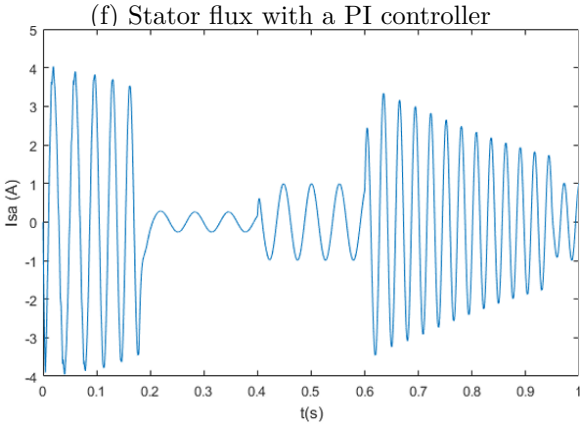

(h) Stator current with a PI controller

Figure 3.25: Comparison of the performance between NN and PI controllers in the FCS-MPC case.

3.6 Sensorless Control Using MRAS for Five-Phase Induction Motors

The Model Reference Adaptive System (MRAS) is used to estimate the rotor speed without relying on a mechanical sensor. This technique is characterized by its simplicity of implementation and is based on a structure composed of three main elements: a reference model, an adaptive model, and an adaptation mechanism, as illustrated in Figure 3.26.

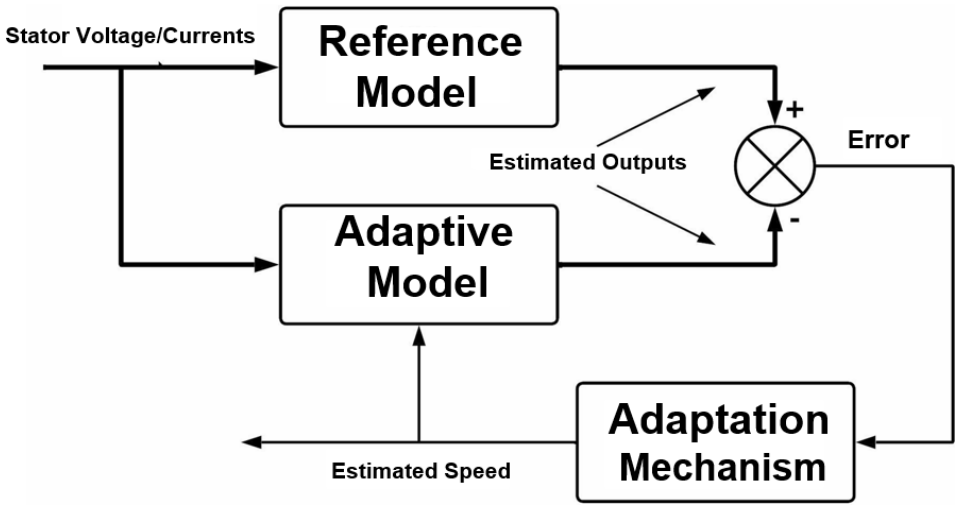

Figure 3.26: Complete structure of the MRAS speed estimator.

The reference model is independent of rotor speed. It calculates the rotor flux based on the measured stator current and the measured stator voltage at the inverter output.

The adaptive model, on the other hand, depends on rotor speed. It takes as inputs the measured stator current and the estimated rotor speed to determine the rotor flux. An error vector is generated by comparing the outputs of both models. This error vector is processed by an adaptation mechanism based on a PI regulator, which dynamically adjusts the parameters of the adaptive model to align its outputs with those of the reference model. When the error between the two models converges to zero, the estimated speed becomes equivalent to the actual rotor speed.

The reference model is defined by the following equations:

$$\Phi_{rd} = \frac{L_r}{L_m}\left(\int (V_{sd} - R_s I_{sd})\, dt - \sigma L_s I_{sd}\right),$$
$$\Phi_{rq} = \frac{L_r}{L_m}\left(\int (V_{sq} - R_s I_{sq})\, dt - \sigma L_s I_{sq}\right).$$

The adaptive model adjusts the estimated fluxes as follows:

$$\hat{\Phi}_{rd} = \frac{1}{T_r}\int \left(L_m I_{sd} - \hat{\Phi}_{rd} - \omega_r T_r \hat{\Phi}_{rq}\right) dt,$$
$$\hat{\Phi}_{rq} = \frac{1}{T_r}\int \left(L_m I_{sq} - \hat{\Phi}_{rq} + \omega_r T_r \hat{\Phi}_{rd}\right) dt.$$

The adaptation mechanism adjusts the estimated speed using the PI regulator, according to the following expression:

$$\hat{\omega}_r = K_p\left(\Phi_{rq}\hat{\Phi}_{rd} - \Phi_{rd}\hat{\Phi}_{rq}\right) + K_i \int \left(\Phi_{rq}\hat{\Phi}_{rd} - \Phi_{rd}\hat{\Phi}_{rq}\right) dt.$$

3.6.1 Simulation Results

To evaluate the performance and verify the robustness of the MRAS estimator based on rotor flux error, simulations were conducted using both FCS-MPC and DTC-SVM with four active vectors. The reference speed profile used consists of multiple steps alternating between transient and steady-state conditions, in both forward and reverse directions. The transient conditions correspond to phases where the speed varies, such as acceleration or reversal of the rotation direction. In contrast, steady-state conditions are characterized by a stabilized speed at a constant value, whether in the forward or reverse direction. These simulations highlight the accuracy, robustness, and efficiency of the MRAS estimator under various operating conditions.

The simulation results, illustrated in Figure 3.27, show that the rotor speed accurately follows the reference speed profile, with negligible errors during steady-state phases. Very small errors are observed during transient phases for both FCS-MPC and DTC-SVM with four active vectors, demonstrating the effectiveness of this estimator.

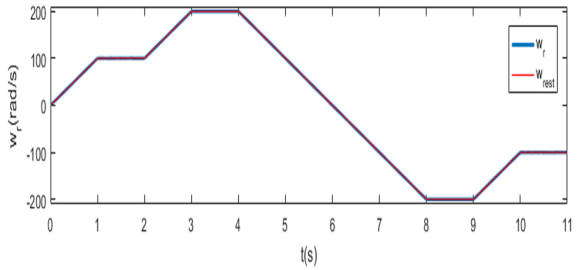

(a) Actual and estimated rotor speeds - DTC-SVM with four active vectors.

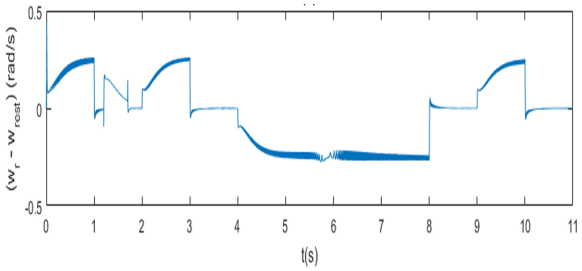

(b) Estimation error - DTC-SVM with four active vectors.

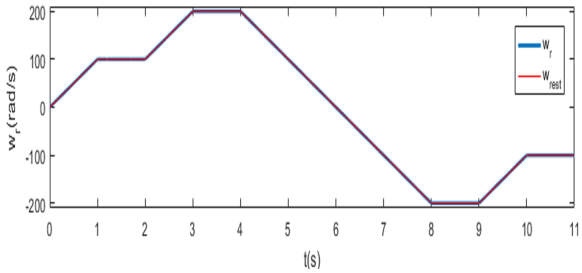

(c) Actual and estimated rotor speeds - FCS-MPC.

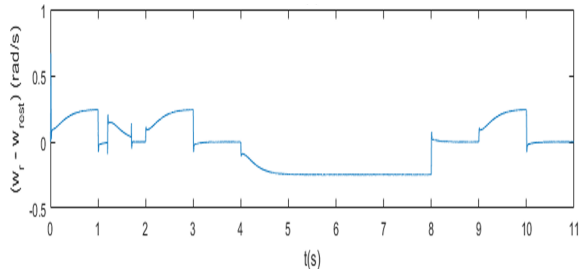

(d) Estimation error - FCS-MPC.

Figure 3.27: Performance of the MRAS estimator based on rotor flux error.

3.7 Conclusion

This chapter presented a comparative analysis of DTC, DTC-SVM, and FCS-MPC control strategies applied to five-phase induction motors. The evaluation was conducted through systematic simulations using MATLAB/Simulink under a range of operating conditions. In terms of dynamic performance, FCS-MPC exhibited the fastest response during speed reference changes and the smallest speed deviation with quicker recovery during load disturbances. DTC followed with satisfactory responsiveness, while DTC-SVM, particularly with four vectors, showed slower speed transitions. All strategies effectively tracked the reference torque, but differences emerged in ripple levels: DTC-SVM with four vectors achieved the lowest torque ripple, followed by the two-vector, whereas classical DTC exhibited the highest. Regarding stator flux regulation, FCS-MPC ensured the most stable flux tracking. DTC-SVM, especially in the four-vector configuration, improved flux control compared to its two-vector counterpart, while DTC

showed the largest flux deviations. In terms of current waveform quality, DTC-SVM with four vectors generated stator currents closest to sinusoidal, while DTC and FCS-MPC showed more waveform variability and higher peak currents during transients. Harmonic analysis confirmed that DTC-SVM with four vectors achieved the lowest total harmonic distortion (THD), due to its ability to eliminate x–y plane components while maintaining a fixed switching frequency. The two-vector version, despite using fixed switching frequency, had the highest THD due to its inability to suppress these components. DTC and FCS-MPC both resulted in elevated THD levels, primarily due to their variable switching frequencies. FCS-MPC, due to its strong reliance on an accurate machine model, proved the most sensitive to parameter variations, leading to noticeable flux deviations and increased ripple. In contrast, DTC-SVM and DTC showed greater robustness, maintaining stable flux behavior under such uncertainties.

The simulation results confirm that each control strategy presents distinct advantages, and the selection should be guided by the specific performance requirements and constraints of the target application:

- **FCS-MPC** is best suited for high-performance applications requiring fast dynamic response and strong disturbance rejection.
- **DTC-SVM** (particularly with four vectors) is ideal when low torque ripple, improved current quality, and fixed switching frequency are essential.
- **DTC** remains a practical and robust solution when simplicity, ease of implementation, and acceptable performance are prioritized.

In addition, the integration of neural networks (NNs) to replace conventional PI regulators has shown potential for enhanced adaptability and control precision. The adoption of MRAS-based speed estimation further enables sensorless operation without compromising control robustness.

The following chapter will focus on experimental validation of these control strategies on a 3.5 kW five-phase induction motor, assessing their practical implementation, real-time performance, and robustness under realistic conditions.

Chapter 4:
Experimental Validation

Chapter 4

Chapter 4: Experimental Validation

4.1 Introduction

Following the simulation-based analysis of control strategies for five-phase induction motors, this chapter presents their experimental validation under real operating conditions. The objective is to assess and compare the practical performance of Direct Torque Control (DTC), Direct Torque Control with Space Vector Modulation (DTC-SVM), and Finite Control Set Model Predictive Control (FCS-MPC). An overview of the experimental test bench, including hardware and software components, is provided, along with the measurement environment used. The evaluation focuses on both steady-state and dynamic behavior in terms of response time, torque and flux ripple, total harmonic distortion (THD), and current waveform quality. This validation serves to confirm simulation trends and offers practical insights into the advantages and trade-offs of each strategy for five-phase motor control.

4.2 Experimental Validation of the Control Strategies

Figure 4.1 presents the experimental test bench used for the implementation of the different control techniques on a 3.5 kW five-phase induction motor, and the detailed motor and control parameters are provided in Appendix A Table 1.

The test bench includes a measurement environment in addition to the two main parts, the power part and the control part.

The power part includes a 3.5 kW five-phase induction motor coupled with a direct current generator, which functions as a load. The generator is connected to adjustable resistors, allowing for manual modification of the total resistance to vary the load torque. The motor is powered by two three-phase voltage source inverters from Semikron, as shown in Figure 4.2. These inverters receive a fixed 400 V DC input voltage from a diode rectifier, which is supplied by an autotransformer.

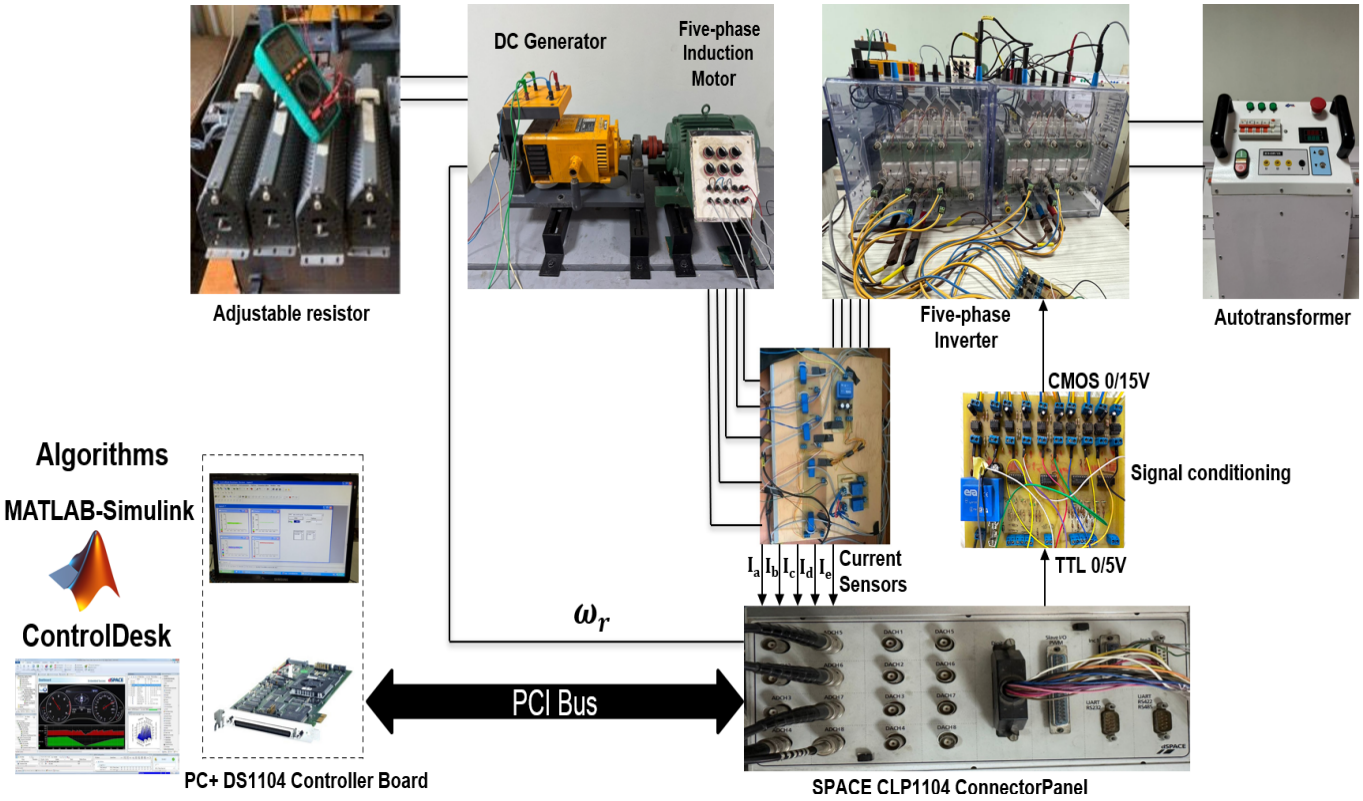

Figure 4.1: Diagram of the experimental setup.

The basic operating principles of a five-phase inverter are developed under the assumption of ideal switching. The upper and lower switches of the same leg operate in a complementary manner, meaning that if the upper switch is "ON," the lower switch must be "OFF," and vice versa. This prevents the risk of a short circuit. Therefore, it is essential to include a delay between the closing and opening of the two complementary switches. This delay is called "dead time" because both switches remain in the "OFF" position simultaneously for a short period.

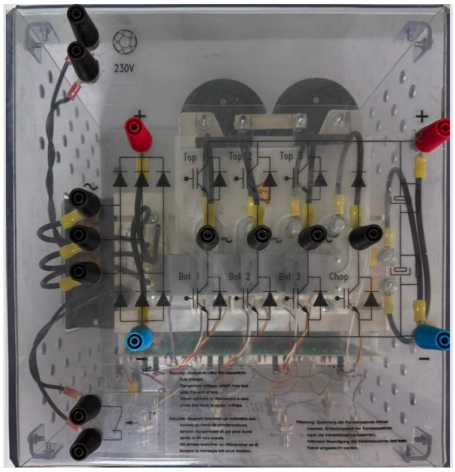

Figure 4.2: Semikron three-phase inverters.

Figure 4.3 shows a typical implementation of a dead-time generation circuit using discrete components such as resistors, capacitors, diodes, and logic gates. This configuration introduces a delay on the rising edge of the control signal while preserving the falling edge, thus creating a short period during which both switches are safely turned off.

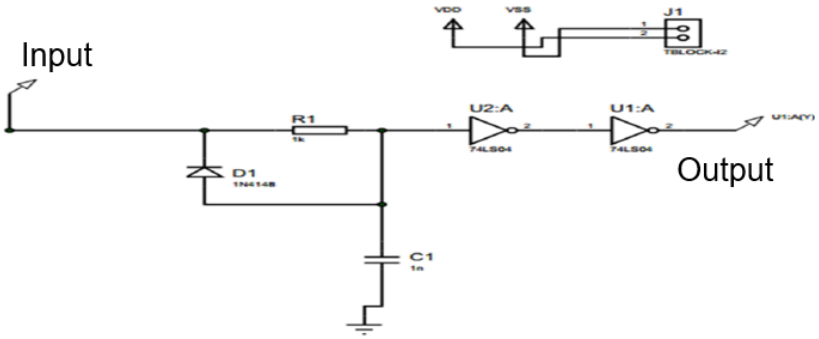

Figure 4.3: RDC Dead-Time Generator Circuit.

However, in the present work, this function is not implemented externally. Instead, the Semikron power modules used are equipped with integrated devices to provide this dead time, eliminating the need for an additional analog circuit.

The control part is based on the DS1104 R&D Controller Board developed by the German company dSPACE GmbH and housed in a computer, as shown in Figure 4.4. This control board consists of two processors. The master processor manages the application, while the slave processor, a Digital Signal Processor (DSP) from TEXAS INSTRUMENTS (model TMS320F240), generates Pulse Width Modulation (PWM) control signals in TTL logic (0/5 V). This constitutes the hardware part of dSPACE.

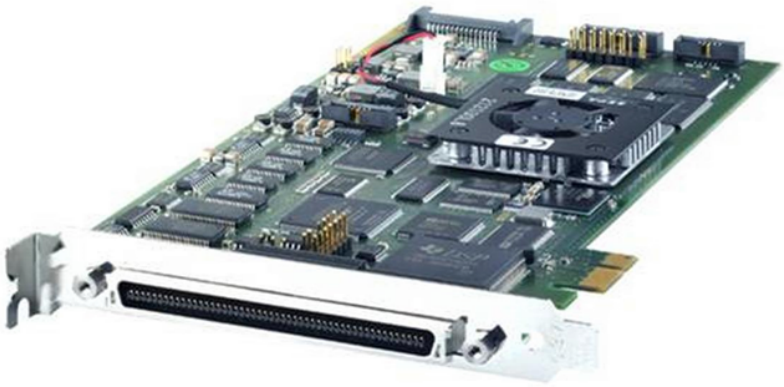

Figure 4.4: DSPACE 1104 Board.

This board (Master PPC) features 8 Analog-to-Digital Converters (ADC) with an input voltage range of -10V to +10V and 8 Digital-to-Analog Converters (DAC) with an output voltage range of -10V to +10V. It also includes several interfaces, such as digital inputs and outputs, incremental encoders, etc. A connection cable links the DSP board to the PC via the RS232 port, transmitting the control signals generated by the PC to the DSP.

The control algorithm, or the software part, primarily revolves around two software tools: Matlab/Simulink and Control Desk. Matlab/Simulink enables easy real-time application programming using blocks from the "Real-Time Interface (RTI)" toolbox. Once validated, the programs are automatically compiled and downloaded to the board using the dSPACE Control Desk Manager software. This second software serves as a graphical interface, allowing control of command signals from Simulink to dSPACE and real-time visualization of available signals within the Simulink environment, as illustrated in Figure 4.5.

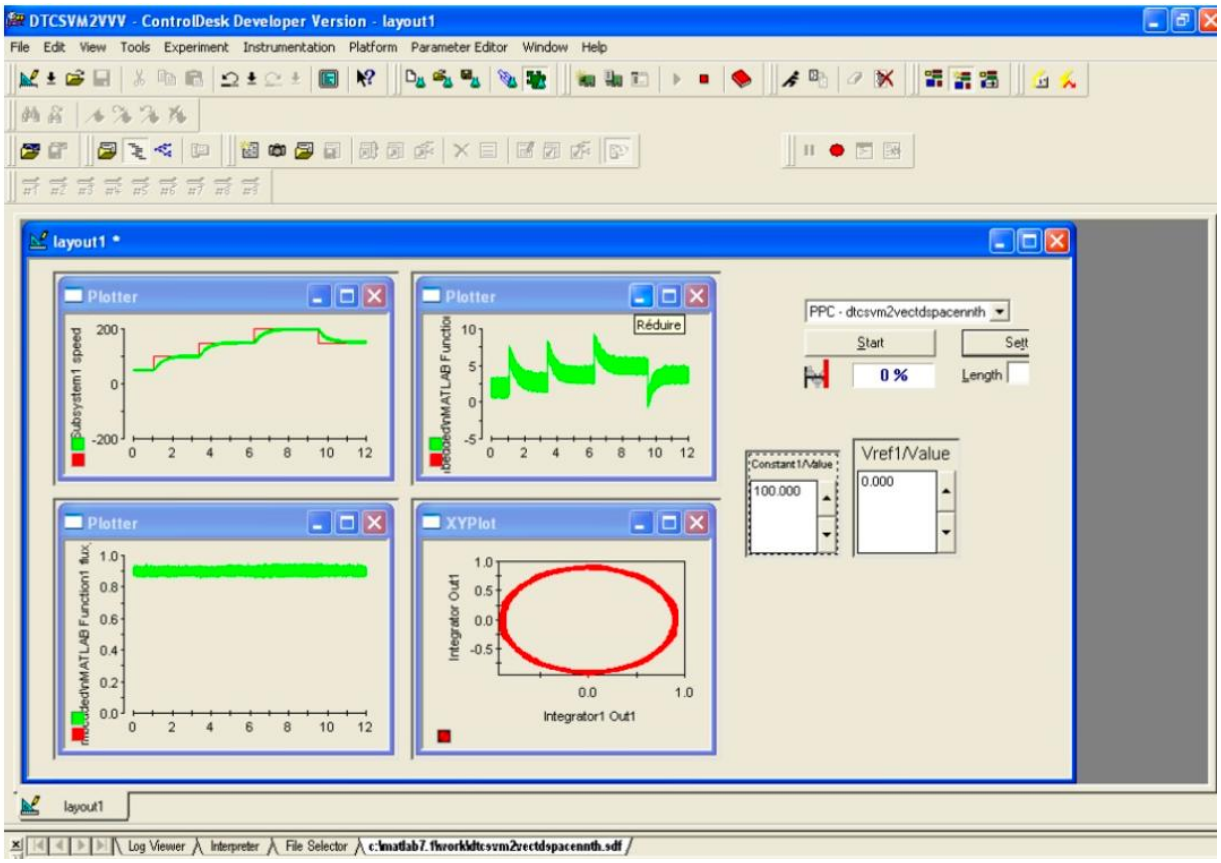

Figure 4.5: Control Desk software window.

The exchange of information between the two parts described above is facilitated through an external connection box (dSPACE Connector Panel CLP1104), as shown in Figure 4.6a. This box is connected to the board via a connection cable and receives analog signals through BNC connectors. It also includes an interface for conditioning PWM control signals and potential error signals sent back by the Semikron converter, along with a measurement environment incorporating various sensors. This signal conditioning interface, illustrated in Figure 4.6b, converts signals from TTL logic (0/5 V) to CMOS logic (0/15 V) and vice versa. This transformation is necessary because the DS1104 control board operates with TTL 0/5 V logic signals, whereas the inverter requires CMOS 0/15 V logic signals.

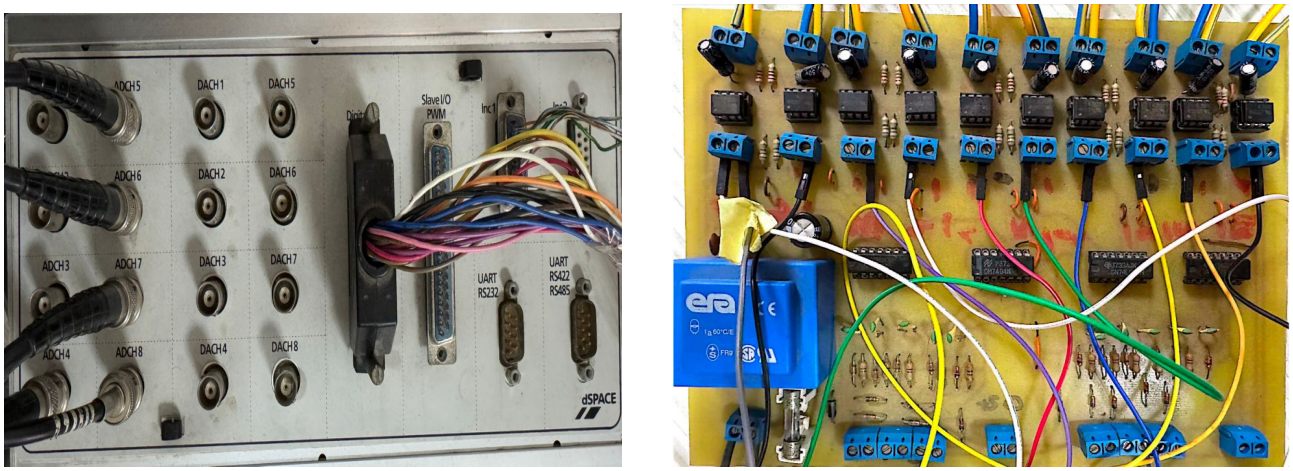

(a) dSPACE Connector Panel CLP1104.

(b) Signal conditioning interface.

Figure 4.6: Hardware components facilitating signal exchange and conditioning.

For the measurement environment, an incremental encoder is used to measure the rotational speed of the motor. The speed sensor used is an incremental encoder, which is a sensor for angular or linear position. It is mounted on the motor shaft, where a light beam passes through a perforated disk with N_b slots evenly distributed around its edge. For each complete rotation of the encoder, the light beam is interrupted N_b times, generating N_b square signals, as illustrated in Figure 4.7.

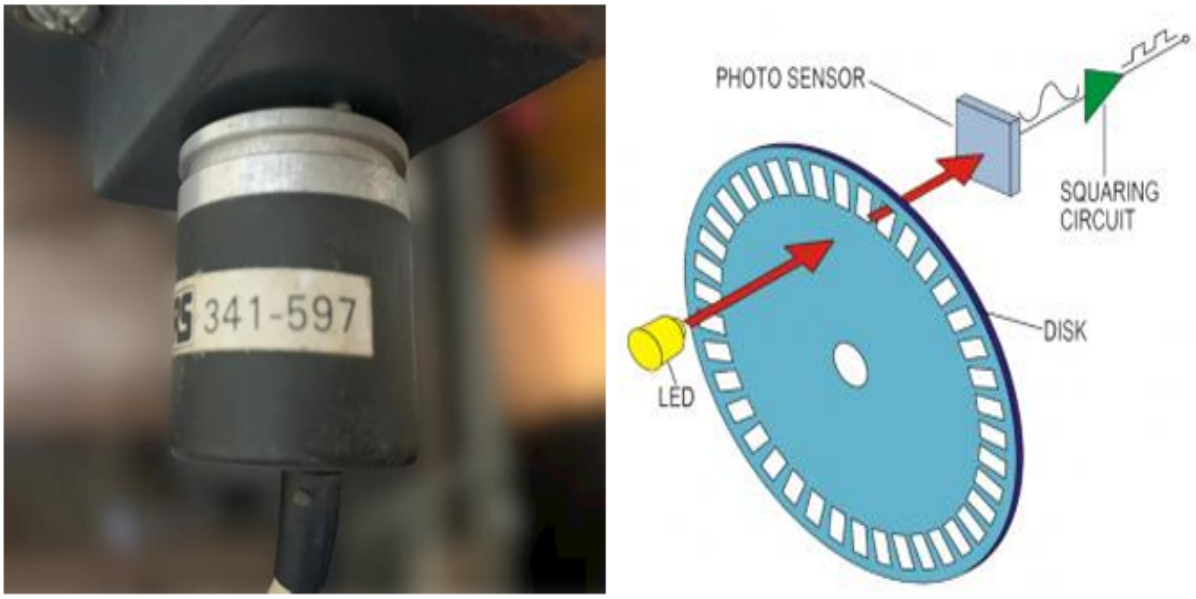

Figure 4.7: Speed sensor.

In addition to speed measurement, current sensing is carried out using LEM LA 55-P Hall-effect current sensors, as illustrated in Figure 4.8. These sensors provide an isolated measurement of the primary current by exploiting the Hall effect, and generate a secondary current proportional to the primary current with a fixed transformation ratio (typically 1:1000). This secondary current is passed through a burden resistor R_M to convert it into a measurable voltage signal. The value of R_M is selected to ensure that the output voltage does not exceed a specified maximum (e.g., 9 V), and is computed using the expression:

$$R_M = \frac{V_M}{I_p \cdot n \cdot r} \tag{4.1}$$

where:

- V_M is the maximum allowable voltage across the burden resistor (set to 9 V),
- I_p is the maximum expected primary current (less than 50 A),
- n is the number of turns of the primary conductor through the sensor aperture,
- r is the transformation ratio between primary and secondary currents.

The sensors are powered using an asymmetric DC supply of ± 15 V and provide a reliable, real-time image of the current waveform. A calibration procedure using a programmable current source is used to determine the actual transformation ratio and offset voltage of each sensor to ensure accuracy.

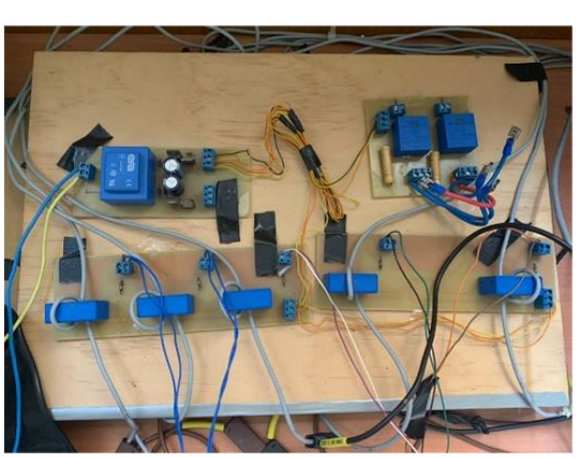

(a) Current measurement board.

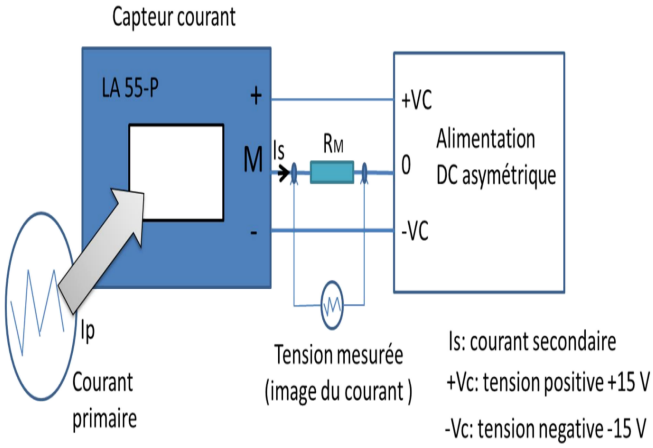

(b) Circuit diagram of the LA 55-P current sensor.

Figure 4.8: Current measurement setup using LA 55-P sensors.

The control strategies were evaluated under different conditions to compare their static and dynamic performances. Static performance was analyzed by studying the steady-state behavior, focusing on indicators such as torque ripple, total harmonic distortion (THD) of the current, and steady-state error. The evaluation of dynamic performance focused on responses to variations in operating conditions, such as speed or load changes, with key indicators including response time, overshoot, settling time, and stability.

The same two test scenarios as in the simulation were performed to assess the control strategies under speed and load variations. In addition, a third scenario was introduced to experimentally evaluate the fault tolerance and reliability of the control methods. This test involved applying a single open-phase fault and a two non-adjacent open-phase fault to assess the system's robustness under abnormal operating conditions.

Figures 4.9 to 4.12 present the experimental results obtained for each control strategy, where the speed reference varies from 50 to 200 rad/s in increments of 50 rad/s before decreasing from 200 to 150 rad/s under constant load conditions. For each strategy, the following electromagnetic and electrical variables were observed: rotor speed, electromagnetic torque, and stator flux magnitude all compared to their respective references as well as the stator current waveform and inverter output voltage, together with their harmonic content.

In Figures 4.9b, the DTC shows the rotor speed closely following its reference without overshoot during both acceleration and deceleration. The motor transitions from 100rad/s to 150rad/s and from 200rad/s to 150rad/s in approximately 0.12 seconds.

Figure 4.9b shows that the electromagnetic torque under DTC tracks its reference accurately in both forward and reverse operations, with an average maximum torque ripple of approximately 0.03851 Nm.

As illustrated in Figure 4.9c, the stator flux magnitude under DTC follows its reference with minor deviations during speed changes, with a flux ripple up to 0.01181 Wb.

For electrical performance, the stator currents under DTC increase in both magnitude and frequency as speed rises, reaching a peak of approximately 7.36 A during speed variations. The current waveforms exhibit variability due to the variable switching frequency characteristic of DTC. The total harmonic distortion (THD) of the stator current under DTC is 22.59% , while the inverter output voltage THD is 129.68% , reflecting the harmonic content of the two-level inverter output under DTC control.

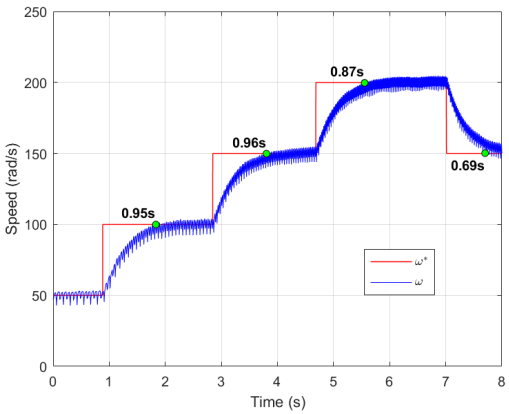

(a) Speed and its reference

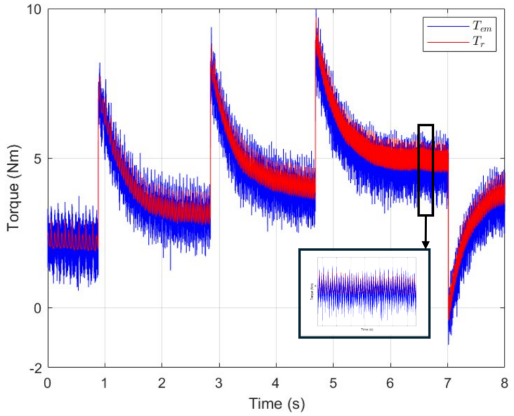

(b) Electromagnetic torque and its reference.

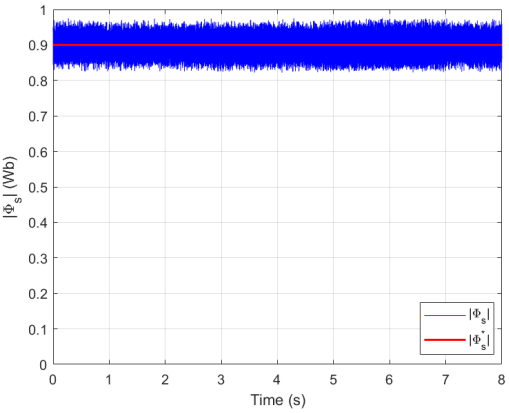

(c) Stator flux and its reference

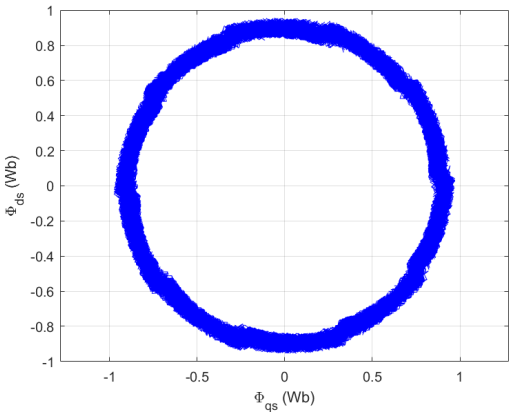

(d) Stator flux trajectory

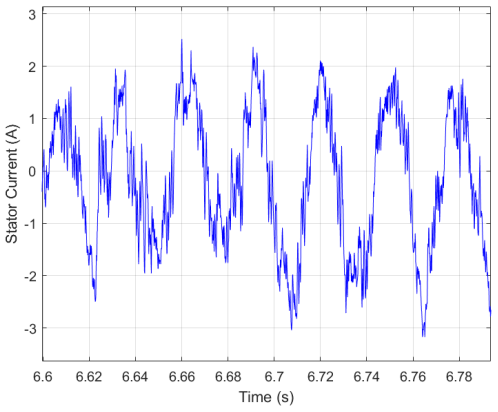

(e) Stator current

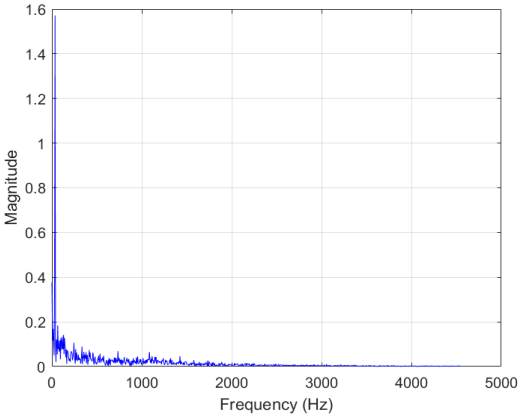

(f) FFT of stator current

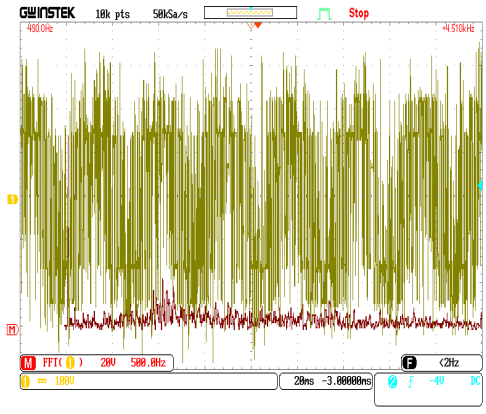

(g) Output voltage

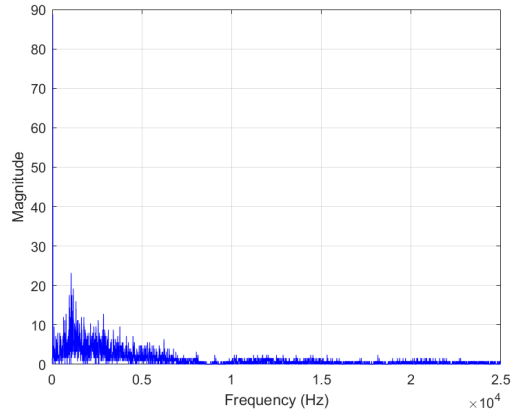

(h) FFT of output voltage

Figure 4.9: Experimental results for the DTC

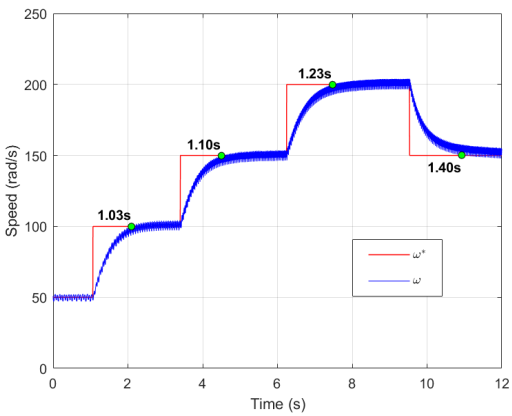

(a) Speed and its reference

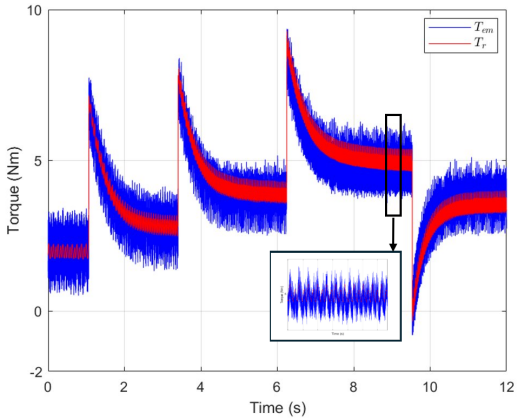

(b) Electromagnetic torque and its reference.

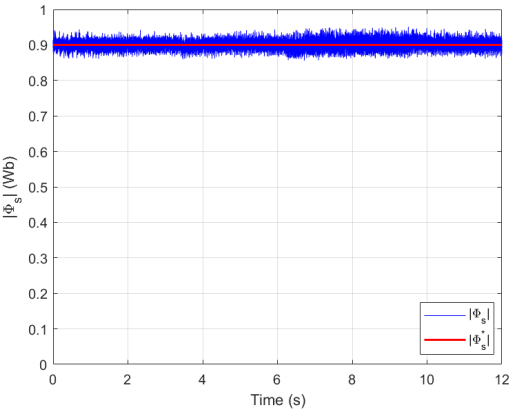

(c) Stator flux and its reference

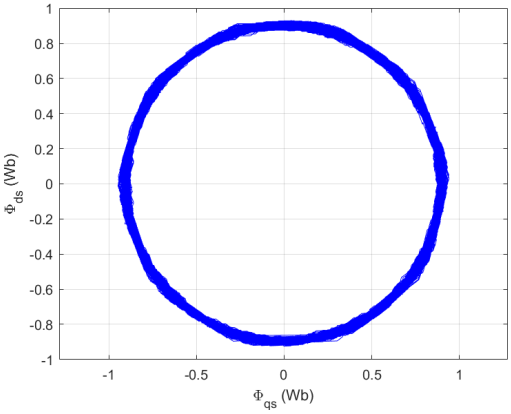

(d) Stator flux trajectory

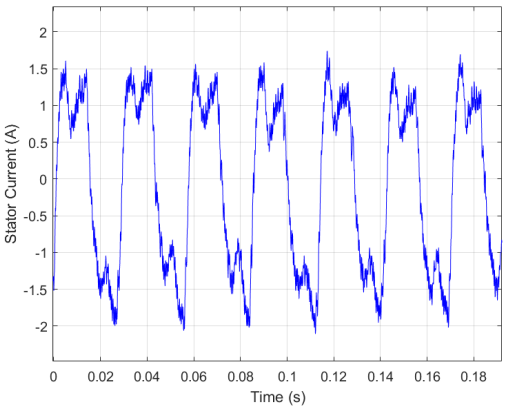

(e) Stator current

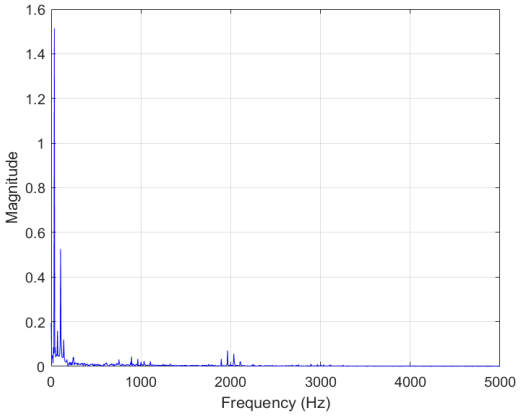

(f) FFT of stator current

(g) Output voltage

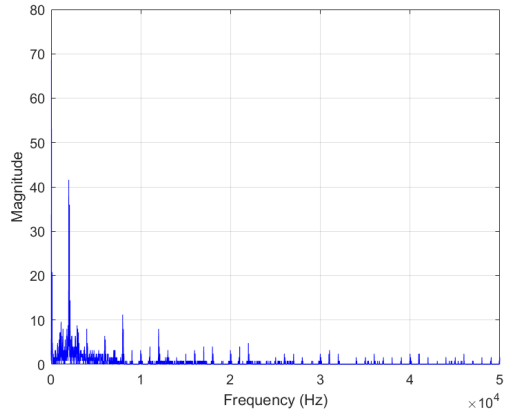

(h) FFT of output voltage

Figure 4.10: Experimental results for the DTC-SVM using two active vectors

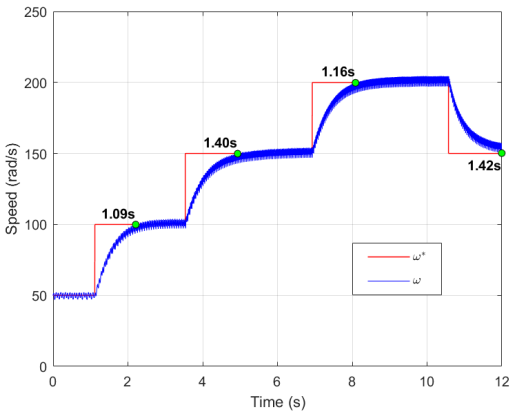

(a) Speed and its reference

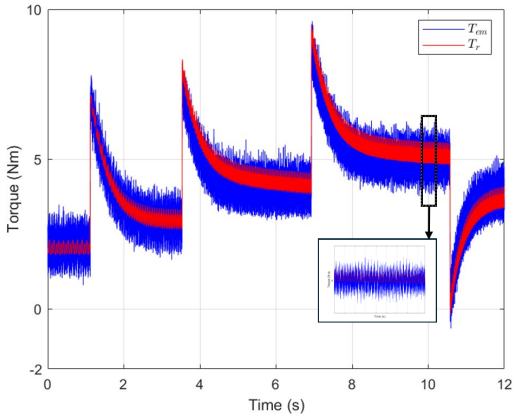

(b) Electromagnetic torque and its reference.

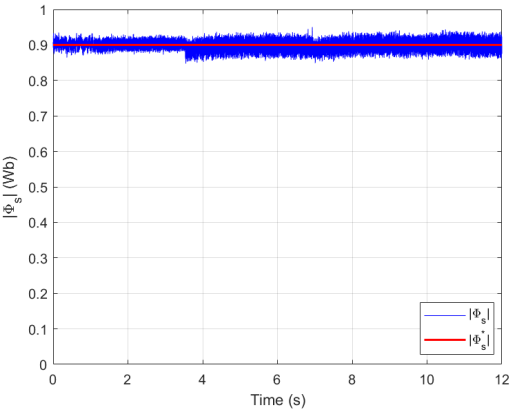

(c) Stator flux and its reference

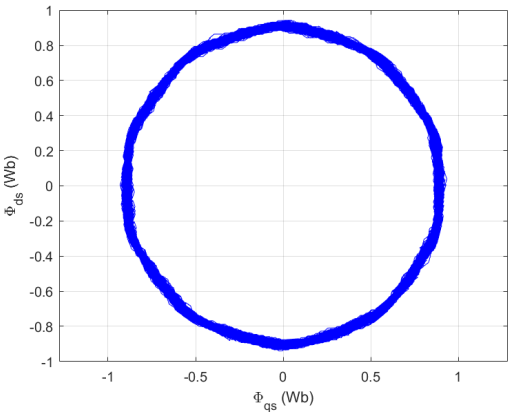

(d) Stator flux trajectory

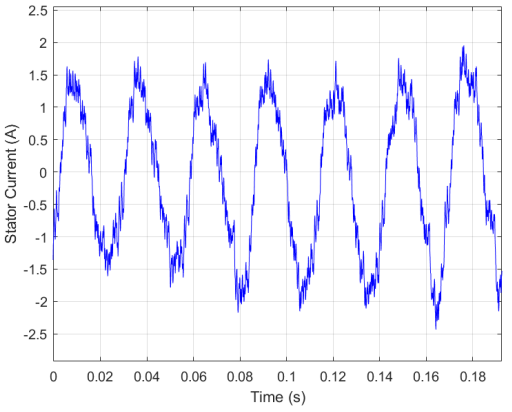

(e) Stator current

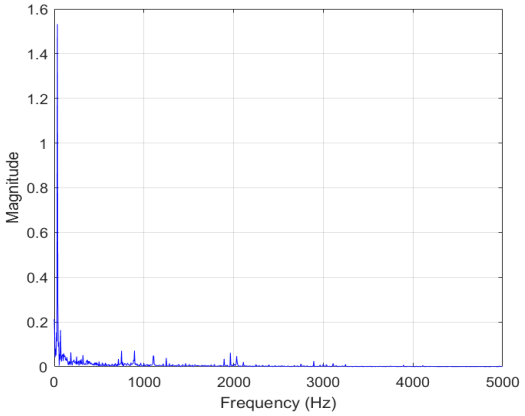

(f) FFT of stator current

(g) Output voltage

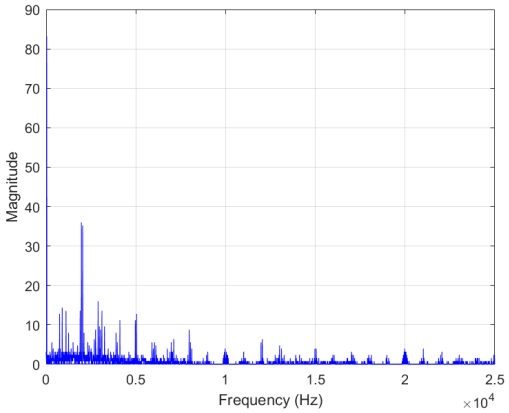

(h) FFT of output voltage

Figure 4.11: Experimental results for the DTC-SVM using four active vectors

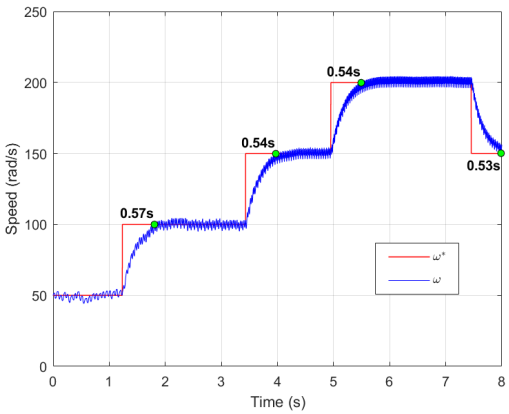

(a) Speed and its reference

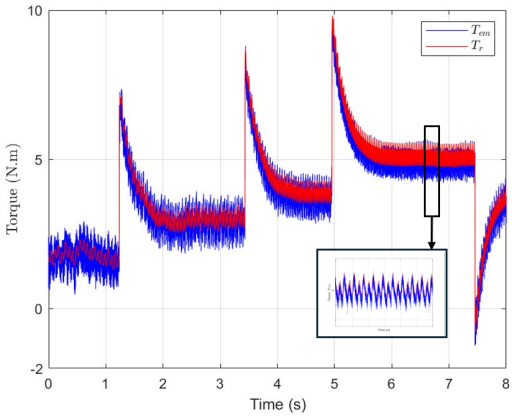

(b) Electromagnetic torque and its reference.

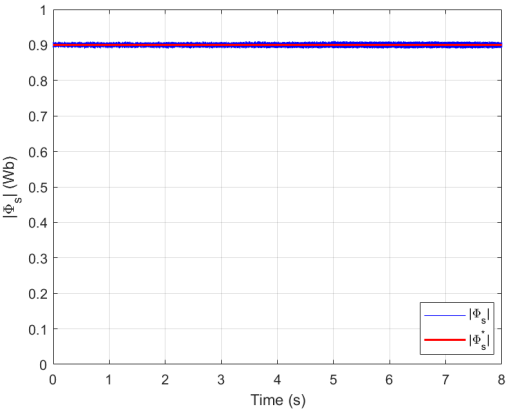

(c) Stator flux and its reference

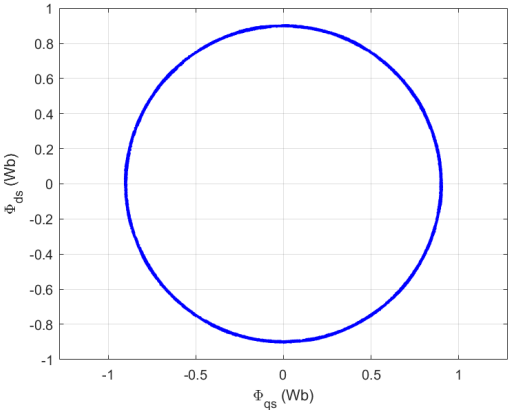

(d) Stator flux trajectory

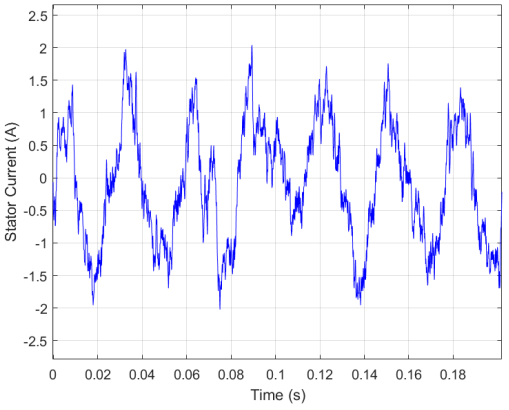

(e) Stator current

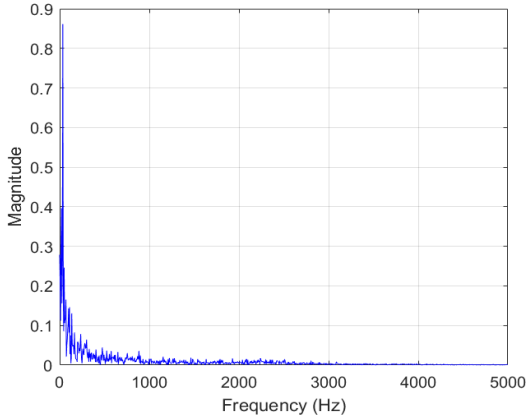

(f) FFT of stator current

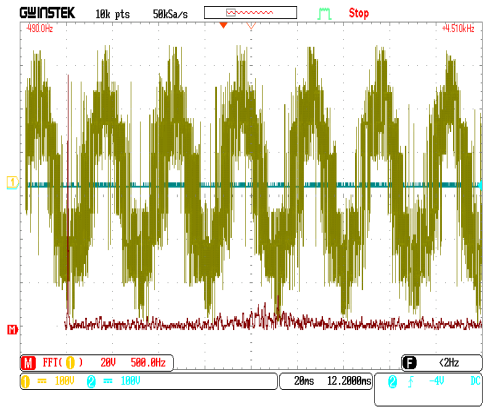

(g) Output voltage

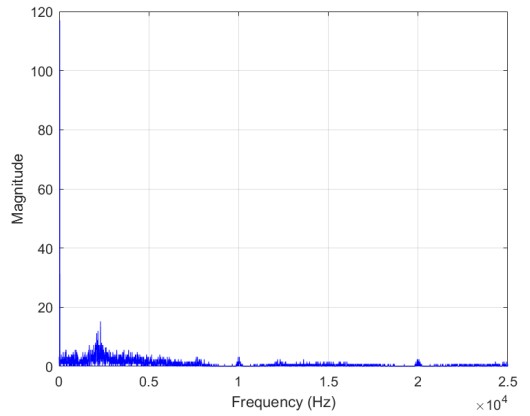

(h) FFT of output voltage

Figure 4.12: Experimental results for the FCS-MPC

Figures 4.13 to 4.16 illustrate the system's dynamic response to sudden load changes at fixed speeds of 100 rad/s and 150 rad/s. Two tests are conducted: a load increase from no-load to full-load, and a load rejection from full-load to no-load.

In the load increase case:

- DTC shows speed drops to 78 rad/s and 122 rad/s, with settling times of 4.5 s and 4.8 s.
- DTC-SVM with two vectors shows drops to 82 rad/s and 124 rad/s, with settling times of 4.2 s and 4.7 s.
- DTC-SVM with four vectors shows drops to 82 rad/s and 126 rad/s, with settling times of 4.2 s and 4.6 s.
- FCS-MPC shows speed drops to 87 rad/s and 132 rad/s, with faster settling times of 3.2 s and 4.2 s.

In the load rejection case:

- DTC shows speed overshoots to 121 rad/s and 177 rad/s, with settling times of 3.4 s and 4.3 s.
- DTC-SVM with two vectors shows overshoots to 119 rad/s and 177 rad/s, with settling times of 3.4 s and 4.1 s.
- DTC-SVM with four vectors shows the same overshoots to 119 rad/s and 177 rad/s, with settling times of 3.4 s and 4.1 s.
- FCS-MPC shows the lowest overshoots to 115 rad/s and 169 rad/s, with the fastest settling times of 2.7 s and 3.2 s.

These results confirm that all methods ensure proper torque tracking during abrupt load changes, but FCS-MPC provides superior speed regulation, while DTC-SVM variants offer balanced performance. DTC remains stable but exhibits the largest deviations and slowest recovery.

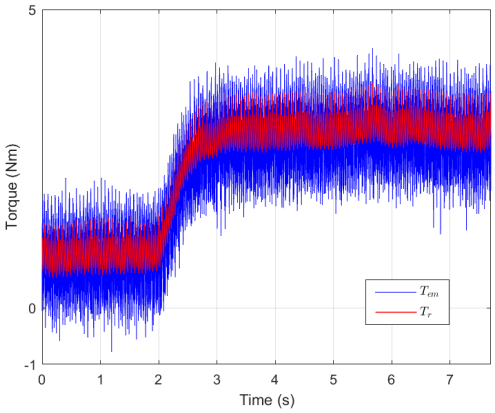

(a) Torque and its reference

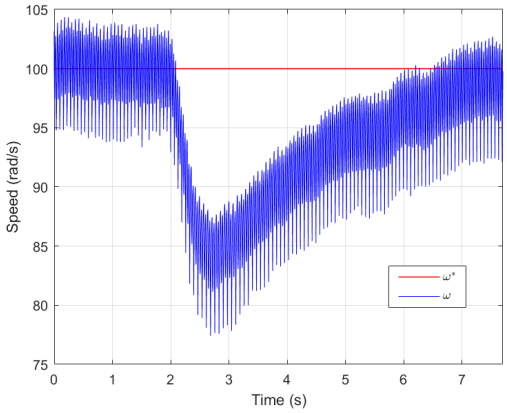

(b) Speed and its reference

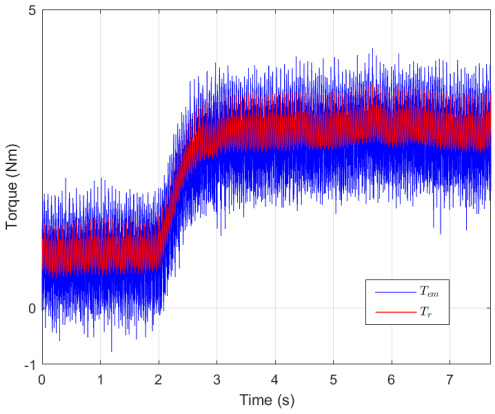

(c) Torque and its reference

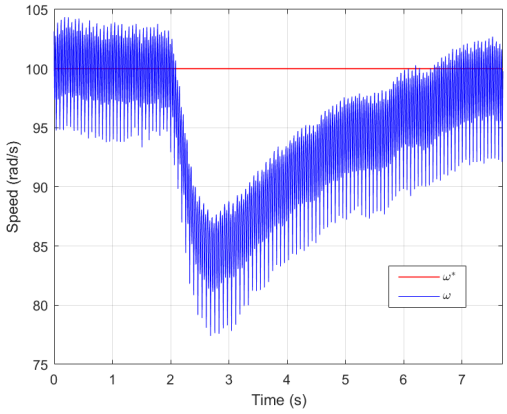

(d) Speed and its reference

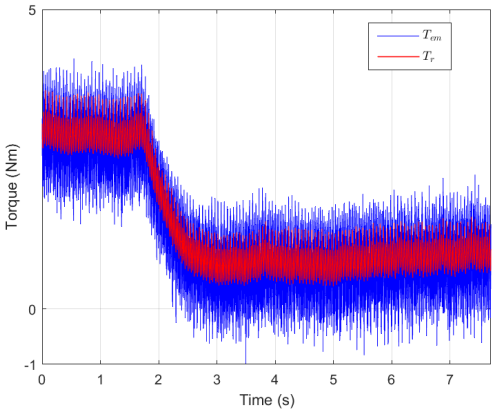

(e) Torque and its reference

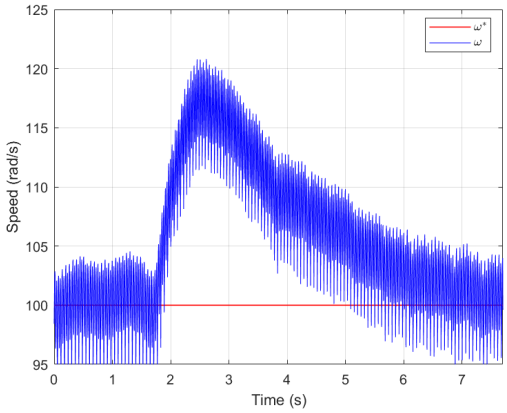

(f) Speed and its reference

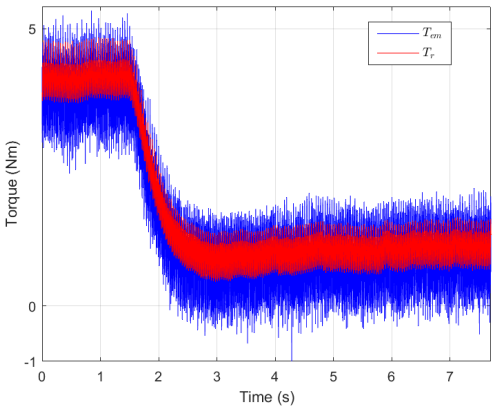

(g) Torque and its reference

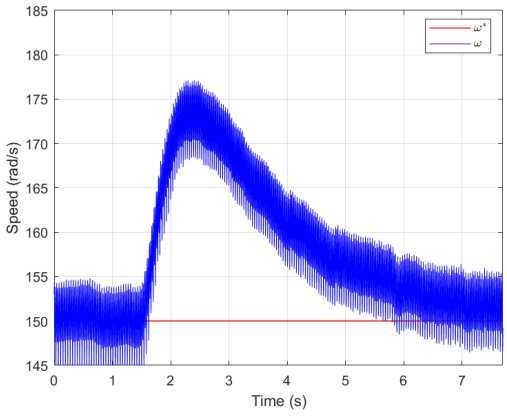

(h) Speed and its reference

Figure 4.13: Torque and speed response of DTC during load variation

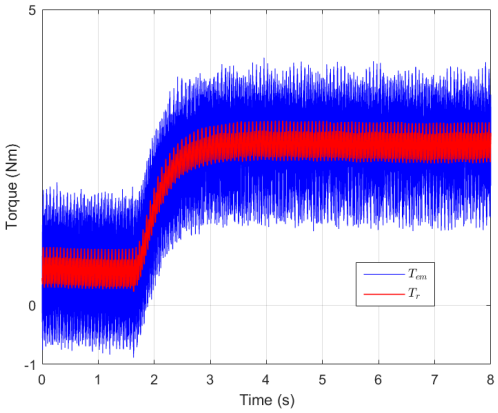

(a) Torque and its reference

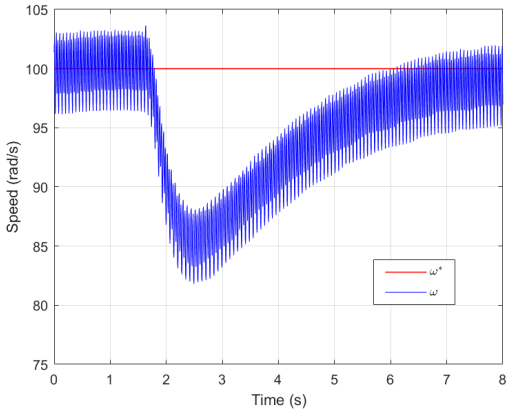

(b) Speed and its reference

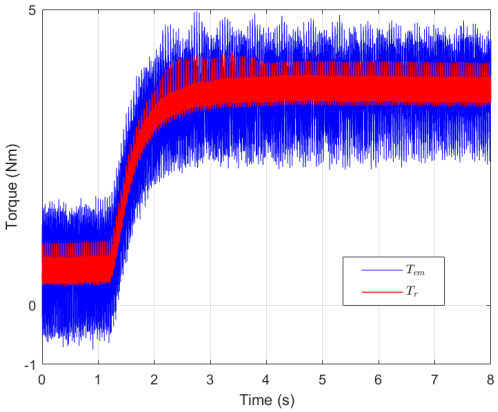

(c) Torque and its reference

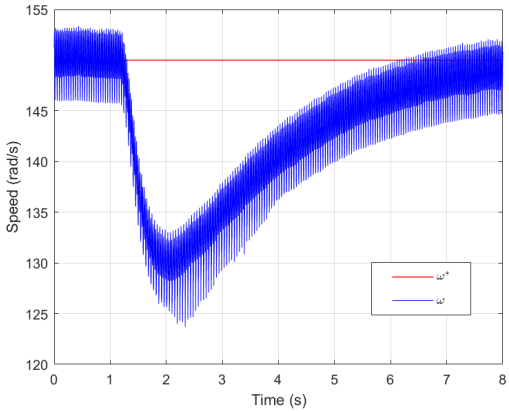

(d) Speed and its reference

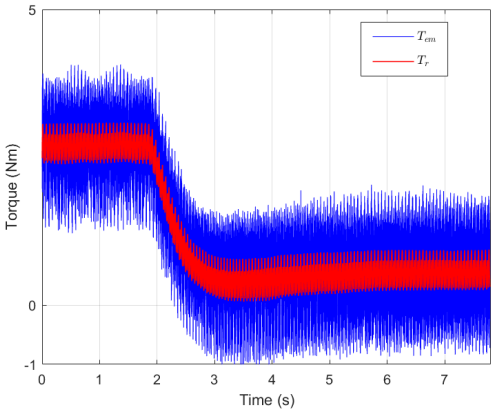

(e) Torque and its reference

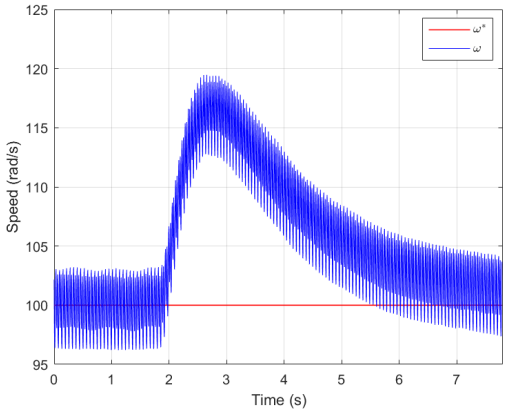

(f) Speed and its reference

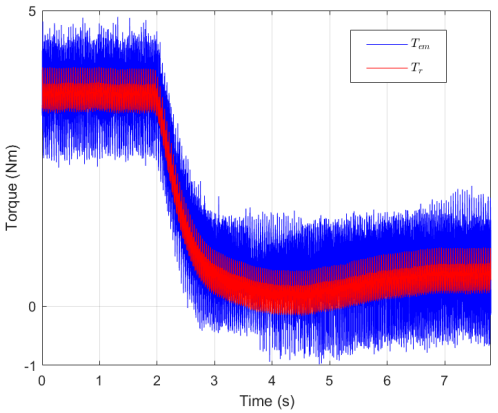

(g) Torque and its reference

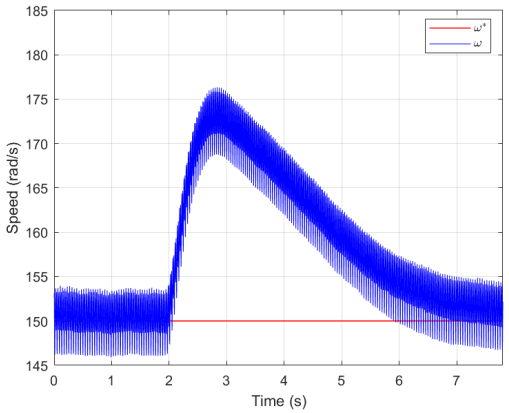

(h) Speed and its reference

Figure 4.14: Torque and speed response of DTC-SVM using two active vectors during load variation

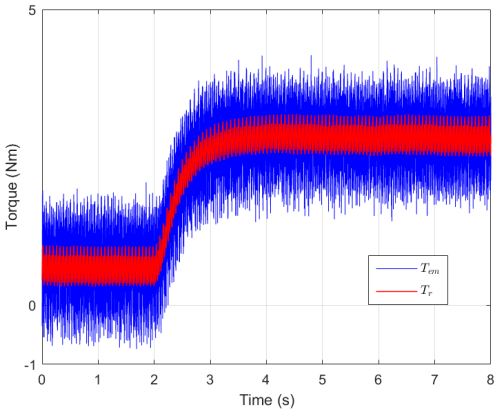

(a) Torque and its reference

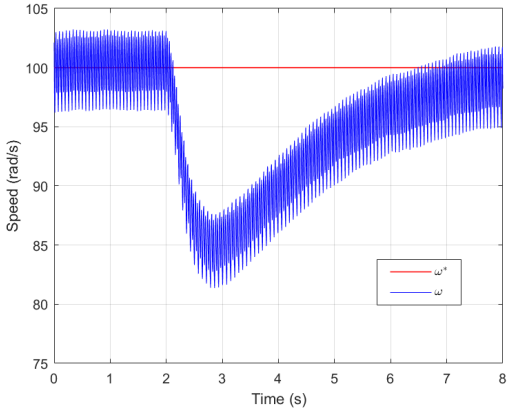

(b) Speed and its reference

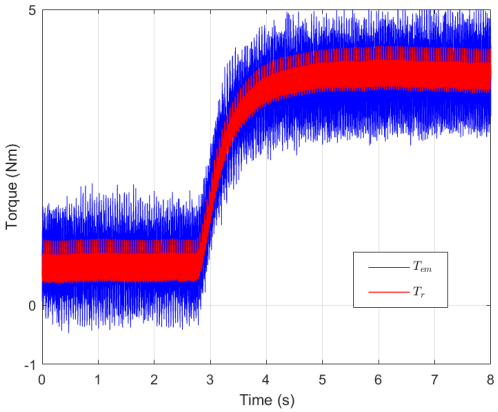

(c) Torque and its reference

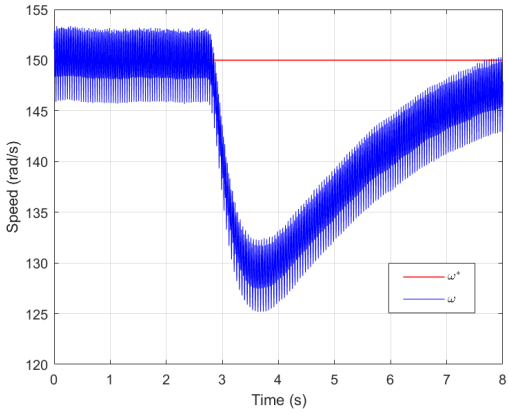

(d) Speed and its reference

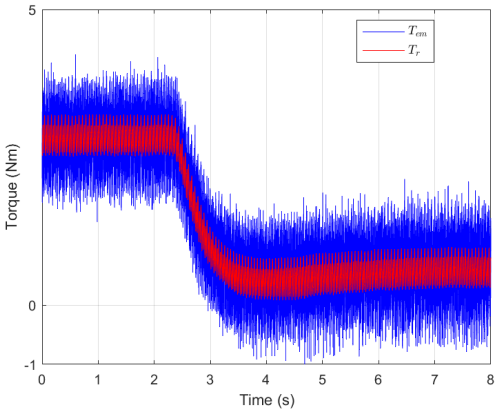

(e) Torque and its reference

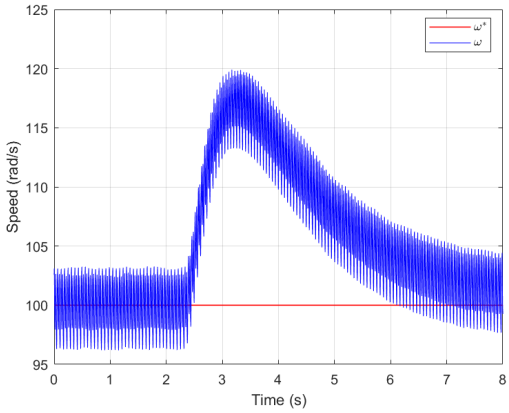

(f) Speed and its reference

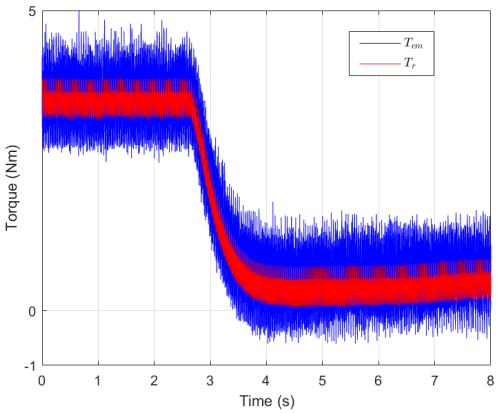

(g) Torque and its reference

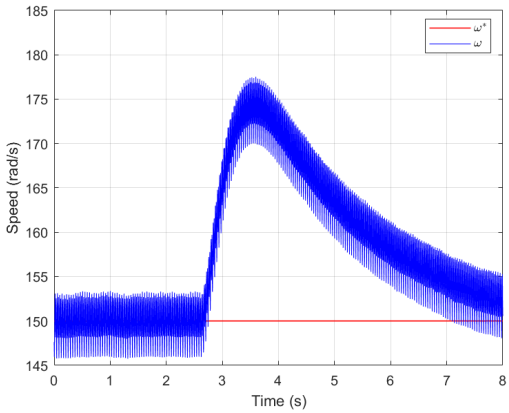

(h) Speed and its reference

Figure 4.15: Torque and speed response of DTC-SVM using four active vectors during load variation

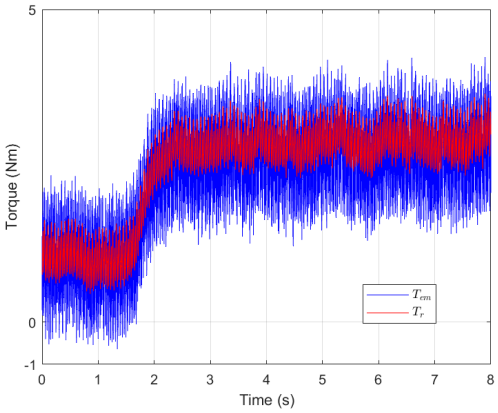

(a) Torque and its reference

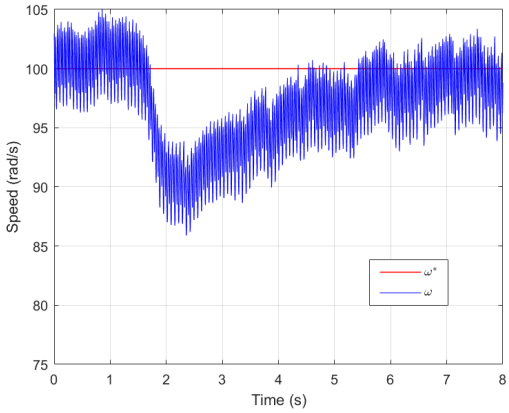

(b) Speed and its reference

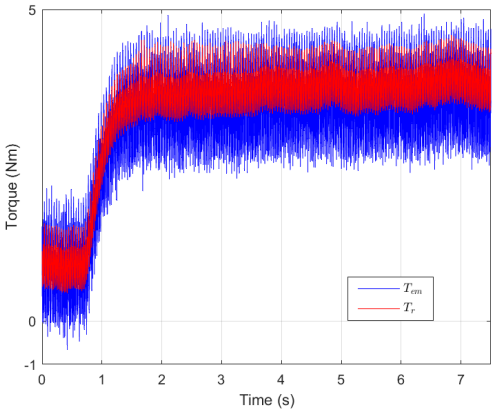

(c) Torque and its reference

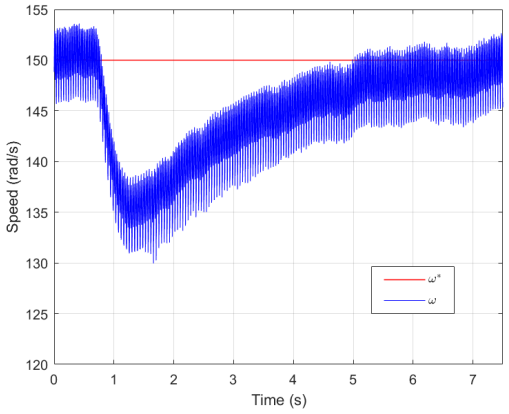

(d) Speed and its reference

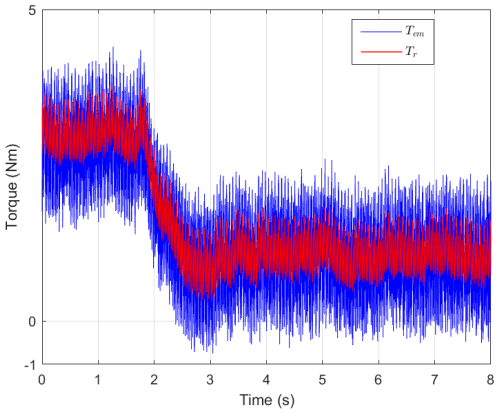

(e) Torque and its reference

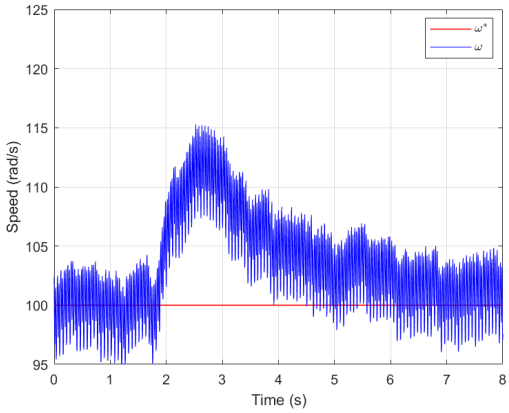

(f) Speed and its reference

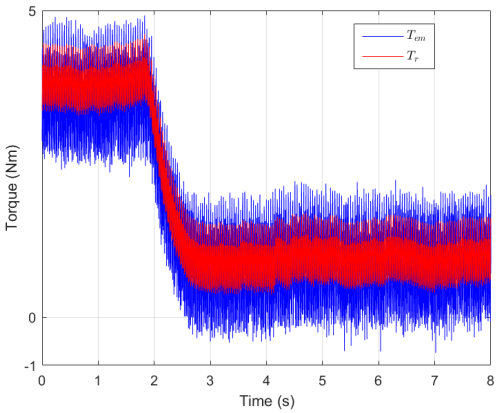

(g) Torque and its reference

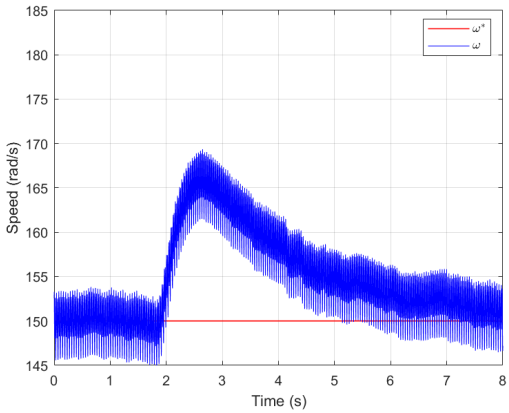

(h) Speed and its reference

Figure 4.16: Torque and speed response of FCS-MPC during load variation

4.3 Experimental Results of DTC under One Open-Phase and Two Non-Adjacent Open-Phase Fault Conditions

4.3.1 One Open Phase

Figures 4.17 presents the electromagnetic variables measured under one open phase fault using DTC strategy. These variables include rotor speed, electromagnetic torque, and stator flux magnitude.

Figure 4.17(a) shows that the actual speed accurately follows the reference. The response times for acceleration are 0.75 s (100 to 150 rad/s), 0.63 s (150 to 200 rad/s), and 0.75 s (200 to 250 rad/s). During deceleration from 250 to 200 rad/s, the system takes 0.68 s without any observable overshoot.

Figure 4.17(b) demonstrates that the torque output follows its reference well. The torque ripple reaches an average of 0.42 Nm at 250 rad/s.

As depicted in Figure 4.17(c), the stator flux magnitude remains close to its reference, with minimal fluctuation. The resulting flux ripple is limited to 0.01 Wb throughout the test.

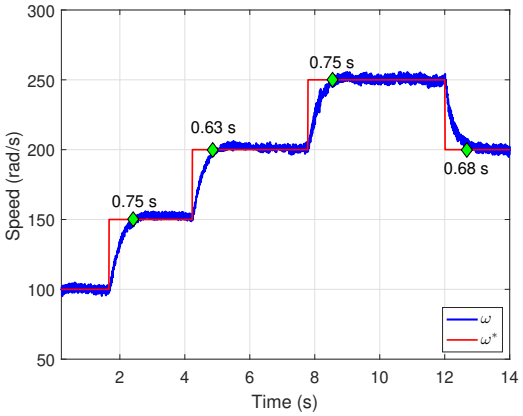

(a) Speed response

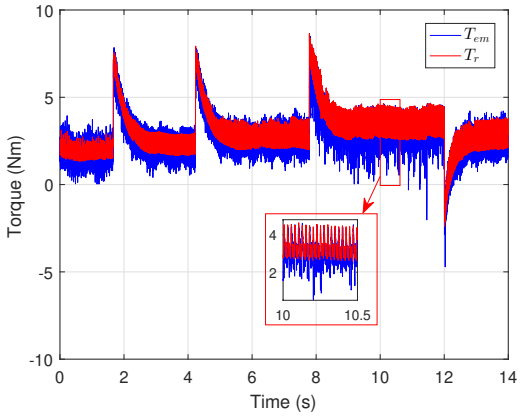

(b) Electromagnetic torque

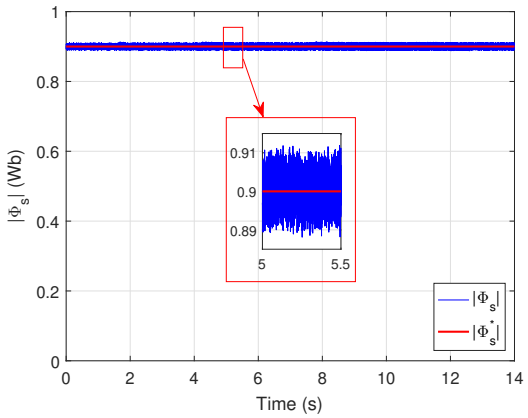

(c) flux magnitude

Figure 4.17: DTC under one open-phase fault (Electromagnetic parameters)

Figure 4.18(a) displays the stator current waveforms. As the speed varies, both the magnitude and frequency of the currents change accordingly. During transients, peak current values reach up to 5.1 A. Finally, Figure 4.18(b) shows the i_x and i_y current components, which reach significant values of 2 A and 3 A, respectively.

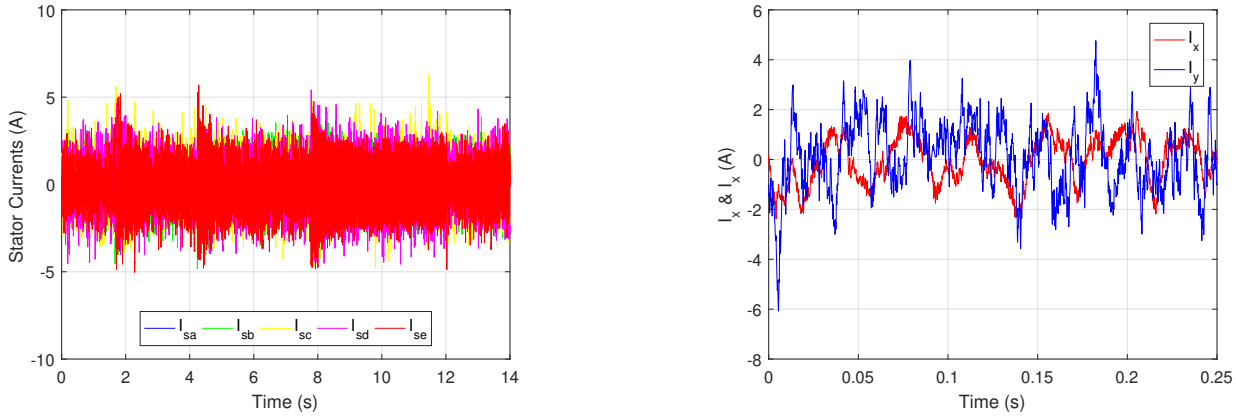

(a) Stator currents

(b) I_x and I_y currents

Figure 4.18: Stator, I_x and I_y currents for DTC under one open-phase fault without adapted modeling

Figures 4.19(a) and 4.19(b) show the stator current waveform and its FFT at a speed of 150 rad/s. The waveform appears significantly distorted, with a Total Harmonic Distortion (THD) of approximately 38.88%. The most prominent harmonic is the third, reaching 21.42% of the fundamental.

Figure 4.19(c) illustrates the inverter output voltage waveform at 150 rad/s. The waveform is periodic but shows considerable variability due to harmonic content. As shown in Figure 4.19(d), the voltage THD reaches 138.51%. The dominant harmonics are the third (14.4%), sixth (12.33%), eighth (11.3%), and thirteenth (12.8%) of the fundamental component.

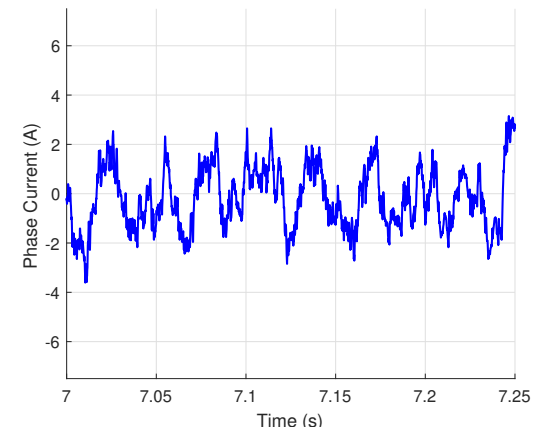

(a) Stator current waveform

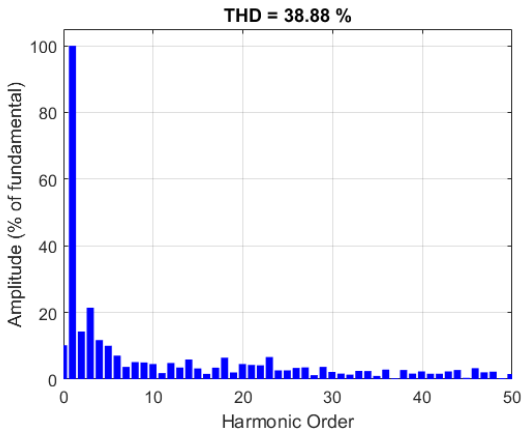

(b) FFT of stator current

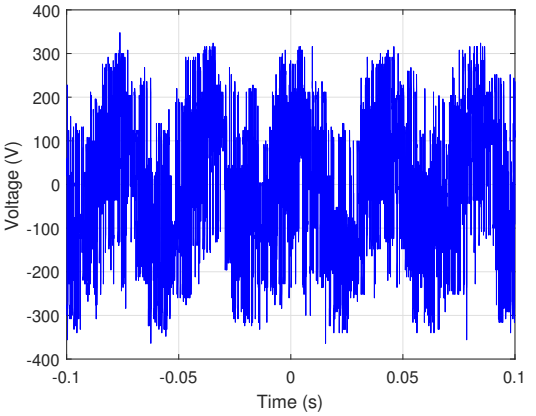

(c) Inverter output voltage

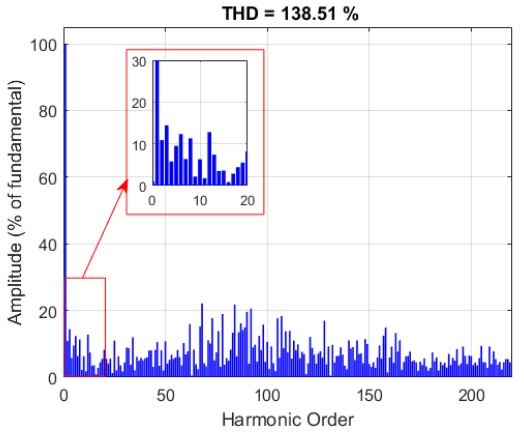

(d) FFT of Inverter output voltage

Figure 4.19: Electric parameters for DTC under one open-phase fault without adapted modeling

4.3.2 Two Open Phases

Figure 4.20 presents the electromagnetic variables measured under two non-adjacent open phase fault using DTC strategy.

Figure 4.20(a) demonstrates that the rotor speed tracks the reference signal accurately in the conducted test, The rotor accelerates within 0.67 s (100 to 150 rad/s), 0.72 s (150 to 200 rad/s), and 0.69 s (200 to 250 rad/s).

As shown in Figure 4.20(b), the electromagnetic torque follows its reference closely. However, a torque ripple averaging 0.453 Nm is observed, which is attributed to the significant phase imbalance introduced by the two open-phase fault.

Figure 4.20(c) reveals that the stator flux magnitude remains close to its reference with minimal fluctuation. The flux ripple reaches up to 0.01 Wb during the tests.

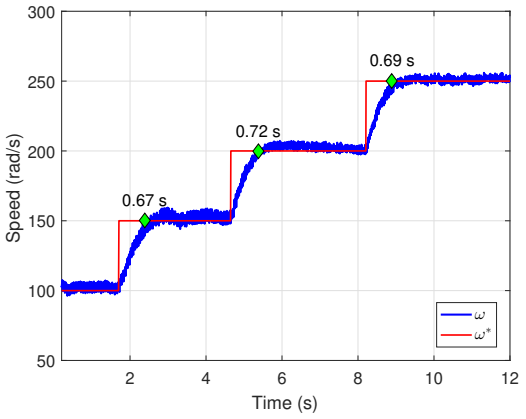

(a) Speed response

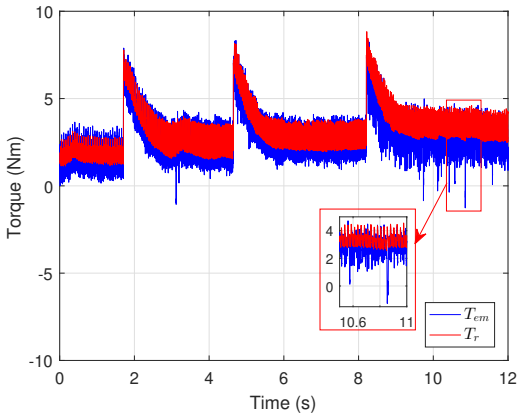

(b) Electromagnetic torque

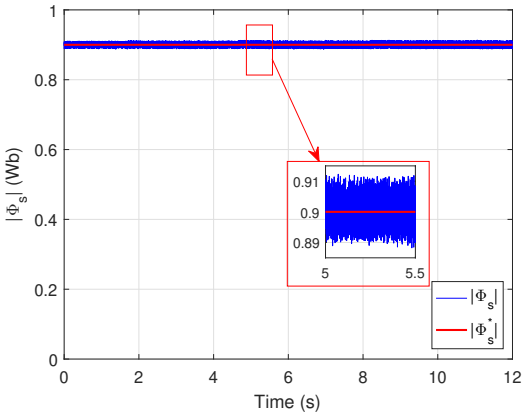

(c) Flux magnitude

Figure 4.20: Electromagnetic parameters for DTC under two open-phases fault

Figures 4.21(a) shows the stator current waveforms. Both current magnitude and frequency vary with speed. During transient operation, the peak current reaches approximately 6 A.

Figure 4.21(b) presents the i_x and i_y current components, which both reach approximately 1.5 A with no apparent phase shift between them. This behavior results from the asymmetrical nature of the machine modeling under the two-phase fault condition.

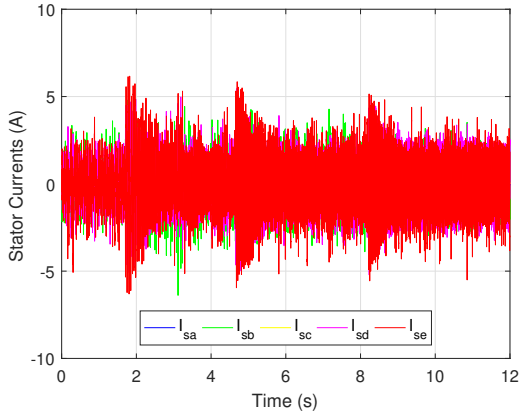

(a) stator currents

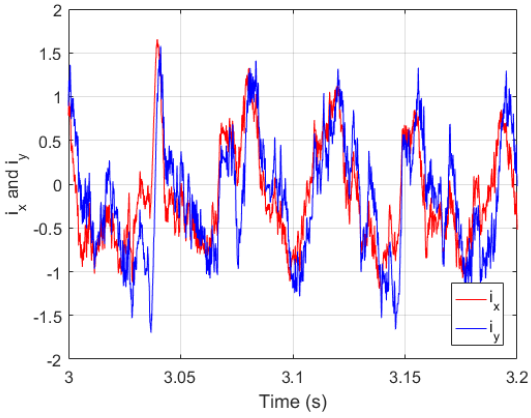

(b) I_x and I_y currents

Figure 4.21: Stator, I_x and I_y currents for DTC under two open-phase fault

Figures 4.22(a) and 4.22(b) display the stator current waveform and its FFT at 150 rad/s. The waveform appears highly distorted with a Total Harmonic Distortion (THD) of approximately 62.95%. The dominant harmonic is the third (33.36% of the fundamental), while both the second and fifth harmonics contribute 27% each.

Figure 4.22(c) shows the inverter output voltage waveform at 150 rad/s. The waveform remains periodic but exhibits increased variability due to a rich harmonic spectrum. As detailed in Figure 4.22(d), the voltage THD reaches 120.48%. The most significant low-order harmonics are the second (17.82%), third (9.8%), and seventh (9.65%). Higher-order components are also present, with amplitudes around 25% of the fundamental, contributing to the substantial waveform distortion.

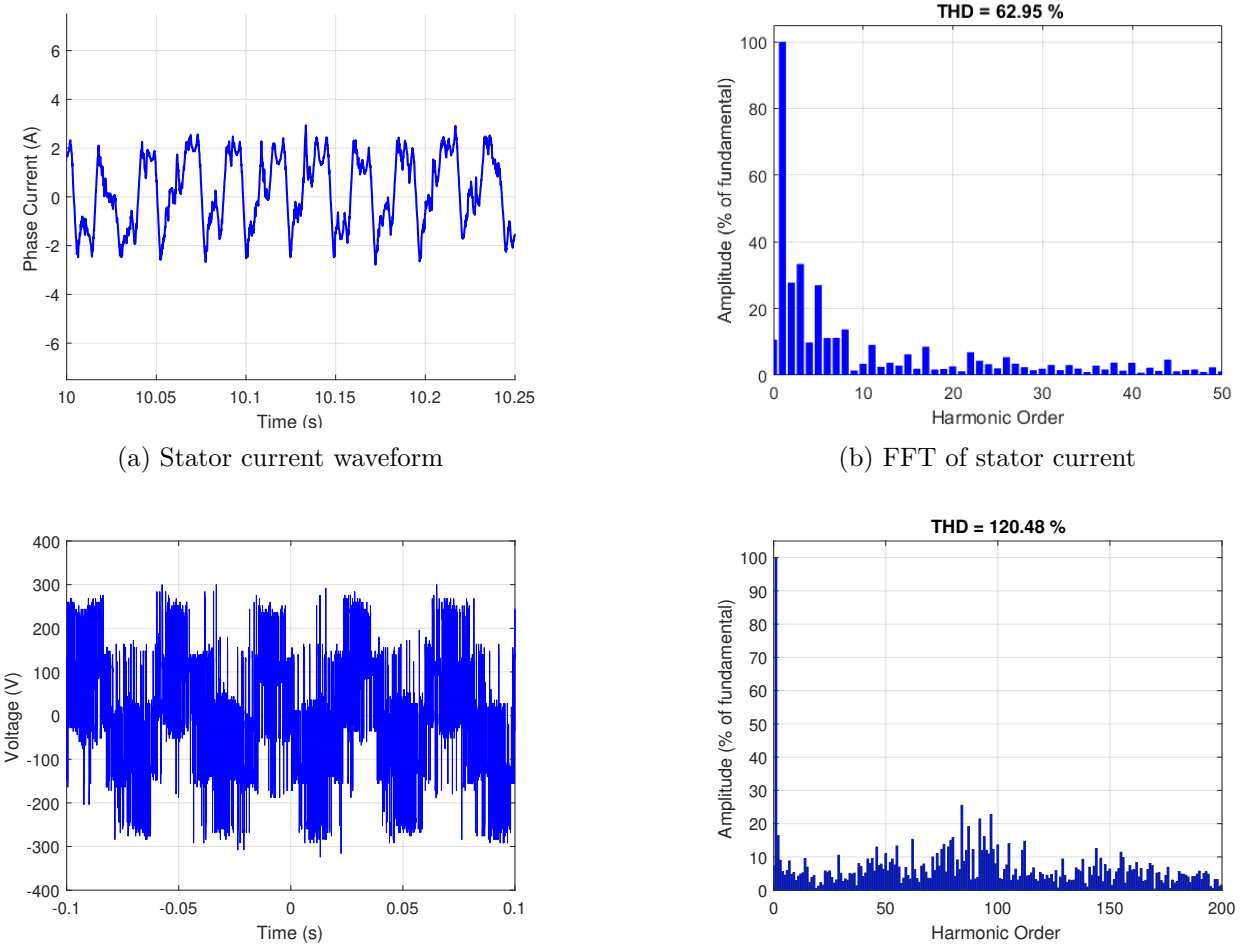

(a) Stator current waveform

(b) FFT of stator current

(c) Inverter output voltage

(d) FFT of inverter output voltage

Figure 4.22: Electric parameters for DTC under two open-phases fault

Despite the occurrence of open-phase faults, the DTC strategy succeeds in maintaining overall control of the system, demonstrating a certain level of **fault tolerance**. The **rotor speed still closely follows its reference** under these fault conditions. The **torque ripple is slightly increased**, especially at high speed, yet still remains within acceptable limits, while the **stator flux ripple remains low**, comparable to the healthy condition.

However, several performance indicators are **noticeably affected** by the severity of the fault. The **stator current distortion** is heavily impacted, with the total harmonic distortion (THD) increasing from **19.58%** in the healthy case to **38.88%** and **62.95%** under one and two-phase faults, respectively. The **peak current** also increases notably with fault severity, from **4.45A** to **5.1A** and **6A**. In addition, the appearance of the i_x and i_y current components,

which reach significant values around **2A**, marks a clear departure from the healthy condition, where these components were practically negligible.

4.4 Experimental Results of DTC-SVM using 2 Active Vectors under One Open-Phase and Two Non-Adjacent Open-Phase Fault Conditions

This section presents the experimental validation of the control strategy based on Direct Torque Control with Space Vector Modulation (DTC-SVM) using two active voltage vectors. Two sets of experimental results are discussed:

- Figures 4.23 to 4.25: Results under a one open-phase fault
- Figures 4.26 to 4.28: Results under a two open-phase fault.

The tests were conducted under a load torque.

4.4.1 One Open Phase

Figure 4.23 presents the mechanical and electromagnetic behavior of the system under a one open-phase fault.

In Figure 4.23(a), the actual rotor speed accurately follows the reference. The response times are 1.15 s (from 50 to 100 rad/s), 1.09 s (from 100 to 150 rad/s), and 1.12 s (from 150 to 100 rad/s), with no overshoot observed.

Figure 4.23(b) shows the electromagnetic torque response, which tracks the reference well, Torque ripple averages approximately 0.3122 Nm.

As seen in Figure 4.23(c), the stator flux magnitude remains close to its reference value with minimal fluctuation, resulting in a flux ripple of up to 0.07 Wb.

The α–β stator flux trajectory, illustrated in Figure 4.23(d), maintains a nearly perfect circular shape, indicating effective flux control.

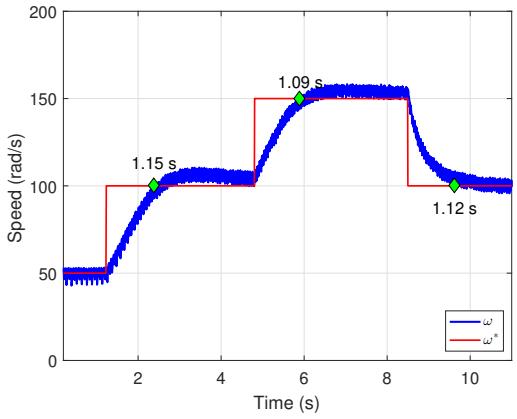

(a) Speed response

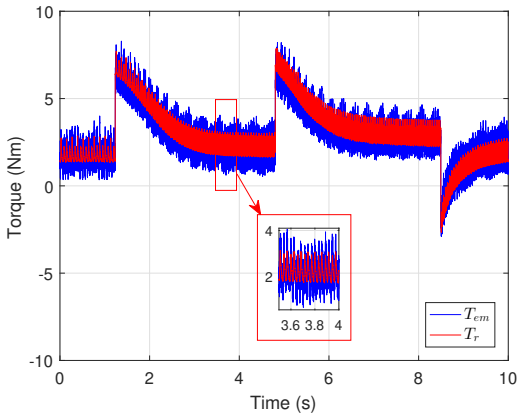

(b) Electromagnetic torque

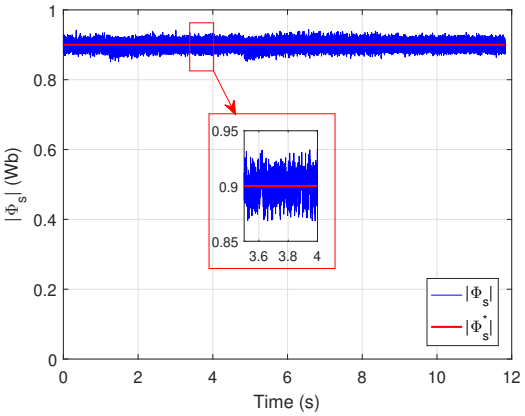

(c) Flux magnitude

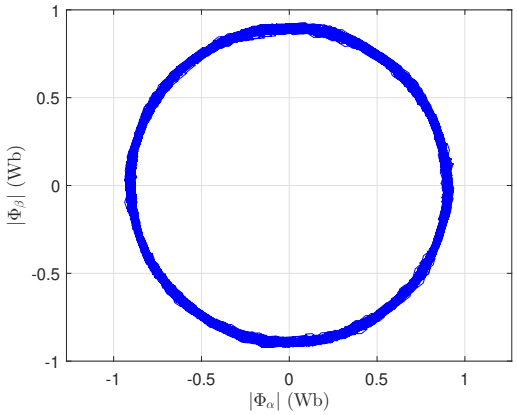

(d) Flux α–β trajectory

Figure 4.23: Electromagnetic parameters for DTC-SVM using two active vectors under one open-phase fault

Figure 4.24(a) shows the stator current waveforms. As speed varies, both the magnitude and frequency of the stator currents vary accordingly. Peak currents reach 5 A during transients. Figure 4.24(b) displays the i_x and i_y current components, which reach peak values of 2 A and 1.3 A, respectively.

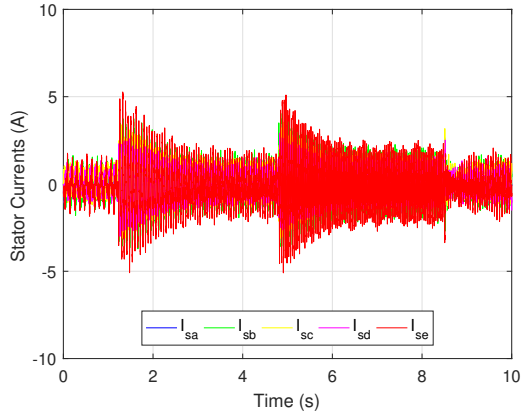

(a) Stator currents

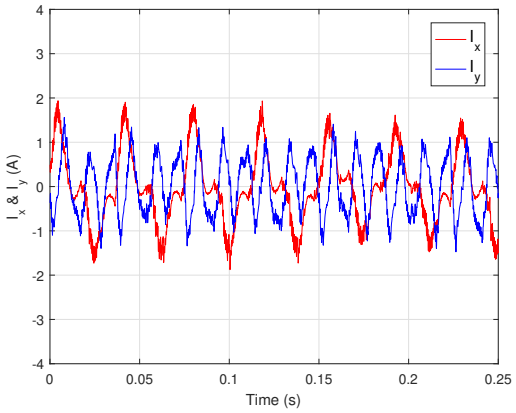

(b) I_x and I_y currents

Figure 4.24: Stator, I_x and I_y currents for DTC-SVM DTC-SVM using two active vectors under one open-phase fault

Figures 4.25(a) and 4.25(b) illustrate the stator current waveform and its FFT at a speed of 150 rad/s. The total harmonic distortion (THD) is approximately 30.78%. The dominant harmonic is the third, contributing around 20% of the fundamental, followed by the second harmonic at approximately 18.9%.

Figure 4.24(c) shows the inverter output voltage waveform at 150 rad/s. The waveform is periodic but significantly distorted due to harmonic content. As seen in Figure 4.37(d), the voltage THD reaches 153.27%. The most prominent harmonic components are the third (31.6%), 79th (74%), and 81st (82.23%) of the fundamental.

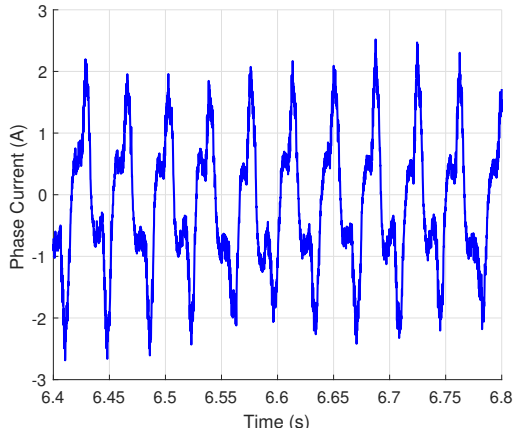

(a) Stator current waveform

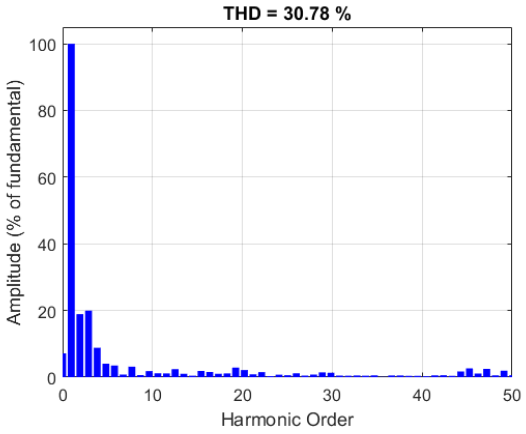

(b) FFT of stator current

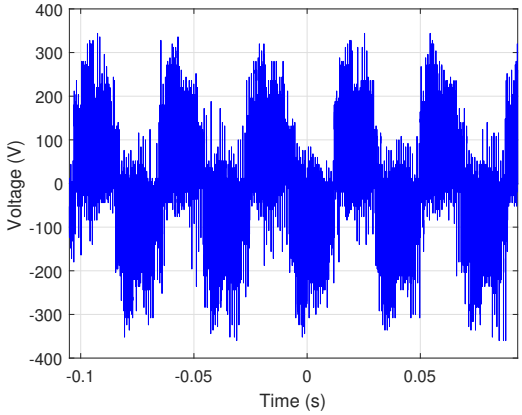

(c) Inverter output voltage

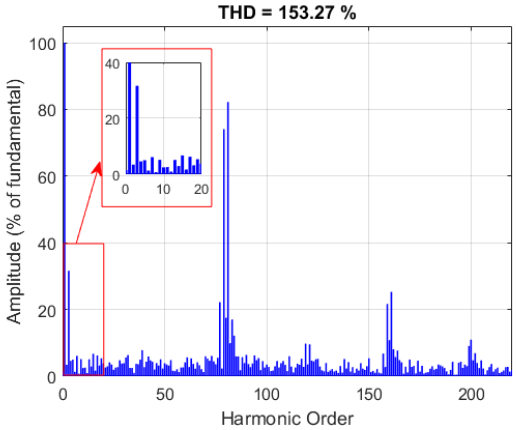

(d) FFT of inverter output voltage

Figure 4.25: Electric parameters for DTC-SVM using two active vectors under one open-phase fault

4.4.2 Two Open Phases

Figure 4.26 presents the mechanical and electromagnetic responses of the system, including speed, torque, and stator flux. The speed increases by step from 100 rad/s to 200 rad/s in 50 rad/s steps, followed by a decrease back to 150 rad/s.

As shown in Figure 4.26(a), the rotor speed tracks the reference closely. The acceleration from 100 rad/s to 150 rad/s occurs in 0.89 s with a slight overshoot of approximately 6.5 rad/s. The subsequent acceleration to 200 rad/s takes 0.68 s, and the deceleration back to 150 rad/s takes 1.73 s.

Figure 4.26(b) illustrates the torque behavior, which follows the reference well. The torque ripple observed during the test averages around 0.33 N · m.

Figure 4.26(c) shows the stator flux magnitude, which remains close to the reference value with minor fluctuations, resulting in a flux ripple of up to 0.08 Wb.

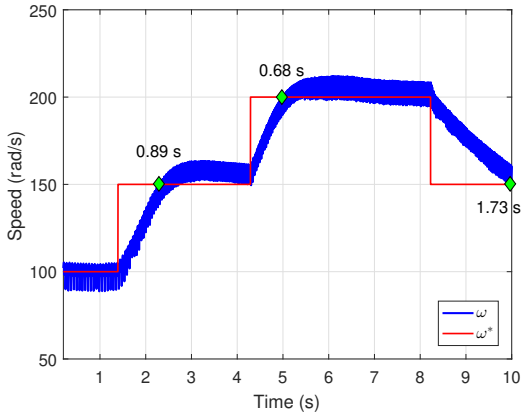

(a) Speed response

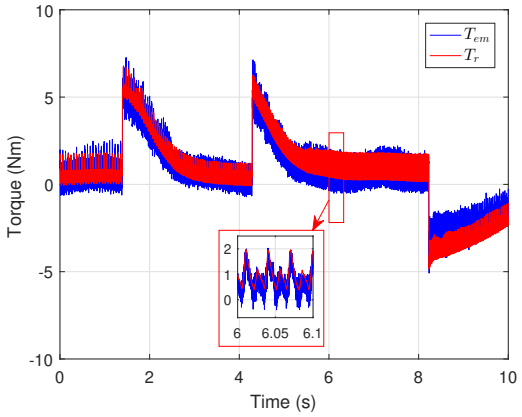

(b) Electromagnetic torque

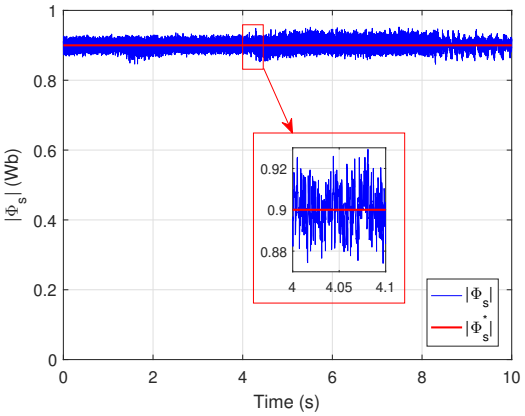

(c) Flux magnitude

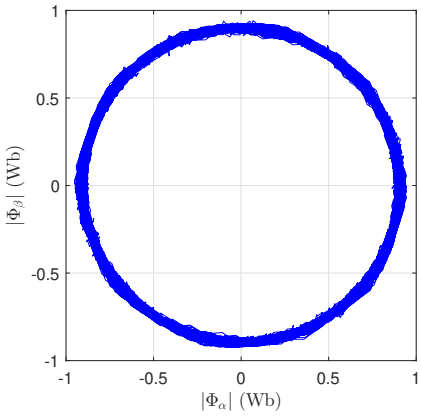

(d) Flux α-β trajectory

Figure 4.26: Electromagnetic parameters for DTC-SVM DTC-SVM using two active vectors under two open-phase fault

The α-β stator flux trajectory shown in Figure 4.26(d) exhibits an ideally circular shape, indicating effective flux control despite the fault condition.

Figure 4.27(a) also displays the stator current waveforms. As speed varies, both the amplitude and frequency of the currents change accordingly. Peak current values reach approximately 5 A during transients. Figure 4.27(b) shows the i_x and i_y current components, which attain values of approximately 0.9 A.

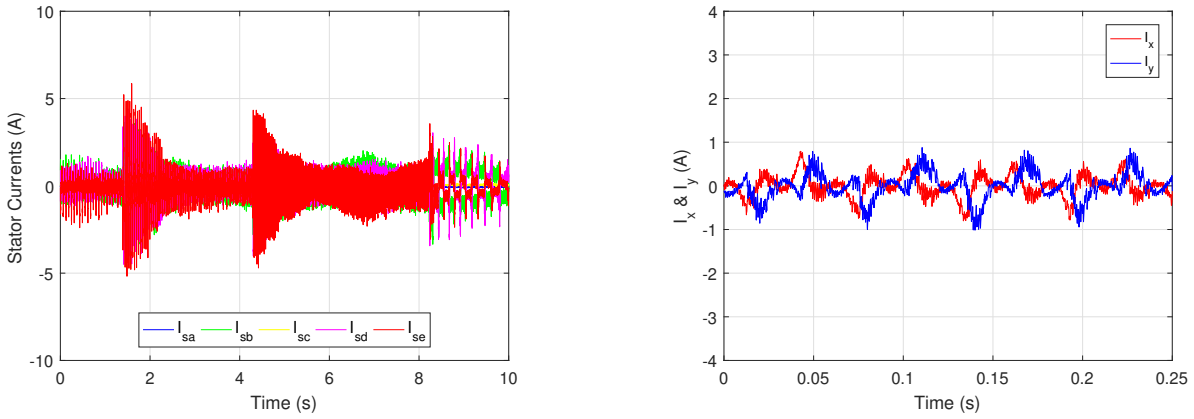

(a) Stator currents

(b) I_x and I_y currents

Figure 4.27: Stator, i_x and i_y currents for DTC-SVM using two active vectors under two open-phase fault

Figures 4.28(a) and 4.28(b) present the stator current waveform and its FFT at a speed of 150 rad/s. The waveform appears periodic but highly distorted, with a Total Harmonic Distortion (THD) of approximately 49.58%. The third harmonic is the most dominant, contributing around 40% of the fundamental. Additional harmonic content is observed around the 60th order, reaching about 15% of the fundamental.

Figure 4.28(c) displays the inverter output voltage waveform at 150 rad/s, which is periodic but significantly distorted due to high harmonic content. As seen in Figure 4.28(d), the voltage THD reaches 162.61%. The third harmonic is the most notable among the lower-order components, contributing 16.6% of the fundamental. High-order harmonics are also present with substantial amplitudes, particularly one reaching 81.16% of the fundamental, which explains the severely distorted voltage waveform.

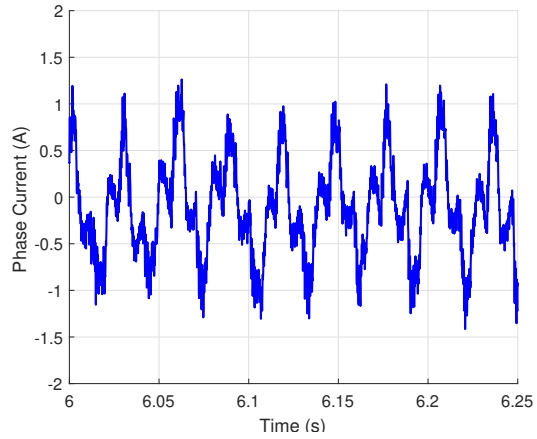

(a) Stator current waveform

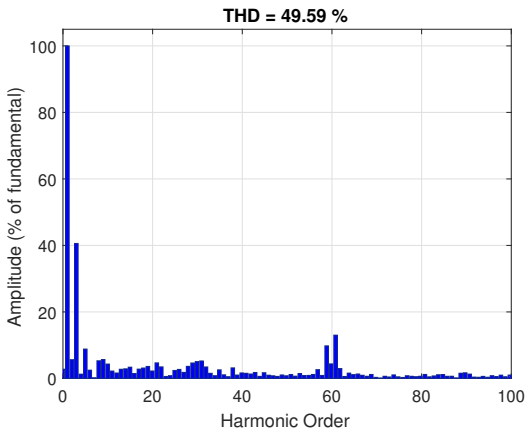

(b) FFT of stator current

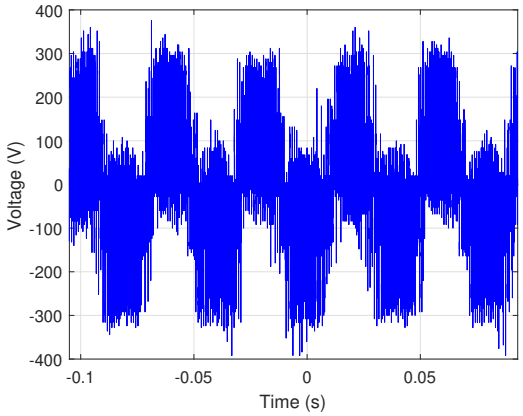

(c) Inverter output voltage

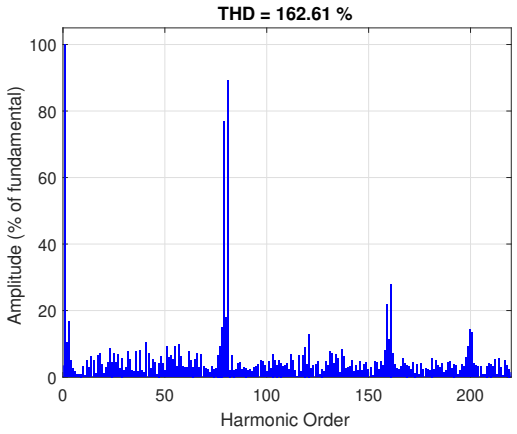

(d) FFT of inverter output voltage

Figure 4.28: Electric parameters for DTC-SVM using two active vectors under two open-phase fault

Despite the occurrence of open-phase faults, the DTC-SVM strategy using two vectors strategy succeeds in maintaining overall control of the system, demonstrating a certain level of **fault tolerance**. The **rotor speed still closely follows its reference** under these fault conditions. The **torque ripple is slightly increased**, especially at high speed, yet still remains within acceptable limits, while the **stator flux ripple remains low**, comparable to the healthy condition.

However, several performance indicators are **noticeably affected** by the severity of the fault. The **stator current distortion** is heavily impacted, with the total harmonic distortion (THD) increasing from **37.48%** in the healthy case to **49.58%** under two-phase faults. The **peak current** also increases notably with fault severity, from **2.85A** to **5.1A**. In addition, the appearance of the i_x and i_y current components, which reach significant values around **2A**, marks a clear departure from the healthy condition, where these components were practically negligible.

4.5 Experimental Results of DTC-SVM using 4 Active Vectors under One Open-Phase and Two Non-Adjacent Open-Phase Fault Conditions

This section presents the experimental results of the Direct Torque Control with Space Vector Modulation using four active vectors (DTC-SVM4V). Two sets of results are included:

- Figures 4.29 to 4.31 correspond to a one open-phase fault.
- Figures 4.32 to 4.34 correspond to a two open-phase fault scenario.

4.5.1 One Open Phase

Figure 4.29 shows the system's mechanical and electromagnetic variables, including speed, torque, and stator flux.

Figure 4.29(a) shows that the actual rotor speed accurately tracks the reference. The response time is 1.15 s for acceleration from 50 to 100 rad/s, and 1.60 s from 100 to 150 rad/s, no overshoot is observed in the test.

Figure 4.29(b) confirms that the electromagnetic torque closely follows its reference, with an average torque ripple of 0.2689 Nm.

As illustrated in Figure 4.29(c), the stator flux magnitude fluctuates slightly around its reference, particularly at 150 rad/s. The flux ripple reaches up to 0.0083 Wb.

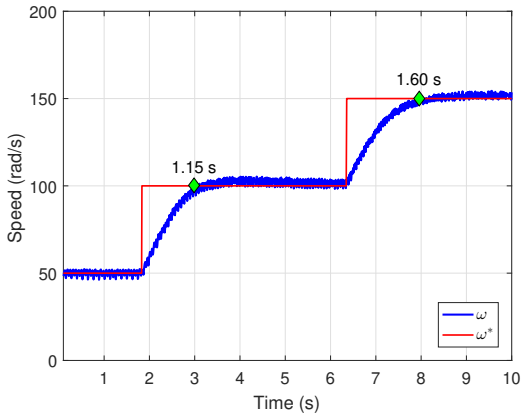

(a) Speed response

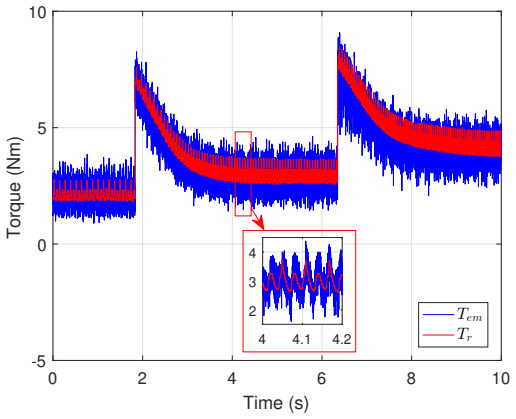

(b) Electromagnetic torque

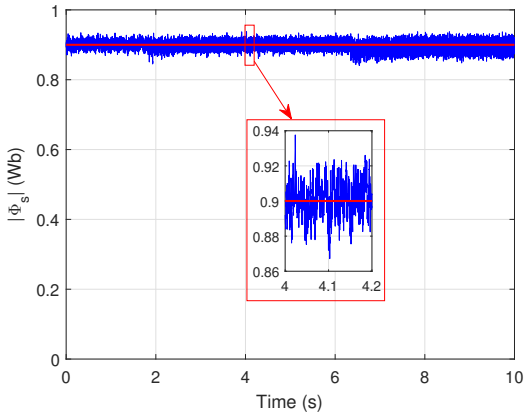

(c) Flux magnitude

Figure 4.29: Electromagnetic parameters for DTC-SVM4V under one open-phase fault without adapted modeling

Figure 4.30(a) presents the stator current waveforms. As the speed varies, both the magnitude and frequency of the stator currents change. During transients, peak current values reach approximately 4,7 A.

Figure 4.30(b)presents the i_x and i_y current components, with respective amplitudes of 2.5 A and 1.5 A.

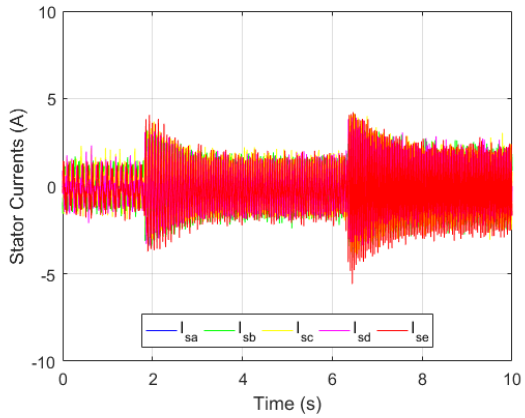

(a) Stator current waveforms

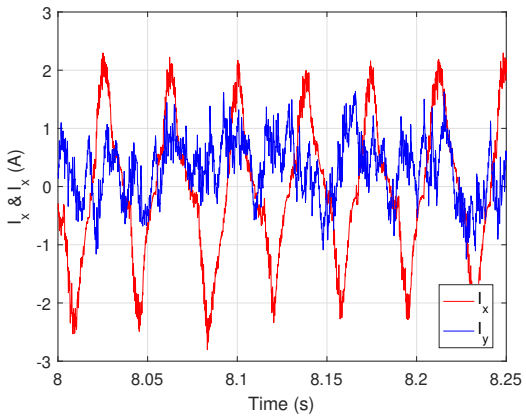

(b) I_x and I_y

Figure 4.30: Stator, I_x and I_y currents for DTC-SVM4V under one open-phase fault without adapted modeling

Figure 4.31(a) and 4.31(b) display the stator current waveform and its FFT at a speed of 150 rad/s. The waveform appears periodic total harmonic distortion (THD) of 23.24%. The third and seventh harmonics are the most dominant, reaching about 10.5% of the fundamental. The second, fifth, and ninth harmonics are also present but remain below 10% of the fundamental.

Figure 4.31(c) shows the inverter output voltage waveform at 100 rad/s, which is periodic but highly distorted due to significant harmonic content. Figure 4.31(d) reveals that the voltage THD reaches approximately 194.78%. The harmonic spectrum is dominated by high-order harmonics (above the 100th), which reach up to 80% of the fundamental. Among the lower-order harmonics, the second is the most significant at 11% of the fundamental.

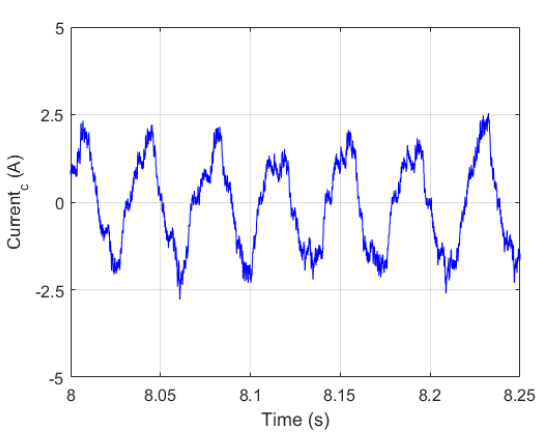

(a) Stator current waveform

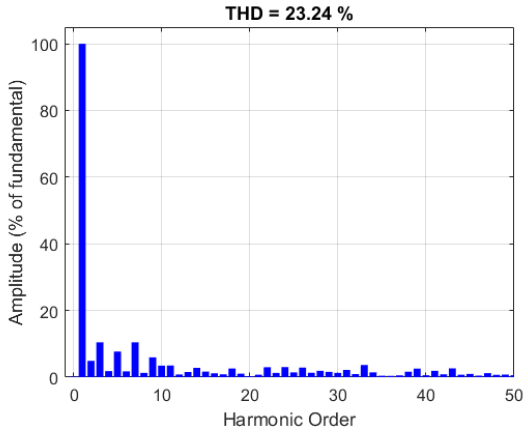

(b) FFT of stator current

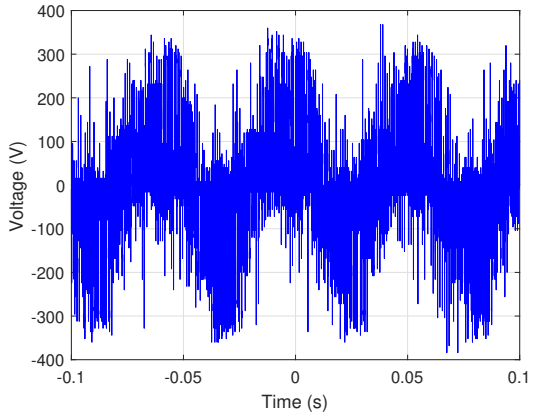

(c) Inverter output voltage

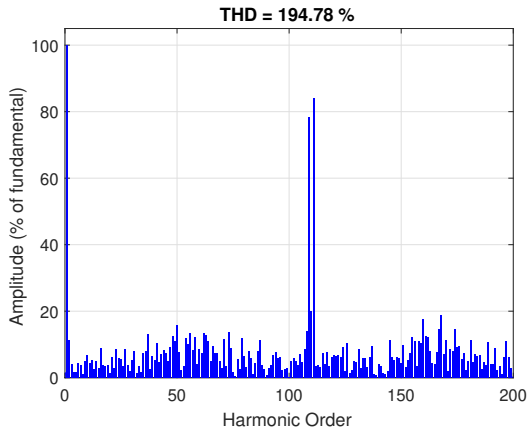

(d) FFT of inverter output voltage

Figure 4.31: Electric parameters for DTC-SVM 4 vectors under one open-phase fault without adapted modeling.

4.5.2 Two Open Phases

Figure 4.32 presents the mechanical and electromagnetic behavior of the system, including rotor speed, electromagnetic torque, and stator flux magnitude.

Figure 4.32(a) shows that the rotor speed accurately follows the reference. The acceleration response times are 1.18 s (from 150 to 200 rad/s) and 1.21 s (from 200 to 250 rad/s), with no overshoot observed.

Figure 4.32(b) demonstrates that the electromagnetic torque closely follows the reference.

The average torque ripple observed is approximately 0.2881 Nm.

As illustrated in Figure 4.32(c), the stator flux magnitude remains close to its reference with minimal fluctuation. The resulting flux ripple reaches up to 0.01 Wb.

Figures 4.32(d) displays the α–β stator flux trajectory, which maintain a nearly ideal circular shape.

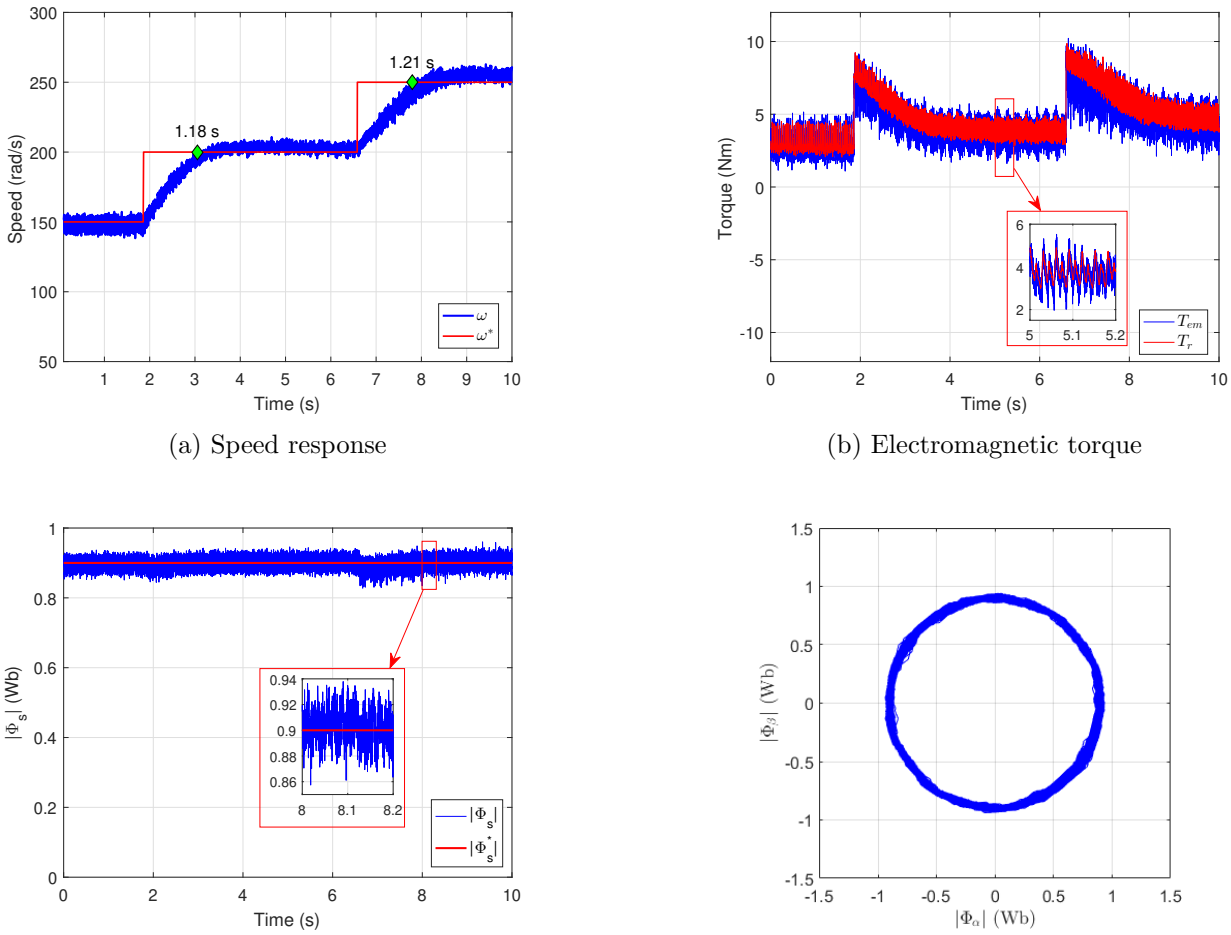

(a) Speed response

(b) Electromagnetic torque

(c) Flux magnitude

(d) Flux α-β trajectory

Figure 4.32: Electromagnetic parameters for DTC-SVM4V under two open-phase fault without adapted modeling

Figures 4.33(a) presents the stator current waveforms. As the speed increases, both the magnitude and frequency of the currents vary accordingly. During transient conditions, peak stator current values reach up to 5 A.

Figure 4.33(b) presents the i_x and i_y current components, which reach peak values of approximately 2 A and 2.5 A, respectively.

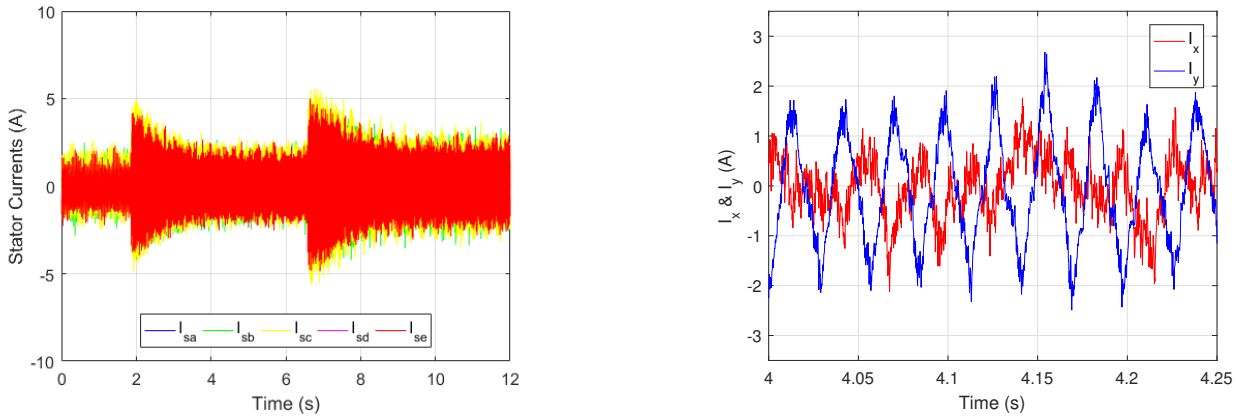

(a) Stator currents

(b) I_x and I_y currents

Figure 4.33: Stator, I_x and I_y currents for DTC-SVM4V under two open-phase fault without adapted modeling

Figures 4.34(a) and 4.34(b) illustrate the current waveform and its FFT at 150 rad/s. The Total Harmonic Distortion (THD) is approximately 26.04%. The most prominent harmonics are the second and the third, contributing approximately 17.9% and 13.1% of the fundamental, respectively.

Figure 4.33(c) shows the inverter output voltage waveform at 150 rad/s. The waveform is periodic but exhibits significant harmonic content. As shown in Figure 4.33(d), the voltage THD reaches 169.57%. The dominant low-order harmonic is the fourth, reaching approximately 14% of the fundamental. Higher-order harmonics (above the 100th order) are also present and can reach up to 78% of the fundamental, which explains the distorted voltage waveform.

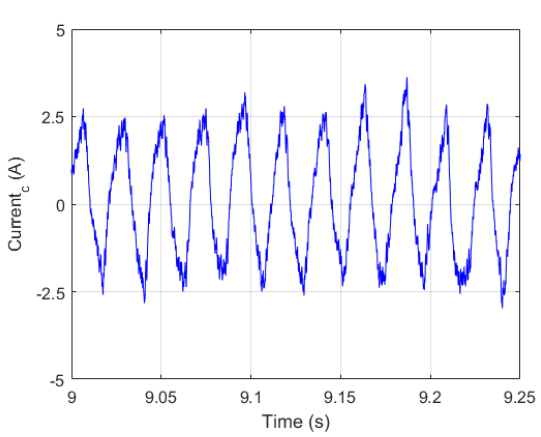

(a) Stator current waveform

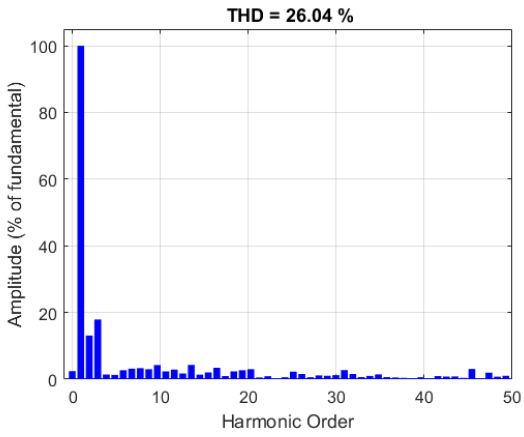

(b) FFT of stator current

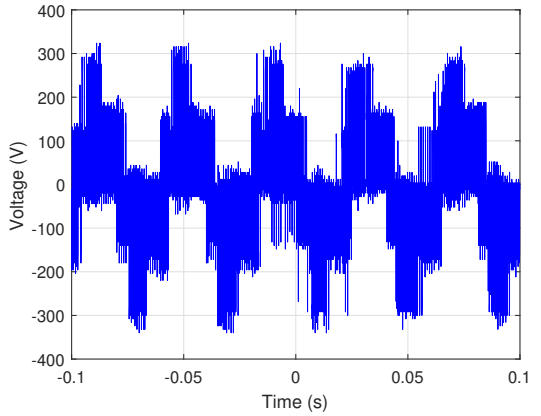

(c) Inverter output voltage

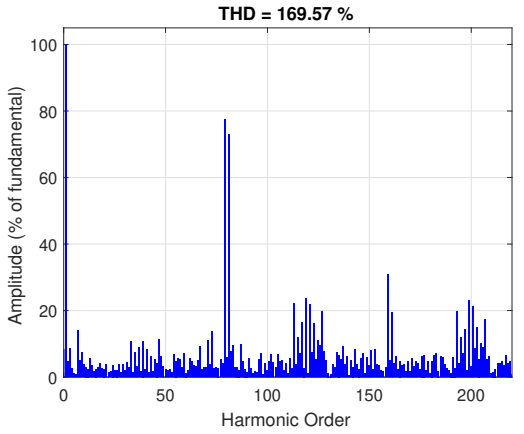

(d) FFT of inverter output voltage

Figure 4.34: Electric parameters for DTC-SVM 4 vectors under two open-phase fault without adapted modeling

Despite the occurrence of open-phase faults, the DTC-SVM 4 vectors strategy succeeds in maintaining overall control of the system, demonstrating a certain level of **fault tolerance**. The **rotor speed still closely follows its reference** under these fault conditions. The **torque ripple is slightly increased**, especially at high speed, yet still remains within acceptable limits, while the **stator flux ripple remains low**, comparable to the healthy condition.

However, several performance indicators are **noticeably affected** by the severity of the fault. The **stator current distortion** is heavily impacted, with the total harmonic distortion (THD) increasing from **12.44%** in the healthy case to **23.24%** and **26.04%** under one and two-phase faults, respectively. The **peak current** also increases notably with fault severity, from **2.93A** to **4.7A** and **5A**. In addition, the appearance of the i_x and i_y current components, which reach significant values around **2.5A**, marks a clear departure from the healthy condition, where these components were practically negligible.

4.6 Experimental Results of FCS-MPC under One Open-Phase and Two Non-Adjacent Open-Phase Fault Conditions

In this section, the experimental results is obtained using the FCS-MPC strategy under different fault conditions.

Figures 4.35 to 4.37 correspond to a one open-phase fault.

Figures 4.38 to 4.40 correspond to a two open-phase fault scenario.

Machine tests were performed with a load torque.

4.6.1 One Open Phase

Figure 4.35 presents the mechanical and electromagnetic variables recorded during experimental testing, including speed, torque, and stator flux. The speed referance increases in 50 rad/s steps from 100 rad/s to 200 rad/s, then decreases to 150 rad/s.

Figure 4.35(a) shows that the actual speed closely follows the reference. Acceleration from 100 to 150 rad/s takes 0.77 s, and from 150 to 200 rad/s takes 0.85 s. The deceleration from 200 to 150 rad/s occurs within 0.75 s, with no overshoot.

In Figure 4.35(b), the torque output follows its reference accurately. The average torque ripple reaches approximately 0.4576 Nm, primarily due to the significant phase shift caused by the open-phase fault.

Figure 4.35(c) demonstrates that the stator flux magnitude remains close to the reference, exhibiting minimal fluctuations. The resulting flux ripple does not exceed 0.009 Wb.

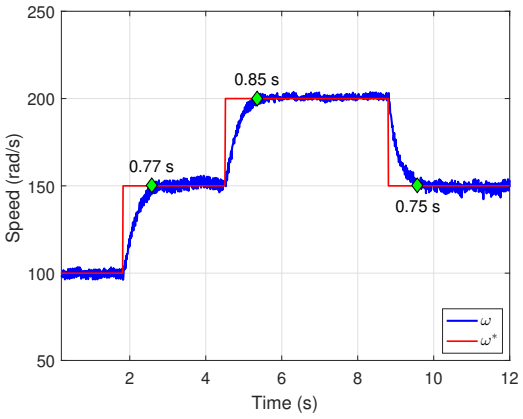

(a) Speed response

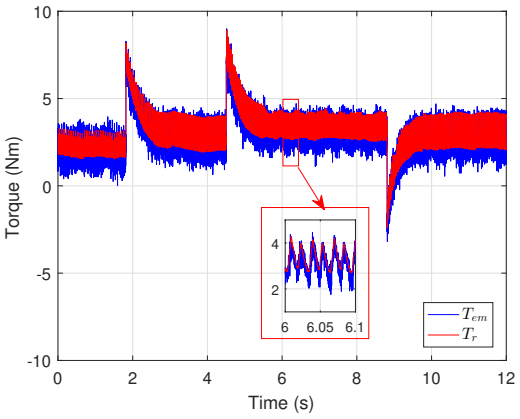

(b) Electromagnetic torque

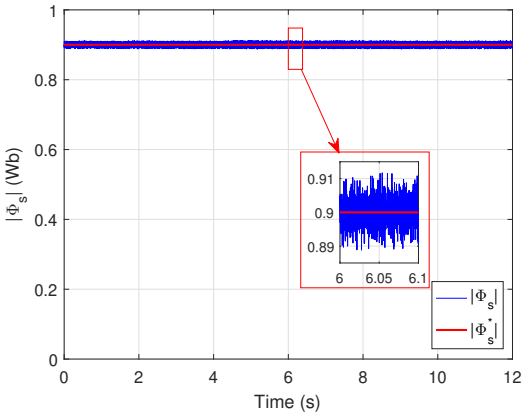

(c) flux magnitude

Figure 4.35: Electromagnetic parameters for FCS-MPC under one open-phase fault

Figure 4.36(a) illustrates the stator current waveforms. As speed changes, both the magnitude and frequency of the currents vary. During transients, the peak current reaches up to 5.2 A. Figure 4.36(b)shows the i_x and i_y current components, which reach values of 1 A and 2 A, respectively. These elevated values result from the asymmetrical behavior of the machine under the one-phase open fault condition.

Figures 4.37(a) and 4.37(b) present the stator current waveform and its corresponding FFT at a speed of 150 rad/s. The total harmonic distortion (THD) is estimated at 32.84%. The most dominant harmonic components include the third and seventh harmonics, each accounting for around 15% of the fundamental. The fourth harmonic contributes approximately 11.85%, while the second, sixth, and ninth harmonics remain below 10%.

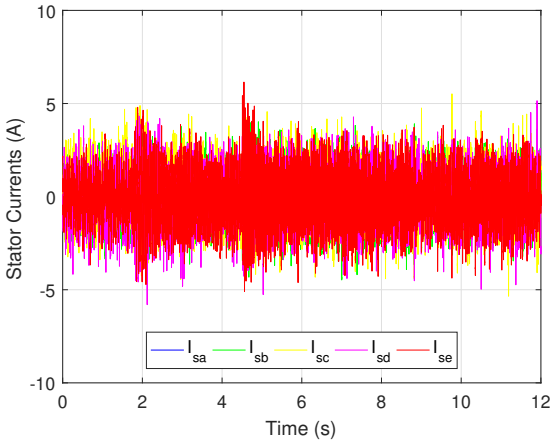

(a) Stator currents

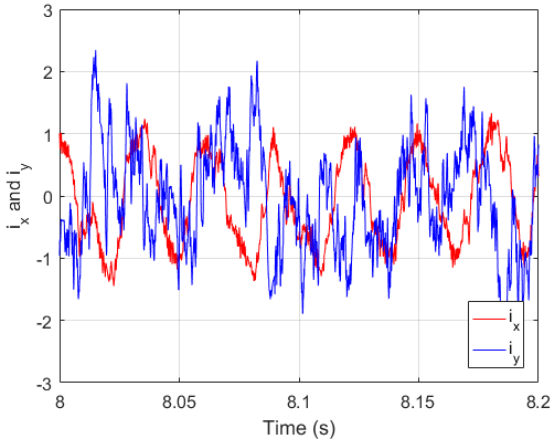

(b) I_x and I_y currents

Figure 4.36: Stator, I_x and I_y currents for FCS-MPC under one open-phase fault

Figure 4.37(c) shows the inverter output voltage at 100 rad/s. Although the waveform is periodic, it exhibits significant variability and high harmonic content.

As shown in Figure 4.37(d), the THD reaches 158.60%. The major contributing harmonics are the second (16.75%), third (17.26%), 4th (11.7%), and 6th (9.36%) of the fundamental.

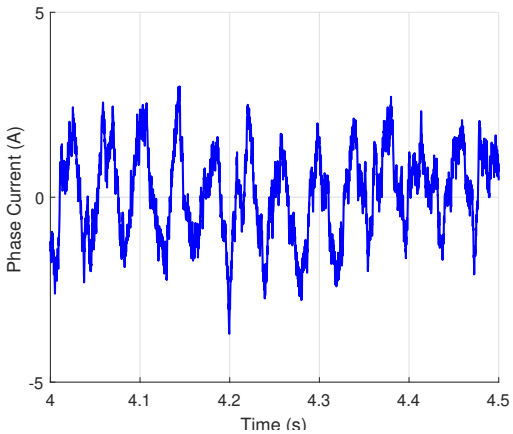

(a) Stator current waveform

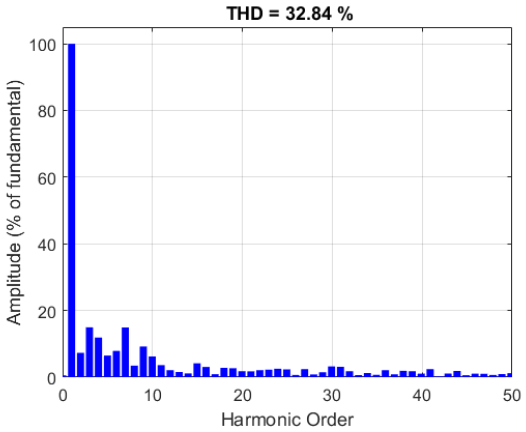

(b) FFT of stator current

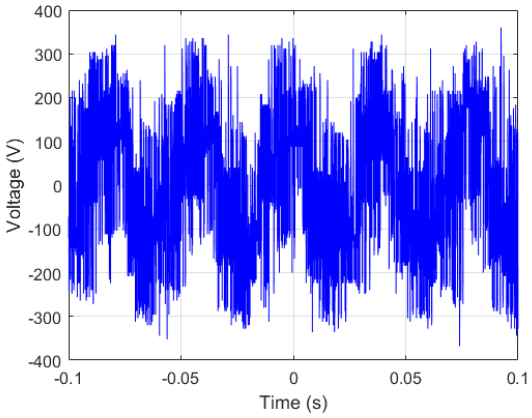

(c) Inverter output voltage

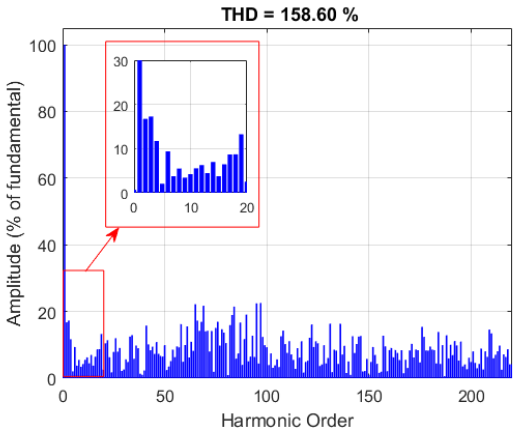

(d) FFT of inverter output voltage

Figure 4.37: Electrical parameters for FCS-MPC under one open-phase fault

4.6.2 Two Open Phases

This test was performed under a two-phase open fault condition, without an adapted machine model. Figure 4.38 presents the mechanical and electromagnetic variables measured during testing, including rotor speed, electromagnetic torque, and stator flux. The same speed reference used in the simulations were applied: the speed was decreased from 250 rad/s to 150 rad/s in steps of 50 rad/s. Figure 4.38(a) shows that the actual speed accurately follows the reference. The acceleration from 100 to 150 rad/s occurs in 0.87 s, and from 150 to 200 rad/s in 0.82 s, with no overshoot observed.

In Figure 4.38(b), the torque response remains closely aligned with its reference throughout both tests. The average torque ripple is approximately 0.4733 Nm, attributed to the significant phase shift induced by the two-phase open fault.

As shown in Figure 4.38(c), the stator flux magnitude remains close to its reference, with only minor fluctuations. The resulting flux ripple does not exceed 0.011 Wb.

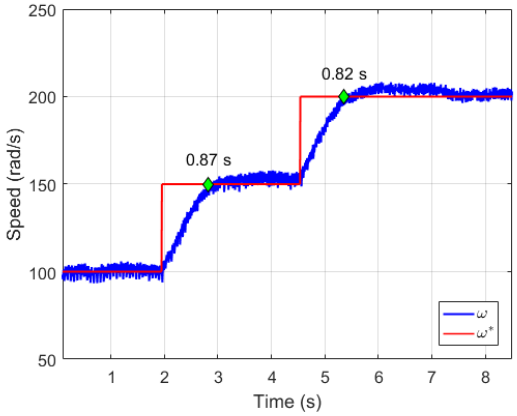

(a) Speed response

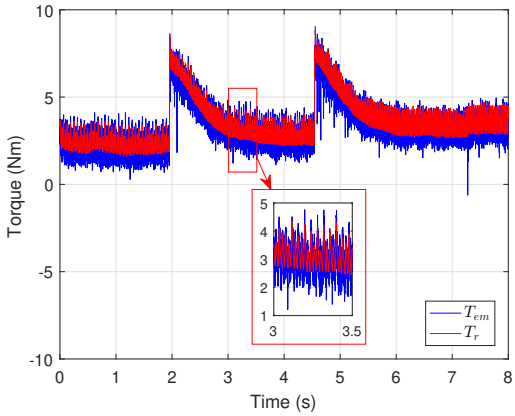

(b) Electromagnetic torque

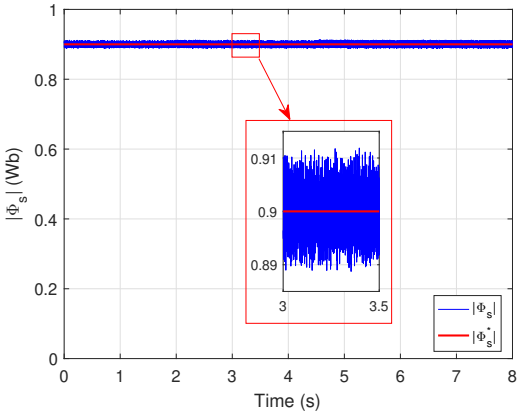

(c) Flux magnitude

Figure 4.38: Electromagnetic parameters for FCS-MPC under two open-phase faults

Figure 4.39(a) displays the stator current waveforms of the conducted test, respectively. As the rotor speed varies, both the amplitude and frequency of the stator currents change accordingly. During transients, peak currents reach up to 7 A. Figure 4.39(b) shows the i_x and i_y current components, which reach 1.5 A with no observable phase shift between them. This behavior is attributed to the asymmetrical operation of the machine under the two-phase open fault condition, combined with the lack of an adapted model.

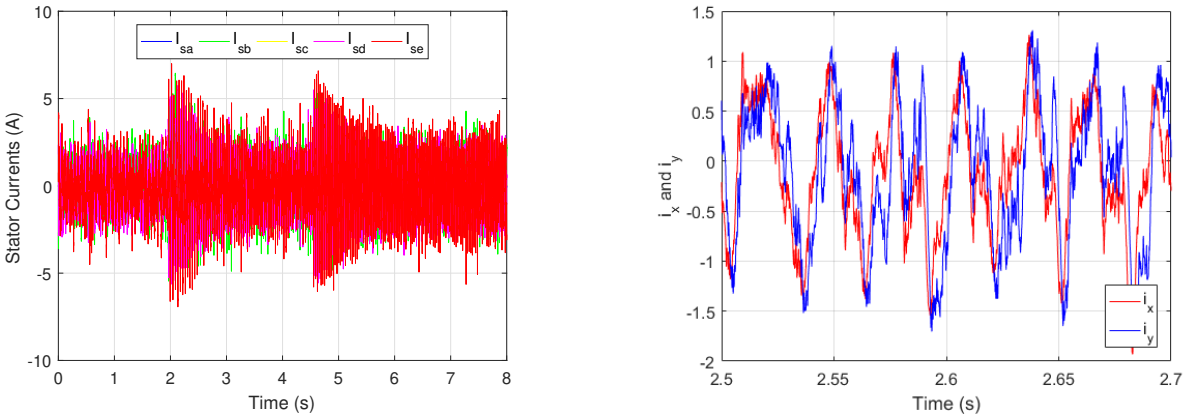

(a) Stator currents

(b) I_x and I_y currents

Figure 4.39: Stator, I_x and I_y currents for FCS-MPC under two open-phase fault

Figures 4.40(a) and 4.40(b) illustrate the stator current waveform and its corresponding FFT at a speed of 150 rad/s. The total harmonic distortion (THD) is estimated at 35.65%. The most dominant harmonic components include the third and fourth harmonics, each contributing around 19% of the fundamental. The second harmonic reaches 11.9%, while the fifth, sixth, seventh, and eighth harmonics remain below 10% each.

Figure 4.40(c) presents the inverter output voltage waveform at 150 rad/s. While the waveform is periodic, it is highly distorted due to significant harmonic content. As shown in Figure 4.40(d), the THD reaches 159.03%. The most prominent lower-order harmonics are the third (11.86%), fifth (10.6%), tenth (10.53%), and thirteenth (14.36%) components. Additionally, higher-order harmonics are present, each contributing up to 25% of the fundamental component, which explains the heavily distorted voltage waveform.

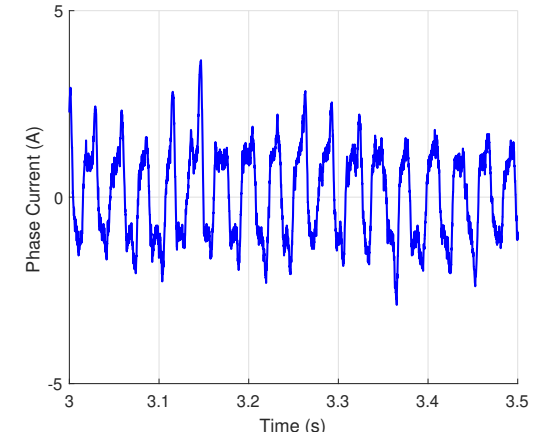

(a) Stator current waveform

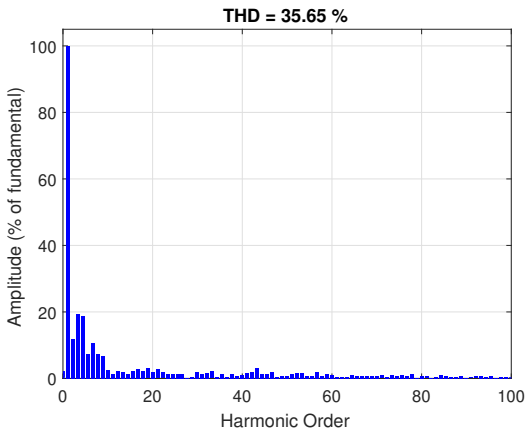

(b) FFT of stator current

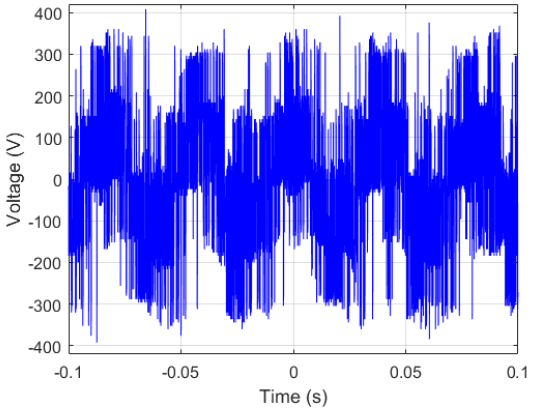

(c) Inverter output voltage

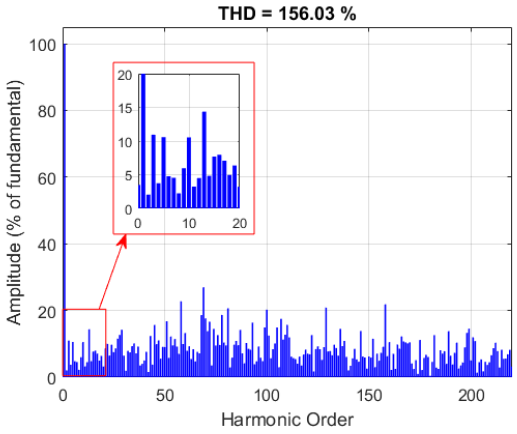

(d) FFT of inverter output voltage

Figure 4.40: Electric parameters for FCS-MPC under two open-phase faults

Despite the occurrence of open-phase faults, the FCS-MPC strategy succeeds in maintaining overall control of the system, demonstrating a certain level of **fault tolerance**. The **rotor speed still closely follows its reference** under these fault conditions. The **torque ripple is slightly increased**, especially at high speed, yet still remains within acceptable limits, while the **stator flux ripple remains low**, comparable to the healthy condition.

However, several performance indicators are **noticeably affected** by the severity of the fault. The **stator current distortion** is heavily impacted, with the total harmonic distortion (THD) increasing from **26.89%** in the healthy case to **32.84%** and **35.65%** under one and two-phase faults, respectively. The **peak current** also increases notably with fault severity, from **5.02A** to **5.2A** and **7A**. In addition, the appearance of the i_x and i_y current components, which reach significant values around **2A**, marks a clear departure from the healthy condition, where these components were practically negligible.

Table 4.1 summarizes the experimental results comparing the performances of the DTC, DTC-SVM with 2 vectors, DTC-SVM with 4 vectors, and FCS-MPC control strategies for the five-phase induction motor.

Table 4.1: Comparative results between DTC, DTC-SVM with 2 vectors, DTC-SVM with 4 vectors, and FCS-MPC.

Parameter	**DTC**	**DTC-SVM (2 vect.)**	**DTC-SVM (4 vect.)**	**FCS-MPC**
Response time	Fast	Moderate	Slow	Very fast
Torque ripple	Very high	Medium	Low	Moderately high
Flux ripple	Very high	Medium	Low	Very low
Stator current shape	More variable	Near-sinusoidal	Near-sinusoidal	More variable
Stator current peak	4.45 A	2.85 A	2.93 A	5.02 A
Stator current THD	19.58%	37.48%	12.44%	26.89%
Voltage THD	131.69%	103.88%	97.24%	57.36%
Load change response (no-load to full-load)	High drop, long recovery	Moderate drop, short recovery	Small drop, fast recovery	Very small drop, very fast recovery
Load change response (full-load to no-load)	High overshoot, long recovery	Moderate overshoot, short recovery	Small overshoot, fast recovery	Very small overshoot, very fast recovery
Fault tolerance	Maintains control performance, but current quality degrades severely	Maintains control performance, with moderate to strong current degradation	Maintains control performance, with mild current degradation	Maintains control performance, with moderate degradation, mainly in peak current
Computational resources	Very low (light processing required)	Moderate	High	Very high (most demanding)

4.7 Conclusion

This chapter presented the experimental validation of Direct Torque Control (DTC), Direct Torque Control with Space Vector Modulation (DTC-SVM), and Finite Control Set Model Predictive Control (FCS-MPC) applied to a 3.5 kW five-phase induction motor. The objective was to perform a comparative evaluation of these control strategies by analyzing their dynamic response, torque and flux regulation, stator current quality, harmonic content, and computational requirements under real operating conditions.

The experimental results confirm that FCS-MPC provides the fastest dynamic response, characterized by the shortest response time during speed variations, as well as the lowest speed deviation and smallest settling time during sudden load changes. It also achieves the lowest flux ripple. However, the stator current waveform is more variable and has the highest peak stator current during speed change. DTC-SVM with four vectors achieves the lowest torque

ripple and the best stator current quality, supported by its fixed switching frequency and its ability to eliminate components in the x–y plane. The two-vector variant of DTC-SVM shows improved performance over conventional DTC but results in higher total harmonic distortion (THD) in the stator current due to its inability to suppress these components. Classical DTC, while offering lower computational complexity, presents the highest levels of torque and flux ripple, along with the highest inverter voltage THD.

These results validate the trends observed in simulation and highlight the practical strengths and limitations of each control technique, offering valuable guidance for selecting the most appropriate strategy based on specific application requirements.

General Conclusion

General Conclusion

The research presented in this thesis focuses on the comparative study of different control techniques, initially designed for three-phase motors, applied to a five-phase induction motor. The studied strategies include Direct Torque Control (DTC), Direct Torque Control with Space Vector Modulation (DTC-SVM), and Finite Control Set Model Predictive Control (FCS-MPC). The analysis and comparison of these techniques, in terms of static and dynamic performance as well as power quality, were conducted through simulations in Matlab/Simulink, followed by experimental validation. This comparison helps guide the selection of the most suitable technique based on the specific requirements of each application while leveraging the advantages of multiphase motors.

To implement these control strategies, the modeling of the five-phase induction motor and its supply by a two-level five-leg inverter was carried out. The Park transformation was applied to simplify the motor equations. The modulation of the two-level inverter was also defined, considering its 32 switching states and the associated voltage vectors. This modeling serves as a fundamental basis for implementing the various control strategies studied in this thesis.

The comparative analysis conducted in this thesis between DTC, DTC-SVM, and FCS-MPC has highlighted several key results, namely:

- **Dynamic response:** The FCS-MPC control demonstrated the fastest dynamic response, characterized by the shortest response time during speed variations, as well as the lowest speed deviation and smallest settling time during sudden load changes. It outperformed all other strategies in both acceleration/deceleration and disturbance rejection. The DTC control follows, showing faster transitions than the SVM-based approaches, though it exhibits larger speed deviations and longer recovery times under load variation. DTC-SVM with two and four vectors provides slower speed tracking, with nearly identical settling behavior under load changes, though the four-vector version shows slightly improved smoothness and consistency in speed recovery time.

- **Torque control:** All control techniques effectively tracked the reference torque. The DTC-SVM control with 4 vectors exhibited the lowest torque ripple, ensuring a more stable torque response. Conversely, the conventional DTC control displayed the highest torque ripple, while the FCS-MPC control, despite its superior dynamic behavior, showed higher torque ripple than SVM-based methods.

- **Stator flux control:** The FCS-MPC control demonstrated superior accuracy and stability in maintaining the desired stator flux amplitude, with minimal deviations even during speed variations. The DTC-SVM strategies improved upon the classical DTC approach, with the 4-vector control offering a slight improvement in flux ripple compared to the 2-vector control.

- **Stator current quality:** The DTC-SVM control with 4 vectors produced stator currents closest to a sinusoidal waveform. In contrast, the DTC and FCS-MPC controls exhibited

more variable current waveforms, with higher current peaks during speed variations.

- **Harmonic content:** The analysis of the harmonic content of the stator current reveals that the DTC-SVM control with 4 vectors achieves the lowest THD, as it effectively eliminates x-y plane components while maintaining a fixed switching frequency. Conversely, using only 2 vectors in the DTC-SVM control does not eliminate these components, resulting in the highest THD despite the fixed switching frequency. Moreover, the higher THD observed in DTC and FCS-MPC control is attributed to their variable switching frequency, leading to increased harmonic distortion.

- **Computational resources:** The FCS-MPC control requires high computational power, making it more demanding in terms of processing, followed by the DTC-SVM control with 4 vectors, then the DTC-SVM control with 2 vectors, while the conventional DTC control requires the lowest computational power, making it more suitable for applications with limited processing capabilities.

- **Fault tolerance:** In addition to the healthy operating conditions, the behavior of the studied control strategies under open-phase fault scenarios was also analyzed. All four strategies (DTC, DTC-SVM with two and four vectors, and FCS-MPC) demonstrated a certain level of fault tolerance, maintaining acceptable control of speed, torque, and flux even under one or two open-phase conditions. However, several performance indicators were noticeably affected. The most critical impact was observed in the stator current quality, particularly in terms of total harmonic distortion (THD) and peak current magnitude. The conventional DTC strategy showed the most significant degradation in current quality, with strongly increased THD and peak current. The FCS-MPC also experienced elevated current peaks, despite preserving good dynamic behavior. In contrast, the DTC-SVM control using four vectors exhibited the least degradation in current quality, confirming its robustness under fault conditions. These observations highlight the need to further adapt and enhance existing control strategies to mitigate performance degradation during fault scenarios.

Furthermore, complementary approaches have been integrated to enhance the overall performance of the control strategies. Artificial Neural Networks (ANNs) have proven to be an effective alternative to Proportional-Integral (PI) controllers, thanks to their ability to dynamically adapt to variations in operating conditions. Additionally, the Model Reference Adaptive System (MRAS), based on rotor flux error, enabled sensorless speed control while ensuring accurate and robust rotor speed estimation.

In summary, while each control strategy presents distinct advantages, the FCS-MPC method demonstrates the fastest dynamic response and the most precise stator flux regulation. However, it exhibits higher torque ripple compared to DTC-SVM approaches, though still lower than that of conventional DTC. Among the studied techniques, DTC-SVM with four vectors achieves the lowest torque ripple and best stator current quality, producing near-sinusoidal waveforms with the lowest THD. This comes at the cost of increased response time. The classical DTC strategy responds faster than DTC-SVM but suffers from the highest torque and flux ripples, as well as greater harmonic distortion.

In terms of computational demand, FCS-MPC requires the most processing resources, followed by DTC-SVM with four and two vectors, while DTC remains the least computationally intensive. The integration of Artificial Neural Networks (ANN) for controller tuning and MRAS-based speed estimation enhances the adaptability and robustness of these control strategies, enabling sensorless operation and improved performance across varying conditions.

These results provide a solid foundation for selecting the most appropriate control technique based on the specific requirements of each application. Looking ahead, hybrid approaches that combine the strengths of different strategies, as well as the adaptation of these control techniques to address fault conditions in five-phase systems, represent promising directions for future research. Such developments would enable optimal utilization of five-phase induction motors while enhancing their performance, reliability, and applicability across a wide range of industrial environments.

Perspectives

This work opens several avenues for future research and practical development:

1. Integration of the five-phase induction machine into solar pumping systems, promoting energy-efficient and sustainable applications.
2. Implementation of a full five-phase system, including a dedicated five-phase inverter, instead of the two three-phase inverters used in this study.
3. Application of other intelligent control techniques, such as fuzzy logic, to enhance robustness and adaptability under uncertain conditions.
4. Implementation of MRAS-based control for improved sensorless performance and reliability.
5. Experimental validation of fault-tolerant control strategies, aiming to ensure system continuity under various fault scenarios.

Bibliography

Bibliography

[1] K. Iffouzar, B. Amrouche, T. Cherif, M. Benkhoris, D. Aouzellag, and K. Ghedamsi. Improved direct field oriented control of multiphase induction motor used in hybrid electric vehicle application. *International Journal of Hydrogen Energy*, 42:19296–19308, 2017. DOI: 10.1016/j.ijhydene.2017.06.195.

[2] S.A. Gaikwad and S.M. Shinde. Review on five-phase induction motor fed by five-phase voltage source inverter with different conduction mode. In *Proceedings of the 2020 International Conference on Industry 4.0 Technology (I4Tech)*, pages 199–202, 2020. DOI: 10.1109/I4Tech48345.2020.9102695.

[3] Lu Shuai and K. Corzine. Direct torque control of five-phase induction motor using space vector modulation with harmonics elimination and optimal switching sequence. In *Proceedings of the Twenty-First Annual IEEE Applied Power Electronics Conference and Exposition (APEC)*, page 7, 2006. DOI: 10.1109/APEC.2006.1620539.

[4] M.J. Duran and F. Barrero. Recent advances in the design, modeling, and control of multiphase machines—part ii. *IEEE Transactions on Industrial Electronics*, 63:459–468, 2016. DOI: 10.1109/TIE.2015.2448211.

[5] J. Kellner, S. Kaščák, and Ž. Ferková. Investigation of the properties of a five-phase induction motor in the introduction of new fault-tolerant control. *Applied Sciences*, 12: 2249, 2022. DOI: 10.3390/app12042249.

[6] H. Xu, J. Zhao, L. Yang, H. Chen, X. Luo, and S. Zhang. Research on open circuit fault modeling and fault tolerant control strategy of five-phase induction motor. *Processes*, 10: 1891, 2022. DOI: 10.3390/pr10091891.

[7] M.A. Mossa and H. Echeikh. A novel fault tolerant control approach based on backstepping controller for a five-phase induction motor drive: Experimental investigation. *ISA Transactions*, 112:373–385, 2021. DOI: 10.1016/j.isatra.2020.11.031.

[8] E. Levi. Multiphase electric machines for variable-speed applications. *IEEE Transactions on Industrial Electronics*, 55:1893–1909, 2008. DOI: 10.1109/TIE.2008.918488.

[9] C.S. Lim, E. Levi, M. Jones, N. Abdul Rahim, and W.P. Hew. Experimental evaluation of model predictive current control of a five-phase induction motor using all switching states. In *Proceedings of the 2012 15th International Power Electronics and Motion Control Conference (EPE/PEMC)*, pages LS1c.4–1–LS1c.4–7, 2012. DOI: 10.1109/EPEPEMC.2012.6397394.

[10] C.S. Lim, E. Levi, M. Jones, N.A. Rahim, and W.P. Hew. Fcs-mpc-based current control of a five-phase induction motor and its comparison with pi-pwm control. *IEEE Transactions on Industrial Electronics*, 61:149–163, 2014. DOI: 10.1109/TIE.2013.2248334.

[11] H. Guzman, M.J. Duran, F. Barrero, B. Bogado, and S. Toral. Speed control of five-phase induction motors with integrated open-phase fault operation using model-based predictive current control techniques. *IEEE Transactions on Industrial Electronics*, 61: 4474–4484, 2014. DOI: 10.1109/TIE.2013.2289882.

[12] H. Guzman, A. Iqbal, and F. Barrero. Reduction of common-mode voltage using a simplified fcs-mpc for a five-phase induction motor drive. *The Journal of Engineering*, 2019. DOI: 10.1049/joe.2018.8045.

[13] M. Bermudez, I. Gonzalez-Prieto, F. Barrero, H. Guzman, M. J. Duran, and X. Kestelyn. Open-phase fault-tolerant direct torque control technique for five-phase induction motor drives. *IEEE Transactions on Industrial Electronics*, 64(2):902–911, 2017. DOI: 10.1109/TIE.2016.2610941.

[14] A. Bhowate, M. Aware, S. Sharma, and Y. Tatte. Predictive torque control for five phase induction motor drive with common mode voltage reduction. In *2018 International Power Electronics Conference (IPEC-Niigata 2018 -ECCE Asia)*, pages 1730–1735, Niigata, Japan, May 2018. doi: 10.23919/IPEC.2018.8508015.

[15] G. Kulandaivel, E. Sundaram, M. Gunasekaran, and S. Chenniappan. Five-phase induction motor drive-a comprehensive review, 2023. DOI: 10.3389/fenrg.2023.1178169.

[16] H. Xu, H.A. Toliyat, and L.J. Petersen. Five-phase induction motor drives with dsp-based control system. *IEEE Transactions on Power Electronics*, 17:524–533, 2002. DOI: 10.1109/TPEL.2002.800983.

[17] M.J. Duran, F. Salas, and M.R. Arahal. Bifurcation analysis of five-phase induction motor drives with third harmonic injection. *IEEE Transactions on Industrial Electronics*, 55: 2006–2014, 2008. DOI: 10.1109/TIE.2008.918470.

[18] S.C. Rangari, H.M. Suryawanshi, and M. Renge. New fault-tolerant control strategy of five-phase induction motor with four-phase and three-phase modes of operation. *Electronics*, 7(9):159, 2018. DOI: 10.3390/electronics7090159.

[19] S. Khadar, H. Abu-Rub, and A. Kouzou. Sensorless field-oriented control for open-end winding five-phase induction motor with parameters estimation. *IEEE Open Journal of the Industrial Electronics Society*, 2:266–279, 2021. DOI: 10.1109/OJIES.2021.3072232.

[20] Y.-S. Lai and J.-H. Chen. A new approach to direct torque control of induction motor drives for constant inverter switching frequency and torque ripple reduction. *IEEE Transactions on Energy Conversion*, 16(3):220–227, 2001. DOI: 10.1109/60.937200.

[21] T. G. Habetler, F. Profumo, M. Pastorelli, and L. M. Tolbert. Direct torque control of induction machines using space vector modulation. In *Conference Record of the 1991 IEEE Industry Applications Society Annual Meeting*, pages 428–436, Dearborn, MI, USA, 1991. doi: 10.1109/IAS.1991.178191.

[22] G. Filliau, A. Alain Bondu, and L. Mazodier. Le navire tout electrique-propulsion et production d'énergie. *Traité « Les Techniques de l'Ingénieur »*, D5610, 2000. Reference: D5610.

[23] Koussaila Iffouzar. *Etude et Contrôle des Machines Asynchrones Polyphasées en Modes Normal et Dégradé. Application dans un Système Embarqué.* PhD thesis, Université de Béjaïa, 2016. Thèse de Doctorat, 2015/2016.

[24] X. Kestelyn. *Modélisation vectorielle multi machine pour la commande des ensembles convertisseurs-machines polyphasés*. PhD thesis, Université des Sciences et Techniques de Lille, 2003. Thèse de Doctorat.

[25] E. E. Ward and H. Harer. Preliminary investigation of an inverter-fed 5-phase induction motor. *Proceedings of the IEE*, 116(6):980–984, 1969.

[26] E. A. Klingshirn. High phase order induction motors - part i: Description and theoretical consideration, and part ii: Experimental results. *IEEE Transactions on Power Apparatus and Systems*, PAS-102(1), 1983.

[27] E. Semail, A. Bouscayrol, and J. P. Hautier. Vectorial formalism for analysis and design of polyphase synchronous machines. *European Journal of Applied Physics*, 22(3):207–221, 2003.

[28] J. P. Martin, S. Pierfederici, F. Meibody-Tabar, and P. Letellier. Synthèse des méthodes de filtrage du couple des msap polyphasées en modes normal et dégradé. *Revue Internationale de Génie Electrique*, 10(1-2):117–149, 2007.

[29] T. M. Jahns. Improved reliability in solid-state ac drives by means of multiple independent phase-drive units. *IEEE Transactions on Industry Applications*, IA-16:321–331, 1980.

[30] F. Locment, E. Semail, and F. Piriou. Design and study of a multi-phase axial-flux machine. *IEEE Transactions on Magnetics*, 42(4):1427–1430, 2006.

[31] F. Scuiller. *Développement d'outils de conception de machines polyphasées à aimants utilisant l'approche multimachine*. PhD thesis, Université des Sciences et Techniques de Lille, France, 2006. Thèse de Doctorat.

[32] H. A. Toliyat, T. A. Lipo, and J. C. White. Analysis of concentrated winding machine for adjustable speed drive applications - part ii: Motor design performance. *IEEE Transactions on Energy Conversion*, 6(4):684–692, Dec. 1991.

[33] D. C. White and H. H. Woodson. *Electromechanical Energy Conversion*. Wiley, New York, 1959.

[34] R. H. Nelson and P. C. Krause. Induction machine analysis for arbitrary displacement between multiple winding sets. *IEEE Transactions*, 93:841–848, 1974.

[35] B. Boussiala. Commande vectorielle d'une machine asynchrone polyphasée alimentée par onduleur à trois niveaux « application sur la machine heptaphasée ». Master's thesis, École Nationale Polytechnique, Algérie, 2010. Mémoire de Magister.

[36] Saad Khadar. *Contribution to Control of Five-Phase Induction Motor with Open-End Windings in Normal and Degraded Modes*. PhD thesis, Ziane Achour University of Djelfa, Department of Electrical Engineering, 2021. Doctoral Thesis.

[37] Fatima Zahra Khemili. *Modélisation et Commande des Machines Polyphasées et leurs Applications*. PhD thesis, Université Mohammed Seddik-Benyahia, Jijel, 2024. Thèse de Doctorat LMD, 2020/2024.

[38] F. Barrero and M. J. Duran. Recent advances in the design, modeling and control of multiphase machines – part 1. *IEEE Transactions on Industrial Electronics*, 2015. doi: 10.1109/TIE.2015.2447733. DOI: 10.1109/TIE.2015.2447733.

[39] W. Cao, B. C. Mecrow, G. J. Atkinson, J. W. Bennett, and D. J. Atkinson. Overview of electric motor technologies used for more electric aircraft (mea). *IEEE Transactions on Industrial Electronics*, 59(9):3523–3531, 2012.

[40] J. Liu, L. Huang, H. Yu, C. Wen, and W. Zhong. Study on the characteristics of a novel six-phase fault-tolerant linear permanent magnet machine for linear oil pumping. *IEEE Transactions on Applied Superconductivity*, 24(3), 2014.

[41] E. Jung, H. Yoo, S. Sul, H. Choi, and Y. Choi. A nine-phase permanent-magnet motor drive system for an ultrahigh-speed elevator. *IEEE Transactions on Industry Applications*, 48(3):987–995, 2012.

[42] BMW Group. Bmw i7 m70 and ix m60 specifications, 2023. Available online.

[43] NASCAR Engineering. Electric prototype motor configurations, 2024. Available online.

[44] Audi Motorsport. Audi e-tron fe07 drivetrain technology, 2023. Available online.

[45] Porsche AG. Porsche 919 hybrid specifications, 2023. Available online.

[46] Advanced Electric Machines. Six-phase motor technology for electric trucks, 2023. Available online.

[47] Bus Stop Sales & Service. Nine-phase electric drive system for buses, 2023. Available online.

[48] Dana TM4. Sumo hp six-phase inverter technology, 2023. Available online.

[49] G. K. Singh. Multi-phase induction machine drive research—a survey. *Electric Power Systems Research*, 61(2):139–147, 2002.

[50] E. Levi, M. Jones, S. N. Vukosavic, and H. A. Toliyat. A novel concept of a multiphase, multimotor vector controlled drive system supplied from a single voltage source inverter. *IEEE Transactions on Power Electronics*, 19(2):320–335, 2004.

[51] C. L. Fortescue. Method of symmetrical co-ordinates applied to the solution of polyphase networks. *Transactions of the American Institute of Electrical Engineers*, XXXVII(2): 1027–1140, 1918.

[52] R. H. Park. Two-reaction theory of synchronous machines generalized method of analysis - part i. *Transactions of the American Institute of Electrical Engineers*, 48(3):716–727, 1929.

[53] E. Clarke. *Circuit Analysis of AC Power Systems, Volume 1.* John Wiley & Sons, New York, USA, 1943.

[54] G. Kron. *Equivalent Circuits of Electric Machinery.* John Wiley & Sons, New York, USA, 1951.

[55] D. Hadiouche. *Contribution à l'étude de la machine asynchrone double étoile : modélisation, alimentation et structure.* PhD thesis, Université de Nancy 1, France, 2001. PhD Thesis.

[56] J. P. Caron and J. P. Hautier. *Modélisation et commande de la machine asynchrone.* Editions Technip, Paris, France, 1995.

[57] K. N. Pavithran, R. Parimelalagan, and M. R. Krishnamurthy. Studies on inverter-fed five-phase induction motor drive. *IEEE Transactions on Power Electronics*, 3(2):224–235, 1988.

[58] E. Robert-Dehault. *Modélisation dynamique, commande et conception de machines pentaphasées alimentées par des onduleurs MLI.* PhD thesis, Université de Nantes, France, 2005. PhD Thesis.

[59] E. Semail. *Outils et méthodologie d'étude des systèmes électriques polyphasés : généralisation de la méthode des vecteurs d'espace.* PhD thesis, Université de Lille 1, France, 2000. PhD Thesis.

[60] E. Levi, M. Jones, S. N. Vukosavic, and H. A. Toliyat. A five-phase two-machine vector controlled induction motor drive supplied from a single inverter. *EPE Journal*, 14(3): 38–48, 2004.

[61] M. Jones. *A novel concept of a multi-phase, multi-motor vector controlled drive system.* PhD thesis, University of Liverpool, 2005. PhD Thesis.

[62] A. Iqbal. *Modeling and Control of Series Connected Five-Phase and Six-Phase Two-Motor Drives.* Phd thesis, University of Liverpool, 2005. URL http://emp.etf.rs/radovi/Doktorski/atif.pdf.

[63] S. Gataric. A polyphase cartesian vector approach to control of polyphase ac machines. In *Conference Record of the 2000 IEEE Industry Applications Conference, Thirty-Fifth IAS Annual Meeting and World Conference on Industrial Applications of Electrical Energy (Cat. No.00CH37129)*, volume 3, pages 1648–1654, 2000.

[64] Y. Zhao and T. A. Lipo. Space vector pwm control of dual three-phase induction machine using vector space decomposition. *IEEE Transactions on Industry Applications*, 31(5): 1100–1109, 1995.

[65] H. A. Toliyat. Analysis and simulation of five-phase variable-speed induction motor drives under asymmetrical connections. *IEEE Transactions on Power Electronics*, 13(4):748–756, 1998.

[66] E. Levi, M. Jones, S. N. Vukosavic, and H. A. Toliyat. Operating principles of a novel multiphase multimotor vector-controlled drive. *IEEE Transactions on Energy Conversion*, 19(3):508–517, 2004.

[67] A. Iqbal and E. Levi. Space vector modulation schemes for a five-phase voltage source inverter. In *2005 European Conference on Power Electronics and Applications*, pages 12 pp.–P.12, 2005.

[68] B.S. Khaldi, A. Kouzou, M. Mahmoudi, and D. Boukhetala. Dtc-svm sensorless control of five-phase induction motor based on two different rotor speed estimation approaches. *Nonlinear Dynamics and Systems Theory*, 21:262–279, 2021. URL https://www.e-ndst.kiev.ua/v21n3/4(78).pdf.

[69] J. Listwan. Dtc-st and dtc-svm control of five-phase induction motor with mrascc estimator. *Przegląd Elektrotechniczny*, 1:254–258, 2016. DOI: 10.15199/48.2016.11.61.

[70] S.K. Barik and K.K. Jaladi. Five-phase induction motor dtc-svm scheme with pi controller and ann controller. *Procedia Technology*, 25:816–823, 2016. DOI: 10.1016/j.protcy.2016.08.184.

[71] E. Benyoussef and S. Barkat. Dtc-svm of sensorless five-phase induction machine using extended kalman filter. *International Journal of Circuits, Systems and Signal Processing*, 17:143–152, 2023. DOI: 10.46300/9106.2023.17.17.

[72] C. Martín, M.R. Arahal, F. Barrero, and M.J. Durán. Five-phase induction motor rotor current observer for finite control set model predictive control of stator current. *IEEE Transactions on Industrial Electronics*, 63:4527–4538, 2016. DOI: 10.1109/TIE.2016.2536578.

[73] A. Iqbal, S.M. Ahmed, M.A. Khan, M.R. Khan, and H. Abu-Rub. Modeling, simulation and implementation of a five-phase induction motor drive system. In *Proceedings of the 2010 Joint International Conference on Power Electronics, Drives and Energy Systems & 2010 Power India*, pages 1–6, 2010. DOI: 10.1109/PEDES.2010.5712373.

[74] S.A. Gaikwad and S.M. Shinde. Five-phase induction motor modeling and its analysis using matlab/simulink. In *Proceedings of the Smart Technologies for Energy, Environment and Sustainable Development, Vol 1*, pages 645–654, 2022. DOI: 10.1007/978-981-16-6875-$3_5$2.

[75] K.S. Aher and A.G. Thosar. Modeling and simulation of five-phase induction motor using matlab/simulink. *International Journal of Engineering Research and Applications*, 6:1–8, 2016. URL https://www.ijera.com/papers/Vol6_issue5/Part%20-%207/A0605070108.pdf.

[76] J. A. Riveros, M. J. Duran, F. Barrero, and S. Toral. Direct torque control for five-phase induction motor drives with reduced common-mode voltage. In *IECON 2012 - 38th Annual Conference on IEEE Industrial Electronics Society*, pages 3616–3621, Montreal, QC, Canada, October 2012. doi: 10.1109/IECON.2012.6389317.

[77] B.S. Khaldi, H. Abu-Rub, A. Iqbal, R. Kennel, M.O. Mahmoudi, and D. Boukhetala. Comparison study between a simple sensorless method and adaptive observer for dtc-svm five-phase induction motor drive. In *Proceedings of the 2012 IEEE International Conference on Industrial Technology*, pages 743–748, 2012. DOI: 10.1109/ICIT.2012.6210027.

[78] T. Yogesh and A. Mohan V. Direct torque control of five-phase induction motor with common mode voltage and current harmonics reduction. *IEEE Transactions on Power Electronics*, 32(11):8644–8654, November 2017.

[79] P. S. N. de Silva, J. E. Fletcher, and B. W. Williams. Development of space vector modulation strategies for five-phase voltage source inverters. In *Second International Conference on Power Electronics, Machines and Drives (PEMD 2004)*, volume 2, pages 650–655 Vol.2, 2004.

[80] M. Zelechowski. *Space Vector Modulated – Direct Torque Controlled (DTC – SVM) Inverter – Fed Induction Motor Drive.* PhD thesis, Warsaw University of Technology, Poland, 2005. PhD Thesis.

[81] V. Blasko. Analysis of a hybrid pwm based on modified space-vector and triangle-comparison methods. *IEEE Transactions on Industry Applications*, 33(3):756–764, 1997.

[82] D. Dujic, G. Grandi, M. Jones, and E. Levi. A space vector pwm scheme for multifrequency output voltage generation with multiphase voltage-source inverters. *IEEE Transactions on Industrial Electronics*, 55(5):1943–1955, 2008.

[83] A. Iqbal, S. Moinuddin, and M. R. Khan. Space vector model of a five-phase voltage source inverter. In *2006 IEEE International Conference on Industrial Technology*, pages 488–493, 2006.

[84] A. Iqbal and S. Moinuddin. Comprehensive relationship between carrier-based pwm and space vector pwm in a five-phase vsi. *IEEE Transactions on Power Electronics*, 24(10): 2379–2390, 2009.

[85] Z. Krzeminski. Nonlinear control of induction motor. *IFAC Proceedings Volumes*, 20 (5, Part 3):357–362, 1987. 10th Triennial IFAC Congress on Automatic Control - 1987, Volume III, Munich, Germany, 27-31 July.

[86] A. Iqbal and M.A. Khan. A simple approach to space vector pwm signal generation for a five-phase voltage source inverter. In *Proceedings of the 2008 Annual IEEE India Conference*, pages 418–424, 2008. DOI: 10.1109/INDCON.2008.4768760.

[87] U. Mahanta, D. Patnaik, B. P. Panigrahi, and A. K. Panda. Dynamic modeling and simulation of svm-dtc of five-phase induction motor. In *2015 International Conference on Energy, Power and Environment: Towards Sustainable Growth (ICEPE)*, pages 1–6, 2015.

[88] Jose Rodriguez, Leopoldo G. Franquelo, Samir Kouro, Jose I. Leon, Ramon C. Portillo, Ma Angeles Martin, and Marcelo A. Perez. Multilevel converters: An enabling technology for high-power applications. *Proceedings of the IEEE*, 97(11):1786–1817, 2009.

[89] Virginie Guennegues. *Contribution à l'étude des convertisseurs multiniveaux destinés aux applications moteurs rapides*. PhD thesis, Unknown Institution, 2009. PhD Thesis.

[90] Lm7815c pdf, lm7815c description, lm7815c datasheets. ALLDATASHEET [Online]. URL https://pdf1.alldatasheet.com/datasheet-pdf/view/1147583/ARTSCHIP/LM7815C.html. [Consulted on April 28, 2021].

[91] Liliang Gao and John E. Fletcher. A space vector switching strategy for three-level five-phase inverter drives. *IEEE Transactions on Industrial Electronics*, 57(7):2332–2343, 2009.

[92] P. Vas. *Sensorless Vector and Direct Torque Control*. Oxford University Press, London, UK, 2003.

[93] C. L. Toh, N. R. N. Idris, and A. H. M. Yatim. Constant and high switching frequency torque controller for dtc drives. *IEEE Power Electronics Letters*, 3(2):76–80, June 2005. doi: 10.1109/LPEL.2005.851316.

[94] N. Muley, A. Chabukswar, R. Sarkar, K. V. P. Kumar, and T. V. Kumar. Reduction of torque and flux ripples in direct torque controlled five-phase induction motor drive based on instantaneous voltage control technique. In *2016 IEEE International Conference on Power Electronics, Drives and Energy Systems (PEDES)*, pages 1–5, Trivandrum, India, December 2016. doi: 10.1109/PEDES.2016.7914433.

[95] B. Chikondra, U. R. Muduli, and R. K. Behera. An improved dtc technique for three-level npc vsi fed five-phase induction motor drive to eliminate common mode voltage. In *2019 National Power Electronics Conference (NPEC)*, pages 1–6, Tiruchirappalli, India, 2019. doi: 10.1109/NPEC47332.2019.9034720.

[96] Y. N. Tatte, M. V. Aware, J. K. Pandit, and R. Nemade. Performance improvement of three-level five-phase inverter-fed dtc-controlled five-phase induction motor during low-speed operation. *IEEE Transactions on Industry Applications*, 54(3):2349–2357, May-June 2018. doi: 10.1109/TIA.2018.2798593.

[97] S. Sabri, A. Benachour, and H.E. Guessar. Analysis and assessment of electrical and thermal performance of five-phase voltage source inverter under different modulation strategies: Comparative study under balanced and unbalanced load. *International Journal of Circuit Theory and Applications*, pages 1–28, 2024. DOI: 10.1002/cta.3971.

[98] A.A. Mekhilef, A. Benachour, E.M. Berkouk, and A. Dali. Fcs-mpc of a dmc-fed induction machine with unity input power factor using rotating vectors. In *Proceedings of the 2021 21st International Symposium on Power Electronics (Ee)*, pages 1–6, 2021. DOI: 10.1109/Ee53374.2021.9628355.

[99] J. A. Riveros, F. Barrero, E. Levi, M. J. Duran, S. Toral, and M. Jones. Variable-speed five-phase induction motor drive based on predictive torque control. *IEEE Transactions on Industrial Electronics*, 60(8):2957–2968, August 2013. doi: 10.1109/TIE.2012.2198034.

[100] H. Miranda, P. Cortes, J. I. Yuz, and J. Rodriguez. Predictive torque control of induction machines based on state-space models. *IEEE Transactions on Industrial Electronics*, 56 (6):1916–1924, June 2009. doi: 10.1109/TIE.2009.2014904.

[101] M. Tim Jones. *Artificial Intelligence: A Systems Approach*. Laxmi Publications, Ltd., 2008.

[102] Archana Mamadapur and G. Unde Mahadev. Speed control of bldc motor using neural network controller and pid controller. In *2019 2nd International Conference on Power and Embedded Drive Control (ICPEDC)*, pages 146–151. IEEE, 2019.

[103] David E. Rumelhart, Geoffrey E. Hinton, and Ronald J. Williams. Learning representations by back-propagating errors. *Nature*, 323(6088):533–536, 1986.

Annexes

Annexe A

Table 1: Parameters of the five-phase induction motor and control settings used in the experimental tests.

Parameter	**Value**	**Parameter**	**Value**
Pole pair number	1	P_{nom} [KW]	3.5
T_{nom} [N.m.]	12.7	R_s [Ω]	9.5
L_s [H]	1.389	L_m [H]	1.323
R_r [Ω]	7.3	L_r [H]	1.331
V_{dc} [V]	450	Switching period T_s [s]	0.001
Kp_{speed}	0.1	Ki_{speed}	0.05
Kp_{torque}	120	Ki_{torque}	50
Kp_{flux}	1000	Ki_{flux}	80

Annexe B

PI Speed Regulator

The speed regulation scheme with a PI controller is presented in Figure 0.1.

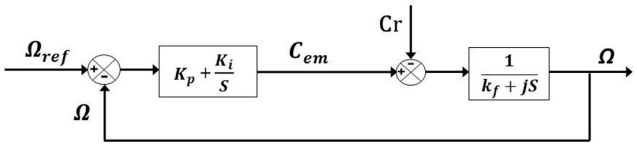

Figure 0.1: Block diagram of the PI speed regulation.

According to the mechanical equation of the machine and Figure 0.1, the closed-loop transfer function can be written as:

$$\Omega = \frac{1}{JS + k_f}\left(\left(k_p + \frac{k_i}{S}\right)(\Omega_{ref} - \Omega) - C_r\right) \tag{2}$$

This equation can be rewritten as follows:

$$\Omega = \frac{k_p S + k_i}{JS^2 + (k_p + k_f)S + k_i}\Omega_{ref} - \frac{k_p S + k_i}{JS^2 + (k_p + k_f)S + k_i}C_r \tag{3}$$

Considering the load torque as a disturbance, i.e., $C_r = 0$:

$$\Omega = \frac{k_p}{J}\frac{S + \frac{k_i}{k_p}}{S^2 + \frac{(k_p + k_f)}{J}S + \frac{k_i}{J}}\Omega_{ref} \tag{4}$$

The system is characterized by a second-order characteristic equation $P(s)$ written as:

$$P(s) = S^2 + 2\xi\omega_n S + \omega_n^2 \tag{5}$$

By identification:

$$\begin{cases} \omega_n^2 = \frac{k_i}{J} \\ 2\xi\omega_n = \frac{(k_p + k_f)}{J} \end{cases} \tag{6}$$

Thus:

$$\begin{cases} k_i = J\omega_n^2 \\ k_p = 2\xi\omega_n J - k_f \end{cases} \tag{7}$$

The gain is determined for a damping coefficient $\xi = 0.707$ and a system response time $t_{5\%} = 0.2$ s.

Annexe C

Total Harmonic Distortion (THD) is given by:

$$THD = \frac{\sqrt{V_2^2 + V_3^2 + V_4^2 + \cdots + V_n^2}}{V_1}$$

Principaux travaux effectués dans le cadre de cette thèse

Publications Internationales

- Abdelfattah Hoggui, Ali Benachour, Mohamed Chafaa Madaoui, and Mohand Oulhadj Mahmoudi, "Comparative Analysis of Direct Torque Control with Space Vector Modulation (DTC-SVM) and Finite Control Set-Model Predictive Control (FCS-MPC) of Five-Phase Induction Motors," *Progress In Electromagnetics Research B*, Vol. 108, pp. 89–104, 2024. doi:10.2528/PIERB24081702.

Communications Internationales

- A. Hoggui, K. Benkouachi, A. Benachour, and M. O. Mahmoudi, "Study and Implementation of DTC-SVM Control of Five-Phase Induction Motor Fed by Five-Phase Voltage Source Inverter," *2024 3rd International Conference on Advanced Electrical Engineering (ICAEE)*, Sidi-Bel-Abbes, Algeria, 2024, pp. 1–6. doi: 10.1109/ICAEE61760.2024.10783210.
- A. Hoggui, A. Mekhilef, A. Benachour, and M. Oulhadj Mahmoudi, "Comparative study between Direct Torque Control (DTC) and Finite Control Set-Model Predictive Control (FCS-MPC) of Five-Phase Induction Motor," presented at the *Eighth International Conference on Artificial Intelligence in Renewable Energetic Systems (IC-AIRES2024)*, Maison de l'Environnement de Tipasa, Algeria, October 26–28, 2024.